A study on state-dependent time-transient rotor dynamics of spur and helical geared rotating machinery

---

A Dissertation

Presented to

the Faculty of the School of Engineering and Applied Science

University of Virginia

In Partial Fulfillment

of the requirements for the Degree

Doctor of Philosophy (Mechanical and Aerospace Engineering)

by

Jason A. Kaplan

December 2015

Abstract

Predictions of the response of rotating machinery to external forces and assessments of system-level stability for different modes are crucial from a reliability and preventative maintenance perspective. Geared systems, in particular, contain many complexities such that the use of extensive computational effort is required to achieve accurate modeling. Sources of dynamic complexity at the gear mesh include non-linear tooth contact loss due to backlash clearance and parametric excitations from state-varying mesh stiffness effects. Although methods for determining the effects of dynamic meshing forces on the vibrations of rotor-bearing systems are in the literature, the models are either overly simplistic or require immense computational effort. Several time-transient and steady-state models for analyzing gear forces and deflections have been proposed, but those authors have focused primarily on the dynamics of the gearbox instead of vibration transmission through the remainder of the drive-train.

More recent models have used the finite element method to couple the lateral, torsional, and axial motions of the gear and pinion to the mesh forces and moments via element stiffness matrices. A finite element formulation of complete rotor-bearing systems, which couples the axial, lateral, and torsional degrees-of-freedom of geared shafts, is developed in this dissertation. The shaft structure is modeled with linear Timoshenko beam elements, and the non-linear gear mesh forces and moments incorporate effects from gyroscopic moments, shaft rotational speed variations, and includes models for parametric excitations from contact loss due to backlash clearance and state-induced mesh stiffness variations. Time-transient state equations for the displacements and velocities of the shafts are solved using the direct Runge-Kutta method, and the methods are applied to three different geared machines. A parametric study investigating the sensitivity of shaft vibration to several sources of excitation is included and the results yield additional insights into proper modeling techniques.

Approval Sheet

This dissertation is submitted in partial fulfillment of the requirements for the degree of

Doctor of Philosophy (Mechanical and Aerospace Engineering)

Jason A. Kaplan

This dissertation has been read and approved by the Examining Committee:

Houston G. Wood, Advisor

Carl R. Knospe, Committee Chair

Zongli Lin

John G. Thacker

Roger L. Fittro

Alexandrina Untaroiu

Accepted for the School of Engineering and Applied Science:

Craig H. Benson, Dean, School of Engineering and Applied Science

December 2015

Acknowledgments

I have been very fortunate to have completed my undergraduate, masters, and now doctoral studies at the University of Virginia. The collaborative and supportive environment within the Rotating Machinery and Controls (ROMAC) Laboratories has been influential in helping me achieve my goals.

I would like to thank my advisors Prof. Houston Wood, Roger Fittro, and Alexandrina Untaroiu for their steadfast support and encouragement. Not only have they challenged me to think more critically about the details of my work, but they have also been influential in helping me think about its broader context. It has been a real pleasure working alongside them in a variety of other projects during my time in ROMAC, and they have ultimately better prepared me for work in industry. I also appreciate them for putting substantial time into revising much of the work done in this dissertation.

I would like to thank all the other members of my committee (Prof. Carl Knospe, Prof. Zongli Lin, and Prof. John Thacker) for reviewing and giving me the feedback needed to produce quality work. Their feedback and comments are greatly appreciated.

I would also like to thank Hunter Cloud and Minhui He from BRG Machinery Consulting for supplying me with details about a gearbox that was not only instrumental to the benchmarking of the work shown, but that also resulted in an important chapter in this dissertation. I hope they find the results encouraging, and that it may advance the work they have been doing.

Much of my time in ROMAC was spent interacting and working with several amazing graduate students. I will always remember the meaningful and often just plain silly conversations I have had with Michael Branagan, Dee Di, Neal Morgan, Day Griffin, Benny Schwartz, Bradley Nichols, and Saeid Dousti. I have learned much from working with them and will greatly miss our graduate office dynamics.

The support of several ROMAC staff has been greatly appreciated. I have Lori Mohr Pedersen to thank for her encouraging words and for all the effort she has put into making ROMAC lively in my final year. Aside from organizing potlucks and lunch outings, she went out of her way to make everyone feel comfortable and appreciated. I will greatly miss her office decorations and her optimistic spirit. I am especially grateful for the many conversations Brian Weaver and I have had in the lab. I have always appreciated his insightful comments and the time he has set aside to talk through research plans.

My parents, Michael Kaplan and Carolyn Kaplan-Solomond, have continuously been a solid rock of support throughout my 10 years at UVa (and even earlier, of course). I suppose the apple did not fall far from the tree considering that they are both engineers with advanced degrees. I also appreciate John Solomond for his keen interest in not only my progress but also in the actual research itself. I am thankful to make them even more proud and to join the family of engineers.

The list of friends and family I could thank would fill at least two pages, so I will have to abbreviate the list. My Bible study group has been so encouraging throughout these past couple years, and I am thankful for the times I could come to them for prayer and support: Robbie Hott, Megan Wilson, Stephen Grado, Anne Kyner, R.J. Santucci, and Christen Fortmuller. I am thankful for my housemates this past year and for how they put up with my odd work hours and increasingly neurotic behavior patterns: Jake Truelove, Andrew Lam, Jeffrey Smith, Conor Gannon, and Nathan Rose. My acknowledgment would be incomplete without thanking Conor Gannon for the inspirational Great Gatsby face he observed in some of my plots. I am glad I could honor his discovery by placing one of them in the conclusion slide of my defense presentation. To all other family and friends, your support has meant the world to me, and I wish I could thank everyone individually.

My girlfriend, Rejina Stallings, has been incredibly supportive from the beginnings of the dissertation writing to its completion. Between sending me power snack packages and encouraging messages, she has gone out of her way to be my best friend through it all. I am so excited and thankful for the adventures we will have together.

I also want to dedicate this dissertation to my grandpa Irv Kaplan, and my Zaidy, Leon Hack. I miss them very much and know they would be proud if they could see the work done. The most important lesson I learned from them was about the value of maintaining integrity and honor in everything that one does, and I can only hope to live up to their examples. May this dissertation honor their memories.

Although I am receiving credit as the author of this dissertation, I recognize and acknowledge that none of this would have been possible without the faithfulness of my Lord my God. “Let us hold unswervingly to the hope we profess, for he who promised is faithful.” Hebrews 10:23

Contents

List of Tables

List of Figures

Chapter 1

Introduction

High-speed rotating machinery such as compressors, turbines, and pumps are used for a wide variety of applications that convert rotational energy into a useful form of work. During steady or transient operating conditions, dynamic forces act on the shafts that tend to increase or decrease their stability from a vibration perspective. Destabilizing forces tend to add energy to, and in phase with, the existing vibration pattern, which may increase its amplitude to potentially dangerous levels. The primary source of stability, however, comes from the damping forces in the bearings and these must be greater than the destabilizing forces to mitigate the instability. Some of these destabilizing forces are external loads such as electromagnetic push-pull from generators, while others are internally generated such as fluid-structure interactions within fluid film bearings and other components or state-varying gear tooth contact. Under circumstances, detailed knowledge of these forces is paramount to ensuring safe operation of high-speed rotating machinery especially since the consequence of failure could be significant financial loss due to machine outage.

1.1 Literature review

The concept of gearing and the benefits of its mechanical advantage have been known since the beginnings of rotating machinery and yet many aspects of gearbox dynamics are still not fully understood. Gearbox dynamics are important to understand because of their prevalence in a wide variety of rotating machinery and because they can transmit and excite vibration throughout the entire structure. Automobile transmissions, jet engines, turbine-generator systems are just a few of many applications that benefit from the inherent torque-speed mechanical advantages.

Despite these advantages, geared systems are susceptible to failure via dynamic tooth stresses, pitting and scoring, and self-exciting instabilities [1, 2, 3, 4]. Noise radiation has also been a concern particularly for naval applications that require stealth. Models of varying complexity and detail have been necessary to explore each of these phenomenon and range from single degree of freedom (SDOF) torsional models to detailed finite element (FE) models of the gear mesh interface [1]. Ozguven et al provides a comprehensive review of geared system analyses and splits them into 4 model categories: dynamic factor, tooth compliance, gears and rotor dynamics, and recent advances [1]. This section will explore the foundation of gear dynamics research and its evolution into modern geared rotor dynamic analyses. Gear dynamics have been systematically studied since the 1920s and early 1930s. The objectives in gear dynamic analyses are vast and include models of the following phenomena: bending and contact stresses; scoring and pitting; transmission efficiency; noise radiation; loads on other machine components; system natural frequencies; stability regions; rotor whirl; reliability; and life [1].

1.1.1 Dynamic factor

The first models focused solely on determining dynamic loads acting on gear teeth through analytical and experimental methods. The purpose of these early studies was to determine the dynamic stresses at the gear roots and to therefore obtain gear life estimates. Studies, such as Tuplin's, determined that dynamic loads were not just influenced by pitch line velocities but also by tooth errors and the inertias of the gear and pinion [6]. The inclusion of vibratory models in the dynamic analysis of gears allowed for the investigation of additional dynamic properties [1].

1.1.2 Tooth compliance

Computationally straight forward mass-spring dynamic models of gears which included the compliance of gear teeth emerged in the 1950s and early 1960s and served as the first transition between analyzing tooth dynamic loads and accounting for the compliance of several gear components [1]. The models that fit within this category assume that compliance is limited to the gear tooth and that all other components are rigid. Various analyses assumed the gear mesh stiffness to be constant in time or to have time-varying properties of sinusoidal or rectangular waves. Manufacturing errors, variation in tooth stiffness, and non-linearity in tooth stiffness from loss of contact were considered to be the three main internal sources of vibration and were incorporated into many of these models in the form of periodic input displacements at the gear mesh location [43]. Despite the simplistic nature of these single DOF models, they could predict dynamic instabilities due to parametric excitations of the gear mesh and from varying the mesh stiffness [2]. An example is shown below in Figure 1.1 and is one of the first models to investigate the effects of gear error on the dynamic loading of gear teeth. Gear error disturbances were introduced into the model by vertically displacing the wedge.

Another classical example of a tooth compliance model is shown below in Figure 1.2. Torsional vibration is considered and the stiffness and damping of the teeth are represented by a spring and dashpot pair. Gear error is introduced into the model in the form of a displacement input at the mesh.

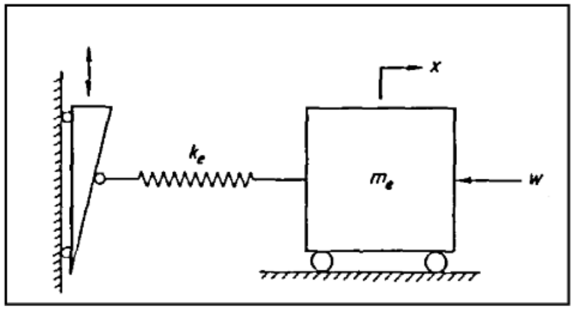

Figure 1.1: Spring-mass model created by Tuplin to investigate the effects of gear error on dynamic loading of teeth [1, 6].

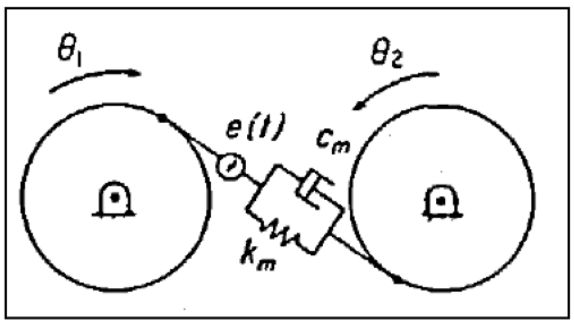

Figure 1.2: Torsional model of gears in mesh with constant stiffness, damping, and a displacement input representing gear error [1].

Additional models of tooth compliance emerged in the 1970s and were the first to include the finite element method. This was a significant departure from treating the gears as lumped inertias and the gear teeth as massless springs since the problem could be formulated much closer to a continuum. Lin, Huston, and Coy investigated the differences in the results obtained using Timoshenko beam and finite element models and discovered that they were substantial for stubby tooth forms [44]. One study used the finite element method to study the effects of dynamic loading on the stress, deformation, and fracture in gear teeth [45]. Wang and Cheng used the finite element method solely to determine the variable tooth stiffness of involute spur gears, which was then included in a single DOF lumped model [46]. Their finite element analysis was used to generate a set of curves relating dimensionless tooth stiffness to the number of gear teeth and the loading position throughout the mesh cycle. The dimensionless tooth stiffness was a function of Young's modulus, load per unit face width, and the root radius of the gears.

Second order effects such as damping and friction appeared in several of these models. Umezawa, Sato, and Kohno modeled the compliance of spur gear teeth as three trapezoidal beams where they determined the bending deflection, shear deflection, and stamp effect at the base of the tooth using Ishikawa's equation [47]. They also determined the Hertzian or contact deflection using Weber and Banaschek's equation [48]. Alternative forms of error such as those in the pressure angle, normal pitch, and tooth profile were included in their model and the simulation results for natural frequencies showed good agreement with experimental values. Despite the increases in the complexity of tooth compliance models using finite element analysis, the results showed little differences from those of the pioneering simple mass-spring category with the exception of high-speed cases [1]. Researchers determined, however, that more general models that incorporate the flexibility of other machine components were necessary for several practical applications. Vibration coupling between the gears and their respective shafts and bearings could no longer be neglected when they have comparable stiffnesses.

1.1.3 Gears and rotor dynamics

The effects of gearing on the lateral behavior of shafts were considered in gear dynamics problems in the late 1960s and early 1970s [1]. It was determined that experimental agreement existed for the earlier models because the experiments were designed to satisfy the assumptions of the models regarding the flexibility of the gear teeth relative to the shafts and bearings. These assumptions were often valid for cases where the geared shafts were short and thick but would fail for longer and more slender shaft components. These discoveries prompted the rise for more general gear models and represent the beginnings of gear dynamics where the lateral and torsional degrees of freedom of the shafts are coupled with those of the gears. Several models, however, are simply torsional and account only for the torsional stiffness of the geared shafts [9, 10, 11, 12]. Others include both torsional and lateral motions and consider the torsional and lateral stiffnesses of the geared shafts [5, 8, 7]. Other studies ignore the flexibility of the gear teeth and construct torsional models of rigid gears while the shafts were considered flexible [13, 14]. Their emphasis was placed less on the gear dynamics and more so on the dynamics of the connected shafts and their interactions with the bearings. An example of a laterally and torsionally coupled model is shown in figure 2.3.1. The shafts have torsional stiffness, and the gears have tooth mesh stiffness and lateral stiffness contributions from the shafts and bearings. Mass moments of inertia of the prime mover, load, and the gears are also included in this model.

Several innovations in gear dynamics emerged in the 1970s and 1980s. Models for 3-D stiffness of gear teeth, and non-linear behavior of system elements such as bearings and gear backlash emerged. In addition, friction models of gear teeth included damping and excitation forces. In the late 1980s, developments in axial, lateral, torsional, and plate mode vibrations of geared systems emerged. Both steady state and transient system responses resulting from many variations of gear errors and time-varying mesh stiffness were considered.

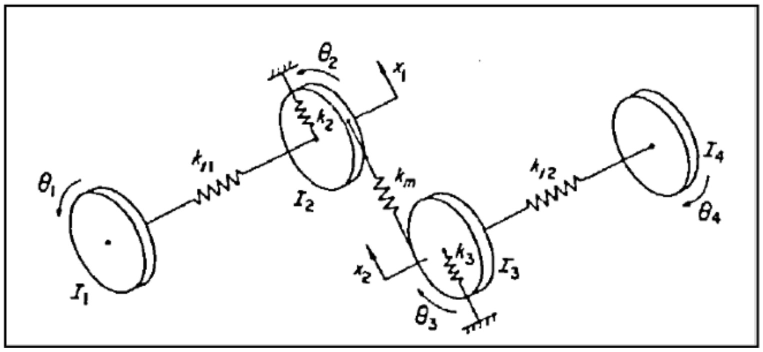

Figure 1.3: Laterally-torsionally coupled model of a shaft-gear system [1].

Johnson's model replaced a varying mesh stiffness by a constant stiffness equal to its mean value and was one of the first attempts at using the gear mesh stiffness to couple the vibration of geared shafts [49]. Kiyono et al focused on constructing helical gear models to compare the results with those of spur gears [50]. They included torsional, lateral, and axial degrees of freedom and treated the gear mesh stiffness as constant. Troeder developed a helical gear pair-shaft-bearing system which involved a torsional, lateral, and axial vibration model where the tooth mesh stiffness was approximated by a Fourier expansion in the form of a square-wave [51]. Kucukay incorporated axial, lateral, and torsional vibration for single-stage helical and spur gear pairs with periodic tooth mesh stiffness, tooth errors, external torques, load dependent contact ratio, and non-linearities from the separation of gear teeth [52]. Kucukay's results indicated that linear model approximate solutions for the steady-state tooth displacements and loads varied negligibly from the non-linear results. Ozguven produced a six degree of freedom non-linear model of a spur geared system with time-varying mesh stiffness [53]. The spur geared system consisted of a prime mover, pinion, gear, and load, and the degrees of freedom corresponded to four angular rotations of all components and two translations of the gear and pinion along the line of action. Several factors were explored, such as damping, tooth separation, backlash, single and double-sided impacts, and various gear errors (pitch, profile, and run-out). A forced response analysis to internal excitations was conducted and demonstrated the effects of the shaft and bearing dynamics on the gear dynamics.

Mathematical models for geared rotor dynamics emerged in the 1960s as researchers sought to consider the whirling behavior of gear-carrying shafts which required lateral analyses in two mutually perpendicular directions. Although the models in the previous group for geared dynamics considered lateral vibration, the motion was usually restricted to one direction along the line-of-action (LOA). Daws and Mitchell constructed a three-dimensional model of gear coupled rotors in which they used a time-varying stiffness tensor to model the variable mesh stiffness [54]. The interaction between the time varying stiffness and gear deflections was used to predict the forced response of the coupled gear rotors to excitations from mesh errors and unbalanced rotors. Another set of studies examined the free and forced vibration of geared shafts using constant and periodically varying tooth mesh stiffness [55]. The forced response was originally due to mass unbalance but was later extended to include tooth profile errors. These studies used the transfer matrix method for computational efficiency especially when the models included non-linear dynamics.

Additional geared rotor dynamic models emerged that incorporate the finite element method to couple the degrees of freedom of connected geared shafts. Neriya, Bhat, and Sankar modeled each gear as a set of two masses, two springs, and two dampers where one set represented the gear and the other a tooth [65]. The shafts were modeled as finite elements and the torsional-lateral coupling could be conveniently introduced at the gear pair locations in the form of stiffness and damping matrices. They assumed constant mesh stiffness and conducted a free vibration analysis to determine the undamped natural frequencies of the linear system. These undamped modes would then be used to calculate the forced response vibration due to mass unbalance and gear eccentricity. They concluded that predictions of geared rotor dynamic behavior, such as critical speeds, mode shapes, and stability onset, are more accurately modeled in finite element analyses when lateral and torsional motions are coupled instead of uncoupled. These results, however, were limited to simple spur-geared systems. Luo produced a general finite element based model of multi-stage and multi-mesh geared rotor systems that incorporates axial, lateral, and torsional coupling which is applicable to both spur and helical geared systems [64]. A modal synthesis technique was employed so that the model may have a large number of degrees of freedom without the need for a large amount of computer memory. The researchers used a gear transmission in an aircraft engine as an example and showed the axial, lateral, and torsional coupling of modes which is in general agreement with field observations.

Lin and Parker developed a systematic method to analyze the effects of mesh stiffness variations on the instabilities of two-stage spur geared systems [25]. The variations in mesh stiffness were produced by altering the following: mesh frequencies, time-varying mesh stiffness amplitude, contact ratio, and mesh phasing. The two gear mesh stiffnesses were modeled as having mean and time-varying components, where the time-varying parts are periodic at their respective mesh frequencies and are expressed in Fourier series. Analytical solutions were obtained for rectangular waveform tooth mesh stiffnesses and support the notion that perturbations in contact ratio and mesh phasing substantially eliminate or decrease the size of instability regions. Other findings suggest that the excitations originating from one gear mesh may interact substantially with those of the other especially when their frequencies are integer multiples of the other. Cai develops a vibration model for involute helical gear pairs that incorporates contact ratio, tooth surface errors in the form of shaft deviation and pressure angle errors, and non-linear tooth separation phenomena [56]. A modified stiffness function was produced for a free vibration analysis of the gear pair that includes the effects of addendum modification coefficients, and number of teeth. The dynamic equations of motion are solved using the finite difference method on a 16-bit computer and yield results similar to the experiments and simulations of previous researchers such as Umezawa [48].

Brauer derived a mathematical set of equations describing the shape of conical involute gears and three other types to be used in finite element models [57]. His work was a significant improvement over previous geometric gear models in CAD programs which required large amounts of computational time to generate highly accurate tooth surfaces. The use of equations to define the tooth surfaces not only presented a quicker method to generate the gear model and its elements but is also more robust. Li, Chiou, et al. developed a module that integrates finite element analysis of gear bodies with gear design optimization [58]. This module offered an automatic design optimization routine using interfacial programs that connected programs that accomplish pre-processing, finite element analysis, and optimization. Consequently, this significantly shortened the procedure of rebuilding gear models through CAD programs to search for an optimal design that satisfies stress/strain requirements obtained from FEA.

Chowdhury produced a model of a helical gear pair mounted on two flexible shafts with rigid bearings using Hamilton's principle [59]. The shafts were modeled as continua with torsional and lateral flexibility while the gears were treated as rigid disks connected by laterally-torsionally coupled mesh springs with time-averaged stiffness. Free vibration analyses of the partially discrete, partially continuous geared system were performed using Galerkin discretization to evaluate eigenvalue sensitivities to rotational speed, and gear mesh stiffness. Forced response analyses due to the effects of static transmission error were conducted using modal analysis. Kahraman et al developed a finite element model of a spur-geared rotor system with flexible shafts and bearings with degrees of freedom in the lateral and torsional directions [60]. The tooth mesh stiffness is modeled as a spring and damper, with constant stiffness and damping, along the pressure line and is used to produce gear mesh stiffness and damping matrices. Variable mesh stiffness effects were modeled by using a displacement excitation originating at the mesh. These mesh matrices would be added to the uncoupled rotor matrices to complete the global matrices. Critical speeds, mode shapes, and the system forced response to gear mass unbalance, runout, and static transmission error were evaluated. Kahraman et al concluded that the relative compliance of the shaft and the bearings greatly influence not only the mode shapes and natural frequencies but also the dynamic tooth load.

Sun derived a new analytical formula to calculate the bending deformation of involute helical gear teeth using more realistic assumptions of the tooth profile, mass, and load distributions [66]. He divides the tooth section into multiple copies along the spiral angle direction and considers the variable cross-section moment of inertia due to the changing tooth profile, and the variable contact distribution caused by the changing length of the contact line. This method was applied to a helical gear pair example and the results were compared with those of finite element analysis and Ishikawa's method [47]. The results indicated that Sun's analytical formula more closely represented those of FEA than previous formulas such as Ishikawa's.

Stringer developed the methodology for generating a 12x12 gear mesh stiffness matrix that couples the axial, lateral, and torsional degrees of freedom of geared-rotor systems and is therefore applicable to both spur and helical gears [36]. The stiffness matrix is derived from force balances taken along the line of action (LOA) using the Influence Coefficient method, and it incorporates the effects of the normal pressure angle, helical angle, and the arbitrary orientation of the meshing gears. This arbitrary orientation angle of the meshing gears offers a significant advantage over other gear mesh finite element methodologies since it is applicable to complicated gear models where a convenient choice of axes may not be available. A model of a spur-geared-rotor system and bearings is used as an example, and it includes gyroscopic forces and the effects of bearing stiffness and damping properties. The results indicate that the inclusion of the stiffness matrix produces many of the same natural frequencies and modes of the non-geared system but also produces additional ones that represent laterally and torsionally coupled modes. The methods used in Stringer's work are very general and are useful in the creation of broader rotor dynamic models where the gear mesh is one of many substructures.

Despite the increases in the complexity of tooth compliance models using FE analysis, the results showed little difference from those of the pioneering mass-spring models with the exception of high-speed cases [1]. Researchers determined, however, that more general models that incorporate the flexibility of other machine components were necessary for several practical applications. Vibration coupling between the gears and their respective shafts and bearings could no longer be neglected when they have comparable stiffness. Some models included lateral and torsional flexibility of the shafts and gear teeth [5, 7, 8], while others focus exclusively on the torsional vibration of the shafts and gears [9, 10, 11, 12] and still other torsional models of the shaft with rigid gear teeth [13, 14].

More recent studies have investigated the effects of the state-varying mesh stiffness and non-linear backlash phenomena on the vibration of geared shafts [15, 16, 17, 18, 19, 20]. Others have explored the influence of non-linearities not only from the gear mesh but from other components such as bearing clearance, oil film, and flexible supports [21, 22, 23]. Some instability studies have extended the inclusion of state-varying stiffness and non-linear backlash to multi-stage geared systems [24, 25, 26, 27]. Parker et al used a semi-analytical finite element formulation with a contact mechanics model to evaluate the mesh stiffness at each time step over a single tooth pass. Vibration results were compared with a couple of single degree-of-freedom models and to experimental data. Such an approach eliminates the need to specify assumptions about the form of the time-varying gear mesh stiffness [28]. The results indicated high sensitivity to the spectral content of the rectangular waves being used to represent the state-varying mesh stiffness. Finally, bifurcation and transitions to chaos have also been studied using SDOF models [29, 30, 31, 32].

1.2 Problem statement

Despite the advances in the literature of modeling the effects of state-varying mesh stiffness and the backlash non-linearity on gearbox dynamics, the studies have focused exclusively on either SDOF systems or simplified lumped parameter models for the geared shafts. Since the mass of the shafts are typically ignored and the shaft stiffness is approximated by single linear springs, significant details for evaluating machine safety, such as rotor whirl orbits, are inherently oversimplified. Detailed knowledge of the rotor whirl orbits are not only essential to recognizing potential for high-amplitude vibration but also provide the analyst with insights that may correct the problem. A classic sign of potential instability in a rotating machine is seeing a flexible rotor mode shape and noticing little displacement at the bearings. The analyst could infer that the bearings are too stiff and should recommend a softer bearing so that journal motion at the bearing sites would allow for more effective damping. Additional insights could also be used to shift rotor natural frequencies further away from operating speed ranges by simply adjusting the bearing span or adding or subtracting mass from the rotor at specific locations. These necessary insights may only be discovered by discretizing the shaft into elements, and modern day computing power is robust enough to use beam finite elements for time-transient calculations within a reasonable amount of time.

Classic rotor dynamic treatment of geared systems has relied on assuming the gear mesh stiffness to be infinitely rigid relative to the shaft. Conversely, there have been many studies where the tooth compliance is the only potential energy storing element in the system and the shafts are considered rigid [1]. Either set of assumptions may reasonably represent some geared systems, but there are many realistic case studies where these do not apply. Developing a model that captures the finite stiffness of the shafts, gear teeth, and bearings is crucial since their relative magnitudes greatly influence the machine dynamics at a system level with no loss of generality.

In addition, these studies have neglected to use excitations beyond external torques and mesh frequency excitations at the gear interface, while conventional rotor dynamic analyses for high-speed machinery typically require the inclusion of lateral excitations such as unbalance. Furthermore, gyroscopic moments play a crucial role in predicting the forward and backward whirl modes of rotors and these have also been omitted from previous studies. Transient phenomenon such as start-up and wind-down are also important operating conditions to consider especially since many rotor systems are designed to pass through their first critical speeds. Other machine natural frequencies may be excited during these operating conditions, and they could have a large influence on the transient predictions.

While commercial FEA codes for geared systems exist, they focus on the design of the gearbox and all of its complexities such as the housing so that it may integrate efficiently with the expected loading conditions from the remainder of the drive-train. 3-D finite elements are used to evaluate the deflections of the shafts, bearings, gear teeth and bodies, and housing for both steady-state and time-transient conditions. In addition, detailed dynamic analyses of the mesh interface reveal the transmission error excitations over a single-tooth pass. Despite the complexity of these models, it is generally understood that the use of 3-D finite elements may require vast computing power and may have substantially longer solve times especially for transient analyses. The emphasis for these analyses is still, nevertheless, focused on the design of the gearbox for mitigating noise and is directed towards consideration of the potential whirling instabilities that may be induced for the rest of the drive-train.

There is currently interest in the rotor dynamics community in understanding the effects of different gear parameters on the vibration characteristics of realistic rotor systems. Although detailed methods have been presented in literature and commercial software is available, the results are rendered impractical to industry when their emphasis is on the dynamics of the gearbox rather than on the dynamics of the complete machine. Furthermore, previous models have neglected to apply relevant forcing functions to realistic geared systems such as gyroscopic moments, which affect the response for both constant velocity and start-up operating conditions.

1.3 Research objectives

A finite element approach to studying the non-linear time-transient behavior of generalized parallel-shaft geared systems is proposed. The axial, lateral, and torsional DOFs of the geared shafts are included and coupled via transformation matrices that relate the generalized displacements and forces along the line of action to those of the shaft nodes [34]. State-varying mesh stiffness is incorporated and contributes to parametric excitations at the gear mesh interface. Gear tooth backlash is modeled as a piecewise-linear function that is dependent on the dynamic transmission error at each time step. Rotational accelerations are accounted for in the equations of motion and are applicable to analyzing start-up or wind-down conditions. The generalized displacements and velocities of each node are evaluated at each time step via the direct Runge-Kutta method.

The primary objective of this study is to extend the existing modeling for parametric excitations due to state-varying mesh stiffness and non-linearities such as tooth backlash clearance to more realistic geared shaft bearing systems. In addition, such a study promotes discussion of the many parameters involved in the modeling of state-varying mesh stiffness and backlash and how they can influence the transient behavior of complete geared systems. This study will benefit members of industry by allowing an assessment of the following parameters and their effects on the system response:

- Mesh phasing on multistage parallel shaft systems
- Unbalance magnitude
- Backlash modeling and clearance
- Operating conditions that lead to loss of tooth contact and non-linear behavior
- Bearing lateral damping coefficients on the torsional response during start-up
- Number of Fourier series rectangular wave coefficients to model state-varying mesh stiffness
- Contact ratio
- Relative amplitude of state-varying mesh stiffness to average mesh stiffness

It is expected that a thorough investigation of these parameters will provide more insights on proper modeling techniques for geared machinery. The following section provides details for the numerical methods and theory used to evaluate the displacements and velocities of geared rotor bearing systems. In addition, a plan for benchmarking the results of these analyses with other simulation tools is discussed.

Chapter 2

Research plan

2.1 Objectives

The research plans laid forth in this chapter have been developed to meet the following objectives for geared systems:

- Assess influence of non-constant stiffness and damping coefficients due to shaft speed fluctuations
- Investigate lateral-torsional coupling of geared systems by observing damping of torsional modes
- Assess influence of shaft dynamics on the overall system response using Timoshenko beam elements
- Discuss sensitivity of vibration response due to the following factors:
    - Unbalance magnitude
    - Size of backlash clearance
    - Number of Fourier series rectangular wave coefficients to model state-varying mesh stiffness
    - Contact ratio
    - Relative amplitude of state-varying mesh stiffness to average mesh stiffness

2.2 Outline of methods

Details for the gear mesh modeling are developed in Chapter 3 of this dissertation and are divided into three areas. Section 3.1 provides the basis for gear mesh modeling by introducing the finite element method as a tool to solving the rotor dynamic equations of motion for both steady-state and time-transient orbits.

The shafts are modeled as 1-D Timoshenko beam elements with 6 degrees of freedom per node and the concept of gear mesh stiffness is introduced as a means of connecting the geared shafts via element stiffness matrices. A discussion of several gear geometric parameters is used to explain the average gear mesh stiffness and the subsequent transformation matrices that relate the generalized forces and displacements along the line of action to their components in a stationary shaft reference frame. This represents the baseline linear time-invariant (LTI) modeling for geared rotor dynamics. Steady-state methods to solve the damped eigenvalue (or free vibration) problem for geared rotors with constant mesh stiffness are also applicable to this section and are instrumental in determining potentially excited modes shapes, natural frequencies, and assessing their stability. Similarly the unbalance forcing function is introduced as an external forcing function to solve the forced vibration equations of motion and the synchronous response may be computed. Comparisons between the steady-state and the transient unbalance response analyses should lend considerable insights that assess the validity of assuming that shaft rotational speed remains constant during operation. The consequences of non-constant shaft rotational speed are also elaborated on in terms of its effect on the external unbalance force and the frequency dependent stiffness and damping coefficients and gyroscopic moments.

Section 3.2 augments the definition of the gear mesh stiffness to include a state-varying contribution due to multiple pairs of teeth going into and out of engagement in time. The frequency of these engagement/disengagement transitions is referred to as the gear mesh frequency, and a Fourier series approximation in the form of rectangular waves is introduced. Furthermore, the methods allow the shaft rotational speed to vary in time, which implies that additional gear mesh harmonics may appear in the rectangular wave form that approximates the change of tooth pairs. Uncertainty in the number of Fourier terms needed to accurately characterize the state-varying mesh stiffness is discussed. Other parameters such as the ratio of the state-varying amplitude to the average mesh stiffness and the contact ratio are investigated.

Section 3.3 incorporates the backlash clearance into the dynamic force calculations and is dependent on the dynamic transmission error, which characterizes the difference in expected tangential displacements of the gear teeth. Backlash is a major source of non-linearity in gear dynamics because of the potential for sudden tooth contact loss. The complete dynamic mesh forces are summarized for a gear pair, and the non-linear state-varying rotor dynamic equations of motion are introduced. The inclusion of these non-linear gear forces, and acceleration-dependent unbalance forces and gyroscopic moments into rotor dynamic models of shaft bearing systems will provide a more realistic toolset for members of industry for either design or diagnostic purposes.

2.3 Outline of application case studies

Three different gear train designs are proposed for benchmarking and validation purposes as shown in Figures 2.1, 2.2, and 2.3. Each of these gear trains exhibit a different instability mechanism and the methods used to determine the root cause vary in complexity. Validation of the steady-state methods using linear and state-invariant (constant) gear mesh stiffness is essential since the explanation of the more complicated problems from the other case studies depend on them. The first gear train in Figure 2.1 serves as a preliminary validation case for the steady-state solver using constant gear mesh stiffness. It is expected that the steady-state solver will identify the mode of a problematic subsynchronous vibration and that the same model may be used to suggest a redesign of either the shaft or bearings.

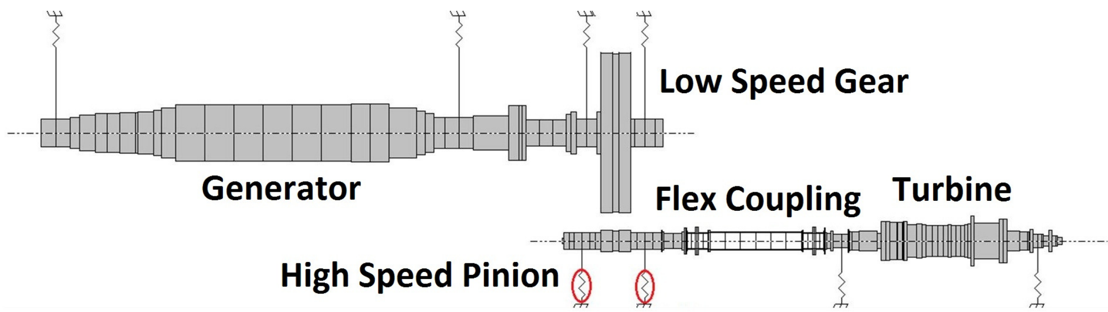

Figure 2.1: Application 1: Steam-turbine generator.

The second gear train design is a single-stage system composed of two identical Jeffcott rotor models with a unity gear ratio as shown in Figure 2.2 and is designed to match the torsional properties of a lumped parameter model proposed by Walha et al. [24]. This gear train design intentionally uses a large length to diameter ratio in contrast to conventional short and stubby gear box shafts. The purpose for the irregularly slender shaft model is to demonstrate the importance and effects of shaft dynamics in contrast with previously used lumped parameter models for the geared shafts. Furthermore, the simple Jeffcott rotor has been studied extensively in rotor dynamics and deviations from the original may be easily compared and contrasted. Damped natural frequencies, mode shapes, and their stability are determined before steady-state unbalance and time transient unbalance response analyses with constant gear mesh stiffness are conducted. Furthermore, the validity of using a synchronous steady-state rotor dynamics solution method for the unbalance response of geared systems will be assessed when compared with transient results that do not assume steady excitation frequencies. Additional state-varying gear mesh excitations, such as gear mesh frequency rectangular wave pulses and backlash clearance non-linearities, are included in a systematic order so as to clearly show their effects on the system response. An outline of the test matrix is shown in Table 2.1. A discussion about the

Table 2.1: Test matrix for transient analysis with Application 2: flexible gearbox with unity ratio.

Unbalance (g-mm)	$\frac{\mathbf{K_a}}{\mathbf{K_g}}$	**Contact Ratio, c**	**Backlash, δ_s (mm)**	**Fourier Number**
360	0	0	0	0
720	0	0	0	0
1080	0	0	0	0
1440	0	0	0	0
720	0.10	1.592	0	5
720	0.20	1.592	0	5
720	0.50	1.592	0	5
720	0.20	1.592	0	10
720	0.20	1.592	0	15
720	0.20	1.592	0	20
720	0	0	0.0254	0
720	0	0	0.0508	0
720	0	0	0.0762	0
720	0	0	0.1016	0
720	0.10	1.592	0.0254	5
720	0.20	1.592	0.0254	5
720	0.50	1.592	0.0254	5
720	0.75	1.592	0.0254	5
360	0.20	1.592	0.0254	5
720	0.20	1.592	0.0254	5
1080	0.20	1.592	0.0254	5
1440	0.20	1.592	0.0254	5
720	0.20	1.25	0	5
720	0.20	1.75	0	5
720	0.20	2.00	0	5
720	0.20	1.25	0.0254	5
720	0.20	1.75	0.0254	5

effects of gear mesh damping on excited torsional modes is also included.

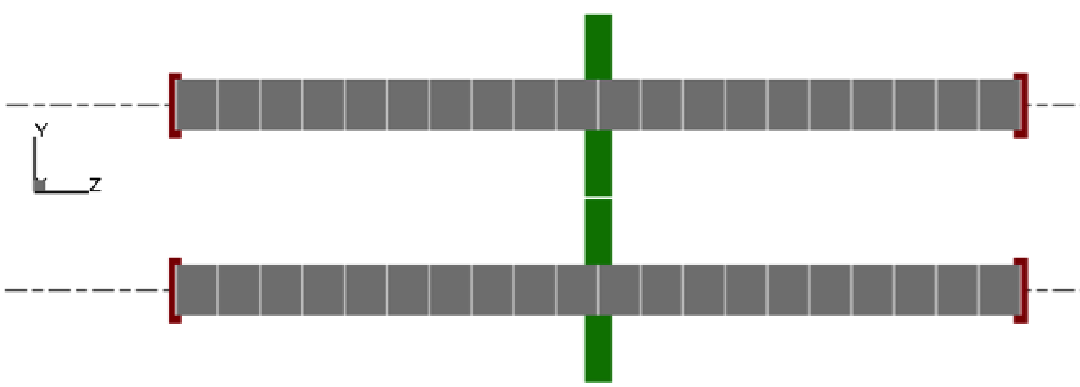

Figure 2.2: Application 2: Flexible Gearbox with Unity Ratio.

Furthermore, preliminary results from the third gear train, shown in Figure 2.3, serve as additional benchmarking for the steady-state solver with constant gear mesh stiffness since they are compared with a

Table 2.2: Test matrix containing the types of analyses performed on each model.

Analyses	**Application 1**	**Application 2**	**Application 3**
Free vibration (K_g only)	X	X	X
Steady-state unbalance (K_g only)	X	X	
Transient (K_g only)		X	X
Transient (K_a and K_g)		X	X
Transient (K_a, K_g, and δ_s)		X	
Fluid Film Bearing (K and C)	X		X

similar solver in collaboration with BRG Machinery Consulting LLC. Agreement between these steady-state solvers is expected and they are used to determine the mode shape of a supersynchronous and sub gear mesh frequency large amplitude vibration problem. Other supersynchronous sub gear mesh frequency cases have been reported in the literature, but there has only been speculation that the gear mesh variational stiffness is the root cause. Studying the effects of increasing the amplitude of the variational gear mesh stiffness on the transient vibration behavior produces new insights into the cause of vibration amplification and promotes ideas to avoid energizing it in earlier design stages.

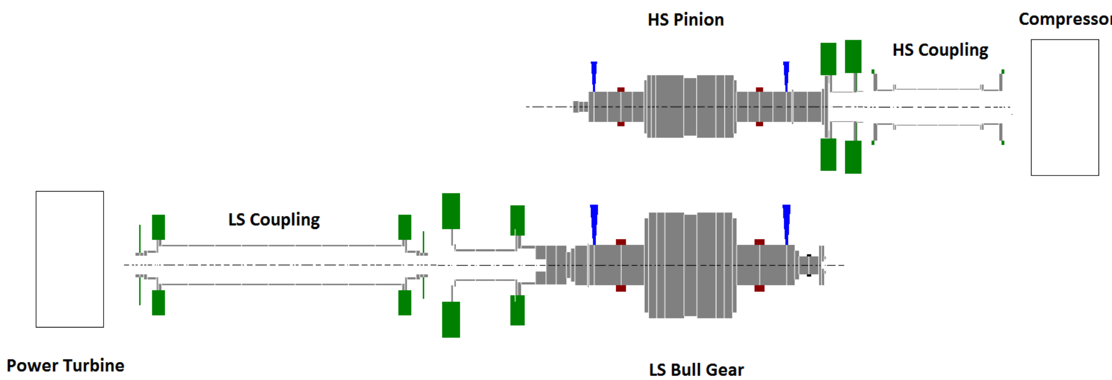

Figure 2.3: Application 3:Power-turbine compressor.

A set of analysis tools using the methods outlined in Chapter 3 that can predict the instabilities inherent in these models would be extremely valuable to industry. No comparable analysis tools are known to presently exist that can couple realistic shaft dynamics with those of the gears without resorting to complex 3-D modeling of the gear teeth and oil film lubrication. Transient simulations with 3-D solid elements tend to be very computationally expensive, and may require days or weeks to run even on a set of parallel-processors or a cluster. One of the objectives of this research is to produce more simple models of the gear teeth interactions with realistic rotor dynamics that drastically reduce the computational effort and reduce run time while minimizing compromises in model fidelity. A summary of the different analyses used in the modeling case studies is shown in Table 2.2.

Chapter 3

Methodology

This chapter explores the finite element methodology for the inclusion of gearbox dynamics into rotor dynamics. Section 3.1 addresses the linear state-invariant modeling of the gear mesh stiffness, and will be extended to include state-varying mesh stiffness and non-linear backlash in sections 3.2 and 3.3. It is based upon a finite element code that uses Timoshenko beam models for shafts and can easily incorporate bearings, disks, and seals into the equations of motion [35]. Beam elements are widely used to model rotors as they have been shown to produce accurate results when compared to experimental data [35]. The methods have applications towards performing steady-state and time-transient rotor dynamic analyses and have lateral, torsional, and axial degrees of freedom.

3.1 Constant gear mesh stiffness

Solving the rotor dynamic equations of motion with coupled degrees of freedom are necessary for geared rotor dynamics and will produce more accurate results than solving the individual non-coupled ones. The gears will be treated as a pair of rigid lumped masses and inertias that influence the mass, gyroscopic, and stiffness properties of the corresponding shaft nodes in the finite element matrices. The free vibration rotor dynamic equations of motion for the entire system model can be represented by the following matrix equation.

$$\mathbf{M}\ddot{\mathbf{u}} + (\mathbf{C} + \boldsymbol{\Omega}\mathbf{G})\dot{\mathbf{u}} + \mathbf{K}\mathbf{u} = \mathbf{0} \tag{3.1}$$

$\mathbf{M}$ represents the inertia matrix, $\mathbf{C}$ represents the damping matrix, $\mathbf{G}$ represents the gyroscopic matrix, $\boldsymbol{\Omega}$ represents the shaft speed matrix, and $\mathbf{K}$ represents the stiffness matrix. In a linear rotor dynamic analysis, the effects of the gears and the gear mesh will significantly contribute to the global mass, speed, gyroscopic,

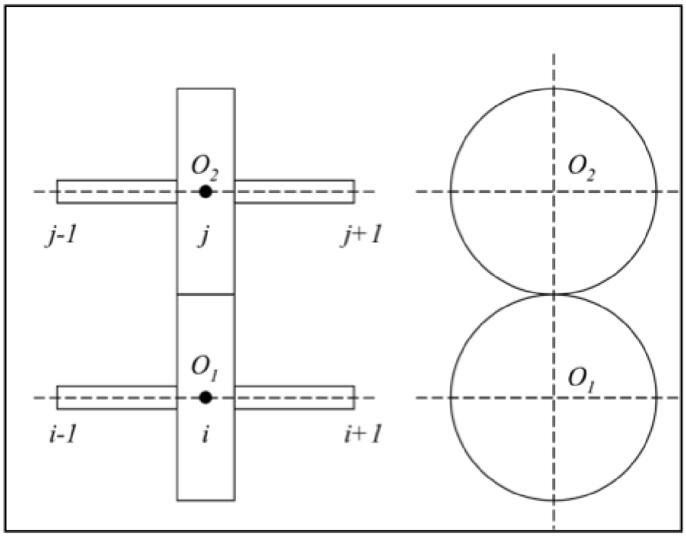

Figure 3.1: Gear mesh finite element representation [36].

and stiffness matrices only. The gear mesh lubricant stiffness and damping effects are neglected. Appendix A describes the finite element formulation of shafts, disks, bearings, and flexible couplings, which are necessary for full-system geared rotor dynamics.

The gear mesh effective lateral, torsional, and axial stiffness is modeled as a 12×12 matrix that relates the gear mesh forces and moments, or generalized forces, with each of their respective DOFs. This gear mesh finite element was previously documented in Stringer [36]. It consists of two nodes, i and j, respectively as shown in Figure 3.1, where the nodes designate the location of the gear or pinion on the parallel connecting shafts. Each node has six degrees of freedom, which consists of three translations and three angular displacements. The incorporation of this axially, laterally, and torsionally coupled mesh stiffness finite element will provide more accurate displacement solutions for a geared system in a free vibration or forced response rotor dynamic analysis.

The generalized displacements are shown in the displacement vector, $\mathbf{u}$, and contain those corresponding to the shaft center of one gear at node i and the other gear at node j, as indicated by the subscripts.

$$\mathbf{u} = \begin{bmatrix} \mathbf{u}_i & \mathbf{u}_j \end{bmatrix}^T = \begin{bmatrix} x_i & y_i & z_i & \theta_{xi} & \theta_{yi} & \theta_{zi} & x_j & y_j & z_j & \theta_{xj} & \theta_{yj} & \theta_{zj} \end{bmatrix}^T \tag{3.2}$$

Correspondingly, the generalized forces acting on both nodes may be represented by the external force vector, $\mathbf{f}$.

$$
\begin{aligned}
\mathbf{f} &= \begin{bmatrix} \mathbf{f}_i & \mathbf{f}_j \end{bmatrix}^T = \\
&\begin{bmatrix} F_{xi} & F_{yi} & F_{zi} & M_{xi} & M_{yi} & M_{zi} & F_{xj} & F_{yj} & F_{zj} & M_{xj} & M_{yj} & M_{zj} \end{bmatrix}^T
\end{aligned} \tag{3.3}
$$

These generalized forces are incorporated into the rotor dynamic model through a shift to the left-hand side of the equations of motion since the generalized forces are treated as linear with respect to the generalized displacements. This equivalent stiffness matrix, K_{mesh}, relates the generalized forces with the generalized displacements through the following matrix equation.

$$
\begin{bmatrix} \mathbf{f}_i \\ \mathbf{f}_j \end{bmatrix} = -\begin{bmatrix} \mathbf{K}_{mesh} \end{bmatrix} \begin{bmatrix} \mathbf{u}_i \\ \mathbf{u}_j \end{bmatrix} \tag{3.4}
$$

The element stiffness matrix K_{mesh} is defined below, where K_g is the average gear mesh stiffness, and K_{ii}, K_{ij}, K_{ji}, and K_{jj} are 6×6 sub-matrices that account for the coordinate transformations from the pitch point of the gear mesh to the global coordinate system of the shaft centers. These sub-matrices will be discussed later in this section.

$$
\mathbf{K}_{mesh} = K_g \begin{bmatrix} \mathbf{K}_{ii} & \mathbf{K}_{ij} \\ \mathbf{K}_{ji} & \mathbf{K}_{jj} \end{bmatrix} = K_g \begin{bmatrix} \mathbf{K}_{ii} & \mathbf{K}_{ji}^T \\ \mathbf{K}_{ji} & \mathbf{K}_{jj} \end{bmatrix} \tag{3.5}
$$

A crucial parameter to the element stiffness matrix is the average gear mesh stiffness, K_g, which accounts for the tooth compliance along the path of force transmission, called the line of action (LOA). It is assumed that the stiffness of the rest of the gear body will be much more rigid than that of the teeth, which suggests that the tooth stiffness will dominate the gear dynamics. The meshing stiffness between a single pair of teeth is found either from experimental data or from previously reported analytical formulas. The analytical formula used to compute single tooth-tooth contact stiffness is provided by Buckingham where w is the tooth face width, and E_1 and E_2 are the gear and pinion elastic moduli [71].

$$
K_g = \frac{wE_1E_2}{9\left(E_1 + E_2\right)} \tag{3.6}
$$

The mesh stiffness formula, however, only represents the stiffness of a single pair of teeth in contact. As the gears rotate, a state-varying mesh stiffness develops because the number of pairs of teeth in contact, also known as the contact ratio, alternate between one and two throughout the mesh cycle.

Since most gear manufacturers provide the average contact ratio, it may be used to modify Buckingham's original formula. The advantage of implementing an assumed constant contact ratio into the finite element model is that the solving time is greatly reduced and yet the accuracy remains reasonable. Buckingham's formula for the average gear mesh stiffness may then be modified to the following where c is the average contact ratio as specified by the gear manufacturer. Again, the contact ratio c represents the average number of tooth pairs in contact over one mesh cycle. The variation of gear mesh stiffness acting along the pressure line for spur gear pairs is better summarized in Section 3.2.

$$K_g = \frac{cwE_1E_2}{9\left(E_1 + E_2\right)} \tag{3.7}$$

The stiffness matrix was also generalized to account for the macro geometry of both spur and helical geared systems. These geometric parameters, which include normal pressure angle, helical angle, pitch radii, and orientation angle, are accounted for when relating the displacement of gear teeth along the LOA to its components in the coordinate system of the shaft center [36]. The LOA is the path of force transmission between a pair of mating gears and is represented as a line that intersects with the pitch point but is not, in general, tangent to the gear pitch circles. The tooth deflections at the pitch point are resolved into the components of the shaft coordinate system through two coordinate transformations. The first transformation makes use of the normal pressure angle and helical angle to resolve components along the LOA into normal and tangential components along the pitch circle. An illustration of this transformation is provided in Figure 3.2 where the X' Y' Z' coordinate system references components acting along or normal to the pitch circle at the pitch point. The second transformation makes use of the shaft orientation angle to relate the components along the pitch circle to those of the shaft center. Figure 3.3 illustrates the use of the shaft orientation angle, φ, in this transformation.

Spur geared systems require only three degrees of freedom per node because the forces and moments act solely in the plane of rotation, or in the X-Y plane in the diagram below. The displacements of interest for each gear node would be x, y, and θ_z, and therefore $\mathbf{u}$ would consist of only 6 unknown displacements. That is, three displacements for the pinion and three displacements for the gear. Helical geared systems, however, as shown in Figure 3.2, require six degrees of freedom per node because the forces and moments now act in 3-D space and must also be functions of the helical angle, β. Therefore, $\mathbf{u}$ must include all 12 generalized displacements if we are to include those of the gear and pinion.

The derivation of this 12x12 stiffness matrix relies on relatively few geometric inputs but is robust enough to account for parameters corresponding to those of helical and spur gear meshes. The geometric inputs for the gear and pinion include the following: pitch radii, normal pressure angle, helical angle, and an orientation

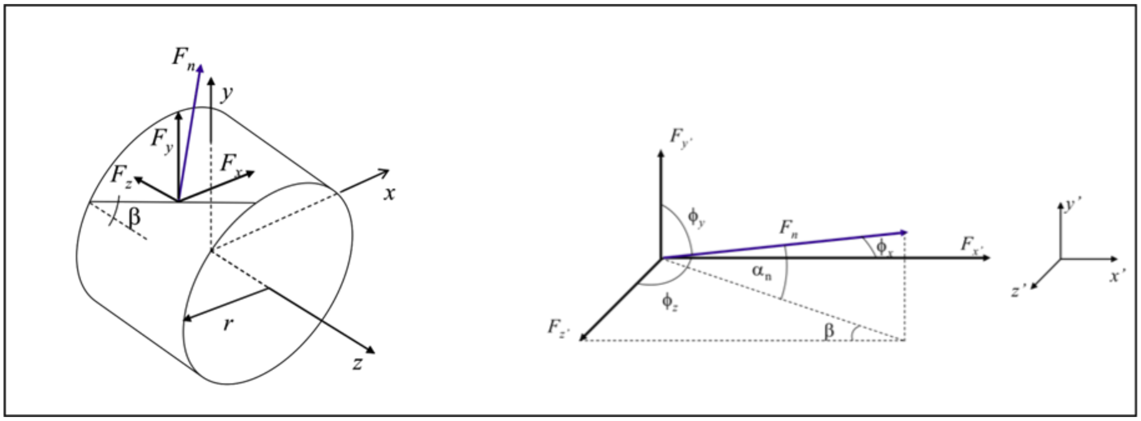

Figure 3.2: Gear forces and parameters [36].

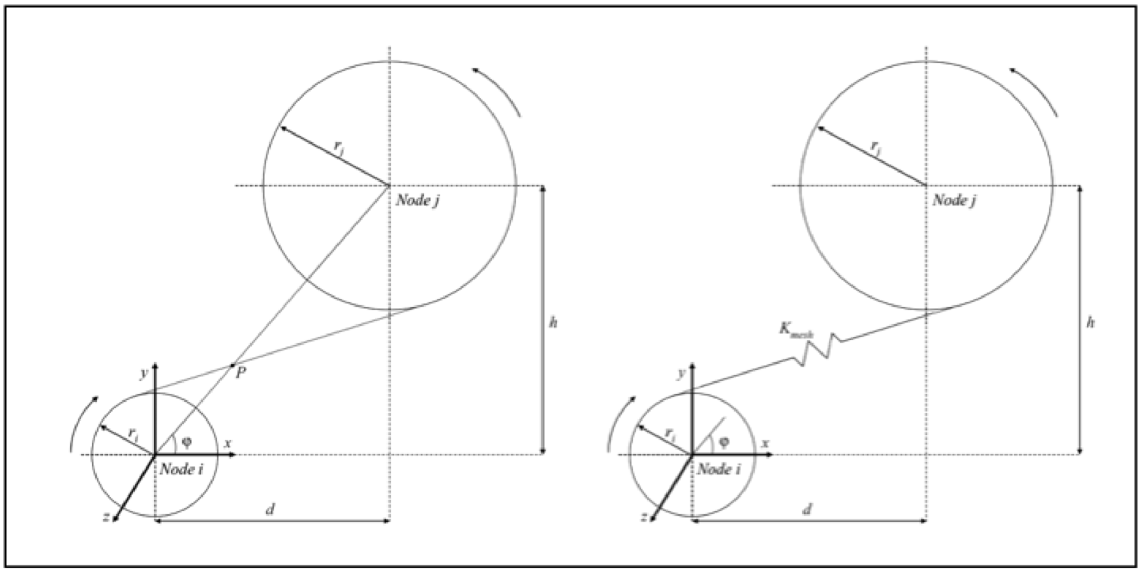

Figure 3.3: Gear pair orientation angle [36].

angle of the shafts holding the gears. Figures 3.2 and 3.3 depict the relevant geometric parameters.

The equations of motion that relate the generalized forces to the generalized displacements were obtained by applying a force balance along the LOA. The transmitted force is proportional to the net displacement of the tooth along the LOA through a component of the mesh stiffness matrix. The transmitted force and displacement along the LOA can be resolved into components of the shaft center coordinate system through the two coordinate transformations involving the parameters mentioned above. Each element of the gear mesh stiffness matrix may then be evaluated using the Influence Coefficient method where one varies individual generalized displacements and determines the resulting generalized forces required to produce that deflection.

The direction cosines are used to resolve the transmitted force into components along the pitch circle and are convenient for notational purposes. They are functions of the helical angle and normal pressure angle.

$$
\begin{aligned}
\cos\phi_x &= \cos\beta\cos\alpha_n \\
\cos\phi_y &= \sin\alpha_n \\
\cos\phi_z &= \sin\beta\sin\alpha_n
\end{aligned}
\tag{3.8}
$$

Using the direction cosines, pitch radii, and shaft orientation angle, the transformation matrices, K_{ii}, K_{ij}, K_{ji}, and K_{jj} may be expressed as

$$
\begin{aligned}
\left[\; K_{ii} \;\right] &= \begin{bmatrix}
(s\varphi c\phi_x + c\varphi c\phi_y)^2 & & & & & \\
(s\varphi c\phi_x + c\varphi c\phi_y)(s\varphi c\phi_y - c\varphi c\phi_x) & (s\varphi c\phi_y - c\varphi c\phi_x)^2 & & & sym & \\
c\phi_z(s\varphi c\phi_x + c\varphi c\phi_y) & c\phi_z(s\varphi c\phi_y - c\varphi c\phi_x) & c\phi_z^2 & & & \\
s\varphi c\phi_z r_i(s\varphi c\phi_x + c\varphi c\phi_y) & s\varphi c\phi_z r_i(s\varphi c\phi_y - c\varphi c\phi_x) & s\varphi c\phi_z^2 r_i & s\varphi^2 c\phi_z^2 r_i^2 & & \\
\text{-}c\varphi c\phi_z r_i(s\varphi c\phi_x + c\varphi c\phi_y) & \text{-}c\varphi c\phi_z r_i(s\varphi c\phi_y - c\varphi c\phi_x) & \text{-}c\varphi c\phi_z^2 r_i & \text{-}c\varphi s\varphi c\phi_z^2 r_i^2 & c\varphi^2 c\phi_z^2 r_i^2 & \\
\text{-}c\phi_x r_i(s\varphi c\phi_x + c\varphi c\phi_y) & \text{-}c\phi_x r_i(s\varphi c\phi_y - c\varphi c\phi_x) & \text{-}c\phi_x c\phi_z r_i & \text{-}s\varphi c\phi_x c\phi_z r_i^2 & c\varphi c\phi_x c\phi_z r_i^2 & c\phi_x^2 r_i^2
\end{bmatrix} \\
\left[\; K_{ji} \;\right] &= \begin{bmatrix}
\text{-}(s\varphi c\phi_x + c\varphi c\phi_y)^2 & [K_{ji}]_{2,1} & [K_{ji}]_{3,1} & \text{-}s\varphi c\phi_z r_i(s\varphi c\phi_x + c\varphi c\phi_y) & c\varphi c\phi_z r_i(s\varphi c\phi_x + c\varphi c\phi_y) & c\phi_x r_i(s\varphi c\phi_x + c\varphi c\phi_y) \\
\text{-}(s\varphi c\phi_x + c\varphi c\phi_y)(s\varphi c\phi_y - c\varphi c\phi_x) & \text{-}(s\varphi c\phi_y - c\varphi c\phi_x)^2 & [K_{ji}]_{3,2} & \text{-}s\varphi c\phi_z r_i(s\varphi c\phi_y - c\varphi c\phi_x) & c\varphi c\phi_z r_i(s\varphi c\phi_y - c\varphi c\phi_x) & c\phi_x r_i(s\varphi c\phi_y - c\varphi c\phi_x) \\
\text{-}c\phi_z(s\varphi c\phi_x + c\varphi c\phi_y) & \text{-}c\phi_z(s\varphi c\phi_y - c\varphi c\phi_x) & \text{-}c\phi_z^2 & \text{-}s\varphi c\phi_z^2 r_i & c\varphi c\phi_z^2 r_i & c\phi_x c\phi_z r_i \\
\text{-}s\varphi c\phi_z r_j(s\varphi c\phi_x + c\varphi c\phi_y) & \text{-}s\varphi c\phi_z r_j(s\varphi c\phi_y - c\varphi c\phi_x) & \text{-}s\varphi c\phi_z^2 r_j & \text{-}s\varphi^2 c\phi_z^2 r_i r_j & c\varphi s\varphi c\phi_z^2 r_i r_j & s\varphi c\phi_x c\phi_z r_i r_j \\
c\varphi c\phi_z r_j(s\varphi c\phi_x + c\varphi c\phi_y) & c\varphi c\phi_z r_j(s\varphi c\phi_y - c\varphi c\phi_x) & c\varphi c\phi_z^2 r_j & c\varphi s\varphi c\phi_z^2 r_i r_j & \text{-}c\varphi^2 c\phi^2 r_i r_j & -c\varphi c\phi_x c\phi_z r_i r_j \\
c\phi_x r_j(s\varphi c\phi_x + c\varphi c\phi_y) & c\phi_x r_j(s\varphi c\phi_y - c\varphi c\phi_x) & c\phi_x c\phi_z r_j & s\varphi c\phi_x c\phi_z r_i r_j & \text{-}c\varphi c\phi_x c\phi_z r_i r_j & \text{-}c\phi_x^2 r_i r_j
\end{bmatrix} \\
\left[\; K_{jj} \;\right] &= \begin{bmatrix}
(s\varphi c\phi_x + c\varphi c\phi_y)^2 & & & & & \\
(s\varphi c\phi_x + c\varphi c\phi_y)(s\varphi c\phi_y - c\varphi c\phi_x) & (s\varphi c\phi_y - c\varphi c\phi_x)^2 & & & sym & \\
c\phi_z(s\varphi c\phi_x + c\varphi c\phi_y) & c\phi_z(s\varphi c\phi_y - c\varphi c\phi_x) & c\phi_z^2 & & & \\
s\varphi c\phi_z r_j(s\varphi c\phi_x + c\varphi c\phi_y) & s\varphi c\phi_z r_j(s\varphi c\phi_y - c\varphi c\phi_x) & s\varphi c\phi_z^2 r_j & s\varphi^2 c\phi_z^2 r_j^2 & & \\
\text{-}c\varphi c\phi_z r_j(s\varphi c\phi_x + c\varphi c\phi_y) & \text{-}c\varphi c\phi_z r_j(s\varphi c\phi_y - c\varphi c\phi_x) & \text{-}c\varphi c\phi_z^2 r_j & \text{-}c\varphi s\varphi c\phi_z^2 r_j^2 & c\varphi^2 c\phi_z^2 r_j^2 & \\
\text{-}c\phi_x r_j(s\varphi c\phi_x + c\varphi c\phi_y) & \text{-}c\phi_x r_j(s\varphi c\phi_y - c\varphi c\phi_x) & \text{-}c\phi_x c\phi_z r_j & \text{-}s\varphi c\phi_x c\phi_z r_j^2 & c\varphi c\phi_x c\phi_z r_j^2 & c\phi_x^2 r_j^2
\end{bmatrix}
\end{aligned}
\tag{3.9}
$$

Note: This transformation assumes that θ_{z1} and θ_{z2} are defined as positive in opposite directions.

After applying the coordinate transformations and multiplying through by the average gear mesh stiffness, we obtain an element stiffness matrix that represents the relationship between the generalized forces exchanged between the gears, and the generalized displacements at the corresponding shaft locations. This method may be applied to both spur and helical gears and illustrates the contribution gear dynamics provide to the deformation and vibration of axial, lateral, and torsionally coupled rotor dynamic systems. This finite element will be beneficial in free vibration and forced response rotor dynamic analyses involving gearboxes.

3.1.1 Steady-state damped eigenvalue solution

After acquiring the global matrices via the finite element method, this subsection shows the solution methodology for solving the free vibration equation as expressed in Equation 3.10.

$$M\ddot{u} + (C + \Omega G)\dot{u} + Ku = 0 \tag{3.10}$$

A change of variables is necessary to convert the 2^{nd} order differential equation into an equivalent 1^{st} order equation, and has the consequence of doubling the number of solution variables as shown in Equation 3.11.

$$[\mathbf{v}] = \begin{bmatrix} u \\ \dot{u} \end{bmatrix}, [\dot{\mathbf{v}}] = \begin{bmatrix} \dot{u} \\ \ddot{u} \end{bmatrix} \tag{3.11}$$

The equations of motion for free vibration may now be written in state-space form, where Ω represents a diagonalized rotational speed matrix containing the speeds of all nodes on multiple shafts. Ω must be of this form since the shafts rotate in opposite directions and operate in accordance with the gear ratio.

$$\begin{bmatrix} M & 0 \\ 0 & M \end{bmatrix} \begin{bmatrix} \dot{u} \\ \ddot{u} \end{bmatrix} + \begin{bmatrix} 0 & -M \\ K & C + \Omega G \end{bmatrix} \begin{bmatrix} u \\ \dot{u} \end{bmatrix} = \begin{bmatrix} 0 \\ 0 \end{bmatrix} \tag{3.12}$$

A transformation may be applied to convert from time to frequency domain using the Laplace variable s as shown in Equation 3.13.

$$\begin{aligned} [\mathbf{v}(t)] &= [\mathbf{V}]e^{st} \\ [\dot{\mathbf{v}}(t)] &= s[\mathbf{V}]e^{st} \end{aligned} \tag{3.13}$$

Substituting this within the state-space equation 3.12 and rearranging terms results in the following damped eigenvalue problem because the e^{st} is common within all terms and may be eliminated.

$$\begin{bmatrix} 0 & -M \\ K & C + \Omega G \end{bmatrix} [\mathbf{V}] = - \begin{bmatrix} M & 0 \\ 0 & M \end{bmatrix} \mathbf{s}[\mathbf{V}] \tag{3.14}$$

All eigenvalue solutions, s, that satisfy Equation 3.14 are complex, where the real part dictates exponential growth or decay and the imaginary portion represents the damped natural frequency of a mode. Equation 3.15 specifies the complex form of each pair of eigenvalues in terms of damping ratio ζ and undamped natural frequency ω_n. The mode is stable if the real part is negative and unstable if positive.

$$s_{1,2} = -\zeta\omega_n +/- j\omega_n\sqrt{1-\zeta^2} \tag{3.15}$$

3.1.2 Steady-state unbalance response solution

The forced response equation of motion is similar to the free vibration equation except that it contains an external forcing function, f on the right side.

$$M\ddot{u} + (C + \Omega G)\dot{u} + Ku = f \tag{3.16}$$

Using the change of variables, as defined in Equation 3.11, the forced response equations of motion may be written in the following state-space form.

$$\begin{bmatrix} M & 0 \\ 0 & M \end{bmatrix}\begin{bmatrix} \dot{u} \\ \ddot{u} \end{bmatrix} + \begin{bmatrix} 0 & -M \\ K & C+\Omega G \end{bmatrix}\begin{bmatrix} u \\ \dot{u} \end{bmatrix} = \begin{bmatrix} 0 \\ f \end{bmatrix} \tag{3.17}$$

Unbalance produces forces that act on the shaft at the same frequency as the shaft rotational speed. This is referred to as a synchronous forcing function, where the X and Y directional forces occur 90° out of phase.

$$\begin{aligned} f_{XUnb} &= me_u\Omega^2\cos(\Omega t + \phi) \\ f_{YUnb} &= me_u\Omega^2\sin(\Omega t + \phi) \end{aligned} \tag{3.18}$$

The forcing function for unbalance and the vector, v, which contains the displacements and velocities, as defined by Equation 3.11, may also be expressed in the following form using the Laplace transform, $s = j\Omega$, and are representative of vectors rotating through the complex plane at frequency Ω. For a linear dynamic system, the input force f of magnitude F acting at a particular frequency Ω results in a response, v, of the same frequency but with different magnitude V and phase angle, ϕ. F is the unbalance force magnitude defined as $me_u\Omega^2$.

$$\begin{aligned} [f(t)] &= e^{j\Omega t}[F] \\ [v(t)] &= e^{j(\Omega t - \phi)}[V] \end{aligned} \tag{3.19}$$

Substituting the complex rotating vectors for force, displacements and velocities, into the state-space equations of motion results in the following because the $e^{j\Omega t}$ appears in all terms and may be eliminated.

$$\left[j\Omega\begin{bmatrix} M & 0 \\ 0 & M \end{bmatrix} + \begin{bmatrix} 0 & -M \\ K & C+\Omega G \end{bmatrix}\right][V] = e^{j\phi}\begin{bmatrix} 0 \\ F \end{bmatrix} \tag{3.20}$$

Multiplying both sides by the inverse of the terms in front of V results in the steady-state unbalance response in terms of nodal displacements and velocities. X and Y displacements and velocities, in terms of magnitude and phase, may be used to compute the orbits of each node of the shafts. The unbalance response analysis is useful for determining actual vibration levels given the unbalance magnitude input.

$$[V] = \left[j\Omega \begin{bmatrix} M & 0 \\ 0 & M \end{bmatrix} + \begin{bmatrix} 0 & -M \\ K & C + \Omega G \end{bmatrix} \right]^{-1} e^{j\phi} \begin{bmatrix} 0 \\ F \end{bmatrix} \tag{3.21}$$

3.2 State-dependent stiffness variation

The derivation for the mesh stiffness, presented in section 3.1, was a substantial simplification of the dynamic meshing forces exchanged between the gears. A closer approximation should include an oscillating state-varying function that is offset by the average mesh stiffness since the number of teeth in contact change as the teeth transition in and out of mesh. The equivalent meshing stiffness $K(t)$ along the LOA and varying with time then becomes the following, where K_g is the average mesh stiffness and $K_v(t)$ is the state-varying contribution.

$$K(t) = K_g + K_v(t) \tag{3.22}$$

Several authors have approximated the state-varying mesh stiffness as a set of rectangular waves via Fourier series as depicted in Figure 3.4 and expressed as

$$K_v(t) = 2K_a \sum_{s=1}^{\infty} \left(a^{(s)} \sin(s\Omega_g t) + b^{(s)} \cos(s\Omega_g t) \right) \tag{3.23}$$

The rotational speed and number of gear teeth dictate the mesh frequency, Ω_g, through the following relation, where N is the number of gear teeth and Ω is its corresponding rotational speed.

$$\Omega_g = N\Omega \tag{3.24}$$

The series coefficients are defined by the following equations, which are dependent upon the contact ratio, c, and the mesh phasing, p.

$$\begin{aligned} a^{(s)} &= -\tfrac{2}{s\pi} \sin(s\pi(c-2p)) \sin(s\pi c) \\ b^{(s)} &= -\tfrac{2}{s\pi} \cos(s\pi(c-2p)) \sin(s\pi c) \end{aligned} \tag{3.25}$$

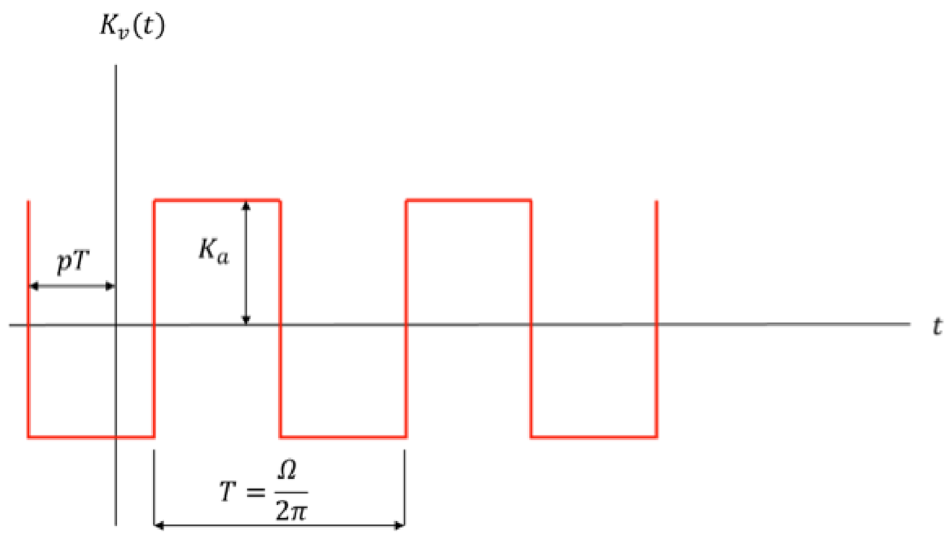

Figure 3.4: Rectangular wave form approximation to state-varying mesh stiffness with $c = 1.5$.

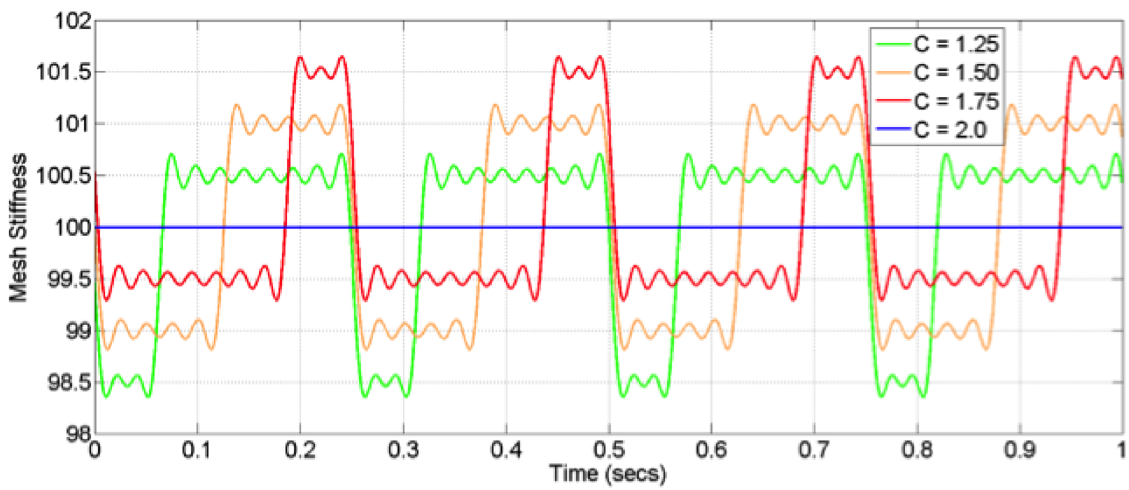

Figure 3.5: K_v Fourier coefficients taken out to 25 terms with varying contact ratio.

This formulation of the gear mesh stiffness allows for additional studies on gear parameters. These include the gear mesh frequency, contact ratio, relative magnitude of the state-varying stiffness, and the phase lead/lag between multiple meshes.

The contact ratio indicates the average number of teeth in contact upon following a single tooth pass in to and out of mesh. Figure 3.5 illustrates the rectangular wave forms of the Fourier series over a range of $1.25 < c < 2.00$ at a mesh frequency of 25 radians per second. The average mesh stiffness, K_g, was set to 100 and the 0-P amplitude of oscillation, K_a, is 1. A contact ratio of 1.5 dictates that 2 pairs of gear teeth will be in contact for the same duration as just 1 pair. Integer values stipulate that there will be no oscillation in the gear mesh stiffness because there is perfect overlap as teeth move into and out of engagement.

One of the objectives of this study is to evaluate an acceptable number of Fourier coefficients, s, that are needed to adequately capture the effects of the state-varying mesh stiffness. The additional minor oscillations that are more visible with fewer Fourier series terms will induce excitations in the forced response analysis and it is questionable as to whether these more accurately reflect the physics of real gear meshes or whether they should be studied as undesirable computational "noise." Conversely, it is expected that although higher-order Fourier series terms produce less errors in the rectangular wave form, their inherent high-frequency noise may excite poorly damped modes at high resonant frequencies.

3.3 Backlash clearance non-linearity

Sections 3.1 and 3.2 considered the gear mesh forces as being directly proportional to the gear tooth displacements and rotations. Gear manufacturers design the teeth to mesh so that there exists a clearance region to provide space for oil film development, thermal expansion, and to account for manufacturing tolerances. The clearance region is formerly referred to as backlash and is the dominant non-linear factor in gear dynamics[15]. This section considers contact loss in the gear teeth due to sufficient tangential displacement differences between the meshing gear and pinion. The dynamic transmission error (DTE) defines the differences between gear i and pinion j tooth tangential displacements and is represented in Equation 3.26 as $\delta(t)$ where r_i and r_j represent the base circle radii for gear i and pinion j.

$$\delta(t) = r_i\theta_{zi}(t) + r_j\theta_{zj}(t) \tag{3.26}$$

If δ exceeds the backlash clearance, b_s, then tooth contact exists and the gear forces are treated as linearly proportional to the difference in tangential displacements. This further deviates from the assumed contact stiffness defined in Sections 3.1 and 3.2 because the stiffness function increases as the net tangential displacement difference increases. When δ is within the backlash clearance, the gear forces must be zero because there is no tooth contact. Equation 3.27 shows the piecewise linear expressions for the gear contact force and Figures 3.6 and 3.7 graphically depicts the criteria for tooth contact.

$$h(\delta) = \begin{cases} \delta - b_s & ,\delta > b_s \\ 0 & ,|\delta| < b_s \\ b_s - \delta & ,\delta < -b_s \end{cases} \tag{3.27}$$

The dynamic meshing forces may now be summarized from the contributions of the static and state-varying mesh stiffness, the non-linear backlash function, transformation matrices, and the nodal displacements of the

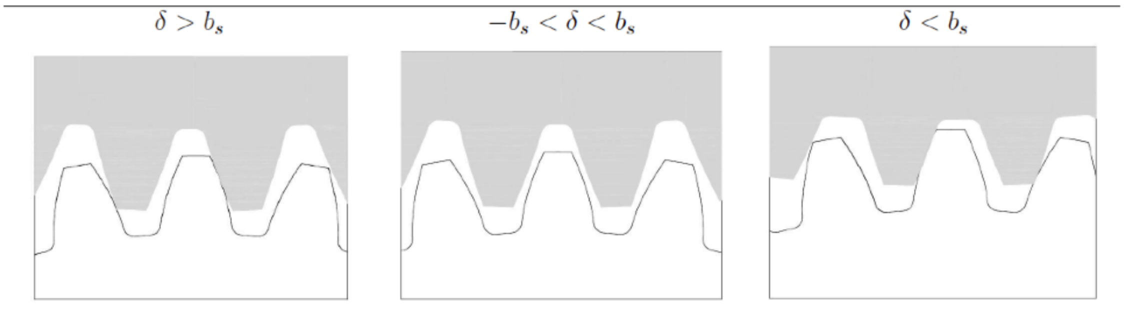

Figure 3.6: Conditions for loss of tooth contact as dictated by the relationship between δ and b_s [17].

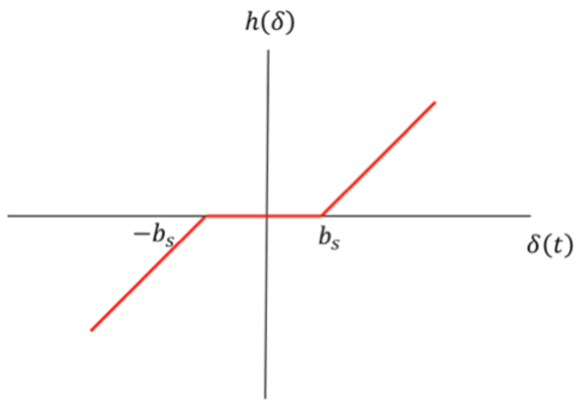

Figure 3.7: Piece-wise linear treatment of the effect of gear tooth contact loss [17].

gear teeth as shown in Equation 3.28.

$$\begin{bmatrix} \mathbf{f_i} \\ \mathbf{f_j} \end{bmatrix} = - \left[\left(K_g + K_v\left(\Omega, t\right)\right) h\left(\theta_{zi}, \theta_{zj}\right) \begin{bmatrix} \mathbf{K}_{ii} & \mathbf{K}_{ij} \\ \mathbf{K}_{ji} & \mathbf{K}_{jj} \end{bmatrix} \right] \begin{bmatrix} \mathbf{u_i} \\ \mathbf{u_j} \end{bmatrix} \tag{3.28}$$

The methods presented thus far may be used to evaluate the dynamic meshing forces at the gear teeth and to translate them into equivalent forces exchanged between the connected shafts. Computing the resulting non-linear gear mesh forces and applying it to a finite element model of a shaft system results in a new set of displacements and velocities at each future time step via the direct Runge-Kutta method. An explanation of the direct Runge-Kutta method used in this dissertation is in Appendix B. These new sets of displacements and velocities subsequently produce a new set of dynamic forces that are applied to the geared rotor-bearing model.

Chapter 4

Application 1: Subsynchronous vibration related to a steam-turbine generator

In this case study, the methods shown in the previous section are applied to an industrial steam-turbine-generator set. Excess levels of rotor lateral subsynchronous vibration were reported in this drive-train which has a rated electrical power output of 12 MW. The train also contains a speed-reducing gearbox, and a flexible coupling in between the turbine and generator. An overall schematic of the rotating machine is shown in Figure 4.1. The steam turbine is designed to run at a nominal operating speed of $10,800$ RPM. The gearbox reduces the rotational speed from 10,800 RPM at the steam turbine to 1,500 RPM at the generator. The electrical generator is coupled to the low-speed output of the gearbox. This arrangement is suitable for the generation of electrical power at 50 Hz, with a four-pole generator, while allowing the turbine to operate at peak efficiency.

The modeling and results of this chapter are included in the author's MS thesis [33] and are published in the 2012 ASME Turbomachinery Exposition [34]. The case study is included in this dissertation because the modeling and methods are used to benchmark transient results with steady-state predictions in Chapters 5 and 6

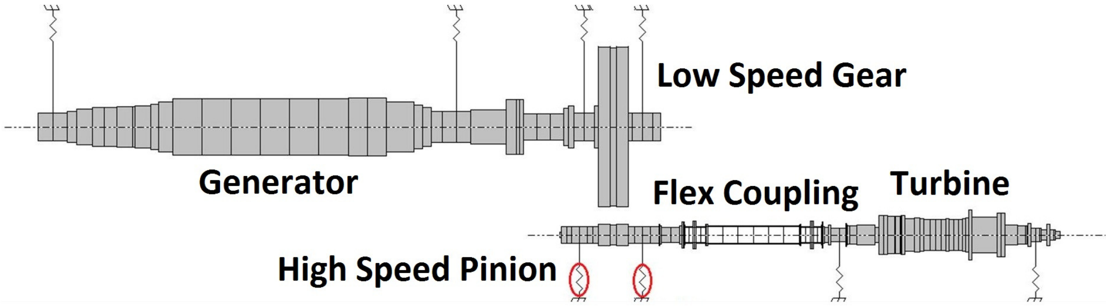

Figure 4.1: Overall schematic of an industrial geared steam-turbine-generator

4.1 Subsynchronous vibration

Measurements indicated sub-synchronous vibration along the high-speed pinion shaft at 9,840 RPM during spin testing of the turbine and gearbox. This vibration increased in amplitude as the running speed was increased to 10,380 RPM. The reported vibration had a 63 μm peak and occurred at about 0.85-0.89x, where x is the operating speed of the high-speed shaft. Since the generator was uncoupled from the turbine and gearbox during the spin testing, the gearbox bearings were lightly loaded.

A frequency spectrum plot of vibration along the high-speed pinion at a running speed of 10,409 RPM is shown in Figure 4.2. The synchronous vibration due to unbalance forces is approximately 35 μm, while the sub-synchronous component, at 0.85x, is 58 μm. Several spectrum plots of different running speeds were provided and illustrate the trend of increasing sub-synchronous amplitude as the running speed was increased.

Free oil was discovered in the high-speed coupling between the turbine and the generator during subsequent investigations. The turbine and gearbox were able to reach the nominal operating speed of 10,800 RPM after the excess oil had been removed. After increasing the speed of the turbine to ensure that over-speed requirements could be met, the high vibration levels were observed again. Afterwards, the turbine and gearbox could not exceed 7,020 RPM without tripping. Leakage from the turbine coupling side bearing was identified as the source of the excess oil in the coupling. No oil seal leakage from the gearbox was reported.

Reports in the literature suggest that trapped liquid in rotors produces sub-synchronous whirl very similar to the above observations. For a nominal deflection of the rotor, the trapped fluid experiences centrifugal forces in the radial direction. The spinning surface of the cavity combined with the viscosity of the fluid, however, produce tangential forces that can induce forward whirl and thus form the basis of sub-synchronous instability [38]. In 1967, Ehrich produced a simple analytical model which predicts whirl frequency and whirl amplitude as a function of supercritical rotor speed, liquid mass ratio, and a parameter related to the fluid Reynolds number and damping ratio [39]. His findings suggest that the ratio of whirl frequency to onset speed

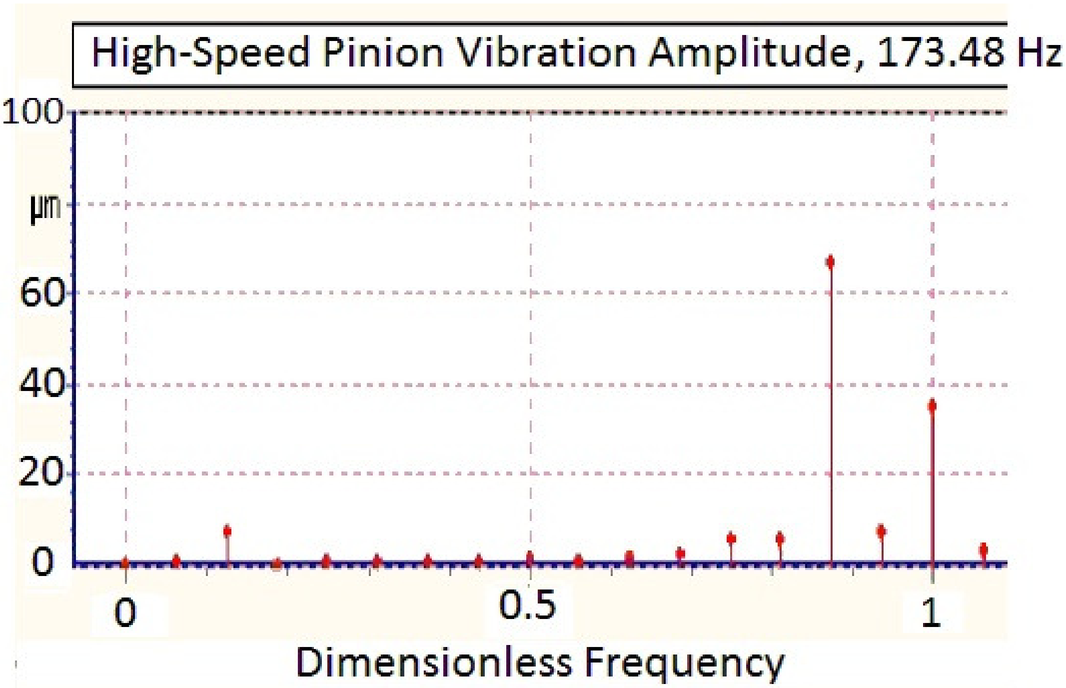

Figure 4.2: Frequency spectrum plot of high-speed pinion running at 10409 RPM

can vary from 0.5-1x depending on the mass ratio and stability characteristics. In 1968, Wolf developed a more advanced analytical model that predicts a rotor speed region of unstable self-excited whirl as a function of liquid mass ratio, fill ratio, and rotor critical speed [40]. His analysis suggests that unstable whirl will not develop for rotor speeds less than the reduced critical or rotor speeds above 1.707 ω_o, where ω_o is the emptied rotor critical speed. This places the unstable whirl frequency approximately between 0.6-1x.

Additional authors have observed and measured vibration resulting from trapped fluid in hollow rotors. Ehrich observed an asynchronous whirling motion induced by small amounts of free oil or condensed water in a hollow rotor of an aircraft gas turbine [39]. Kirk reported that entrained oil in the couplings of compressors has repeatedly produced sub-synchronous vibration ranging from 0.83-0.94x [41]. Subsequent rotor dynamic modeling and simulations are conducted to verify that the entrained oil in the high-speed coupling would produce the observed sub-synchronous vibration for this steam-turbine generator.

4.2 Rotor dynamic analysis

The complete steam-turbine generator rotor dynamic system can be decomposed into subsystems, which allows various models of components to be integrated into the full system. Accurate results are obtained from performing free vibration and unbalance response analyses on this subsystem because the gearbox connections to the low-speed and high-speed shafts are flexible enough to expect vibration isolation. An

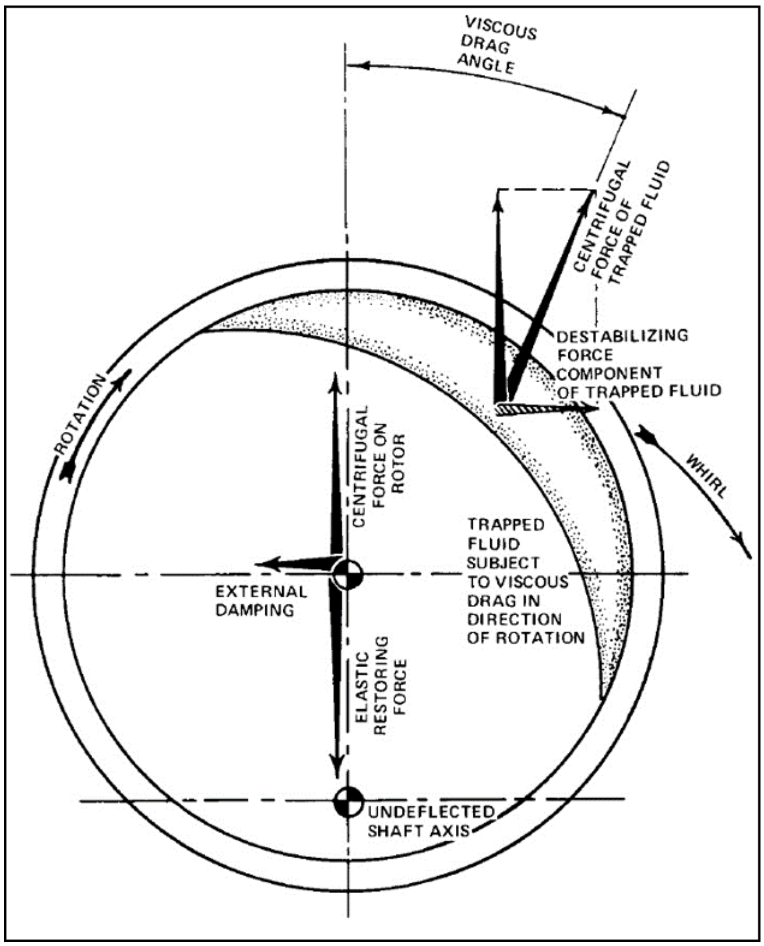

Figure 4.3: Free body diagram of liquid forces acting on whirling hollow rotor [38].

Table 4.1: Generator loads acting on high-speed pinion bearings

Load case	$F_x(N)$	$F_y(N)$
1	2	−826
2	100	−588
3	995	1605
4	1991	4043
5	4978	11352
6	8959	21098
7	12940	30848
8	16921	40594
9	20902	50341
10	24883	60087

analysis of the full rotor dynamic system was conducted and confirmed this assumption. This section will focus on developing a rotor dynamic model of the gearbox using Timoshenko beam elements. This type of beam element is widely used to model rotors as they have been shown to produce accurate results when compared to experimental data [35].

Stability analyses of the drive-train were completed using ten different load cases for the high-speed pinion bearing set, resulting from generator loads. The high-speed pinion fluid film bearings were 2-lobe offset-halves fixed geometry types. Since the instability originated from the coupling on the high-speed shaft, it was necessary to analyze this bearing set under several operating conditions to obtain a range of stiffness and damping coefficients. The minimum and maximum bearing clearances were also used to evaluate the range of bearing stiffness and damping coefficients. The bearing load cases are provided in Table 4.1 and show the Cartesian force components in the shaft global coordinate system. Each load case was run at the prescribed operating speed of 10,800 RPM. Load cases 1, 5, and 10 were taken to represent light, medium, and heavy load cases and were examined in greater detail. Emphasis is placed on load case 1 in this study because it is most consistent with the conditions described during spin testing since the generator was uncoupled from the drive-train.

The eccentricity plot of the bearing in Figure 4.4 reveals that, at low load cases, the journal orbits with an eccentricity ratio close to the origin. Eccentricity values near the origin are one indicator of possible instability [42], which further suggests that the bearing dynamic coefficients from load case 1 are most suitable for more detailed stability analyses.

Figure 4.5 shows the pressure profile for the first load case. The pressures on each graph throughout this section have been non-dimensionalized and the maximum values are provided in the chart key. Pads 1 and 2 demonstrate very similar pressure profiles of almost equal magnitude in opposite directions. With essentially equal pressure profiles on both sides and very little external load, the journal rests very close to the center of

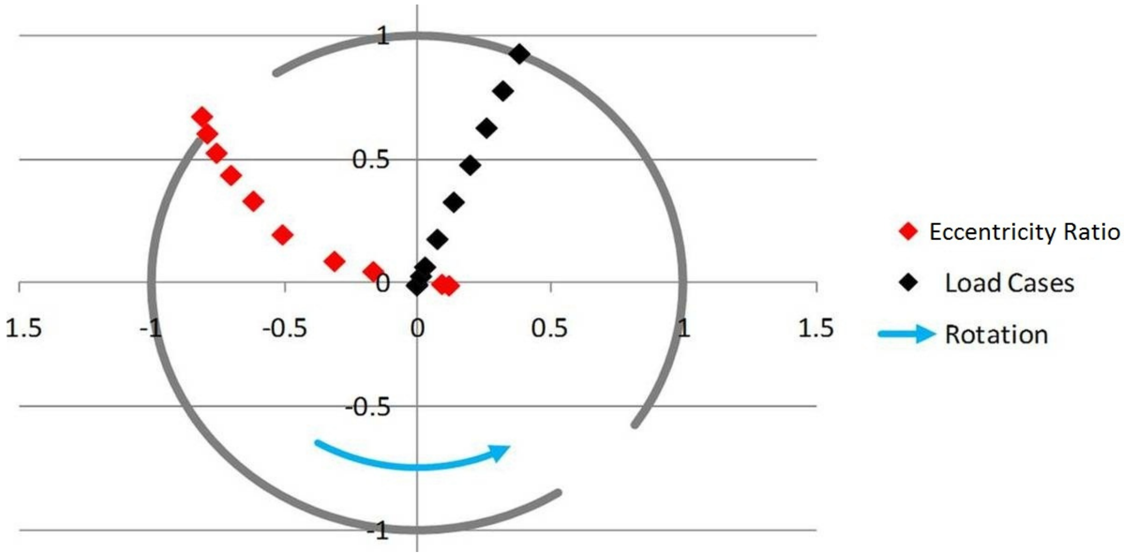

Figure 4.4: Eccentricity plot of high-speed pinion bearings acting under generator loads

the bearing. As mentioned, this behavior is an indication of unstable behavior in this bearing [42]. Figure 4.6 shows the bearing stiffness and damping coefficients as a function of load.

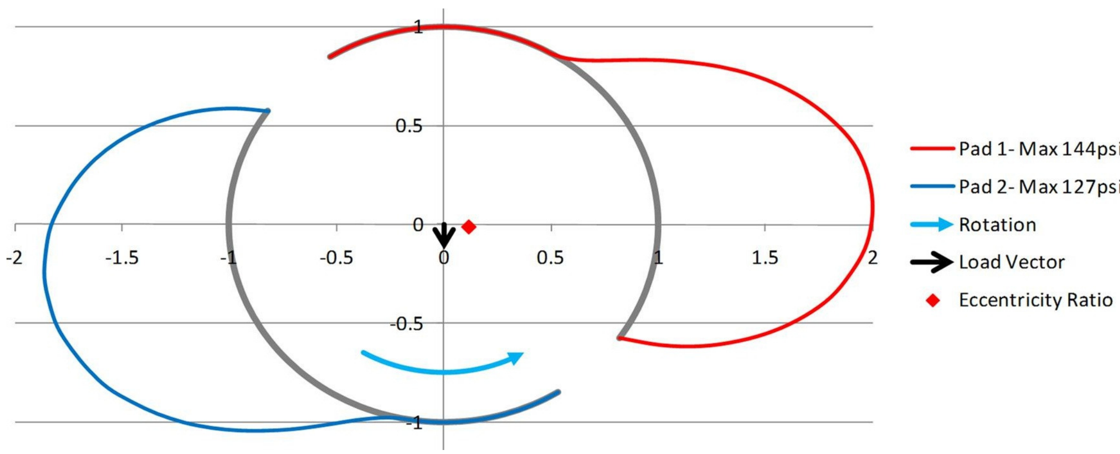

Figure 4.5: Pressure profile of high-speed pinion bearings under Load case 1

Using the gear mesh finite element model shown in the methods section, the specific stiffness matrix for the gearbox is developed and placed at the appropriate nodal locations in the global stiffness matrix. The inertial and gyroscopic properties of the gears are accounted for by lumping their mass, and mass moments of inertia at the same nodal locations within the global mass and gyroscopic matrices. Table 4.2 shows the relevant parameters used to model the mesh stiffness of this herringbone gearbox.

Rotor dynamic instability is fundamentally a free-vibration phenomenon where external fluid cross-coupled stiffness, or other external forces, act on the rotor. These tangential forces can excite natural frequencies of

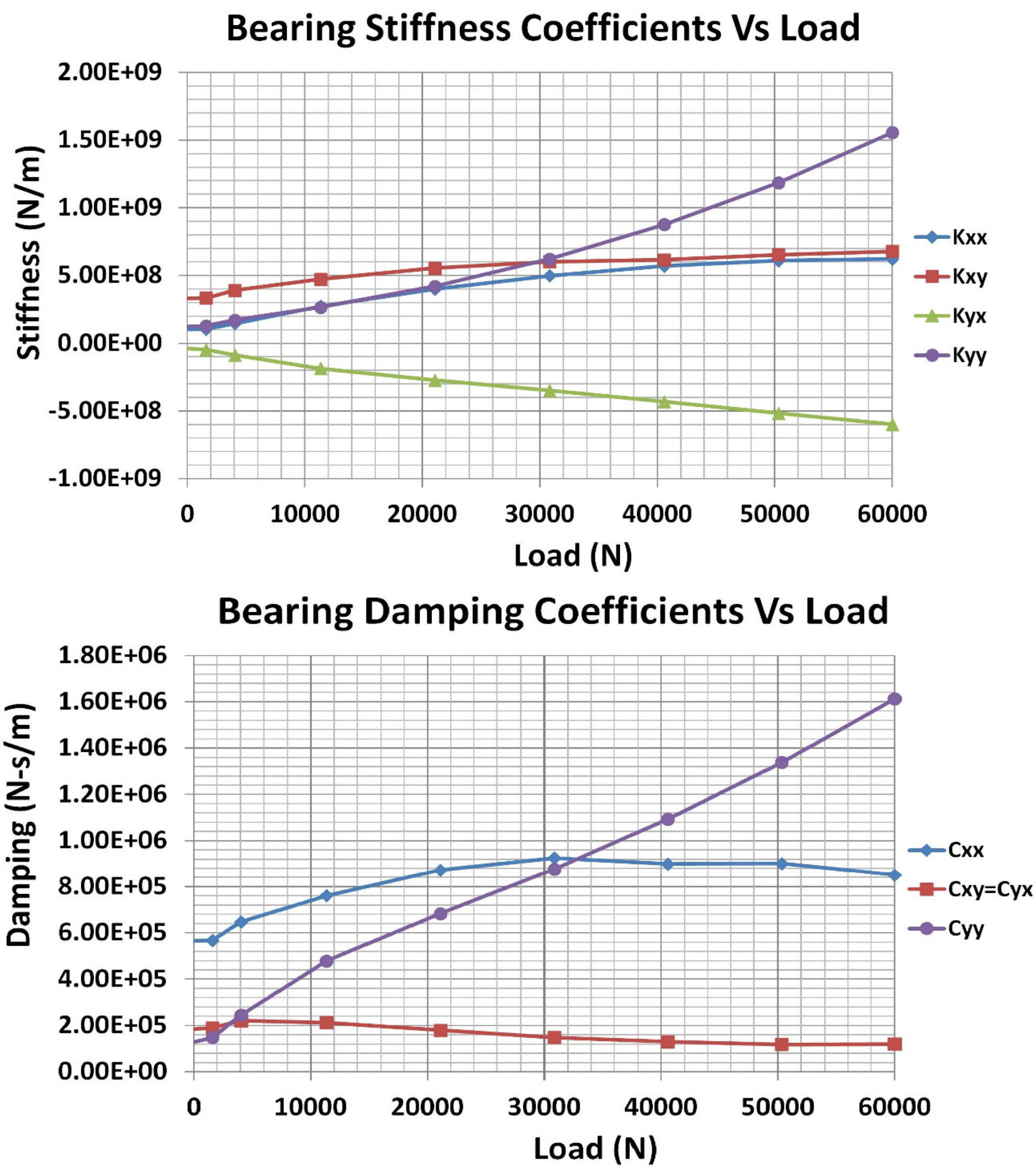

Figure 4.6: High-speed pinion bearing stiffness and damping coefficients as functions of generator loads

Table 4.2: Gear mesh parameters used to produce mesh stiffness matrix

Parameter	Value	Units
E_{gear}	206×10^9	Pa
E_{pinion}	206×10^9	Pa
R_{gear}	653.2	mm
R_{pinion}	90.9	mm
α_n	0.349	rad
β	0.471	rad
b	200.5	mm
φ	0	rad

vibration. In rotor dynamic models, these stiffnesses are represented as cross-coupled stiffnesses. Typical sources of destabilizing stiffnesses include fluid-structure interaction in fixed pad fluid film bearings and seals, rotor internal friction, and other components. The destabilizing stiffness resulting from the free oil in the coupling was introduced into the rotor dynamic model in the form of cross-coupled stiffness at the coupling side of the high-speed pinion.

The free vibration equations of motion are solved and the critical speeds, mode shapes, and log decrement values are evaluated over a range of cross-coupled stiffness values. The gearbox bearings are modeled as lightly loaded. Since there is no indication of large axial vibration and because the herringbone gearbox configuration is designed to eliminate thrust loads, the free vibration equations are solved with lateral and torsional degrees of freedom only. When a cross-coupled stiffness of $5.68 \times 10^7 \ \frac{N}{m}$ was applied to the coupling hub, it produced instability in the rotor dynamic model that was consistent with the observed measurements. The eigenvalue results, shown in Table 4.3, reveal an unstable conical whirl mode with a damped natural frequency matching 0.88x, where x is the high-speed pinion running speed. The unstable conical whirl mode is shown in Figure 4.7 This seems to indicate that the entrained oil in the coupling is the likely source of the destabilizing stiffness. The oil came from leakage from the turbine inboard bearing.

4.3 Bearing redesign

A three-lobed pressure dam bearing was designed as a proposed replacement for the original 2-lobe offset halves bearing. The three-lobe design with two pressure dams is based on bearing designs previously reported by Nicholas [42]. Given the load direction, a three lobed bearing with pad parameters reported in Table 4.4 is deemed appropriate for the analysis. Pressure dams are added to pads 2 and 3 as shown in Table 4.5.

A shaft diameter of 5.501 inches (140 mm) and radial clearance of 0.006 inches (152.4 μm) were used in this model. Figure 4.8 gives the stiffness and damping values obtained from this new design.

Table 4.3: Damped coupled lateral torsional free vibration analysis results

Mode Num	Damped Nat Freq. (RPM)	Log Dec	Whirl Ratio	Mode Type
1	511.2	0.00	0.05	Tor
2	884.4	4.55	0.08	Lat
3	952.2	4.61	0.09	Lat
4	1553	5.91	0.14	Lat-Tor
5	2148	1.80	0.20	Lat
6	2462	0.41	0.23	Lat
7	4731	0.00	0.44	Lat-Tor
8	5127	0.88	0.48	Lat
9	5259	-0.03	0.49	Lat-Tor
10	5604	0.77	0.52	Lat
11	6343	1.46	0.59	Lat-Tor
12	6669	0.15	0.62	Lat-Tor
13	8413	1.12	0.78	Lat
14	8629	0.26	0.80	Lat
15	**9446**	$\mathbf{-2.41}$	**0.88**	**Lat**
16	11100	2.92	1.03	Lat

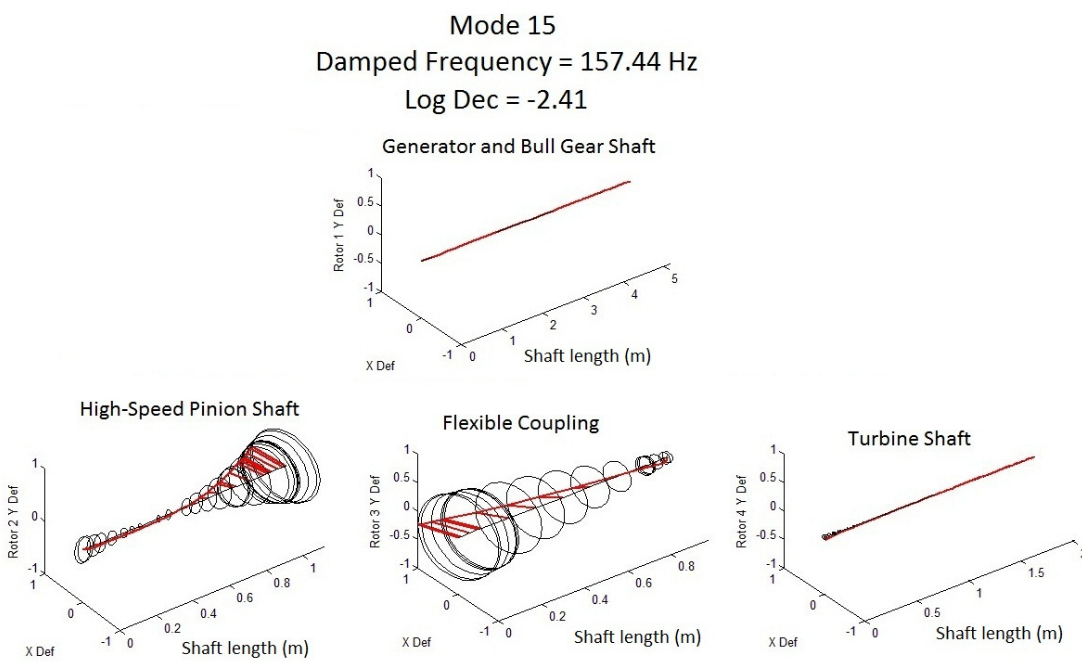

Figure 4.7: Unstable conical whirl mode 15.

Using these pad and dam geometries, the pads containing the pressure dams are predicted to force the journal into a stable position for the low load cases. For the higher load cases, the pressure dams should become increasing less influential and the load itself should force the journal to a stable position. Figure 4.9 illustrates the eccentricity plot for the new bearing design. The eccentricity ratios for this bearing design look

Table 4.4: Three lobe bearing pad geometry.

Pad	Pivot Angle, deg	Arc Length, deg	Axial Length, mm	Preload	Offset
1	52.5	97	130	0.33	0.5
2	172.5	97	130	0.33	0.5
3	292.5	97	130	0.33	0.5

Table 4.5: Three lobe bearing pressure dam geometry on pads.

Pad	Arc Length, deg	Axial Length, mm	Depth, mm
1	0	0	0
2	60	90	0.22
3	60	90	0.22

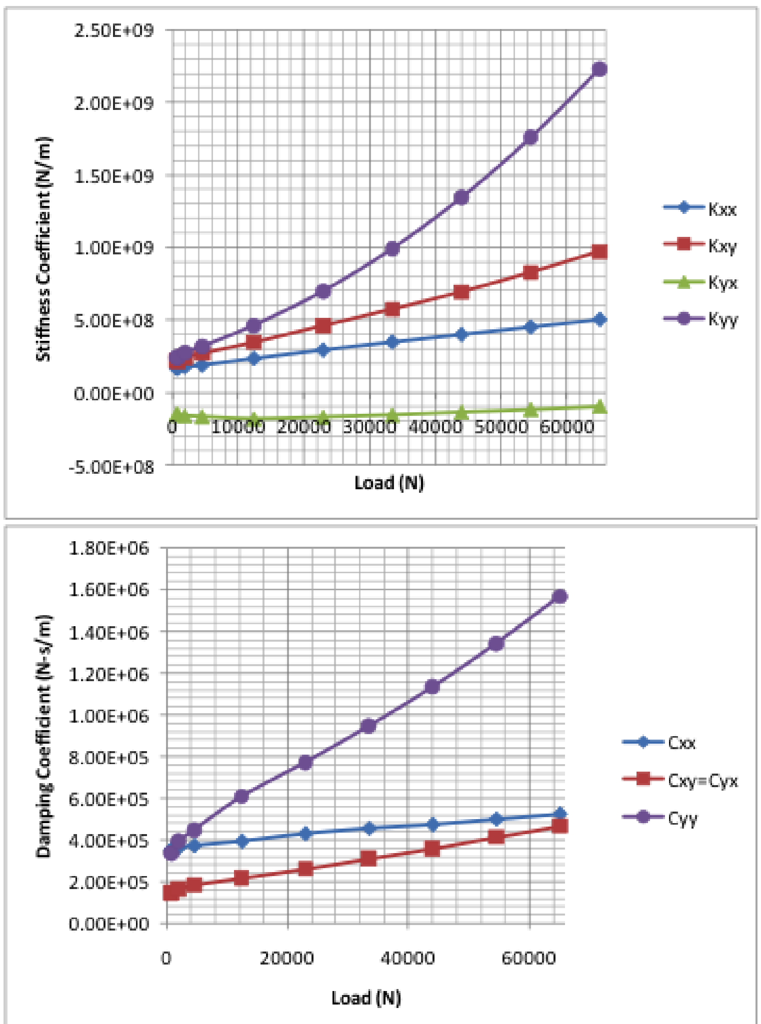

Figure 4.8: Redesigned pressure dam bearing stiffness and damping coefficients as functions of generator loads.

very satisfactory for all load cases. They range in value from 0.3305 to 0.8862, which are generally indicative of a very stable bearing. They are not located anywhere near the center of the bearing nor do they cross the center.

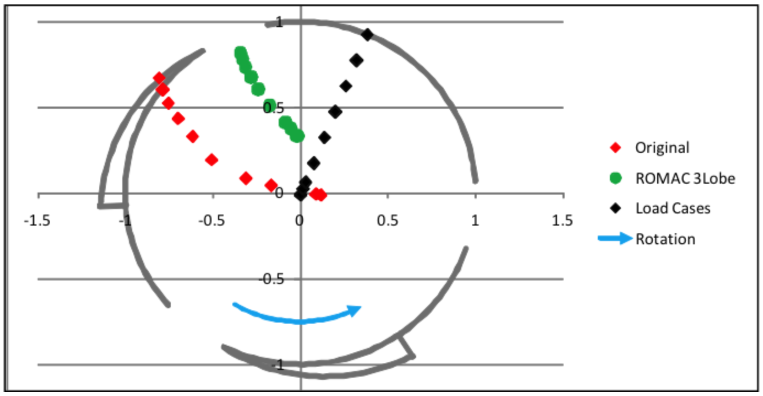

Figure 4.9: Eccentricity plot- 3-lobed bearing.

Pressure profiles over the pads of the new bearing design verify that the bearing is operating as predicted. Figure 4.10 illustrates pressure profiles for the first load case. As anticipated, the pads containing the pressure dams dominate the third pad in this case and force the eccentricity ratio to a safe distance from the center. The pressure dams are acting as desired for the low load cases. Figures 4.11 and 4.12 display pressure profiles for load cases 5 and 10, respectively. As the strength of the load increases, it dictates the position of the journal. The load places increasing pressure on pad 1 and the pressure dams become less influential. The eccentricity ratios for these cases remain in stable positions and a safe distance from the bearing wall. The three-lobed pressure dam bearing is performing as expected and appears to be a very good design for the given load conditions.

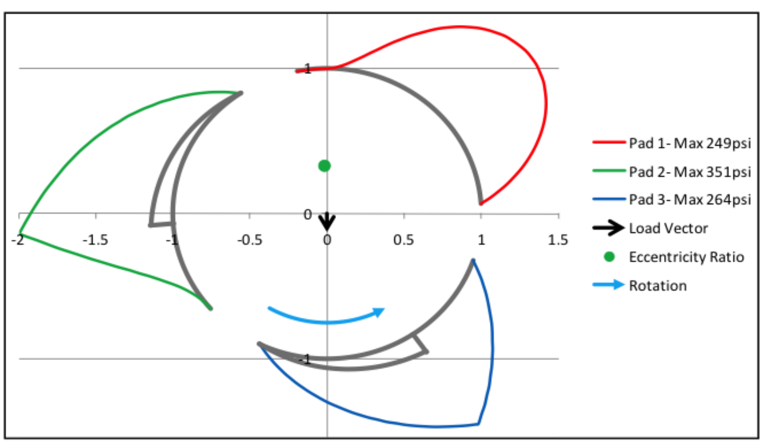

Figure 4.10: Pressure profile- 3-lobed bearing for load case 1.

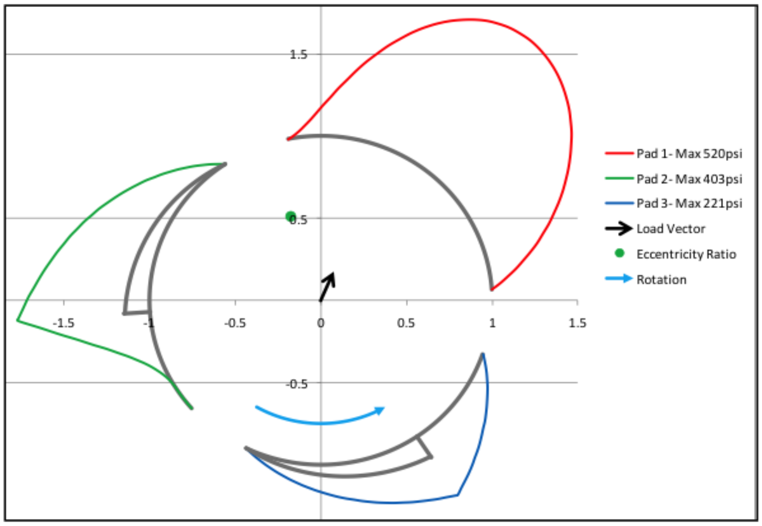

Figure 4.11: Pressure profile- 3-lobed bearing for load case 5.

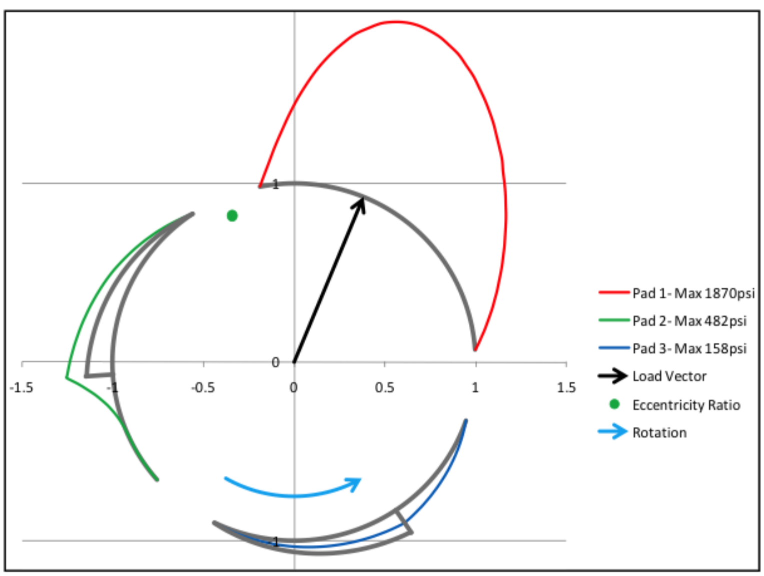

Figure 4.12: Pressure profile- 3-Lobed Bearing for Load case 10.

Table 4.6: Three lobe pressure dam bearing minimum and maximum clearance cases.

	Shaft Diam, mm	Radial Clearance, μm	Pad Preload	Pocket Depth, mm
Min Clearance	139.75	119.9	0.39	0.18
Max Clearance	139.73	152.4	0.33	0.22

In order to assure that manufacturing tolerances would not adversely affect the performance of the bearing, a sensitivity analysis was conducted. The previous 3-lobed bearing design was taken to be the maximum clearance design. A minimum clearance design was also tested with the following changes in geometry, documented in Table 4.6. The bearing design proved to be robust as it performed very similarly in both cases. Figure 4.13 shows eccentricity ratios for these cases. Given the results of this analysis, the 3-lobe bearing design is a very good bearing for the steam-turbine-generator drive-train and should replace the existing 2-lobe offset halves bearings.

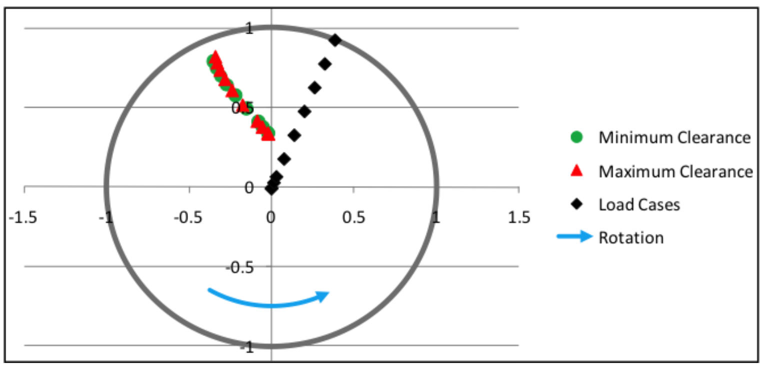

Figure 4.13: Eccentricity plot of 3-Lobed Bearing with min and max clearances.

Figure 4.14 compares the stiffness and damping coefficients for the minimum and maximum clearance cases for the 3-lobe bearing design. The general trend for all coefficients is nearly the same. A slight shift in magnitude can be seen; however, all values remain within the same order of magnitude and the small shift is trivial. These coefficients further illustrate the robustness of the new design.

4.4 Damped eigenvalue assessment with redesigned bearing

Another stability analysis is performed on the steam-turbine generator system, but with the modified 3-lobe pressure dam bearings supporting the high-speed pinion. The stability analysis was performed for all generator load cases and with minimum bearing clearance. The critical speeds, mode shapes, and log decrement values for the lowest load case are shown in Table 4.7 and Figure 4.15. As expected from the bearing analysis, the complete steam-turbine generator model has well-damped modes through the operating range. The

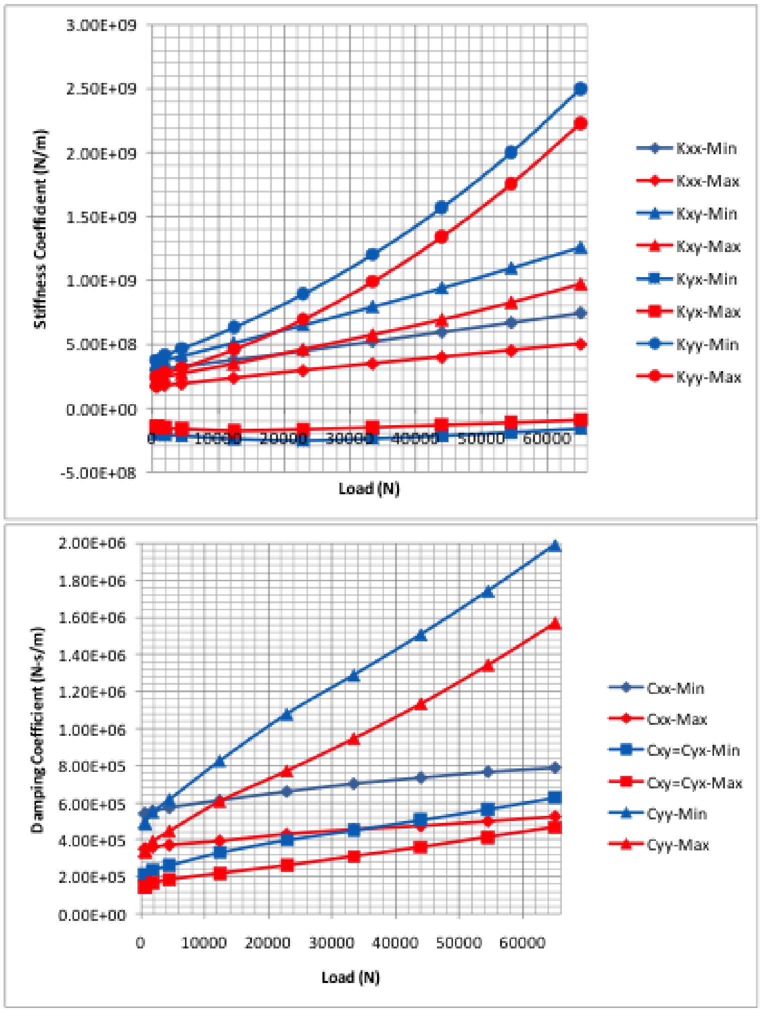

Figure 4.14: Redesigned pressure dam bearing stiffness and damping coefficients as functions of generator loads with minimum and maximum clearances.

high-speed pinion conical whirl mode that is analogous to the original bearing design is mode 4. The damped natural frequency shifted up from the original bearing to 11,404 RPM and Table 4.7 shows a substantially raised logarithmic decrement of 3.368, which is very stable. Such a frequency shift and log decrement change may be attributed to reduced cross-coupled stiffness at the bearings and reduced direct stiffness. Reduced direct stiffness allows more journal motion, which results in higher damping forces that can more effectively dissipate excess vibration.

An unbalance response analysis is conducted in Section 4.5 using the final 3-lobe pressure dam bearings. Even though the steam-turbine generator is expected to be stable under all operating conditions, it is important to assess the vibration level to insure that the journals operate safely within the bearing clearance.

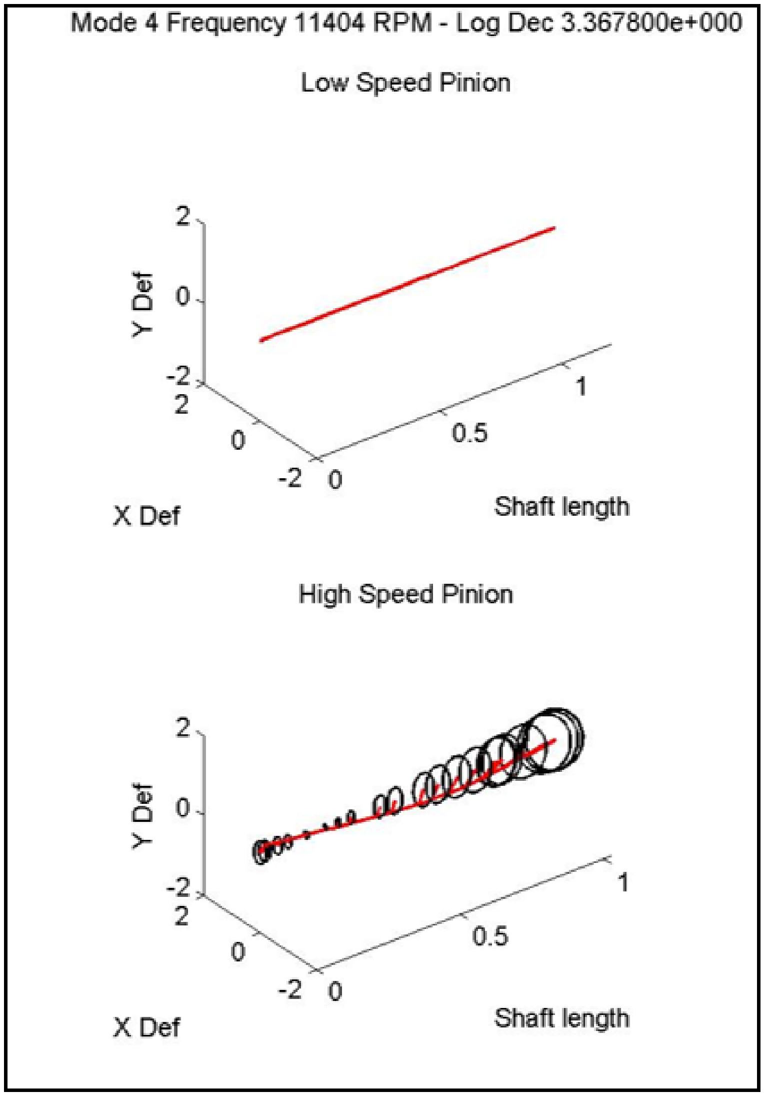

Figure 4.15: Stable high-speed pinion mode with 3-lobe pressure dam bearing.

Table 4.7: Eigenvalues for final 3-lobe pressure dam bearing with no-load.

Mode	Damped Nat Freq (RPM)	Log Dec
1	1325	5.286
2	1572	4.435
3	6746	6.914
4	**11404**	**3.368**
5	12694	10.270
6	17055	0.107
7	17528	0.214
8	17921	0.619
9	26501	3.779
10	28338	0.603

4.5 Unbalance response

All rotor systems have some amount of unbalance. These small unbalances amplify the vibration of the rotor when it passes through critical modes and can have a significant impact on the behavior of the rotor system. These vibration levels, if not analyzed properly, can lead to catastrophic failure. Therefore to predict the response of the rotor system due to the unbalance, we analyze the worst case scenario and place the unbalance weights at the locations with the largest mass in the finite element model. The unbalance response was evaluated in accordance with the requirements set by API and is determined from a damped forced response analysis of the rotor model [37].

The locations of the unbalance weights are determined based on the mode shapes for critical speeds that occur in the operating range of the rotor. The high-speed unbalance was placed at the coupling end of the HS pinion shaft. For the evaluation of the unbalance response, the maximum acceptable unbalance level is based on the following formula, as required by API [37].

$$me_u = \frac{12700W}{N} \tag{4.1}$$

W is the weight in kg and N is the operating speed in RPM. During the design phase, the amount of unbalance applied to the rotor in the analysis is required to be four times the amount specified in Equation 4.1 to provide a factor of safety. The probes are placed at the bearing locations of the HS pinion shaft. The analysis was performed on 3 load cases (no-load, load case 5, max load) to give a range of the response across the load range for the final 3-lobe pressure dam bearings. The response plots and phase plots were produced for each load case using minimum bearing clearances since that is the worst-case scenario. All three load case unbalance response plots are depicted in Figures 4.16, 4.17, and 4.18.

The unbalance response shows that the peak response around the operating range even at the worst condition is less than 4 microns and under all conditions the amplification factor is below 2.5. The only mode that was excited was the high frequency coupling bending mode around 28,000 RPM. This mode is well above the operating range and thus can be ignored.

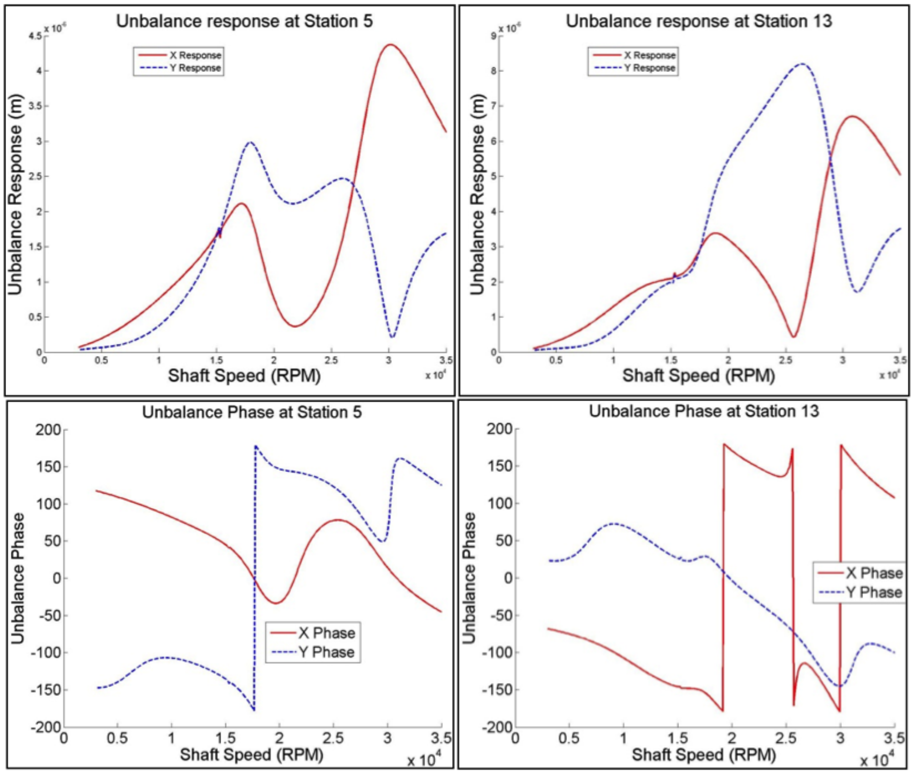

Figure 4.16: High-speed pinion bearings unbalance magnitude and phase response with minimum clearance at load case 1.

4.6 Conclusions

The gearbox of the steam-turbine-generator set exhibited high lateral vibration in the high-speed pinion consistent with a sub-synchronous instability at $0.86 - 0.89$x, where x is the running speed of the high-speed pinion. The instability was shown by analysis to be a rigid-body conical whirl mode. The instability occurred when the gearbox bearings were lightly loaded as the generator was decoupled for spin testing of the turbine.

It was discovered that an oil leak occurred from the turbine inboard bearing housing, and the oil became entrained in the high-speed coupling. Assuming that the entrained oil would produce destabilizing forces, the effects were modeled as a cross-coupled stiffness and were applied to the coupling. The instability was successfully reproduced in the model when the original bearings were lightly loaded and produced a log decrement of -2.41 and a whirl frequency ratio of 0.88x.

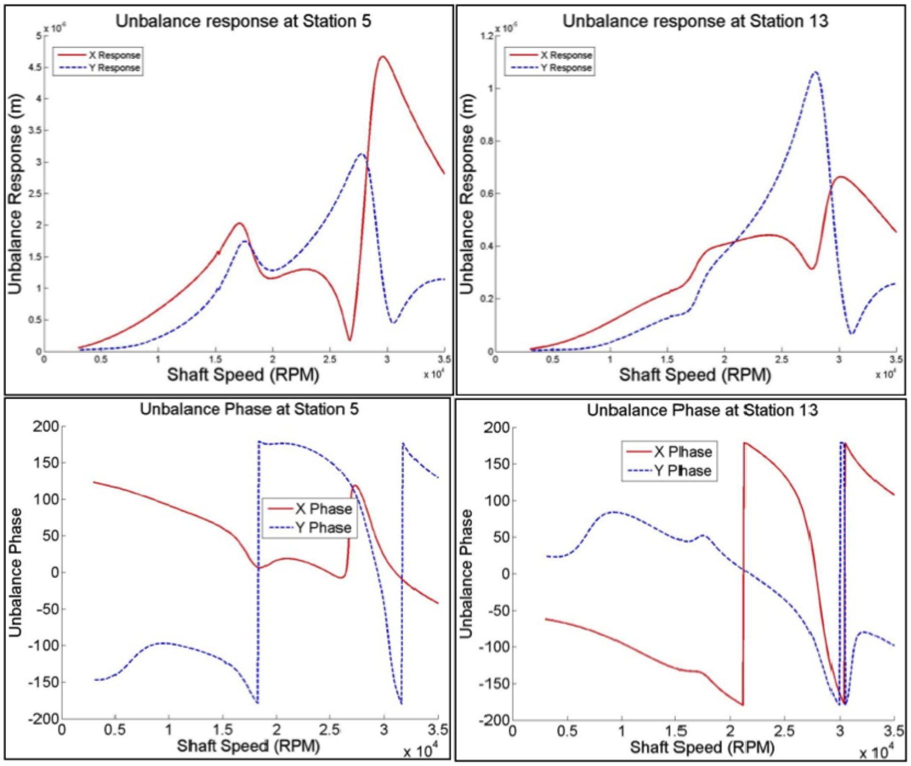

Figure 4.17: High-speed pinion bearings unbalance magnitude and phase response with minimum clearance at load case 5.

The analysis was able to reproduce the observed sub-synchronous frequency with low levels of cross-coupled stiffness applied to the flexible coupling. A 3-lobe bearing with two pressure dams on two of the pads was predicted to stabilize the gearbox high-speed pinion over the full range of generator load cases. Since replacing the existing bearings with the 3-lobe ones, the instability has vanished. These results validate the accuracy of the methods used to model not only the rotors and bearings but the gearbox dynamics too.

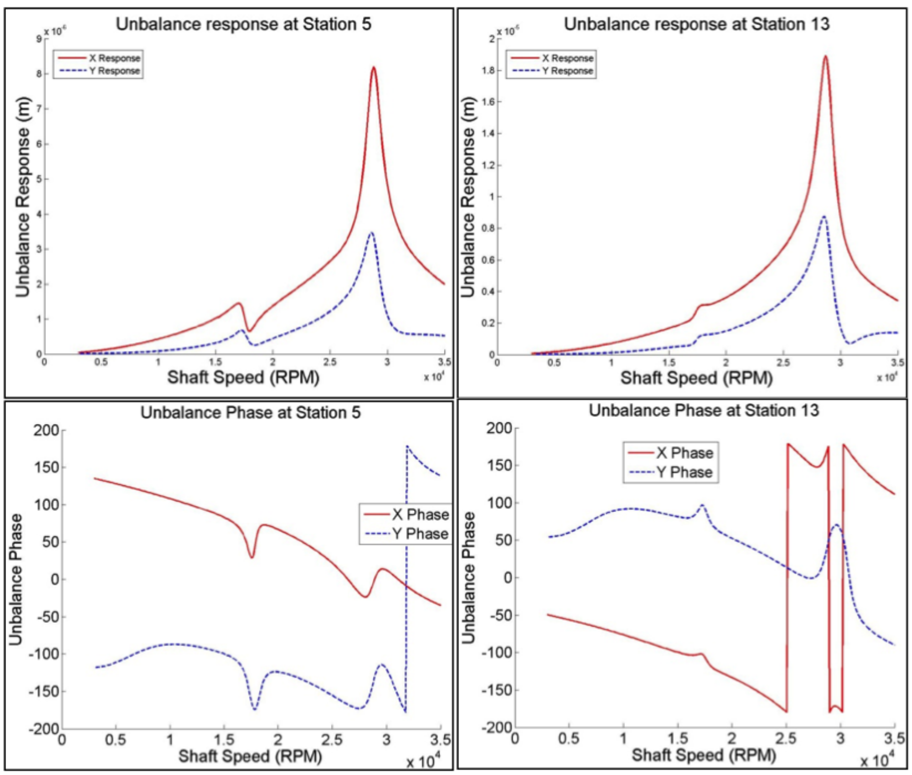

Figure 4.18: High-speed pinion bearings unbalance magnitude and phase response with minimum clearance at load case 10.

Chapter 5

Application 2: Flexible gearbox with a unity ratio

The methods shown in Chapter 3 are applied to a simple gear pair, of unity gear ratio, connecting two idealized Jeffcott rotors. This case study is used for academic purposes and is not a model of a real machine unlike the previous and subsequent chapters. The purpose of this study is to parametrically examine the effects of different parameters used in modeling state-dependent gear mesh stiffness on the rotor dynamics of a simple geared system. The Jeffcott rotor is a classic example that is ubiquitous across a wide variety of rotor dynamics textbooks because its whirling behavior due to unbalance forces or cross-coupled stiffness effects may be solved analytically. Aside from being flexible, it must have uniform diameter and be supported by simple bearings at the ends of the shaft. Point masses, typically used to represent rigid disks, may be lumped at the center along the shaft axis. Since the rotor dynamic behavior of a single Jeffcott rotor is well understood, it is expected that the contributions of the gear forces applied to them will be easier to understand.

The specifications of our simple spur geared system may be summarized in Table 5.1 and they refer to Figure 5.1. As mentioned in Chapter 2, it is important to characterize the rotor dynamics of just one shaft before drawing conclusions about the effects of the gear forces on both shafts. A linear damped eigenvalue analysis, in section 5.1, is conducted on the single-shaft system to show damped natural frequencies and their mode shapes. Such knowledge of these modes will help explain various responses encountered in later analyses.

Subsequently, a linear damped eigenvalue analysis is conducted on the complete geared system followed by an unbalance response analysis in section 5.2. Equal magnitude and phase unbalances are placed at the gear

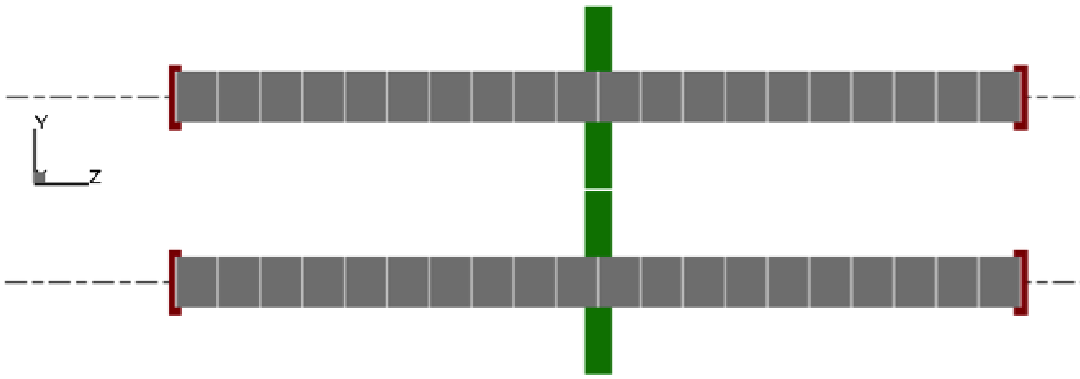

Figure 5.1: Unity ratio spur-geared shafts discretized into finite elements.

Table 5.1: Physical properties of both shafts.

Parameters	**Value**	**Units**
Shaft Length	1.02	m
Shaft Outer Diameter	0.06	m
Shaft Density	7890	$\frac{kg}{m^3}$
Bearing Stiffness	1.00 x 10^7	$\frac{N}{m}$
Bearing Damping	1.75 x 10^4	$\frac{Ns}{m}$
Operating Speed	6500	RPM
Shaft Mass	11.3	kg
Lat Stiffness	4.676 x 10^7	$\frac{N}{m}$
Tors Stiffness	2.01 x 10^5	$\frac{Nm}{rad}$

nodes on both shafts. A critical assumption used in this and preceding analyses is that the shafts operate at constant rotational speed.

A series of time-transient rotor dynamic analyses of increasing complexity are then evaluated in section 5.3. The first follows the constant gear mesh stiffness modeling shown in section 3.1. In sections 3.2 and 3.3, models of increasing complexity are evaluated as time-dependent gear mesh stiffness and backlash clearance non-linearities are included. One of the objectives of using this model is to evaluate the sensitivity of the unbalance response due to variations in several gear mesh and other numerical parameters. Please refer to Table 5.5 for the complete list of parameters that are varied for this model.

5.1 Linear damped eigenvalue analysis of single shaft

Using the standard rotor dynamic free vibration equation of motion, shown in Figure 3.10, the first 10 modes (eigenvectors) and their damped natural frequencies and stability are evaluated for the single shaft model. The first bending mode (mode 6) is of interest because most of the modal participation occurs around the center of the shaft and much less near the bearings as shown in Figure 5.2. The first bending mode, therefore, is

Table 5.2: Physical properties of gear mesh

Parameters	Value	Units
K_g	3.00 x 10^7	$\frac{N}{m}$
φ	0	rads
α	0.349	rads
β	0	rads
r_i	0.11	m
r_j	0.11	m
N_1	30	teeth
N_2	30	teeth

Table 5.3: First 10 modes of single shaft system at $\Omega = 6500$ RPM

Mode Number	ω_d (RPM)	Log Dec	Direction
1	5.41	8902	B
2	6.65	5980	B
3	836	1063	F
4	838	1060	F
5	6243	0.76	B
6	6261	0.77	F
7	27478	1.32	B
8	27571	1.33	F
9	64614	1.13	B
10	64862	1.15	F

typically of greatest concern in rotor dynamics because the bearings are less able to dissipate whirl promoting energy because they rely on journal motion to produce adequate damping forces. The relative stiffness of the bearings to the shaft is a strong indicator for stability of the first bending mode because too much bearing stiffness prevents journal motion. Unbalance forces acting at the location of the gears are likely to excite the first bending mode although it is expected to be stable because of the 0.77 log dec. All other modes below the operating speed of 6500 RPM in Table 5.3 are very well damped.

5.2 Linear damped eigenvalue and unbalance response analyses of geared system

The free vibration equations of motion are now applied to the geared system to numerically evaluate the damped natural frequencies, mode shapes, and their stability. The results are beneficial in establishing differences from the single shaft model and will explain how the gear mesh stiffness influences certain modes. Since the gear mesh, shaft, and bearing lateral stiffness values are within the same order of magnitude, the gear pair is expected to have a noticeable effect on the critical speeds and mode shapes. The gyroscopic

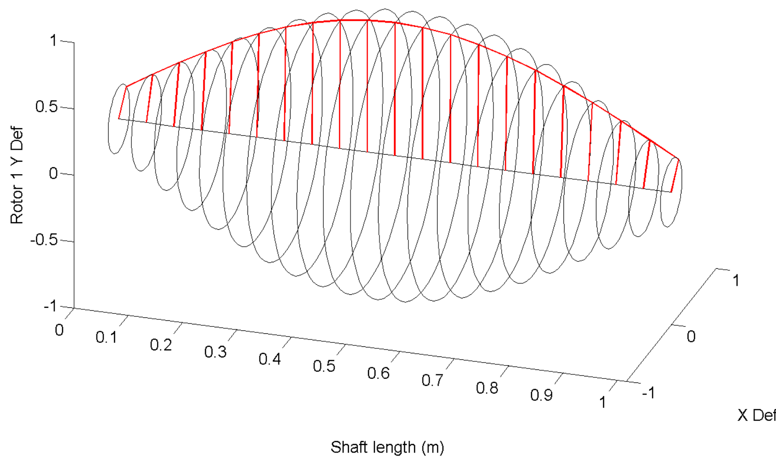

Figure 5.2: Single shaft lateral mode 6. $\omega_d = 6261$ RPM and log dec $= 0.77$.

influence should be considered because the shafts are rotating in opposite directions although with the same magnitude of speed. It is also necessary to examine the directions of the displacements since the lateral-torsional coupling of the gear mesh element may produce modes that exhibit lateral, torsional, and even axial participation for the same mode.

Using the gear parameters from Table 5.2 for the gear mesh, the geared system free vibration equation is solved. The first 20 mode shapes, critical speeds, and logarithmic decrement values are evaluated and shown in Table 5.4. Nearly double the number of modes are present within 10x shaft speed when compared with the single shaft case. Unlike the single shaft modes that come in pairs, the geared system modes come in sets of 3 or 4. In addition, several lateral-torsional coupled modes appear and an example is illustrated for mode 8 in Figure 5.4. Modes 8-11 have a similar shape to the first bending mode in the single shaft, except that the bending occurs on both shafts. Mode 11 is shown in Figure 5.3. It is expected that unbalance added at the gear nodes at an operating speed of $6,500$ RPM would excite one of those four modes.

A steady-state unbalance response is also conducted on the geared system to assess vibration magnitude as the shafts operate through critical speeds. Although the damped eigenvalue analysis predicts that operation at the first critical speed will result in a stable steady-state orbit, the unbalance response analysis is used to determine the actual amplitude of vibration in response to a known unbalance input. The American Petroleum Institute (API) dictates several specifications that insure adequate testing before a machine may be safely operated in the field [37]. Among these are standards for the expected level of unbalance. In SI units, the expected unbalance mass may be determined either by Equation 5.1 or the level that results in 250 μm displacements, whichever is greater. The mass unbalance, U is specified in units of g-mm, shaft weight,

Table 5.4: First 20 modes of geared system at $\Omega_1 = 6500$ and $\Omega_2 = -6500$ RPM.

Mode Number	ω_d (RPM)	**Log Dec**	**Direction**
1	5.41	8902	L
2	6.65	5980	L
3	6.65	5980	L
4	835.7	1063	L
5	835.7	1063	L
6	837.7	1060	L
7	837.8	1060	L
8	6016	0.74	L-T
9	6243	0.76	L
10	6252	0.77	L
11	6261	0.77	L
12	27480	1.32	L
13	27480	1.32	L
14	27570	1.33	L
15	27570	1.33	L
16	57970	0.57	L-T
17	64610	1.13	L
18	64740	1.14	L
19	64860	1.15	L
20	71520	0.59	L-T

W in kg, and maximum continuous operating speed, N, in RPM.

$$U = 12700\frac{W}{N} \tag{5.1}$$

An unbalance mass of 720 g-mm is applied to the gear nodes on both shafts and at the same phase angle to produce peak amplitudes that reach approximately 250 μm. Steady-state X and Y displacement magnitude results are shown in Figure 5.5. As expected, the peak amplitudes occur at the critical speed of 6500 RPM, which is the operating speed. In single shaft models with isotropic bearings, it is expected that the X and Y magnitudes would be the same. That is indicative of circular whirl orbits. For the geared system, however, the mesh stiffness is oriented along the line of action, which is 20° from the vertical and results in the first shaft having a horizontally-oriented elliptic orbit and the second having a vertically-oriented elliptic orbit. Because the directions of whirl of the two shafts are in opposite directions, the net displacement vector between the gear nodes aligns with the 20° pressure angle from the the vertical.

The methods incorporated in these analyses come from [34] and assume that the dynamic mesh forces are linear with respect to the gear tooth displacements. In addition, the unbalance response assumes that the unbalance forces act synchronously with shaft rotational speed.

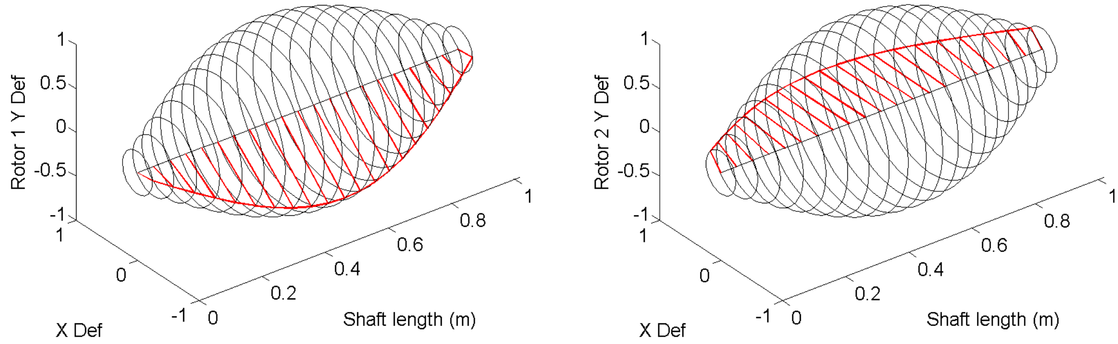

Figure 5.3: Geared system lateral mode 11 at $\Omega_1 = 6500$ and $\Omega_2 = -6500$ RPM with $\omega_d = 6261$ RPM and log dec = 0.77.

5.3 Nominal transient unbalance response

The previous sections focused on a linear time-invariant approach to modeling the geared system. Many assumptions, especially regarding only synchronous excitation at operating speed, are relaxed in the analysis undertaken in this section. An unbalance mass of 720 g-mm is applied to the center nodes on both shafts and are at the same locations as the gears. It is expected that the transient response with constant gear mesh stiffness will match steady-state results after sufficient time has elapsed.

5.3.1 Operating speed

Both shafts begin at a rotational speed of 6,500 RPM at $t = 0.0$ seconds with no external torques. It is expected that both shafts will maintain this operating speed since no torsional damping is modeled and the gear mesh stiffness is held constant. The simulation time step is 9.00 x 10^{-6} seconds and it terminates at $t = 3.0$ seconds. The response at gear 1 immediately reaches the steady-state unbalance response amplitude determined in the previous section, but there are additional dynamics present. The X and Y displacements steadily decrease afterwards until about $t = 2.5$ seconds and then abruptly drop to reach a new steady-state with much lower amplitudes as shown in Figure 5.6. The X and Y displacement FFTs reveal that the response is primarily synchronous with shaft rotational speed, but a small 2x vibration component emerges after $t = 2.5$ seconds.

Additional knowledge of the gear forces and torques are needed to better understand this response and are calculated via Equation 3.28 but with $K_v = 0$ and $h = 0$ for all t. Figure 6.12 shows the X and Y forces and torques versus time and includes FFT results for each.

Opposite to the trend in the X and Y displacements, the X and Y gear forces and torques have an abrupt increase at around $t = 2.5$ seconds. The FFTs reveal that several rotational speed harmonics are present in

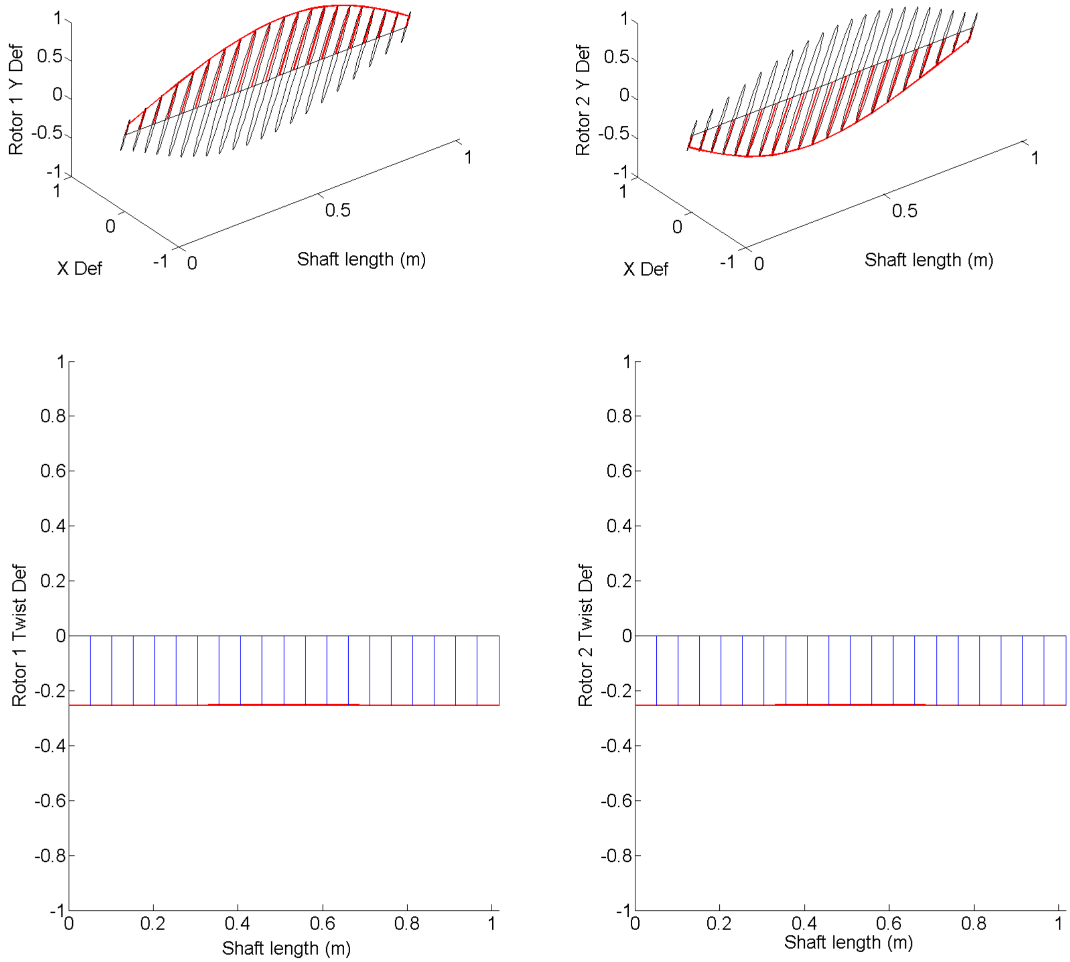

Figure 5.4: Geared system lateral-torsional mode 8 at $\Omega_1 = 6500$ and $\Omega_2 = -6500$ RPM with $\omega_d = 6016$ RPM and log dec = 0.74.

the gear forces and torques. Small components may be seen for 2x and 3x but there is a substantial excitation around 230,000 CPM (35x) that nearly equals the magnitude of the synchronous component. The gear forces and torques follow a similar trend because of the lateral-torsional coupling inherent in the geared system. These phenomena, after $t = 2.5$ seconds, are indicative of and consistent with potential numerical instability inherent in the Runge-Kutta method. Observing the shaft rotational speeds as a function of time provides further insight into the source of this high-amplitude high-frequency excitation.

The presence of oscillating torques implies that the shafts must undergo rotational acceleration because of their finite inertia. Non-zero rotational acceleration indicates that the shaft rotational speeds are not constant in time. Figure 5.8 shows the shaft rotational speed for gear 1 as a function of time and also includes the FFT. Initially the shaft speed varies by 12 RPM (0.2%) before gradually decaying to a lower amplitude but then abruptly increases around $t = 2.5$ seconds. The same high frequency harmonic that was present in the

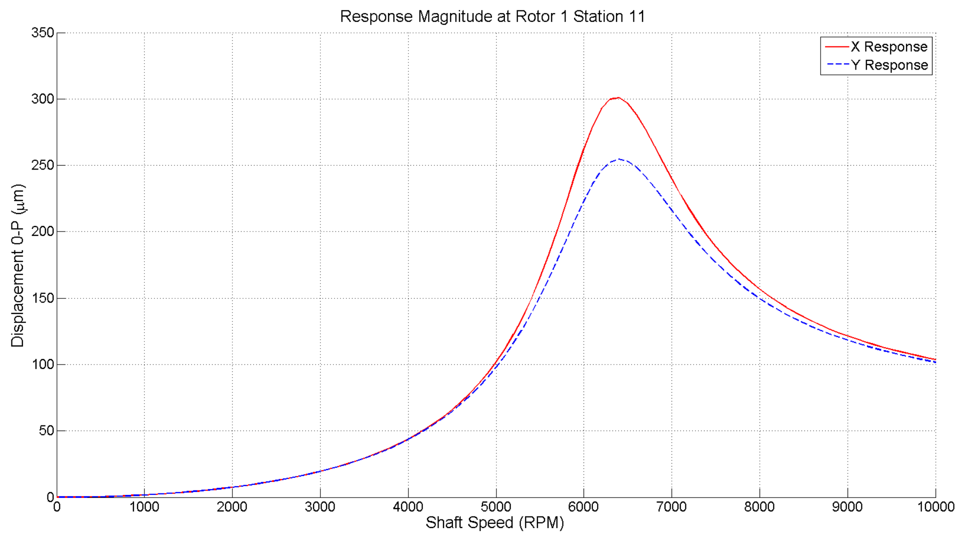

(a) Unbalance response X and Y magnitudes at Gear 1.

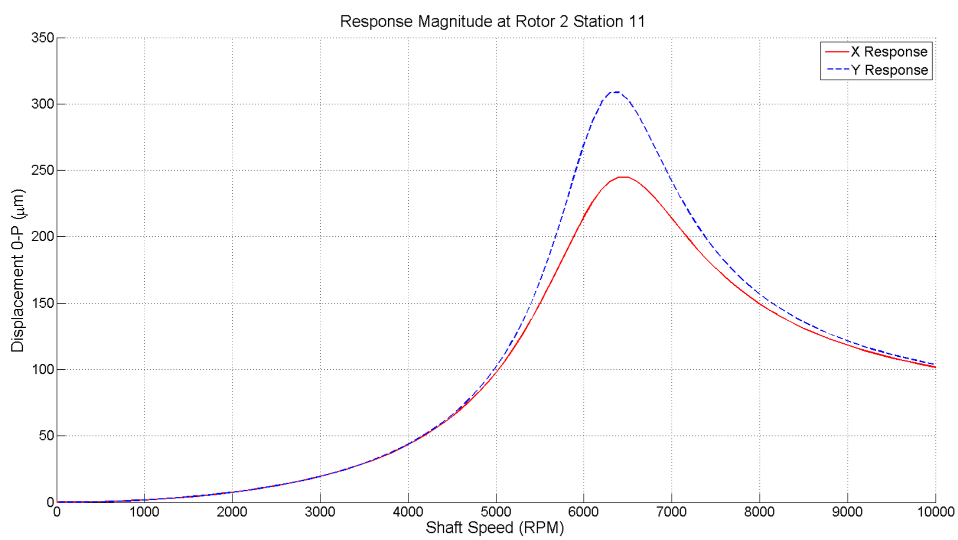

(b) Unbalance response X and Y magnitudes at Gear 2.

Figure 5.5: Unbalance response X and Y magnitudes for both gear nodes.

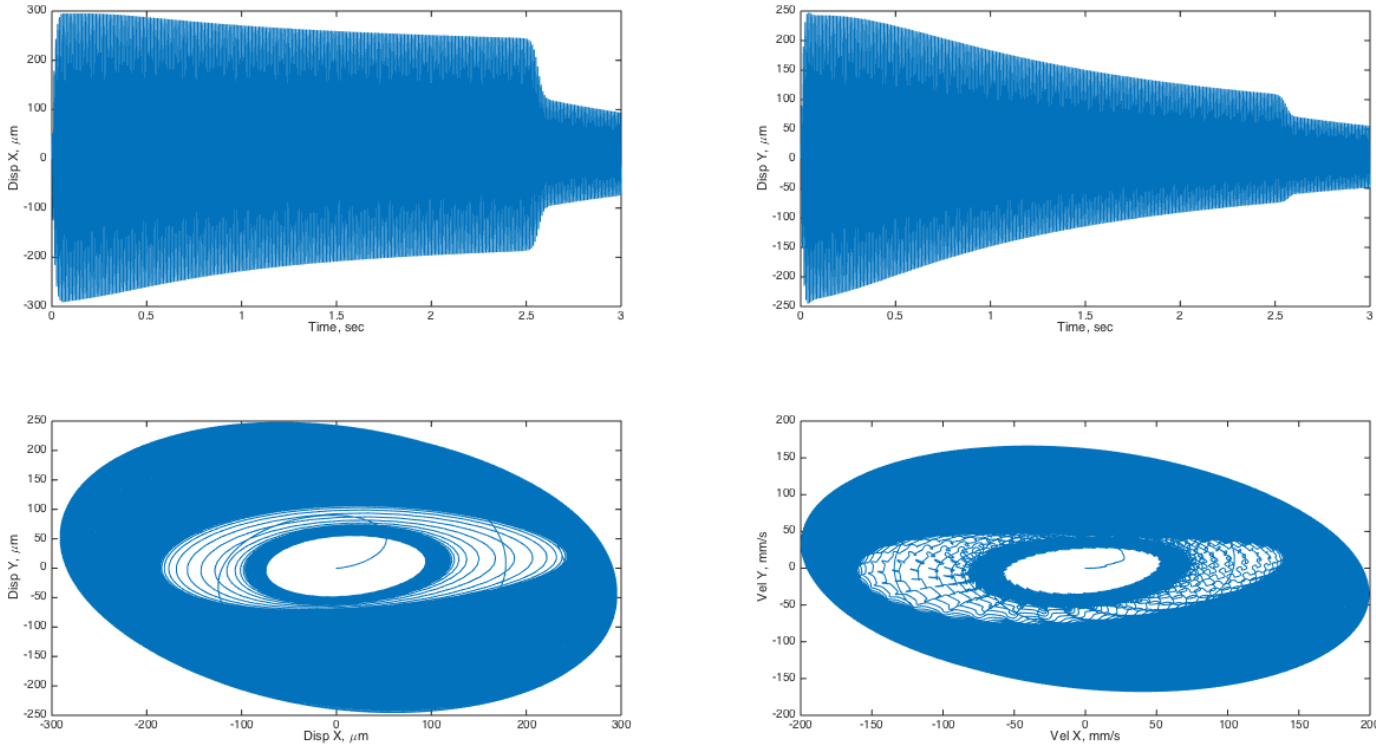

(a) Nominal orbit plot.

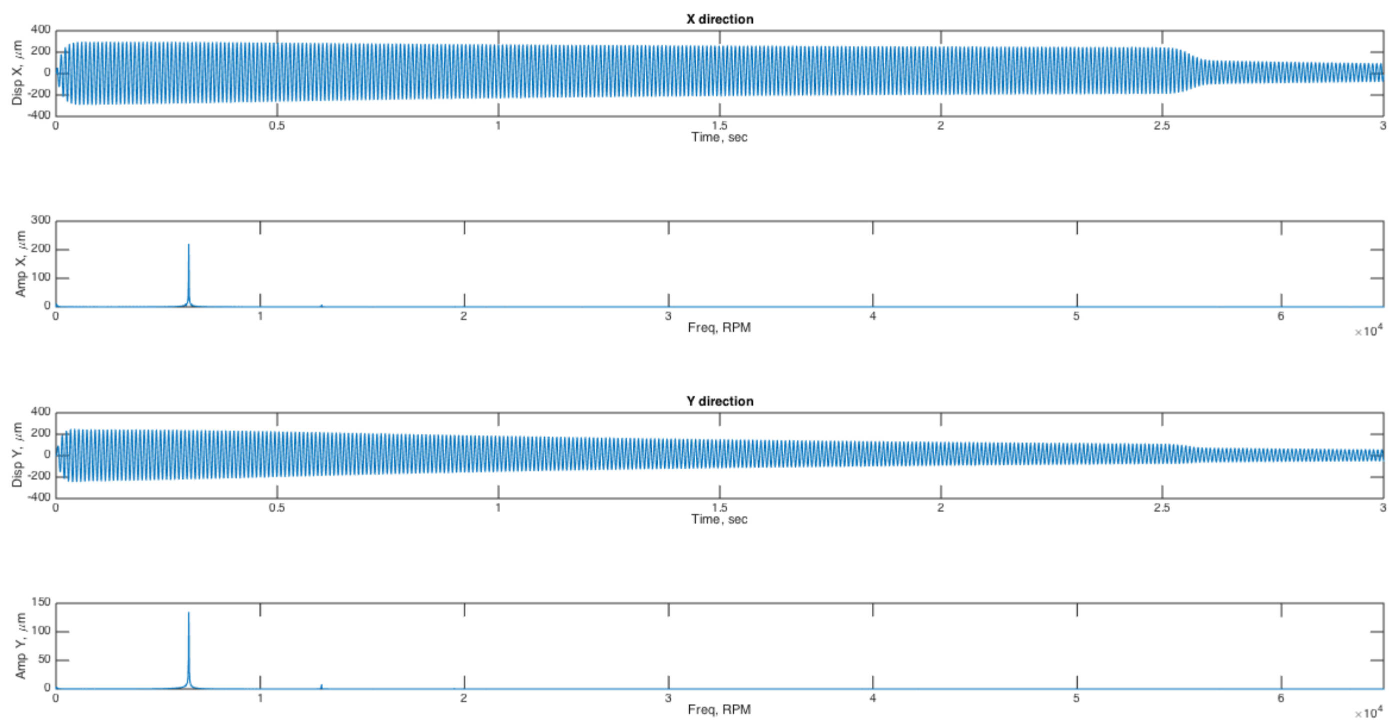

(b) Nominal X and Y displacements vs time.

Figure 5.6: X and Y displacements of nominal unbalance response.

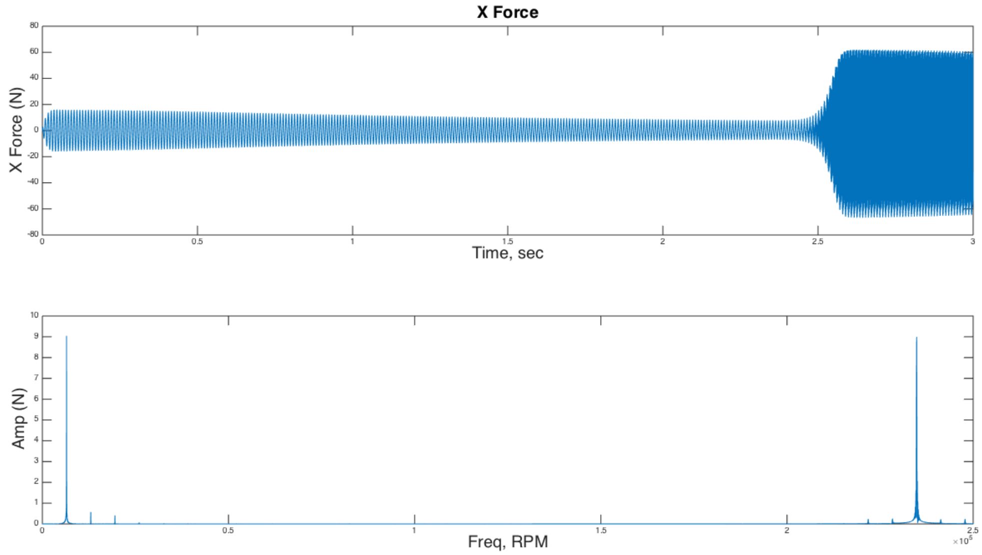

(a) Gear 1 F_X vs Time.

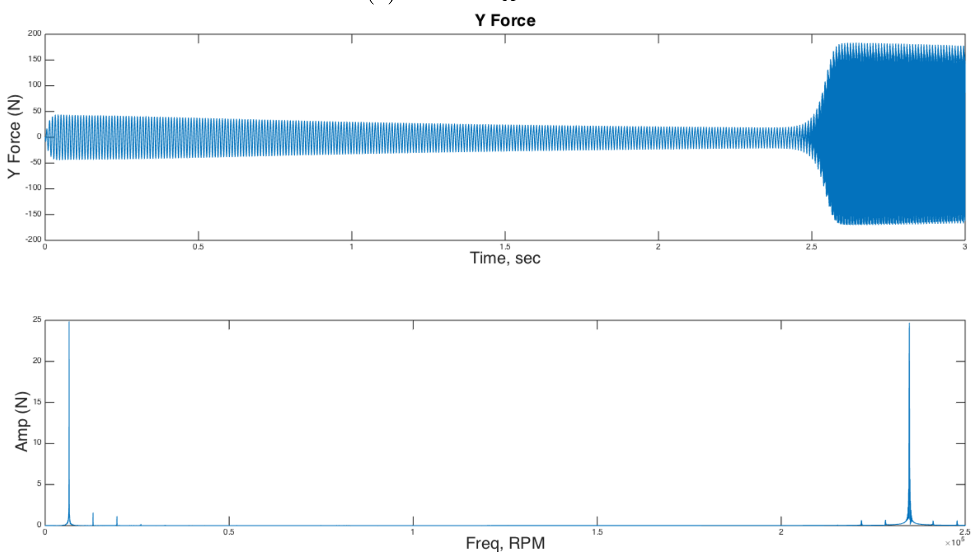

(b) Gear 1 F_Y vs Time.

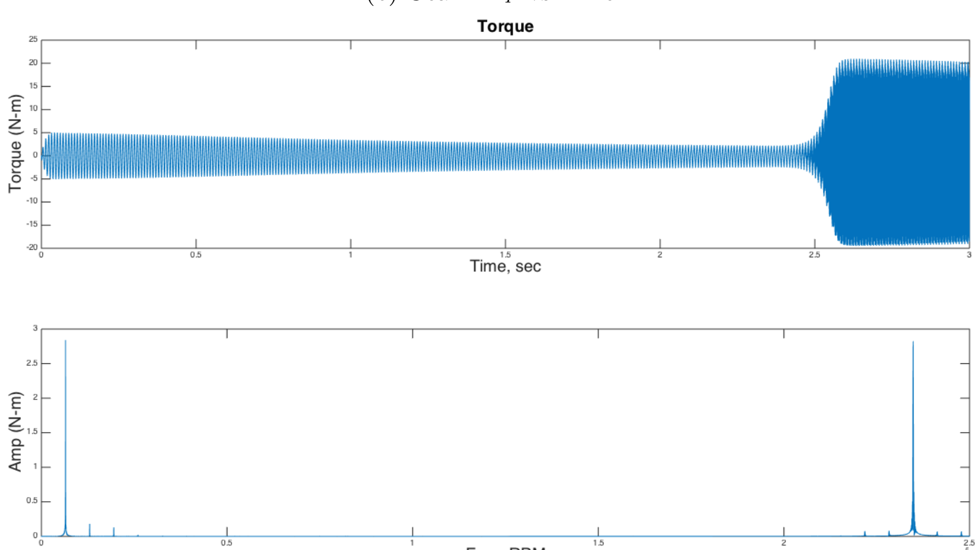

(c) Gear 1 M_Z vs Time.

Figure 5.7: Gear 1 forces and torques with $K_a = 0$.

force and torque plots becomes prevalent just after the abrupt increase. Zooming in around $t = 2.5$ seconds illustrates the growth of the high-frequency harmonic in Figure 5.7b. Shaft rotational speed variation has the following consequences in the rotor dynamic equations of motion.

- Unbalance force magnitude and frequency are modulated in time as shown in Equation B.2.
- Damping terms have non-constant coefficients – $\left[C_{brg}(\Omega) + \Omega\,(t)\,G\right]\dot{u}$
- Stiffness terms have non-constant coefficients – $\left[K_{brg}(\Omega) + \dot{\Omega}\,(t)\,G\right]u$

Modulating the unbalance forcing frequency implies that the previous assumptions used in the linear steady-state unbalance response are invalid. If the geared system were truly linear, an input of multiple forcing frequencies would generate an output with the same frequencies but with different amplitudes. Although the gear forces in this particular analysis are treated as linear with respect to their displacements, the rotor dynamic equations of motion are non-linear due to non-constant global coefficient matrices being multiplied in front of the generalized displacement and velocity vectors. The importance of capturing rotor and disk gyroscopic moments may become significant for finite elements that have large polar to transverse moment of inertia ratios $\left(\frac{I_p}{I_t} > 2\right)$. Furthermore, the bearing stiffness and damping coefficients would typically vary with shaft rotational speed, which may also contribute to non-linearities in the response. These effects vary in strength on a case-by-case basis. In this case, the modulation in unbalance force magnitude and frequency are contributing towards the tendency for smaller shaft orbits. The high frequency excitations (230,000 CPM) in the shaft rotational speeds and gear mesh forces, however, are likely due to the excitation of some lightly-damped high-order modes. An investigation of the geared system natural frequencies in the vicinity of 230,000 CPM, their mode shapes, and their stability is necessary to better understand this numerical instability.

A linear damped eigenvalue analysis of the geared system reveals damped natural frequencies, mode shapes, and their stability about the high frequency excitation of 230,000 CPM. A lateral-torsional mode with a damped natural frequency (ω_d) of 217,000 RPM is shown in Figure 5.9 for both shafts. The mode is torsionally dominant and lightly damped since bearing damping is modeled as only acting in the lateral direction. Most of the modal participation takes place along the middle of the shaft and the dip indicates the participation of the gear mesh stiffness. Although unbalance forces act laterally on the shafts, the gear mesh couples the lateral and torsional displacements and generalized forces. It is because of the lateral and torsional coupling that unbalance forces acting at the middle of the shaft could excite lightly-damped high-frequency torsional modes.

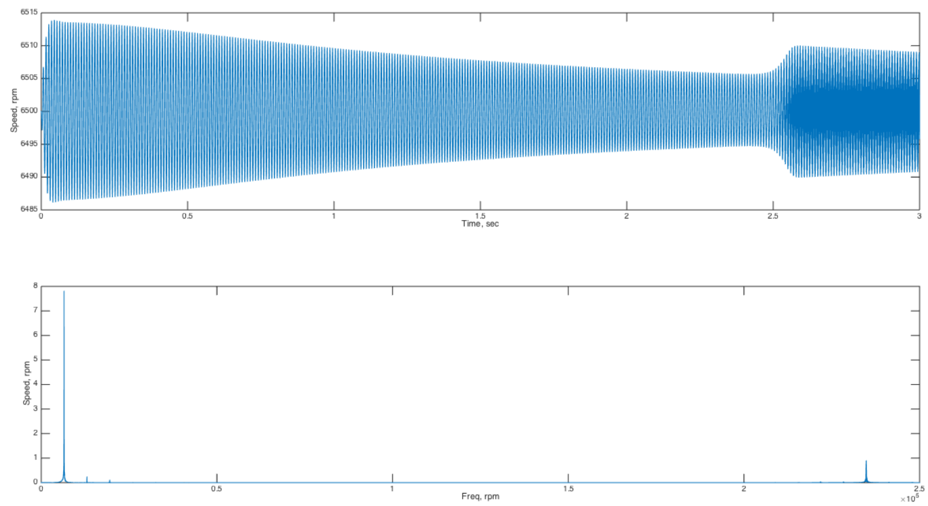

(a) Gear 1 $\dot{\theta}_Z$ vs Time.

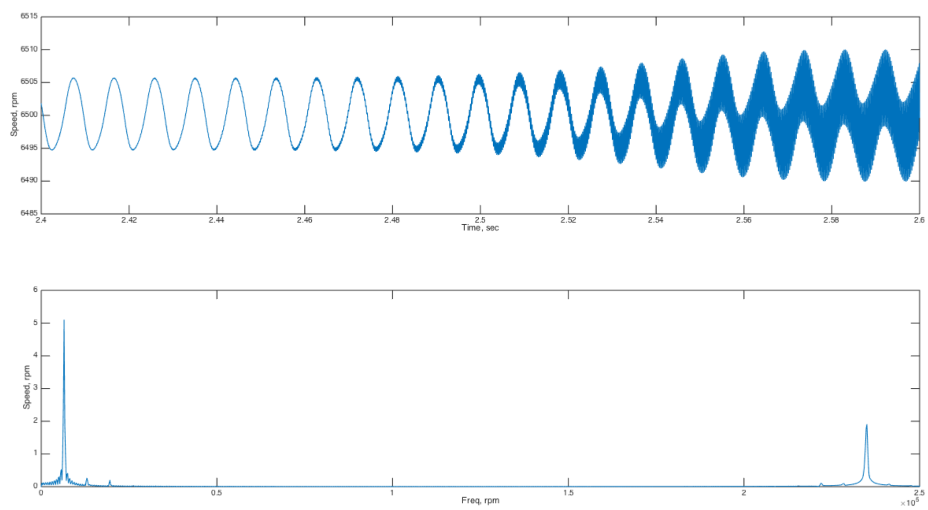

(b) Gear 1 $\dot{\theta}_Z$ vs Time showing amplification of torsional mode.

Figure 5.8: Gear 1 rotational speed vs Time

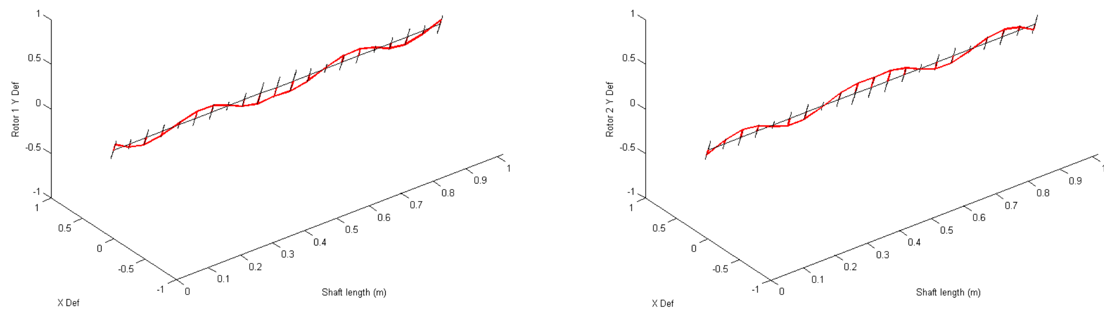

(a) Lateral component of mode

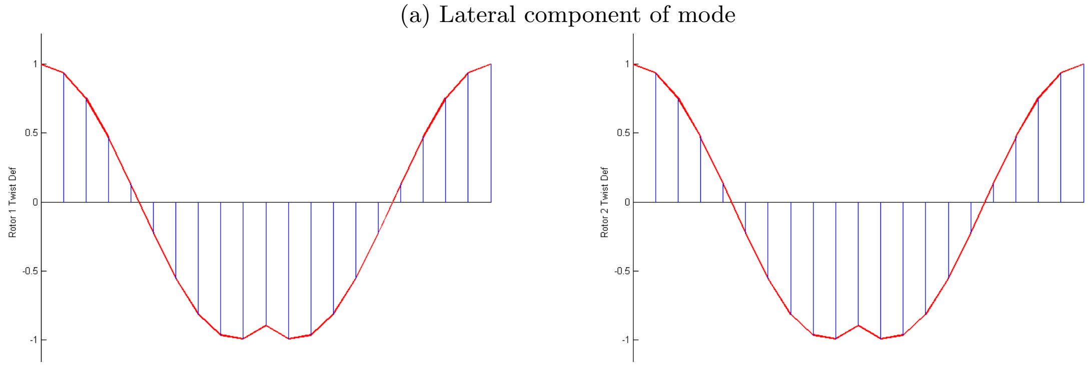

(b) Torsional component of mode

Figure 5.9: Marginally stable lateral-torsional mode of interest. $\omega_d = 217,000$ RPM (33.4x) and $\delta = 0.01$.

Several approaches may be used to mitigate the undesired excitation of this high-frequency lateral/torsional mode. Shortening the previously-used time step of 9.00×10^{-6} seconds has the effect of decreasing the onset time of the appearance of the high frequency effects, which further indicates the presence of numerical instability. The other approach uses light, and artificial, torsional damping at the gear mesh to eliminate the high-frequency mode. Previous analyses in this dissertation have assumed that no damping is present at the gear mesh, and this is the justification for this new source of damping. For an equivalent SDOF system, modal damping may be computed using Equation 5.2 where m, c, and k are the modal mass, damping, and stiffness coefficients.

$$\zeta = \frac{c}{2\sqrt{km}} \tag{5.2}$$

Since this is primarily a torsional mode of interest, the mass, stiffness, and damping coefficients need to be replaced with their torsional analogues which refer to I_p, c_{tor}, and k_{tor} respectively. Using torsional damping coefficients that would produce modal damping less than 5%, the responses are recalculated.

5.3.2 Torsional damping

X and Y displacement FFTs are presented in Figures 5.10 and illustrates the effect of torsional damping across a range of frequencies. The torsional damping produces no change in the synchronous and 2x magnitudes for the X and Y displacements. There was no high-frequency component of vibration for the lateral displacements as expected.

Torsional damping did produce a significant effect on the rotational speed FFT as shown in Figure 5.11. 1% damping reduced the amplitude of the high-frequency component and the side harmonics by more than half. Torsional damping values exceeding 2% eliminate the high-frequency component and all side bands. The 1x and 2x components remained unaffected.

Gear 1 force and torque FFTs with torsional damping are directly related to the results obtained for the rotational speed FFT. Figure 5.12 spans the entire frequency range of excitations. Similar to the results for the rotational speed FFT, 1% torsional damping at the gear mesh attenuates the forces and torques by more than half. Exceeding 2% torsional damping eliminates the high-frequency forces and torques and the side band harmonics. The 1x, 2x, and 3x components remain unaffected by the torsional damping, which is desirable and physically intuitive.

Although the FFTs depict the attenuation of frequency components in the response, additional figures illustrating the results in the time domain are necessary for qualitative purposes. Figures 5.13 and 5.14 show the X and Y orbits vs time and the time-varying rotational speed of shaft 1. The initial X and Y

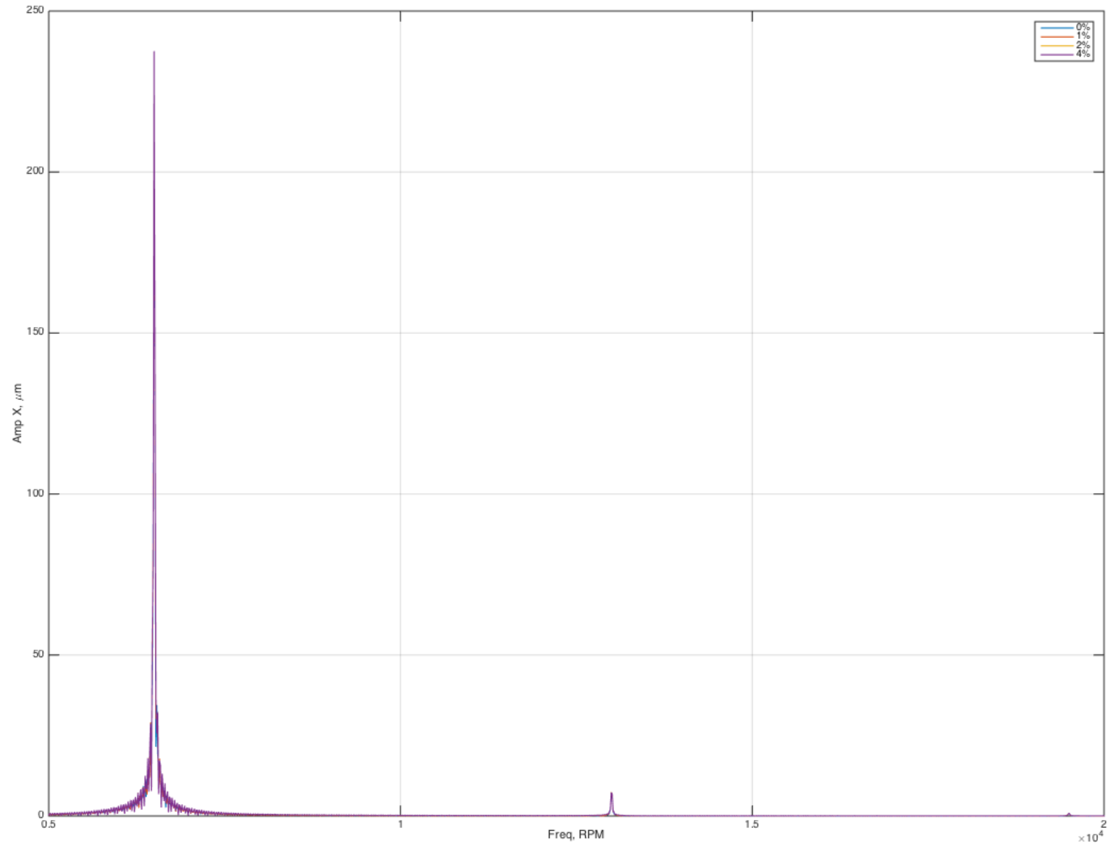

(a) Gear 1 X displacement FFT with modal damping up to 4%.

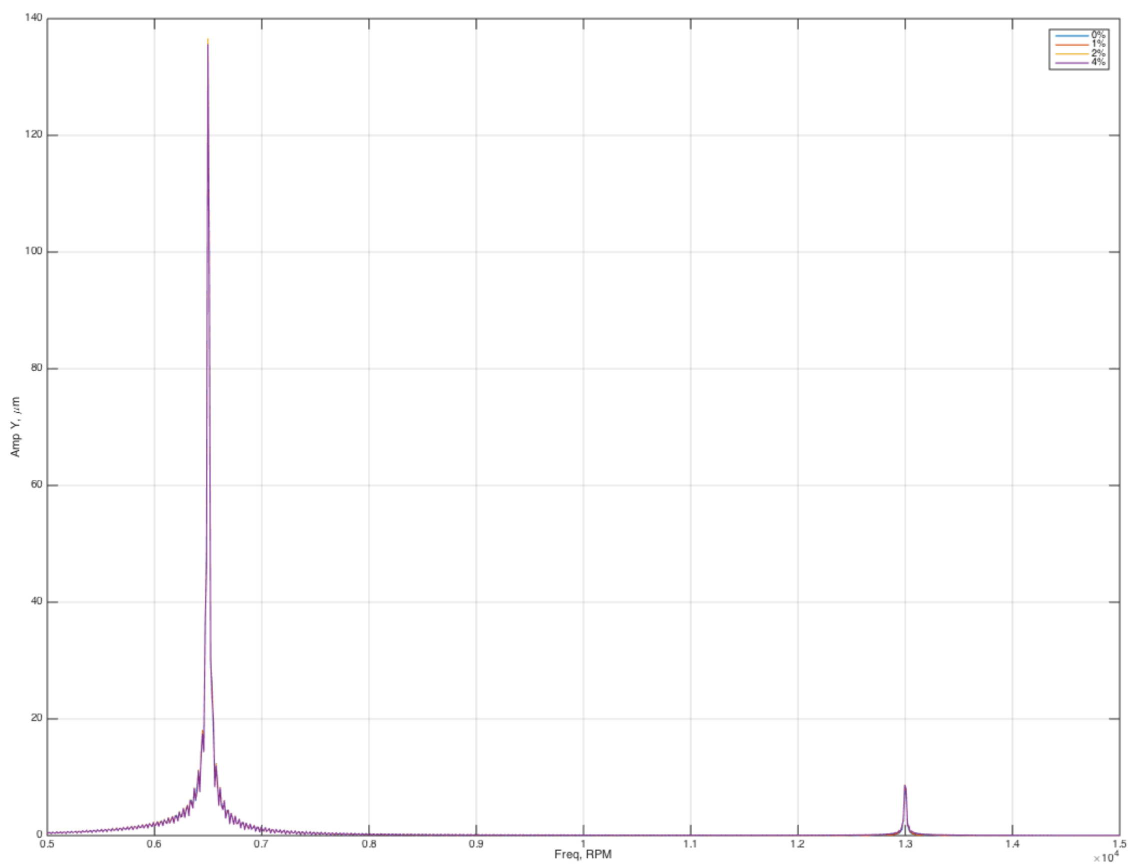

(b) Gear 1 Y displacement FFT with modal damping up to 4%.

Figure 5.10: Gear 1 X and Y displacement FFTs with varying torsional modal damping.

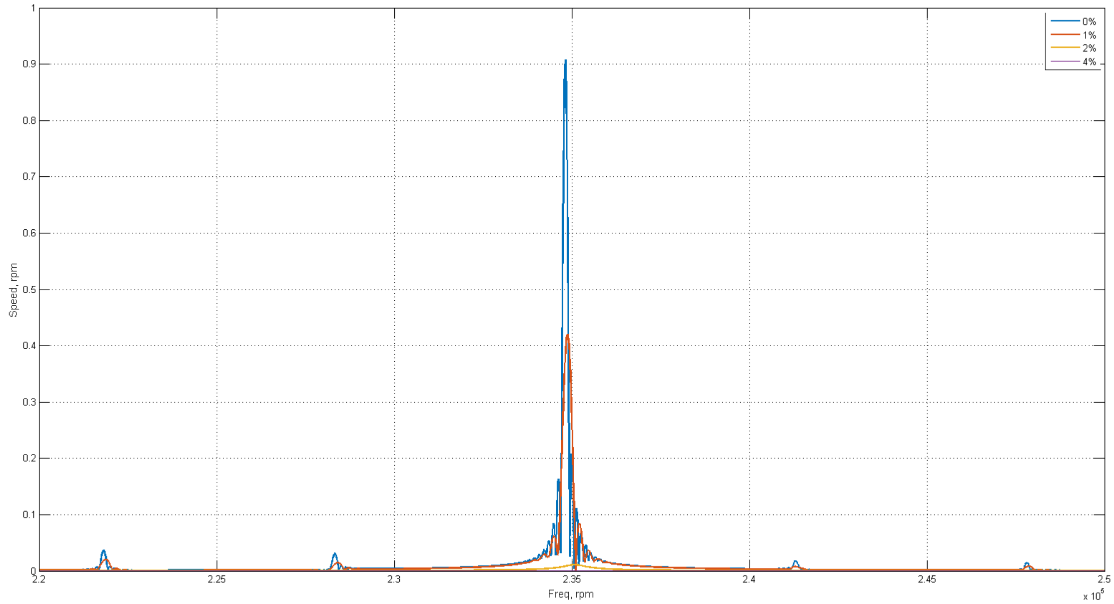

Figure 5.11: Gear 1 rotational speed FFT with modal damping up to 4%.

displacements are similar to what was shown with 0% torsional damping in Figure 5.6 except that steady-state is reached over a shorter time span and the secondary attenuation at $t = 2.5$ seconds is removed. In addition, the Y displacement amplitude decays more for the 4% damping case, which results in a horizontally elliptical orbit as t approaches 3.0 seconds. As expected, torsional damping at the gear mesh reduces the rotational speed variation over time until steady-state is reached. No high frequency components are excited in the rotational speed versus time in Figure 5.14, which is desirable and physically intuitive.

Furthermore, the Y displacements attenuated much more than X which results in highly elliptic steady orbits as shown for gears 1 and 2 as shown in Figure 5.15. The 4% damping case has larger elliptical orbits compared with those from the 0% case, which is non-intuitive because larger modal damping should generally decreases the displacements. It is suspected that the gear mesh forces and reaction torques are, therefore, working against the rotating unbalance. Observing the gear mesh forces and torques provides further insight into why the orbit shapes and displacements changed substantially.

The gear mesh forces and torques follow similar dynamics to the rotational speed variation and are plotted versus time in Figure 5.16. It is also important to discern why adding torsional damping increases the orbit sizes and promotes ellipticity while simultaneously decreasing the steady-state gear forces and torques. With both 0% and 4% torsional damping, it is evident that the magnitude of F_y is approximately 3x the magnitude of F_x for all t. In addition, the steady-state gear forces with 0% torsional damping are approximately 10x those with 4% torsional damping. Observing the generalized forces in conjunction with their respective

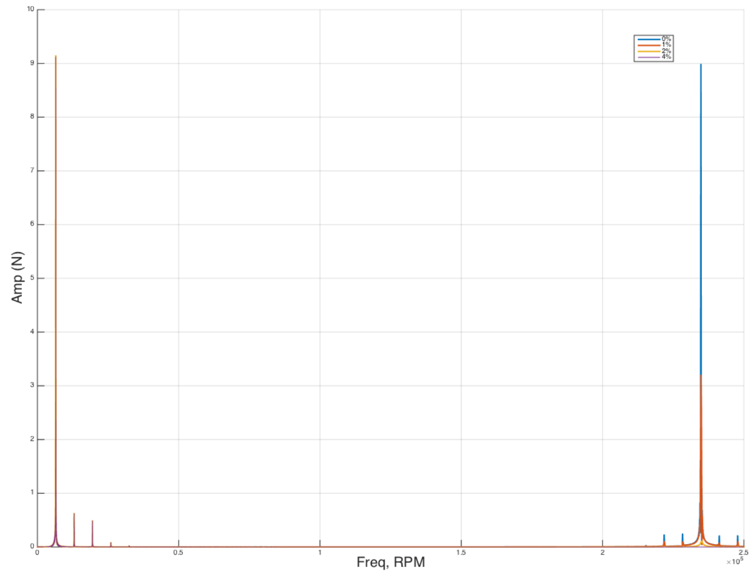

(a) Gear 1 F_x FFT with modal damping up to 4%.

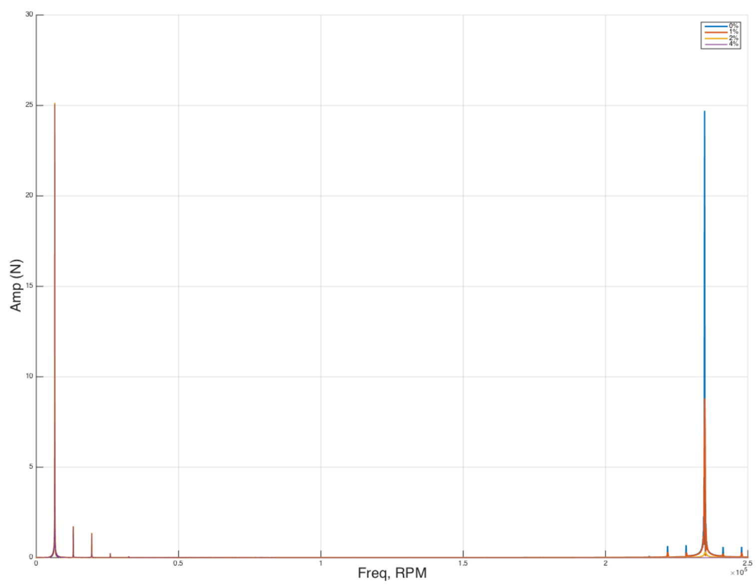

(b) Gear 1 F_y FFT with modal damping up to 4%.

(c) Gear 1 T_z FFT with modal damping up to 4%.

Figure 5.12: Gear 1 forces and torques with variation in torsional modal damping.

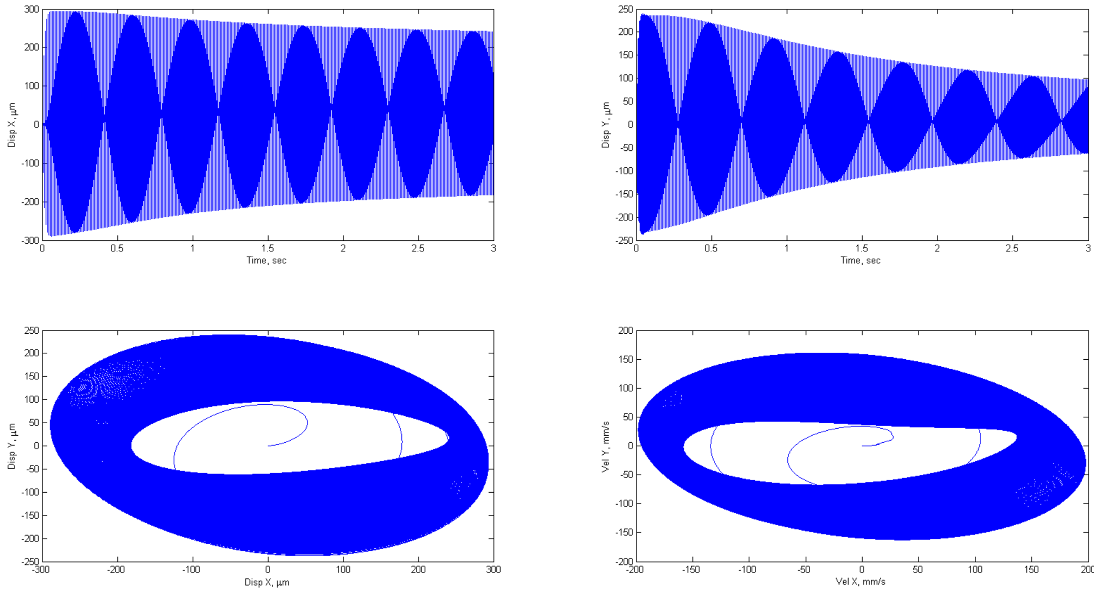

Figure 5.13: Gear 1 X, Y displacement orbits for 4% modal damping.

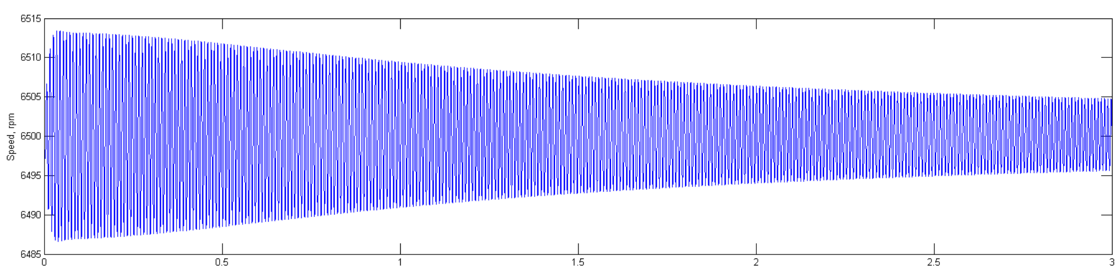

Figure 5.14: Gear 1 rotational speed for 4% modal damping.

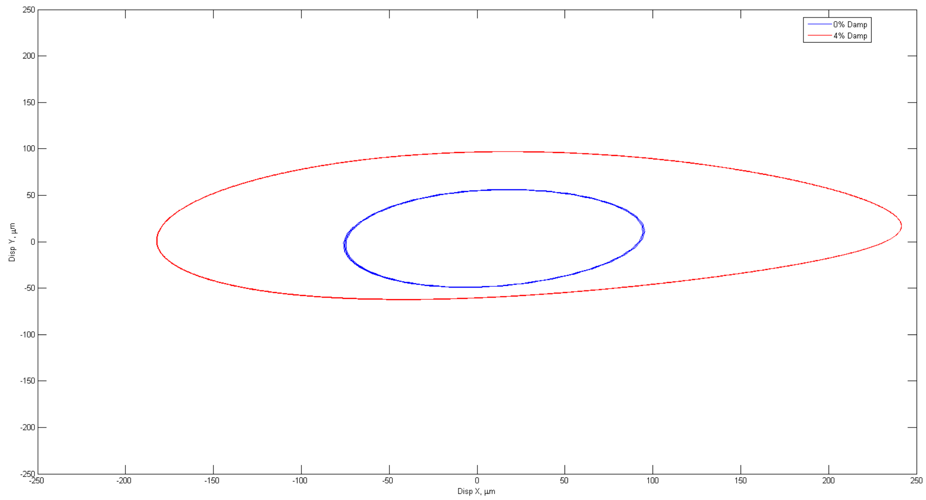

(a) Gear 1 orbit with and without 4% modal damping.

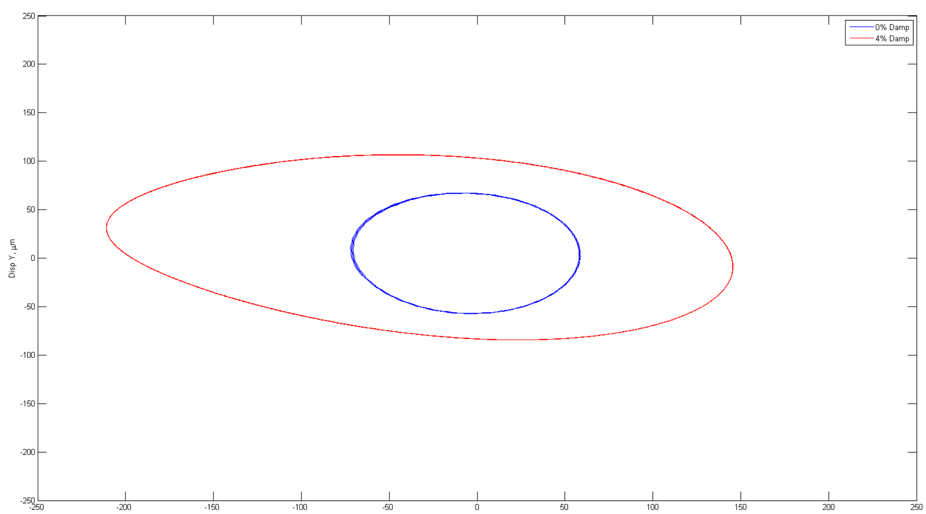

(b) Gear 2 orbit with and without 4% modal damping.

Figure 5.15: Gears 1 and 2 orbits with and without 4% modal damping.

generalized velocities should provide insights into the whirl promoting energy inherent in the gears, bearings, and unbalance forces.

These results indicate that the addition of light torsional damping at the gear mesh eliminates the excitation of the non-physical high-frequency lateral/torsional mode. The results from the 0% torsional damping care are shown to be qualitatively similar to the 4% case well before $t = 2.5$ seconds. Understanding how the gear mesh forces and torques influence the geared shaft displacements and velocities is the objective of the next section, and the 0% and 4% torsional damping cases are used for comparison purposes.

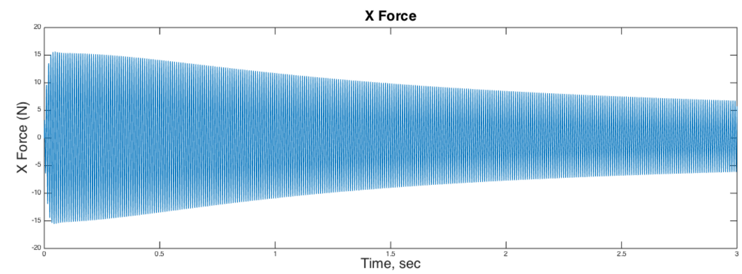

(a) Gear 1 F_x with 4% modal damping.

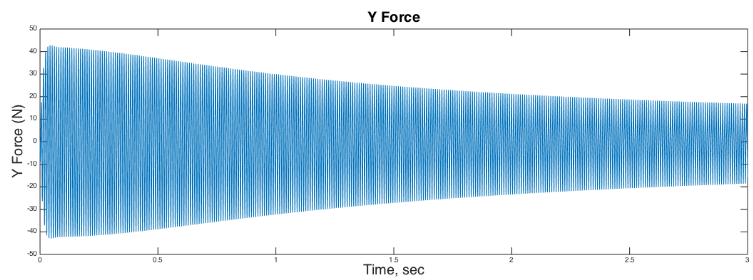

(b) Gear 1 F_y with 4% modal damping.

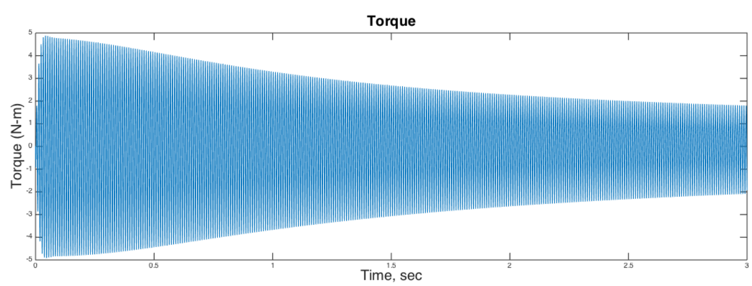

(c) Gear 1 T_z with 4% modal damping.

Figure 5.16: Gear 1 forces and torque FFTs with 4% torsional modal damping.

5.3.3 Whirl promoting energy with no torsional damping

The equivalent whirl promoting power for the bearings, gears, and modulated unbalance force may be computed for all t via Equation 5.3. For values of t when $P > 0$, the component is exerting forces on the shaft that promote whirl energy. If $P < 0$, then the component is dissipating whirl energy from the shaft. Since the bearings modeled in this example have no cross-coupled stiffness, their force contributions may be calculated through Equation 5.4. The sum of all of the contributions of whirl promoting power are used to evaluate the net gain in whirl energy over the elapsed time and depend on the force velocity relationships for the bearings, gears, and the modulated unbalance force.

$$P = F_x \dot{x} + F_y \dot{y} \tag{5.3}$$

$$\begin{aligned} F_{xbrg} &= -K_{xx}\Delta x - C_{xx}\Delta\dot{x} \\ F_{ybrg} &= -K_{yy}\Delta y - C_{yy}\Delta\dot{y} \end{aligned} \tag{5.4}$$

Figure 5.17 illustrates how the shaft unbalance, bearings, and gears contribute to whirl promoting energy in shaft 1 without torsional damping. For circular whirl orbits in non-geared systems, the unbalance force would contribute little to whirl promotion since it would be acting radially to the whirl direction and thus 90° out of phase with the instantaneous velocities. However, the gear mesh stiffness produces oscillating torques and forces that produce variations in the rotational speeds and other velocity components. Therefore, the unbalance force contribution to whirl promotion shows strong oscillatory behavior and maintains a net positive influence. The bearing damping, as expected, dissipates much of the whirl promoting energy from the unbalance, and has strong oscillatory behavior because of the gear mesh. The whirl promoting contribution from the gears appears to be much smaller than the bearings and unbalance before $t = 2.5$ seconds.

Analysis of the phasing between these power contributions near $t = 0.0$ and $t = 3.0$ seconds provides additional insights and these are shown in Figures 5.18 and 5.19. For $t < 2.5$ seconds, almost all of the dynamics are shared between the unbalance force and the bearings, where the unbalance force contributes towards forward whirl and the bearings resist it. These dynamics are indicative of the shaft experiencing whirl dominated motion instead of gear rattle. The gear mesh contribution to whirl power is insignificant in this time region. In addition, the contributions of the unbalance force and the bearing dissipation forces oscillate with increasing amplitude until the transition time of $t = 2.5$ seconds.

At $t = 2.5$ seconds, the whirl promoting power of the unbalance and dissipation of the bearings undergoes a drastic decrease at the same time as the effective whirl power at the gear mesh undergoes an increase shown in Figure 5.19. This suggests that the energy storage in the shaft becomes more concentrated at the gear mesh as it departs from shaft whirl. Again, this is the interpretation with numerical instabilities present in the system dynamics.

Since this transition happened as the lightly damped high frequency torsional mode became active, this

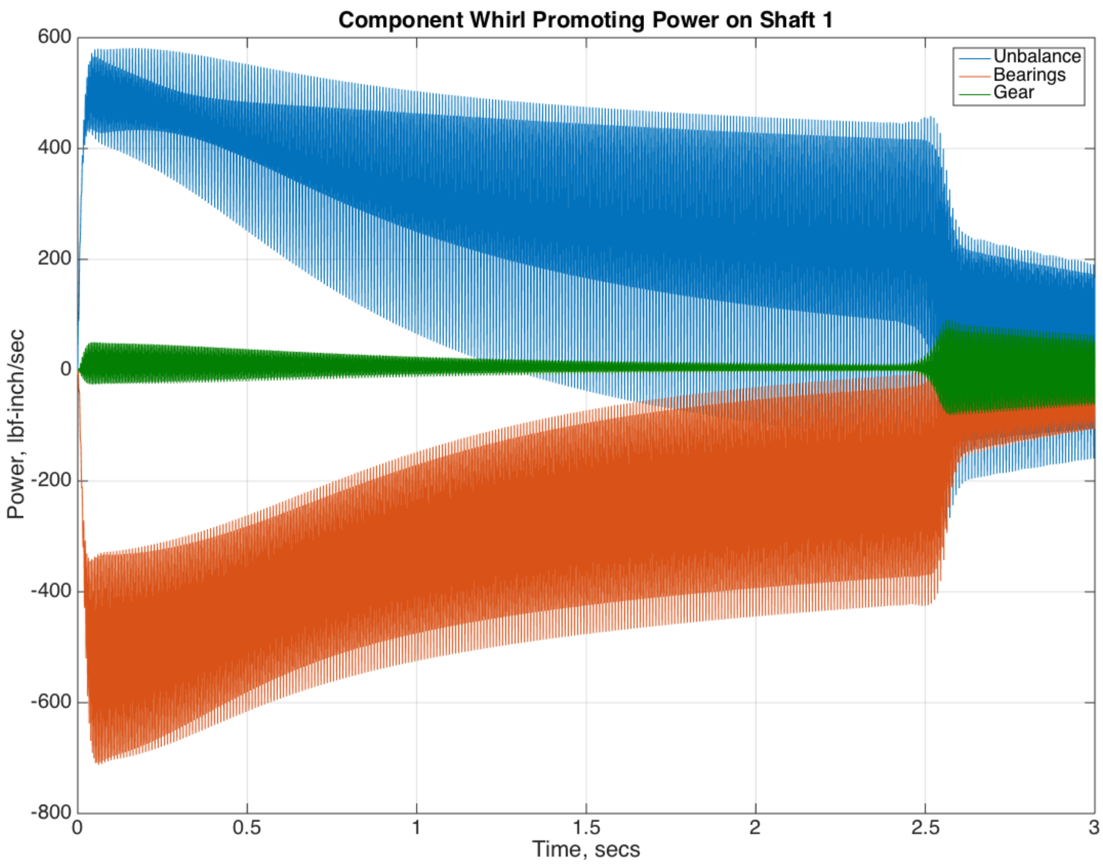

Figure 5.17: Component power with no damping.

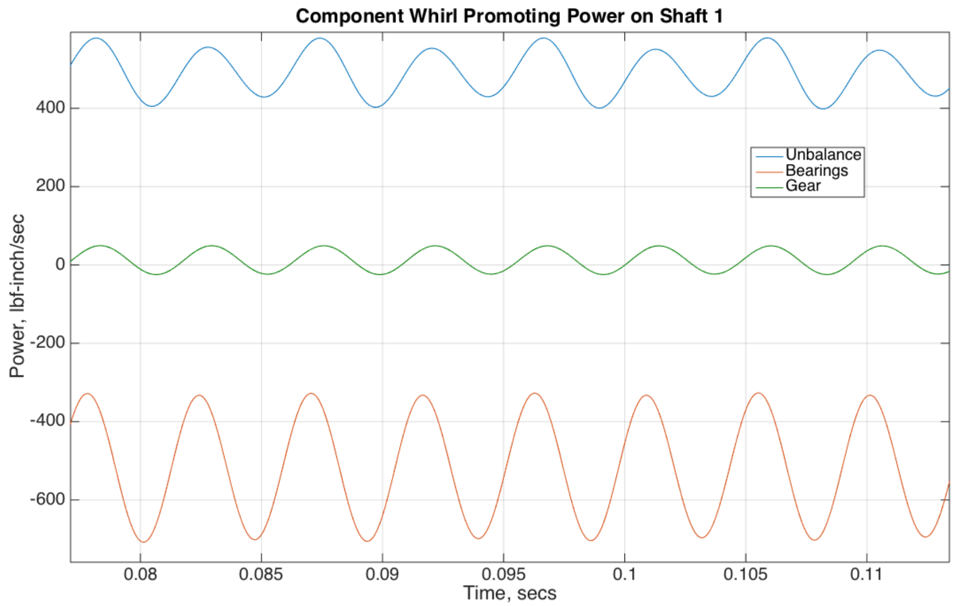

(a) Power components near $t = 0.0$ seconds.

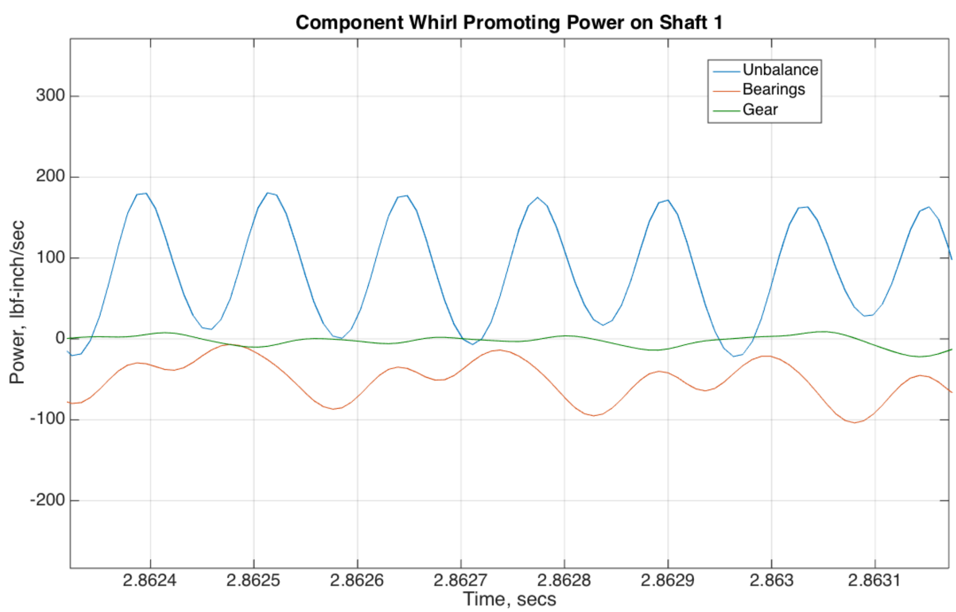

(b) Power components near $t = 3.0$ seconds.

Figure 5.18: Whirl power components at beginning and end with no damping at gear mesh.

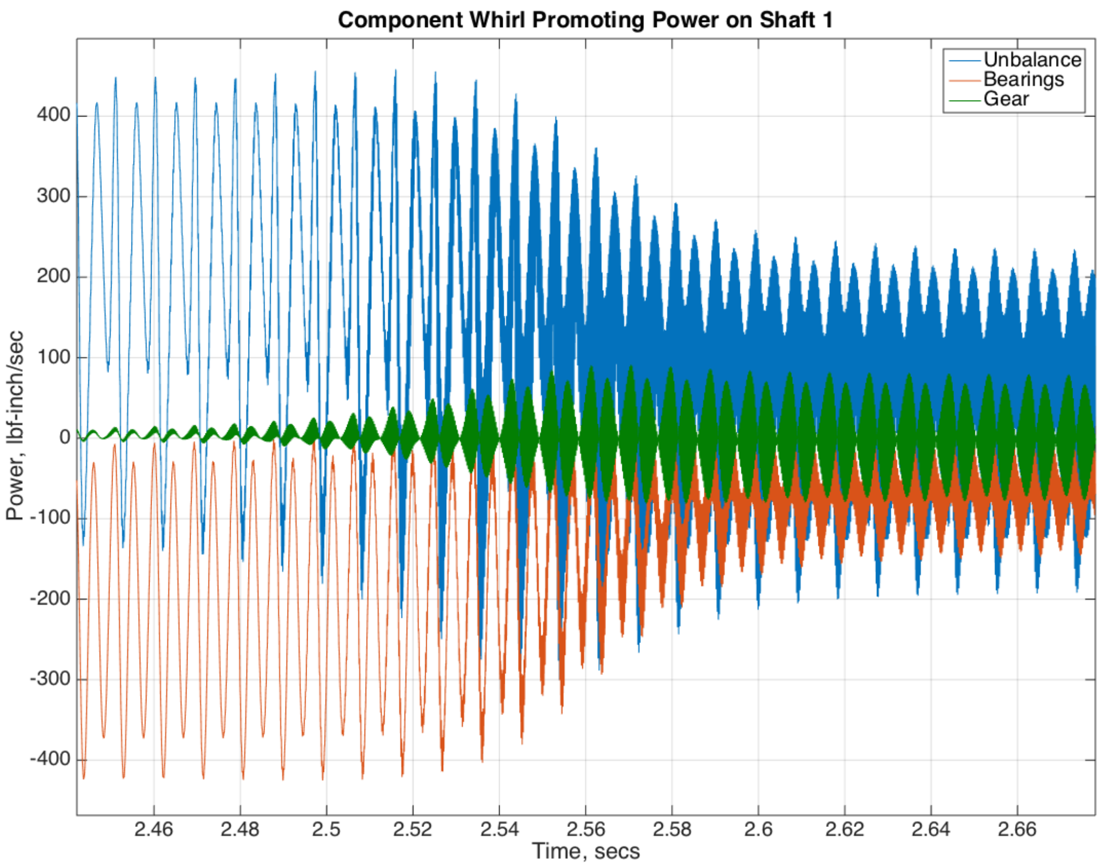

Figure 5.19: Component power with no damping while zoomed in towards transition.

may be evidence of gear noise and rattle and that the majority of the power comes from the force of the meshing surfaces as shown in Figure 5.20. Although the gear velocity decreased from 20 $\frac{cm}{s}$ to 10 $\frac{cm}{s}$, the gear force increased from 15 N to 60 N, which is double the original whirl promoting power.

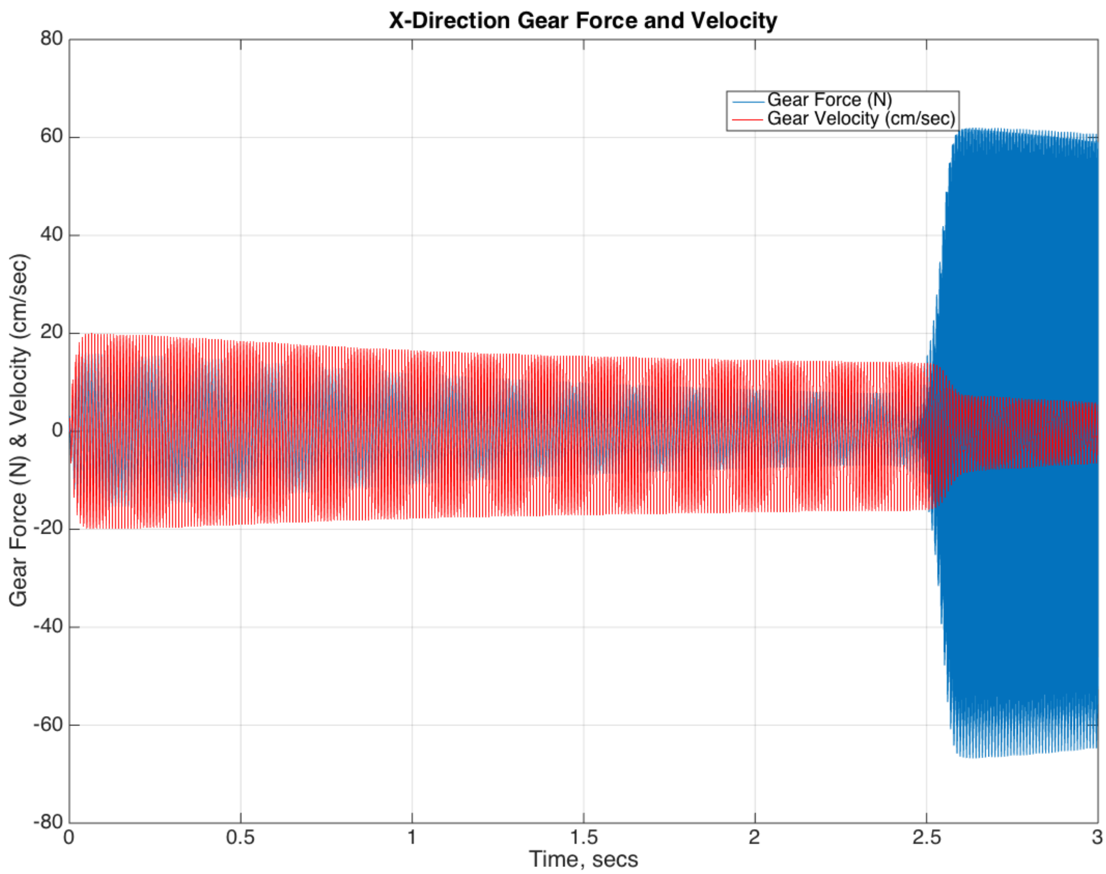

Figure 5.20: X directional gear force and velocity.

Figure 5.21 depicts the force velocity relationships in the X direction at the beginning and end of the transient simulation. Near $t = 0.0$ seconds, the X forces and velocities are nearly in phase with each other, which suggests that they promote shaft whirl. In contrast, the force velocity relationship shown near $t = 3.0$ seconds suggests that there is negligible whirl promoting power gain or loss. The high frequency gear force influences the velocities by introducing high frequency ripples in the original 1x response that are 180° out of phase with the forces. Since the net power gain or loss is approximately zero near $t = 3.0$ seconds, it is understood that the transient solution has reached steady-state. Bifurcation is a likely explanation for this change in dynamics, which results from the amplification of the non-physical high frequency lateral torsional mode. Although whirling of the shafts accounted for much of the initial whirl power, the energy abruptly transitions towards the forces in the gear mesh and low amplitude rattling after $t = 2.5$ seconds.

Figure 5.22 illustrates the Y direction gear forces and velocities. Similar to the results in the X direction,

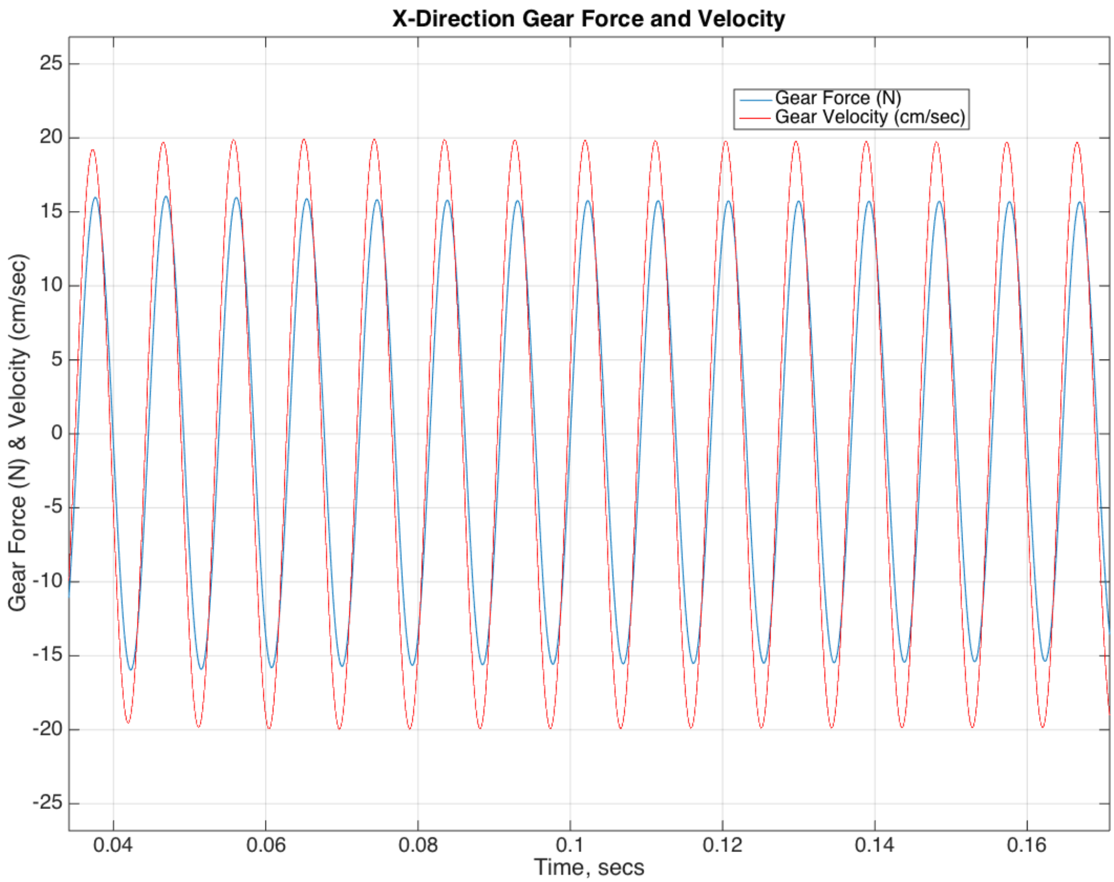

(a) X Forces and Velocities of gear 1 near $t = 0.0$ seconds.

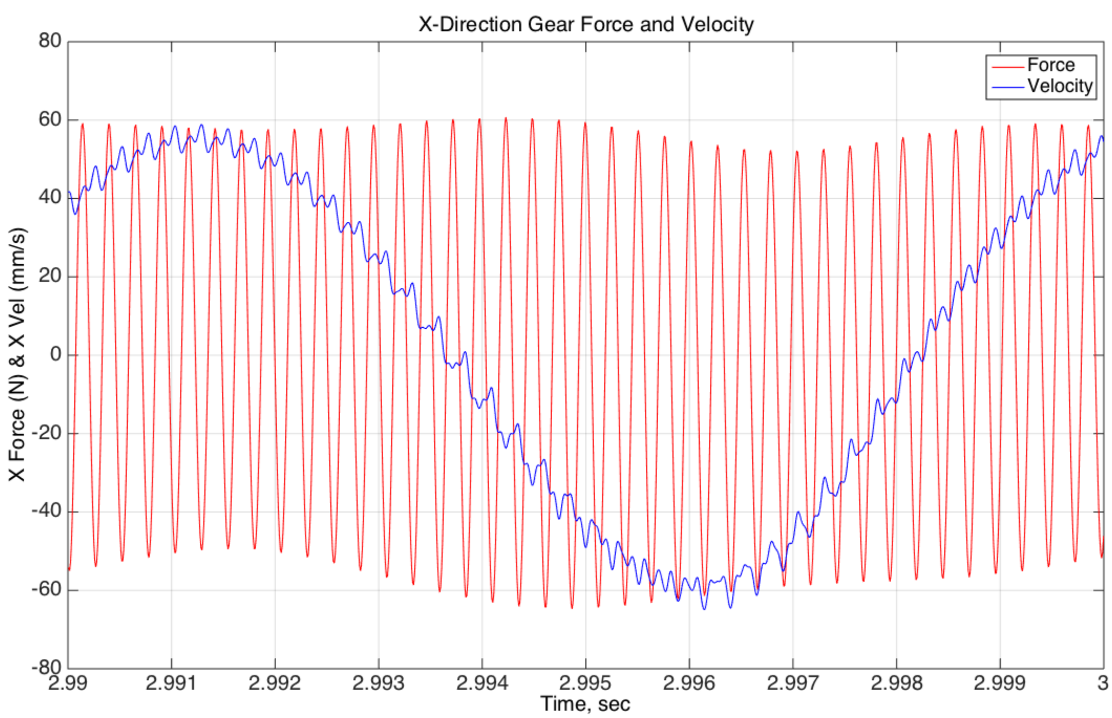

(b) X Forces and Velocities of gear 1 near $t = 3.0$ seconds.

Figure 5.21: X direction forces and velocities of gear 1 at beginning and end.

the gear force magnitude undergoes a rapid increase around $t = 2.5$ seconds. In contrast, the Y velocity magnitude gradually decreases across the entire time span. An in-depth analysis of the force-velocity phasing during the beginning and end times provides more insights into this dynamic behavior.

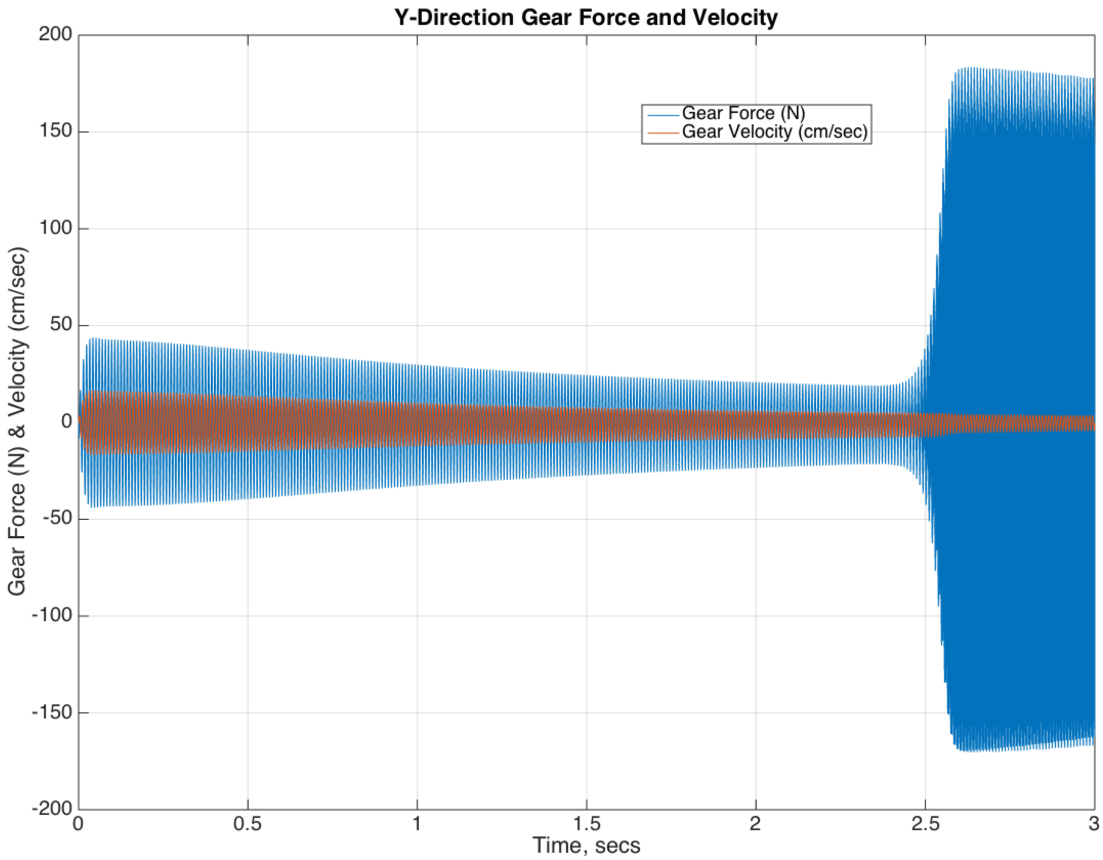

Figure 5.22: Y directional gear force and velocity.

Initial and final force velocity components in the Y direction are shown in Figure 5.23 and illustrate similar trends as to what was observed in the X direction. During the initial time period, the peaks of the forces and velocities are offset by a noticeable phase shift. This suggests that the contribution to whirl in the Y direction is not as strong in the initial time period as it was for the X components. The frequencies of the forces and velocities remain identical until after crossing $t = 2.5$ seconds. A noticeable change in the Y component gear force and velocity dynamics takes place after $t = 2.5$ seconds. Gear force magnitude increased from 40 N to 160 N, while the velocity magnitude decreased from 15 $\frac{cm}{s}$ to 4 $\frac{cm}{s}$, which implies a slight power increase in the gear vibration from the initial time. Furthermore, high frequency ripples in the Y velocity component match those of the force but they appear to be 180° out of phase with one another. This is further evidence of bifurcation as the train vibration shifts from being dominated by shaft whirl to that of the gear mesh forces as the non-physical high frequency lateral/torsional mode amplifies.

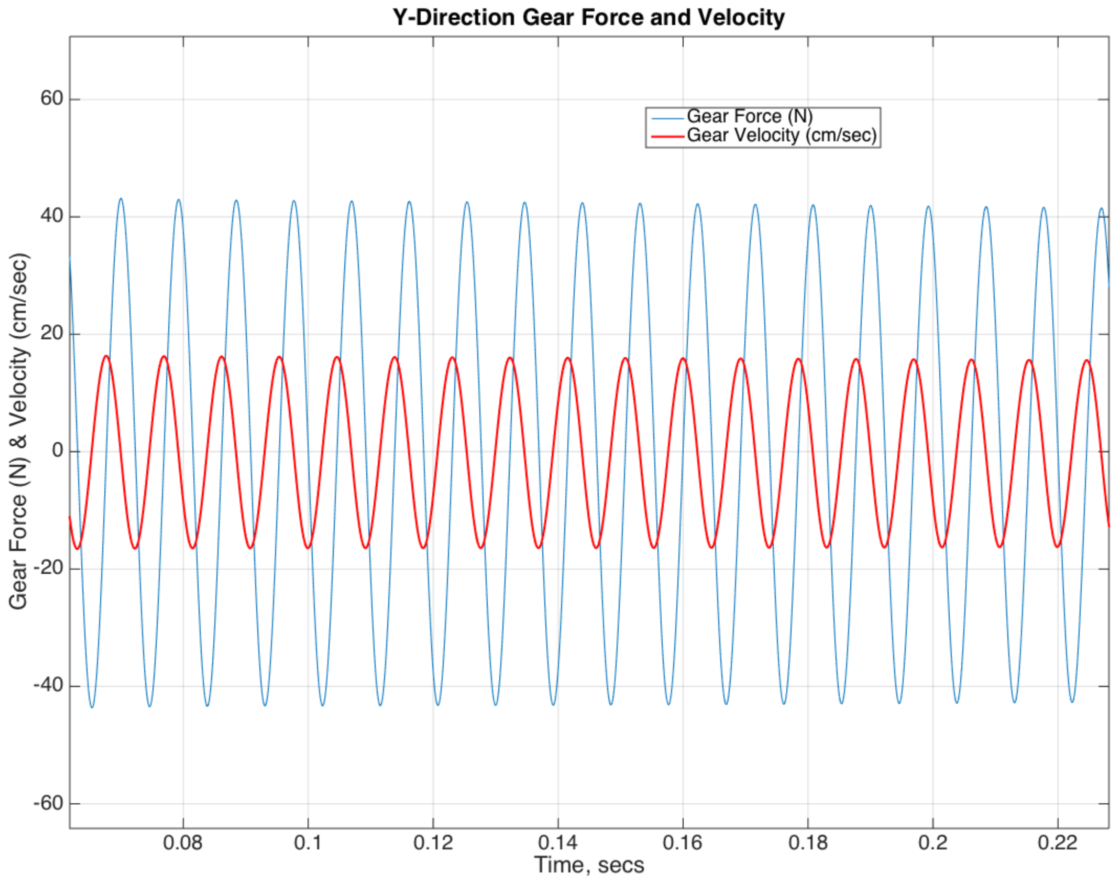

(a) Y Forces and Velocities of gear 1 near $t = 0.0$ seconds.

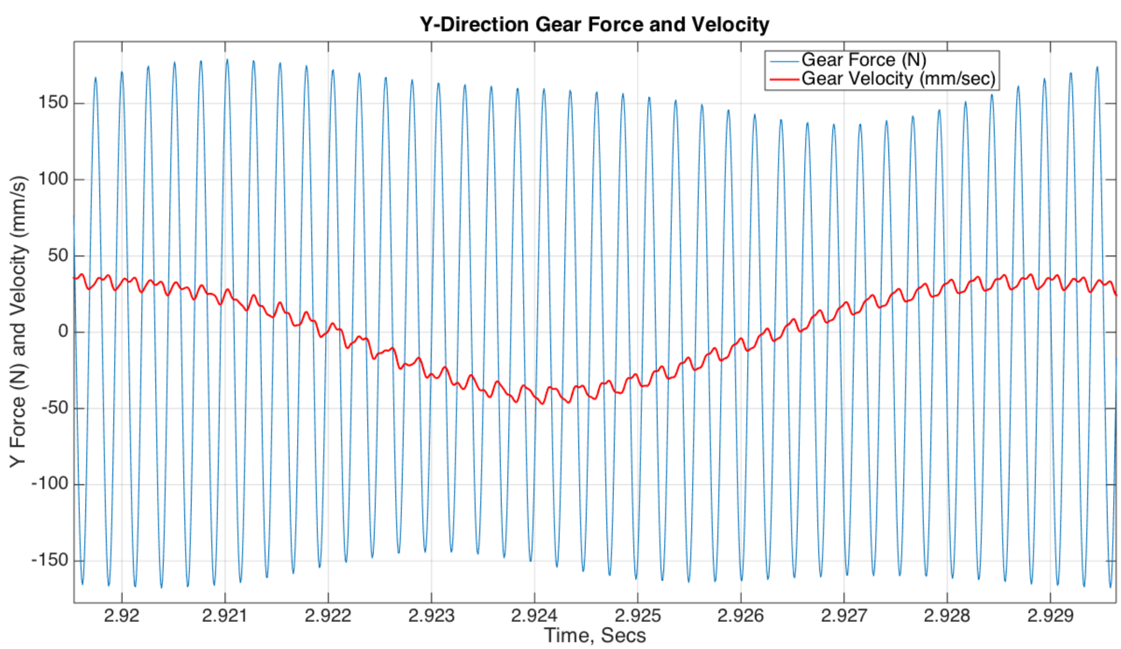

(b) Y Forces and Velocities of gear 1 near $t = 3.0$ seconds.

Figure 5.23: Y direction forces and velocities of gear 1 at beginning and end.

5.3.4 Whirl promoting energy with 4% torsional damping

Results regarding whirl energy have been focused on the root cause behind the abrupt change in dynamics without torsional damping. The excitation of the non-physical lightly-damped high frequency lateral/torsional mode has been shown to be the root cause for the abrupt change of dynamics from shaft whirl dominated vibration to small displacement gear mesh rattle. Now the analysis is applied to the case with 4% torsional damping. Whirl promoting power versus time for unbalance, bearings, and the gear on shaft 1 are plotted in Figure 5.24. The trend is similar to what was observed with the non-damped case in Figure 5.17 except that the magnitudes for the gear, bearings, and unbalance do not undergo an abrupt transition. As the geared shafts begin to reach their steady-state orbits, it is expected that the power contributions to whirl of unbalance and those of the bearings will gradually decline as shown. Also, the whirl promoting power contribution of the gear also gradually declines.

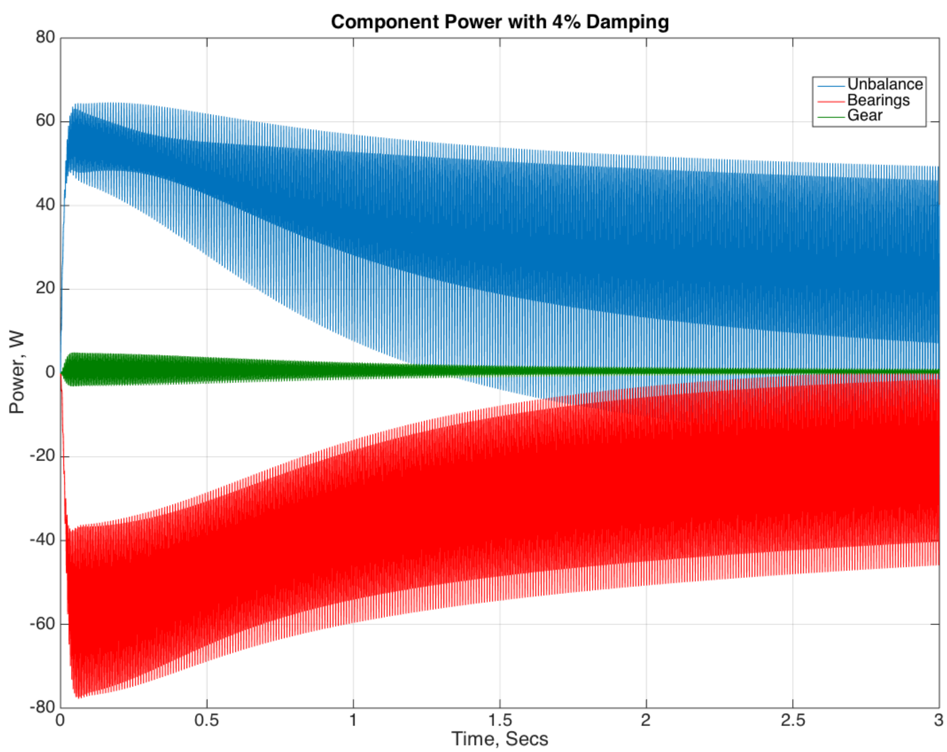

Figure 5.24: Component power with 4% torsional damping at gear mesh.

Observing the power components and their phasing at the beginning and end provide additional insights regarding the dynamics in contrast to the zero-damping torsional case, as shown in Figure 5.25. Near $t = 0.0$ seconds, the gear, bearings, and unbalance appear to be in phase and at the same frequency. As expected, the unbalance and bearings oscillate about nearly equal and opposite values although the bearings have larger variation. A secondary frequency immediately appears in the unbalance power contribution due to the resulting gear torques that influence the shaft rotational speeds. The bearing power dissipation develops the same secondary frequency in response to the unbalance. These alternate frequencies become more apparent near $t = 3.0$ seconds. The unbalance and bearing power contributions have decreased significantly and so have the gear contributions. No bifurcation is apparent because the gear, unbalance, and bearing power contributions continue to remain in phase as they were around $t = 0.0$ seconds.

The remainder of the analyses presented in the next section include non-constant gear mesh stiffness models, but they do not include the 4% torsional damping. This was done to remain consistent in analyzing the same geared system without artificial influences to the numerical method. Although the gear mesh frequency of the system can excite modes in its vicinity, this example demonstrates the need for discernment between numerical and physical results when dealing with high-frequency excitations.

5.4 State-varying stiffness effects

Previous sections addressed the transient response with constant gear mesh stiffness. The effects of state-varying stiffness on the transient unbalance response are explored in a systematic order. Using the same parameters for the nominal transient unbalance response in Section 5.3, the following test matrix of runs was constructed (see Table 5.5). The parameters, which were varied, are unbalance magnitude, ratio of variational mesh stiffness K_a to average mesh stiffness K_g, contact ratio, backlash clearance, and the number of Fourier terms. Aside from the X and Y displacements, outputs such as shaft rotational speed variation, and the gear mesh stiffness are shown.

5.4.1 Unbalance variation with constant mesh stiffness

The X and Y displacement FFT results from the first 4 rows of Table 5.5 are shown in Figures 5.26, and 5.27. There is no variational mesh stiffness or backlash clearance. They illustrate the effect of unbalance magnitude variation on the 1x and 2x displacements. It is expected that, for a linear system, doubling the unbalance magnitude would result in a doubled 1x response. Figure 5.26 show that doubling the unbalance magnitude results in synchronous X and Y displacements that are less than double. The plots also suggest that there is a maximum limit as the unbalance magnitude is increased. This dynamic behavior is clearly non-linear even though the bearings and the shaft elements are treated as linear.

Figure 5.27 shows that doubling the unbalance magnitude results in 2x X and Y displacements that are also less than double. It is apparent that the 2x amplitudes are nearly an order of magnitude smaller than the peak amplitudes at 1x. The trends also suggest that there is a 2x maximum limit as the unbalance magnitude

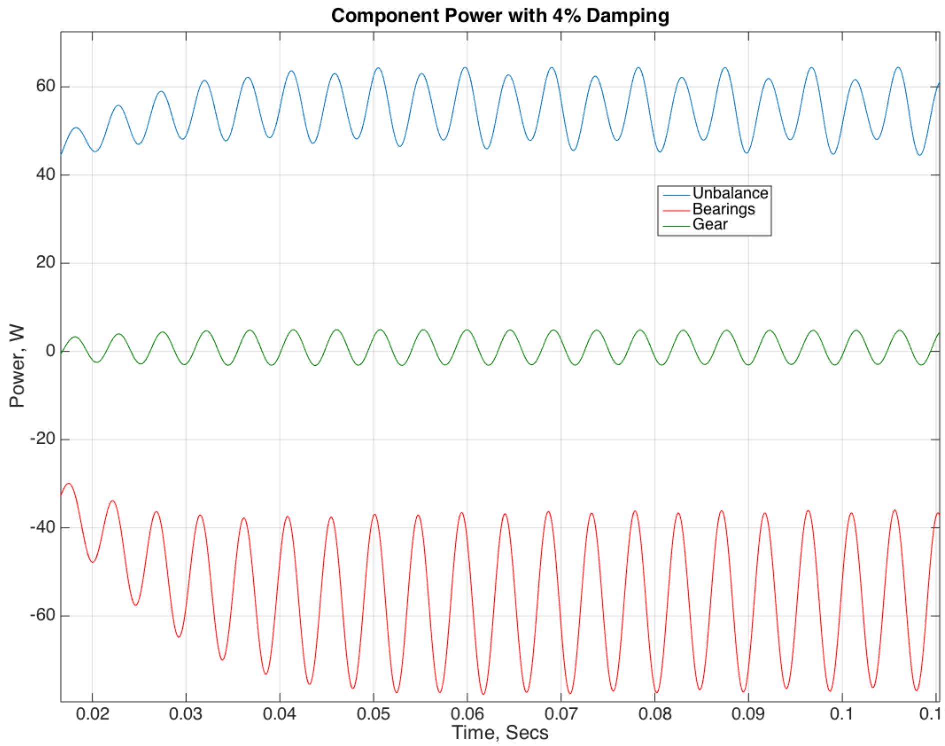

(a) Power components of torsionally damped gear near $t = 0.0$ seconds.

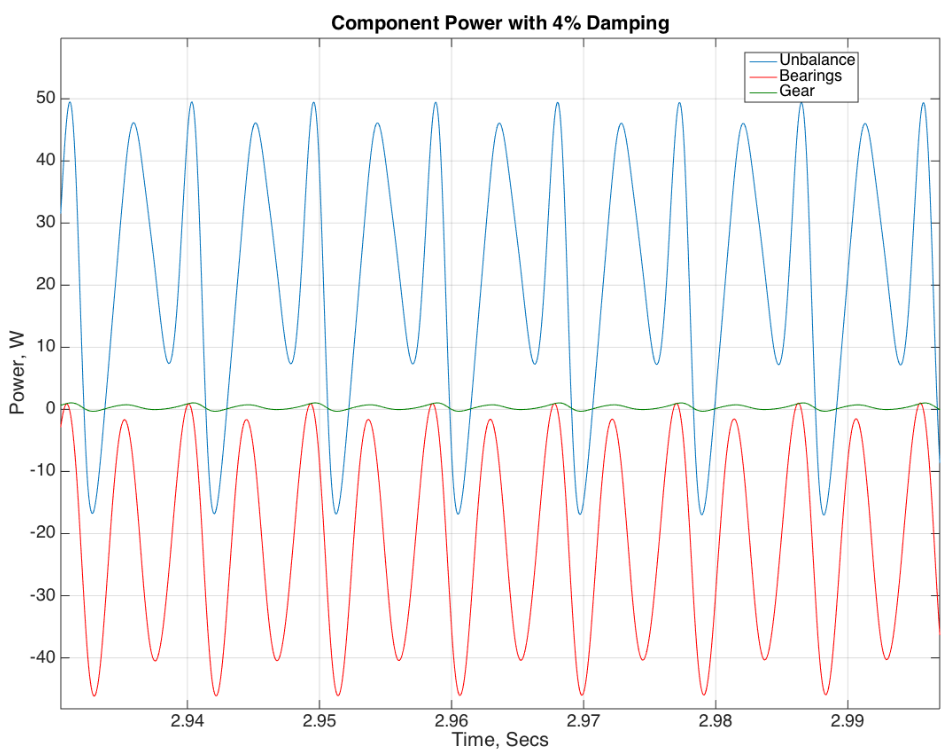

(b) Power components of torsionally damped gear near $t = 3.0$ seconds.

Figure 5.25: Whirl power components at beginning and end with 4% torsional damping at gear mesh.

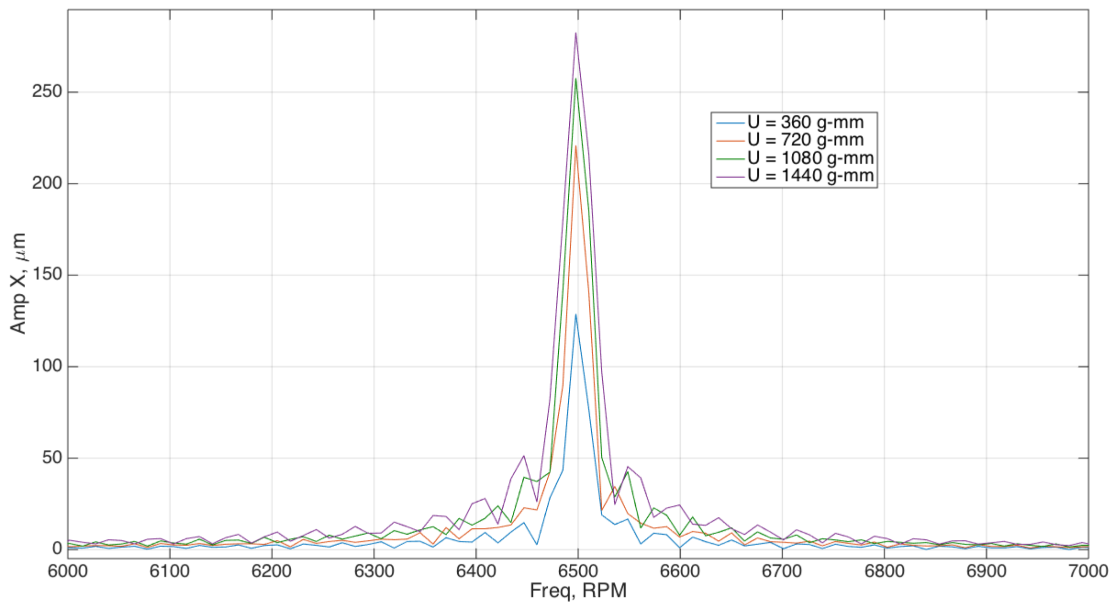

(a) Gear 1 X displacement FFT centered around 1x with unbalance magnitude variation.

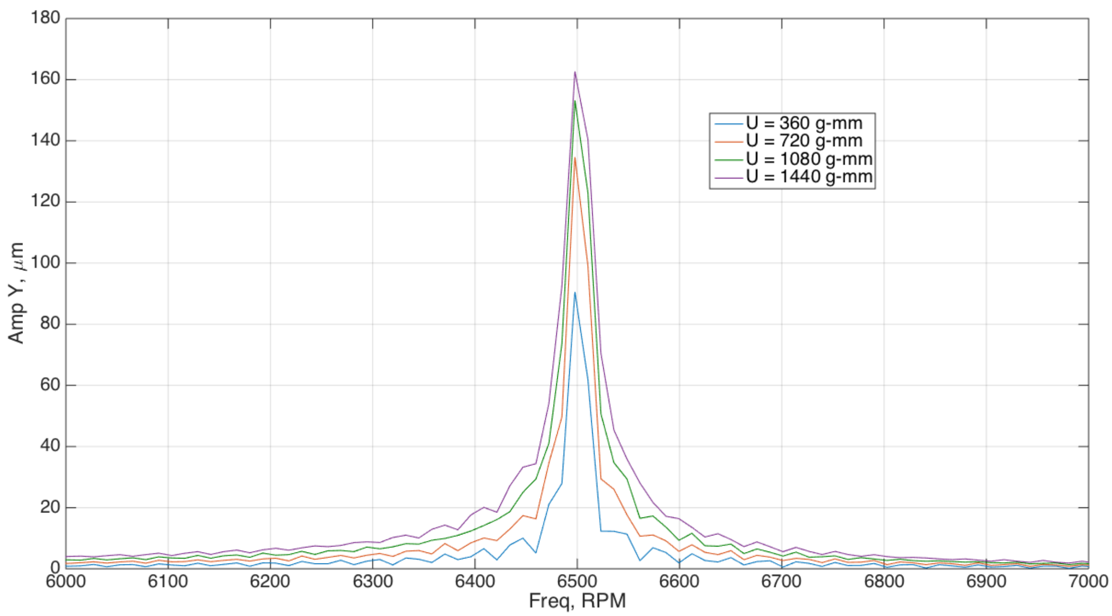

(b) Gear 1 Y displacement FFT centered around 1x with unbalance magnitude variation.

Figure 5.26: Gear 1 X and Y displacement FFTs with unbalance variation centered around 1x.

Table 5.5: Test matrix for the unity ratio model with $\Omega_1 = 6500$ and $\Omega_2 = -6500$ RPM.

Unbalance (g-mm)	$\frac{\mathbf{K_a}}{\mathbf{K_g}}$	**Contact Ratio**	**Backlash (mm)**	**Fourier Number**
360	0	0	0	0
720	0	0	0	0
1080	0	0	0	0
1440	0	0	0	0
720	0.10	1.592	0	5
720	0.20	1.592	0	5
720	0.50	1.592	0	5
720	0.20	1.592	0	10
720	0.20	1.592	0	15
720	0.20	1.592	0	20
720	0	0	0.0254	0
720	0	0	0.0508	0
720	0	0	0.0762	0
720	0	0	0.1016	0
720	0.10	1.592	0.0254	5
720	0.20	1.592	0.0254	5
720	0.50	1.592	0.0254	5
720	0.75	1.592	0.0254	5
360	0.20	1.592	0.0254	5
720	0.20	1.592	0.0254	5
1080	0.20	1.592	0.0254	5
1440	0.20	1.592	0.0254	5
720	0.20	1.25	0	5
720	0.20	1.75	0	5
720	0.20	2.00	0	5
720	0.20	1.25	0.0254	5
720	0.20	1.75	0.0254	5

is increased since the peak amplitudes increase less with each increase in unbalance magnitude. Furthermore, this is evidence that the unbalance is contributing to the 2x whirl which goes against expectations that unbalance acts only at the synchronous frequency. The cause of this phenomenon comes from the rotational speed oscillations resulting from gear reaction torques at each time step. This reaction torque is induced by the relative displacements of the gear nodes and results in temporary acceleration of one shaft and deceleration of the other. The direction and magnitude of the reaction torque changes according to the states of the gear nodes. Consequently, rotational accelerations and decelerations with time imply changes in rotational speeds, which directly affects both the unbalance magnitude and the frequency.

5.4.2 Ratio of gear mesh variation to the average mesh stiffness

The 2^{nd} set of rows in Table 5.5 correspond to changes in the ratio of varying mesh stiffness K_a to the average K_g. The unbalance magnitude is held fixed at 720 g-mm and the contact ratio at 1.592. The number of Fourier terms used to approximate the rectangular wave form is 5 and the ratio $\frac{K_a}{K_g}$ varies from 0 to 0.5.

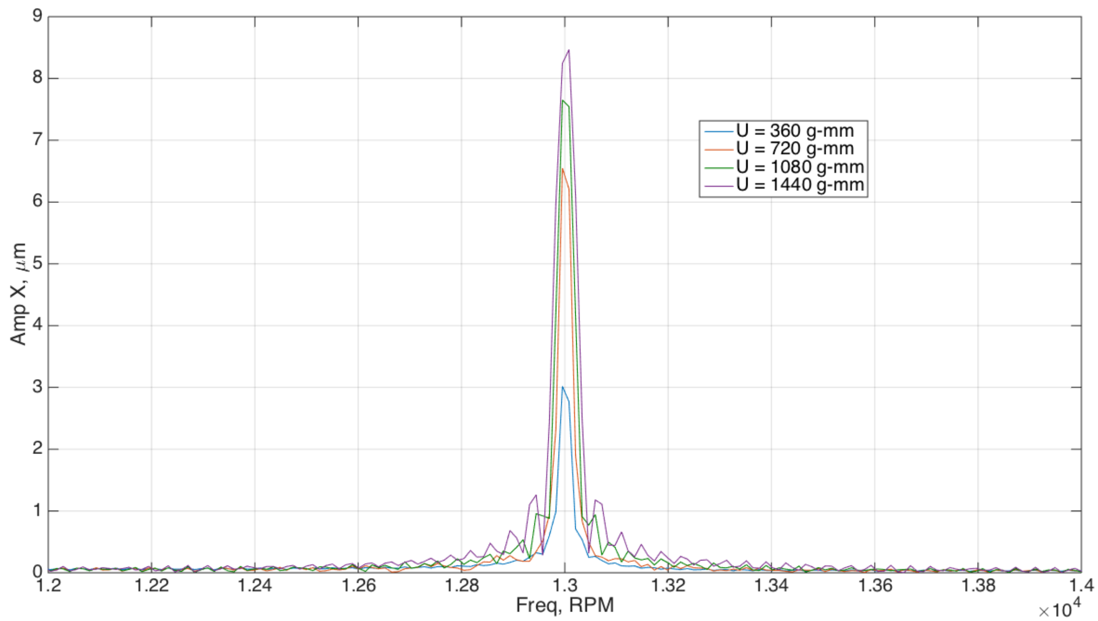

(a) Gear 1 X displacement FFT centered around 2x with unbalance magnitude variation.

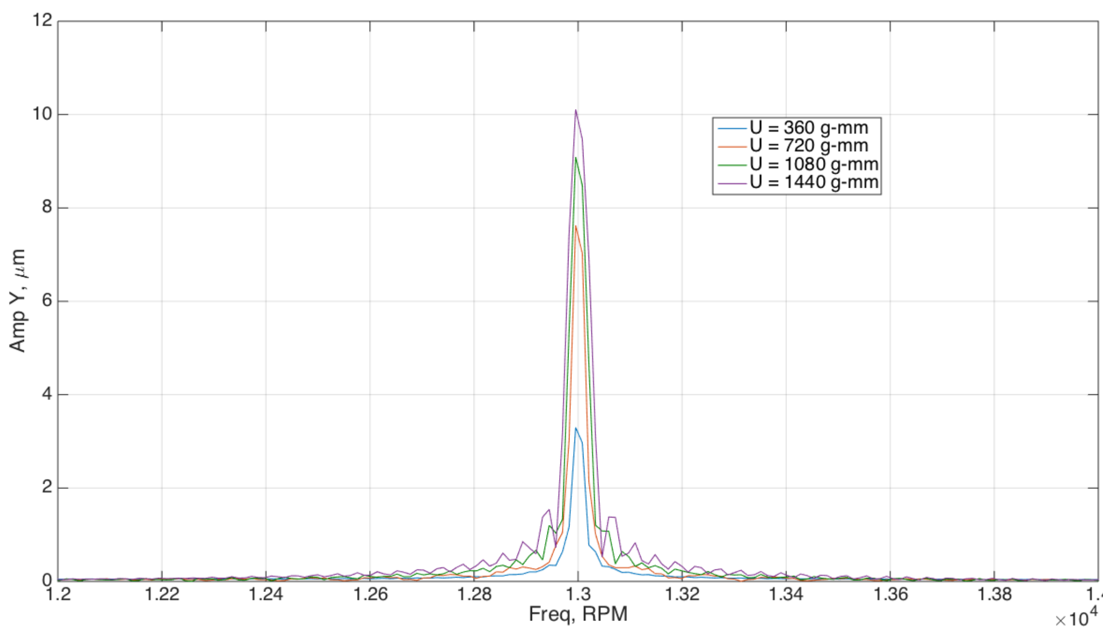

(b) Gear 1 Y displacement FFT centered around 2x with unbalance magnitude variation.

Figure 5.27: Gear 1 X and Y displacement FFTs with unbalance variation centered around 2x.

Figure 5.28 illustrates the X and Y displacement FFTs centered around 1x. The overall trend suggests that increasing the magnitude of the gear mesh stiffness variation, K_a, decreases the synchronous response component. The one exception to the trend is the $K_a = 10\%K_g$ case, which has a peak amplitude that is smaller than the $K_a = 20\%K_g$ case. When K_a equals 0, the peak X magnitude is substantially larger than Y which is indicative of elliptical whirl. However, as K_a increases, the peak X and Y magnitude displacements become closer, which suggests smaller and more circular whirl shapes. Since the variation in mesh stiffness primarily occurs at the gear mesh frequency, which is 30x of shaft rotational speed, its force contributions have a noticeable effect on the displacement response and is dependent on the phase relationship between the gear and unbalance forces. Also, because the average gear mesh stiffness is slightly less than the shaft bending stiffness, it is expected that the response should be fairly sensitive to this parameter as shown in Figure 5.28. Increases in gear stiffness are expected to decrease the vibration response of the 1^{st} bending mode and the reverse trend is also expected to hold true.

Figure 5.29 shows similar X and Y displacement FFT data but centered around 2x. The peak amplitudes at the 2x frequency are substantially smaller than the values at 1x. Similar to the 1x component, the overall trend suggests that increasing the magnitude of the gear mesh stiffness variation, K_a, decreases the response. The one exception to the trend is the $K_a = 10\%K_g$ case, which has a peak amplitude that is smaller than the $K_a = 20\%K_g$ case.

Gear mesh stiffness variation is also included in FFTs as shown in Figure 5.30. The first shows the spectral content over a range of frequencies from $(0.0 - 3.3)\text{x}10^6$ CPM. Although noticeable peaks may be discerned for the gear mesh stiffness, there is much computational noise due to its rotational speed dependence. Subplot 5.29b zooms in to the frequency range $(1.85 - 2.10)\text{x}10^5$ CPM. As expected, $\frac{K_a}{K_g} = 0.5$ consistently maintains a higher amplitude over the frequency range. In addition, larger ratios of $\frac{K_a}{K_g}$ produce larger computational noise. Several peaks may be discerned with different amplitudes, and they are separated in increments of 6,500 CPM, which is the shaft rotational speed. This is indicative of multiple harmonics that the gear mesh stiffness may parametrically excite when paired with the dynamics of the shafts. The peak of the largest amplitude is at 195,000 CPM and this is the gear mesh frequency $\Omega_g = N_1\Omega_1$ since the number of gear teeth N_1 is 30.

5.4.3 Fourier coefficient variation

The next comparison explores the change in the number of Fourier coefficients while keeping the unbalance magnitude, variational mesh stiffness amplitude, and contact ratio fixed at values of $U = 7,200$ g-mm, $\frac{K_a}{K_g} = 0.2$, and $c = 1.592$ respectively . This comparison is consistent with the 3rd set of rows in Table 5.5,

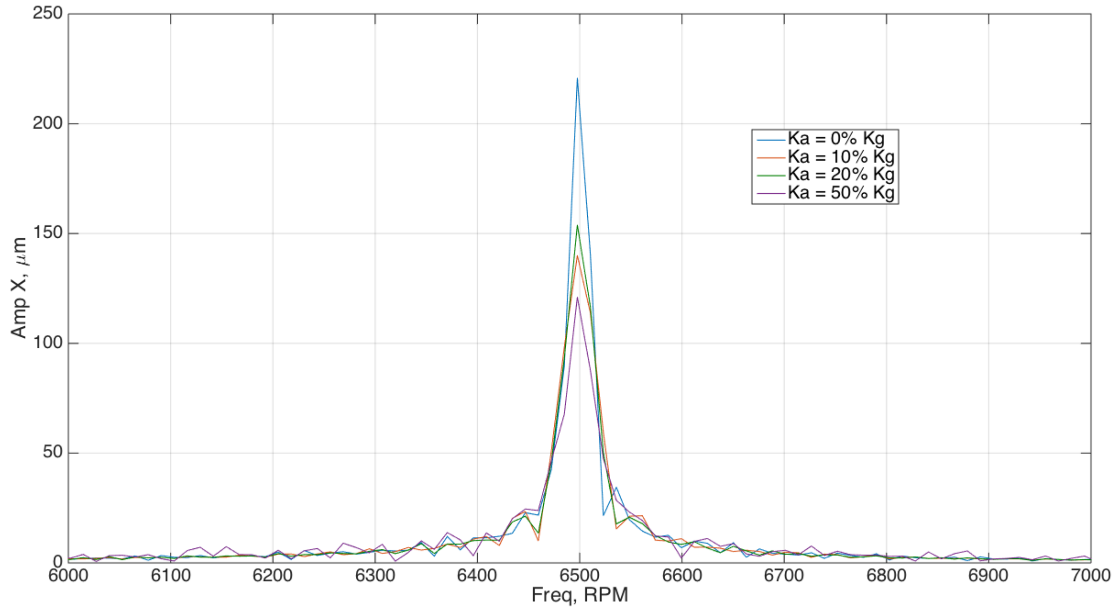

(a) Gear 1 X displacement FFT centered around 1x while varying K_a.

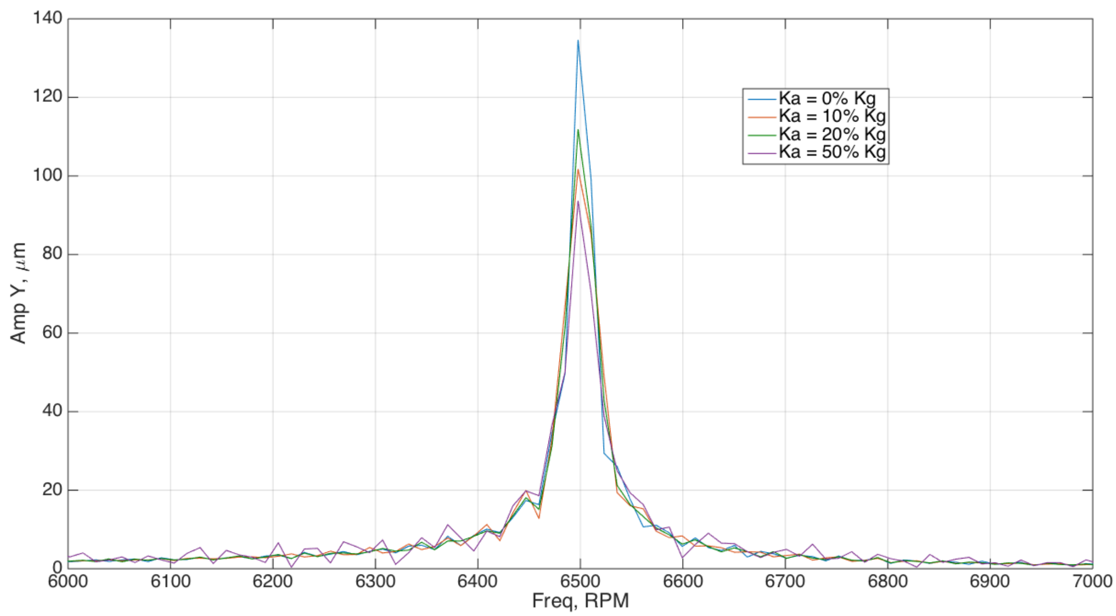

(b) Gear 1 Y displacement FFT centered around 1x while varying K_a.

Figure 5.28: Gear 1 X and Y displacement FFTs with variation in $\frac{K_a}{K_g}$ centered around 1x.

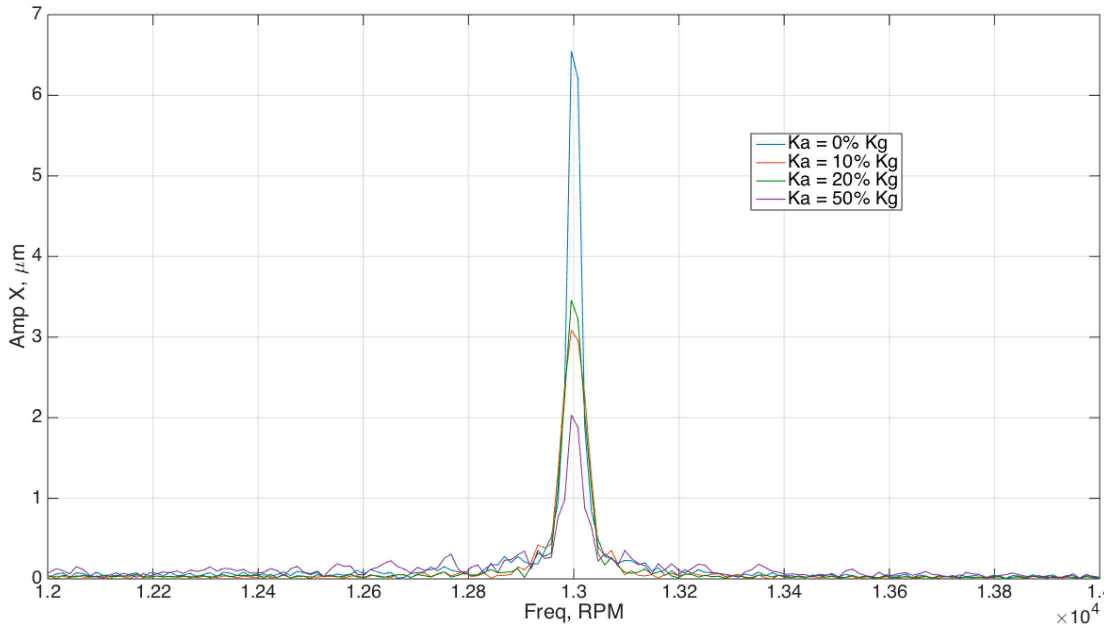

(a) Gear 1 X displacement FFT centered around 2x while varying K_a.

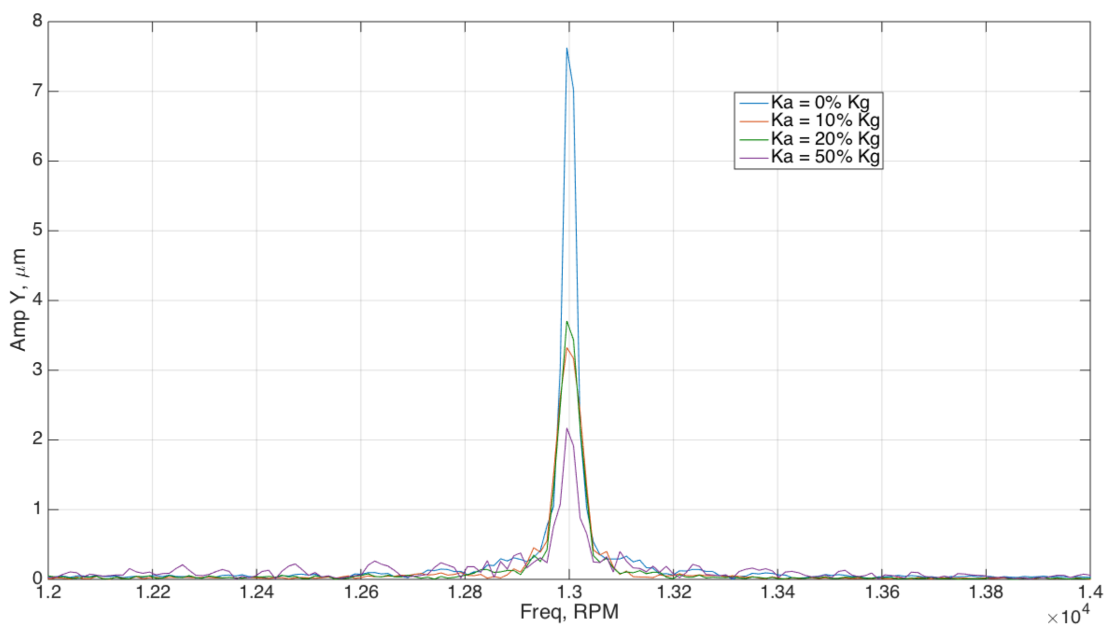

(b) Gear 1 Y displacement FFT centered around 2x while varying K_a.

Figure 5.29: Gear 1 X and Y displacement FFTs with variation in $\frac{K_a}{K_g}$ centered around 2x.

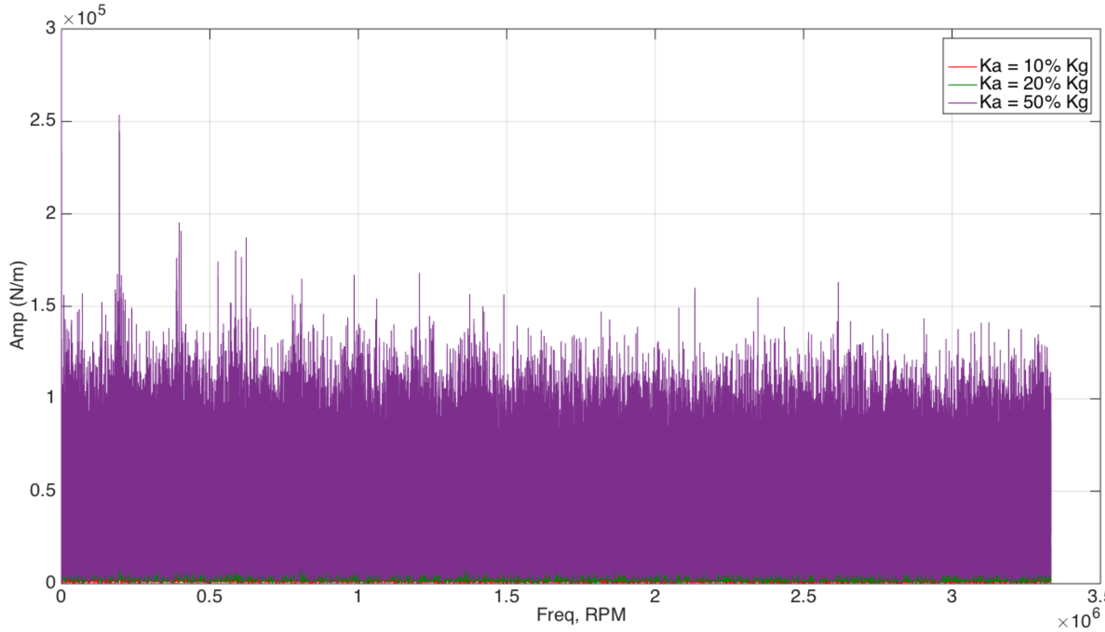

(a) Gear mesh stiffness FFT with varying K_a.

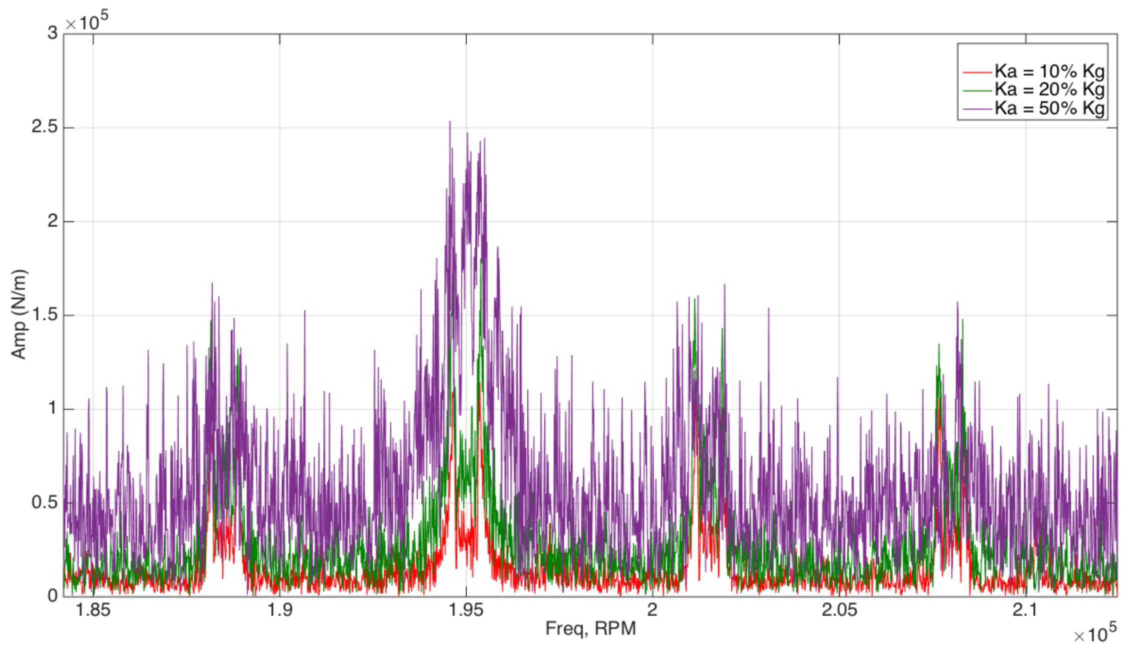

(b) Gear mesh stiffness FFT with varying K_a zoomed in to $200,000$ CPM.

Figure 5.30: Gear mesh stiffness FFT with varying K_a across the frequency range and zoomed in towards the GMF.

and there is no backlash present. Figures 5.31 and 5.32 illustrate the gear X and Y displacement FFTs with frequency ranges centered about 1x and 2x for variations in the value of the maximum number of Fourier coefficients used to approximate the gear mesh stiffness. The number of Fourier coefficients range from 5 through 20. Results centered around 1x show that the X and and Y displacements are fairly insensitive to Fourier coefficient variation since the peak amplitudes vary up to 10 μm for a scale that ranges up to 180 μm. The 2x magnitudes are 2 orders of magnitude smaller than the 1x peaks and the results also remain insensitive to the number of Fourier coefficients. No other frequency ranges are affected and these results confirm that using more than five Fourier coefficients produces negligible changes to the X and Y displacements.

FFTs of shaft rotational speed with variations in the maximum number of Fourier coefficients are shown in Figure 5.33. In contrast to the displacements, several additional high frequencies appear in the rotational speed FFTs and they are depicted up to 500,000 CPM. The most prominent peaks occur at 6,500, 217,000, and 400,000 CPM and suggest that the rotational speeds vary up to 10 RPM in response to the gear reaction torque. Both the 217,000 and 400,000 CPM peaks correspond with the excitations of lightly damped high frequency modes. Comparisons of the effects of Fourier coefficient number may be observed more concretely at the peak frequencies and are shown in Figure 5.34.

Results pertaining to the synchronous component (6,500 CPM) show no sensitivity to Fourier coefficient variation. This is to be expected because the synchronous component is at a much lower frequency than gear mesh. Significant sensitivity can be observed for the 217,000 and 400,000 CPM components since these high frequencies can be more accurately captured with a higher number of Fourier terms. Excitation in rotational speed at 217,000 CPM is expected since this is the damped natural frequency of the marginally stable lateral-torsional mode discussed earlier. Results at this frequency reveal that there is little rotational speed variational magnitude for Fourier terms up to 15, but the magnitude change increases from 1.3 to 3.3 RPM with 20 Fourier coefficients. At 399,000 CPM, the trend of increasing the number of Fourier coefficients with increased rotational speed variation response is reversed. Fourier coefficients from 5 to 15 generate rotational speed variations between 3.5 and 4.5 RPM at a frequency of 400,000 CPM, but Fourier coefficients up to 20 decreases the magnitude to 2 RPM. These results suggest that the number of Fourier coefficients does affect the magnitudes of rotational speed fluctuations of the geared system, and this reinforces the notion that an excessive number of Fourier coefficients can alter results in gear mesh stiffness variation modeling and can be non-physical. 5 to 10 Fourier coefficients should be sufficient to capture high frequency excitations of the gear mesh without amplifying non-physical ones.

FFTs of the gear mesh stiffness are shown in Figure 5.35 and illustrate the effect of changing the number of Fourier coefficients on the stiffness magnitude at different frequencies. The excitation frequency range varies from 0 to 400,000 CPM and in addition to the noise there are discrete peaks that can be observed.

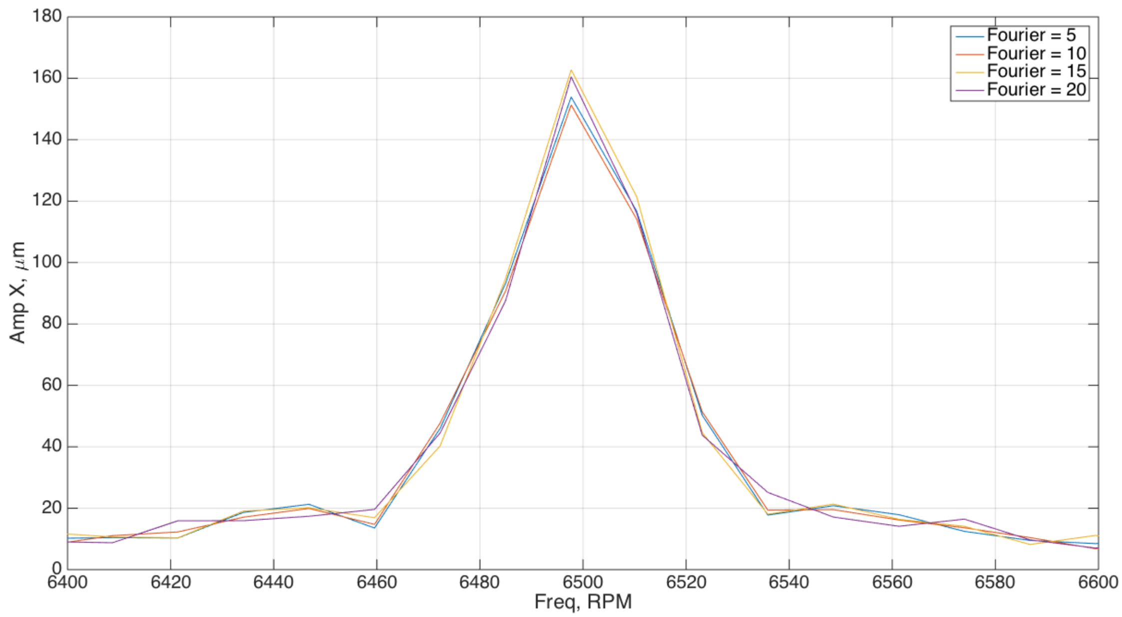

(a) Gear X displacement FFT with $\frac{K_a}{K_g} = 0.2$ with varying Fourier number at 1x.

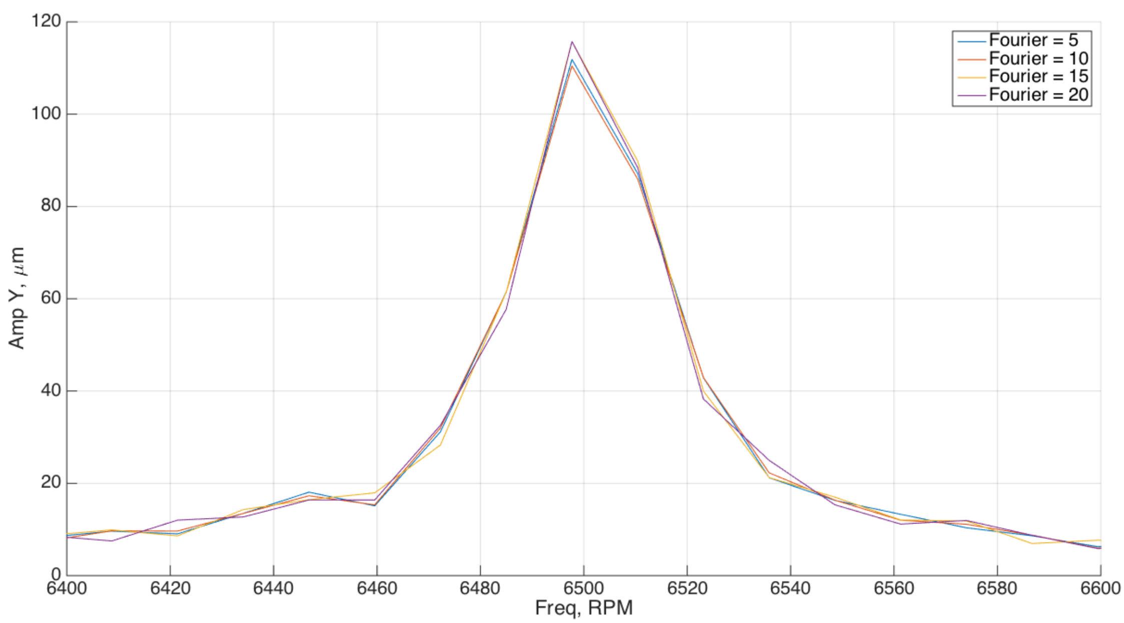

(b) Gear Y displacement FFT with $\frac{K_a}{K_g} = 0.2$ with varying Fourier number at 1x.

Figure 5.31: Gear X and Y displacement FFT with $\frac{K_a}{K_g} = 0.2$ with varying Fourier number shown at 1x.

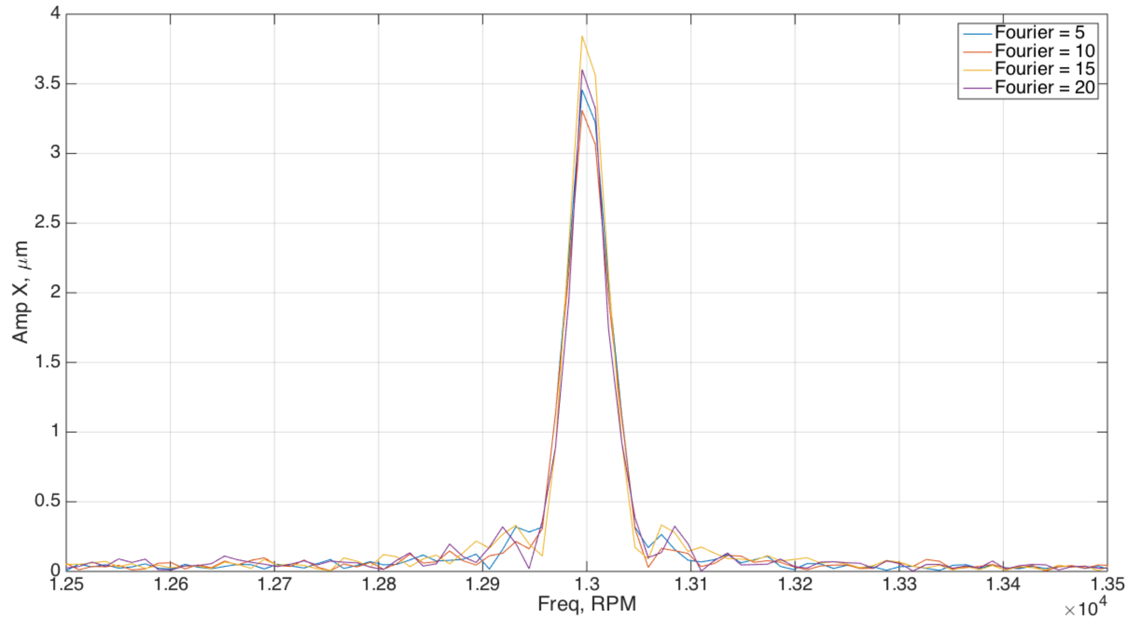

(a) Gear X displacement FFTwith $\frac{K_a}{K_g} = 0.2$ with varying Fourier number at 2x.

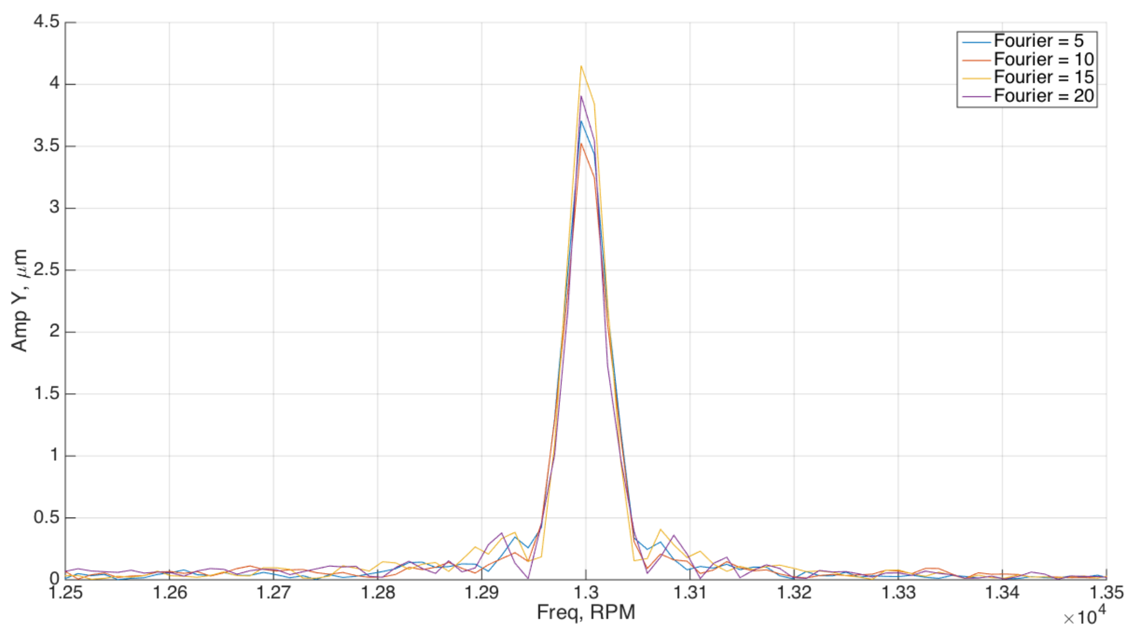

(b) Gear Y displacement FFT with $\frac{K_a}{K_g} = 0.2$ with varying Fourier number at 2x.

Figure 5.32: Gear X and Y displacement FFT with $\frac{K_a}{K_g} = 0.2$ with varying Fourier number shown at 2x.

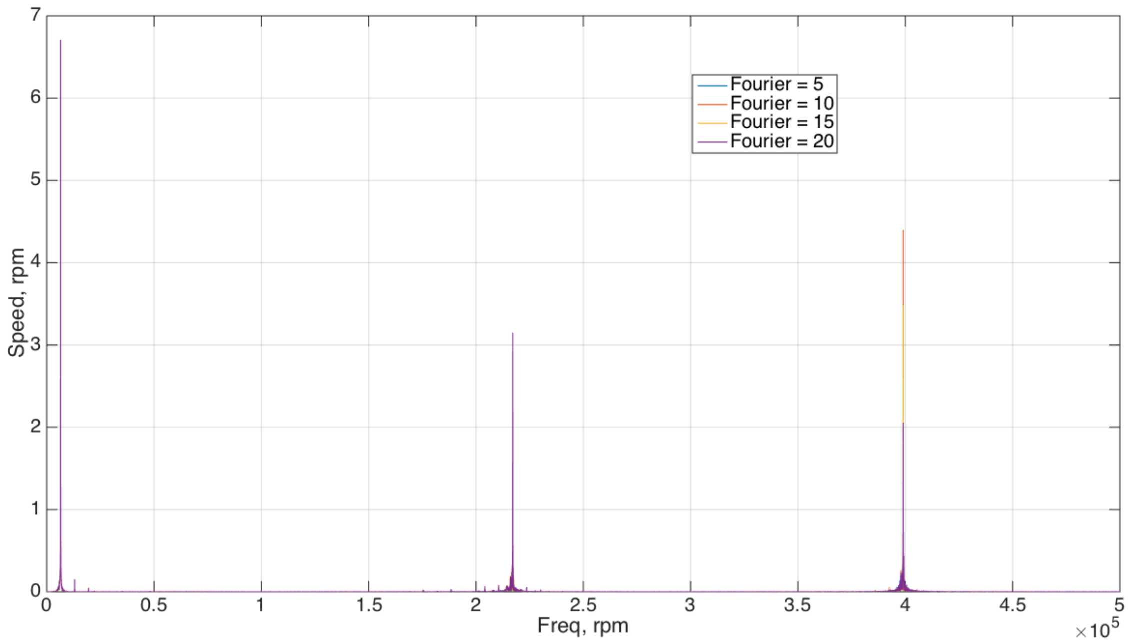

Figure 5.33: Rotational speed FFT with $\frac{K_a}{K_g} = 0.2$ with varying Fourier number the frequency range.

Because the frequency of the gear mesh stiffness variation is driven by the number of gear teeth and the shaft rotational speed, it is expected that the 6,500, 217,000, and 399,000 CPM components should be more noticeable. In addition to these peaks, harmonics in increments of 6,500 CPM are also prominent about the major frequencies and their amplification also shows sensitivity to the maximum number of Fourier coefficients. Fewer Fourier coefficients are expected to amplify fewer harmonics of 6,500 CPM than results with more coefficients, but the magnitude of the amplification of certain harmonics is difficult to correlate. More Fourier coefficients are expected to produce a greater spread across more harmonics, which implies that they may produce lower amplitudes across that broader frequency range for the same amount of power.

In summary, varying the maximum number of Fourier coefficients used to approximate the state-varying gear mesh stiffness produced noticeable changes in the amplitudes for shaft rotational speed variation, and gear mesh stiffness variation for frequencies well above the operating speed of 6,500 RPM. However, the X and Y displacements remained fairly insensitive to the maximum number of Fourier coefficients ranging between 5 and 20. Since the X and and Y displacements primarily contained only the synchronous frequency, it is to be expected that they are insensitive to Fourier coefficient variation. If a higher order mode appeared in the X and Y displacements, then it is likely that the number of Fourier coefficients used would have to be more carefully examined to insure that the observed phenomenon is physical and not numerical. Otherwise, it is recommended to maintain a lower number of Fourier coefficients (5-10) since that has been shown to capture the dominant frequency ranges of the varying mesh stiffness.

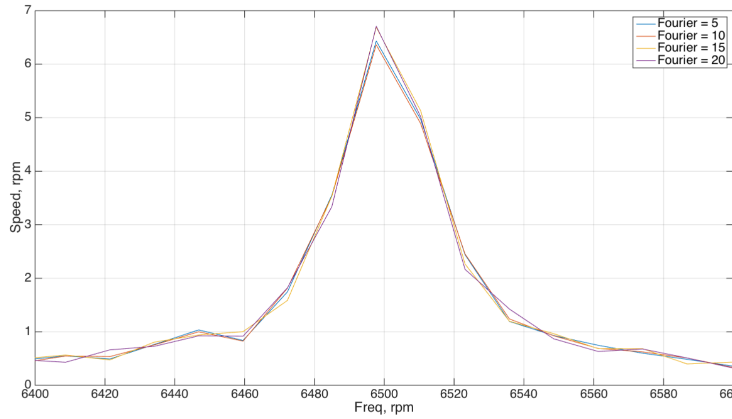

(a) Rotational speed FFT with $\frac{K_a}{K_g} = 0.2$ with varying Fourier number at 1x.

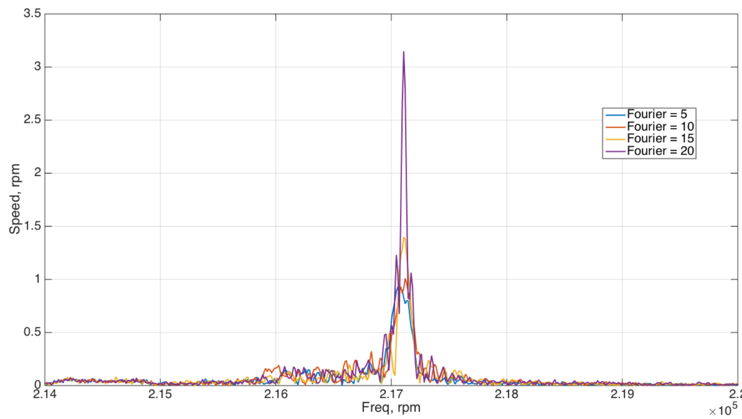

(b) Rotational speed FFT with $\frac{K_a}{K_g} = 0.2$ with varying Fourier number at $\omega_d = 217,000$ CPM.

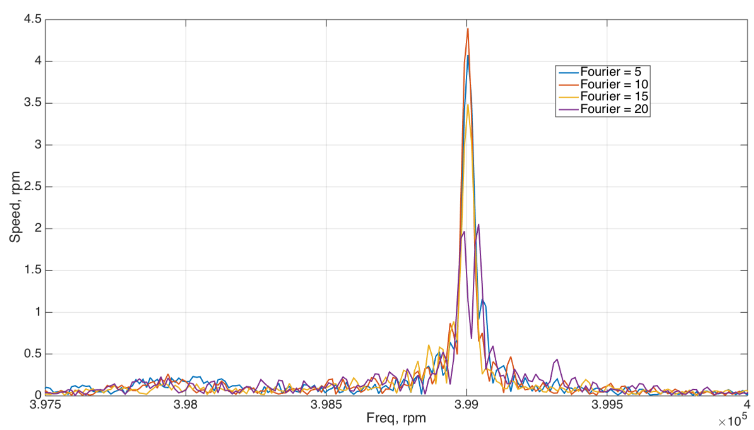

(c) Rotational speed FFTwith $\frac{K_a}{K_g} = 0.2$ with varying Fourier number at $\omega_d = 399,000$ CPM.

Figure 5.34: Shaft rotational speed with $\frac{K_a}{K_g} = 0.2$ with varying Fourier number at each peak frequency.

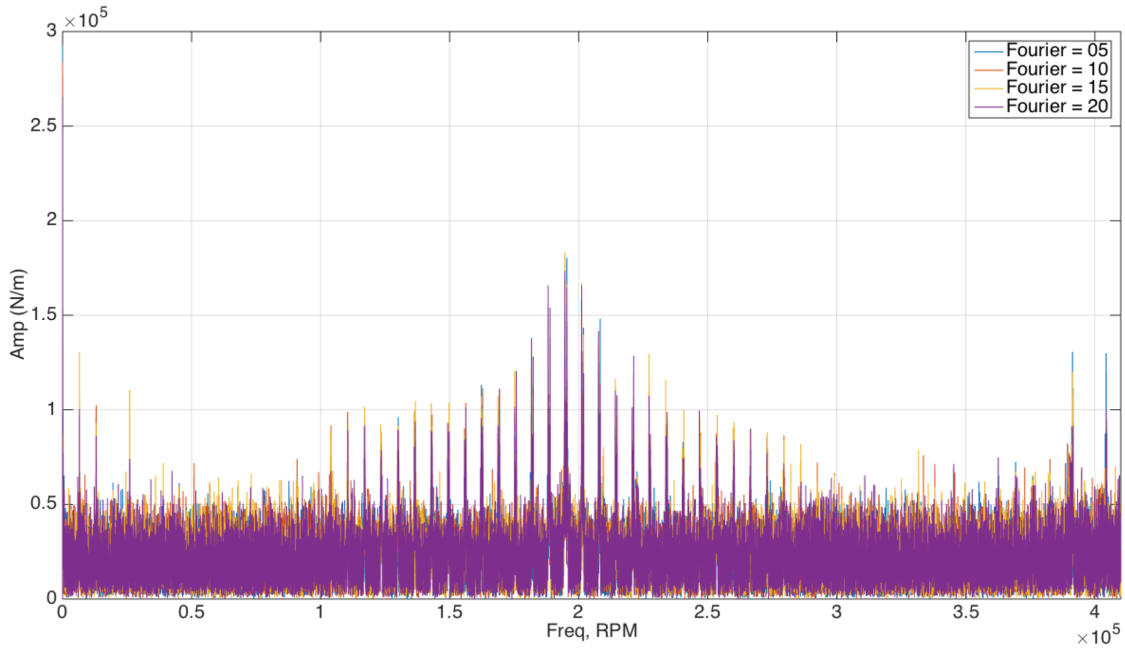

Figure 5.35: Gear mesh stiffness FFT with $\frac{K_a}{K_g} = 0.2$ with varying Fourier number over a frequency range of 0 to 400,000 CPM.

5.4.4 Backlash clearance, b_s, variation

This subsection describes the effects of varying only the backlash clearance, b_s, on the X Y displacements, shaft rotational speed variation, and the gear mesh stiffness. Unbalance remains fixed at 720 g-mm and there is no gear mesh stiffness variation aside from backlash. Backlash clearance variation assumes values ranging from 0.0254 mm (1 mil) to 0.1016 mm (4 mils). These analyses follow the 4$^{\text{th}}$ set of rows in Table 5.5.

X and Y displacement FFTs are shown in Figure 5.36 and are centered about 1x because the remainder of the frequency range shows no other noticeable peaks. Introducing backlash non-linearities produce noticeable differences in the vicinity of 1x. Smaller clearances appear to produce larger amplitudes below 1x but smaller peak displacements at 1x. Because the gear mesh stiffness model treats the actual contact zone as a linear function that grows with larger tooth tangential displacements, using smaller clearances implies that the gear teeth act with greater stiffness for the same amount of tangential displacement. This is because having a smaller clearance zone implies a larger contact zone.

An FFT of the shaft rotational speed variation with ranging backlash clearance is illustrated in Figure 5.37 and depicts three dominant frequency regions: 6,500, 188,000, and 383,000 CPM. All three peak frequency regions are fairly close to what has been observed in previous subsections without backlash clearances. The reason for the frequency differences can be explained by the reduced gear mesh stiffness since it is now a function of tangential displacement differences between the gear and pinion. Reducing the effective modal

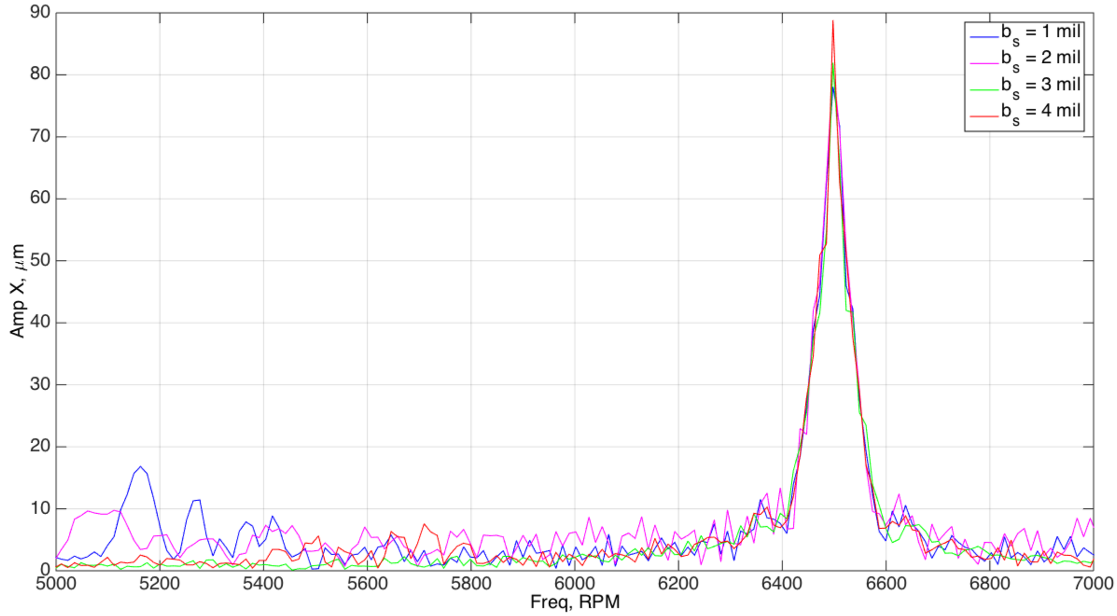

(a) Gear X displacement FFT with only backlash clearance variation at 1x.

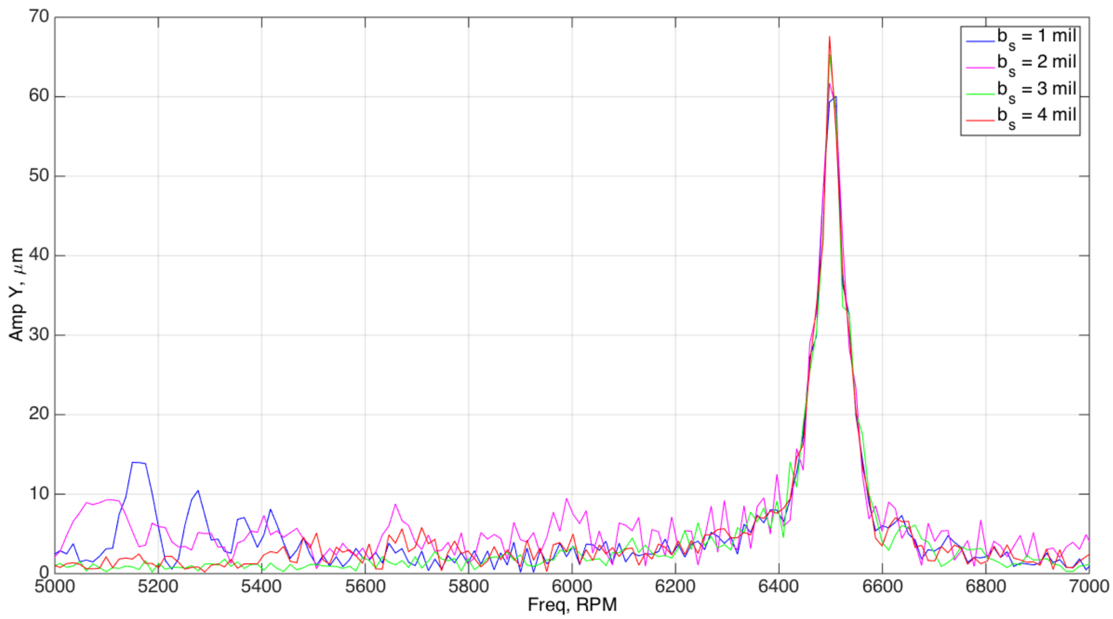

(b) Gear Y displacement FFT with only backlash clearance variation at 1x.

Figure 5.36: Gear X and Y displacement FFT with only backlash clearance variation at 1x.

stiffness for each mode lowers the natural frequency of those modes.

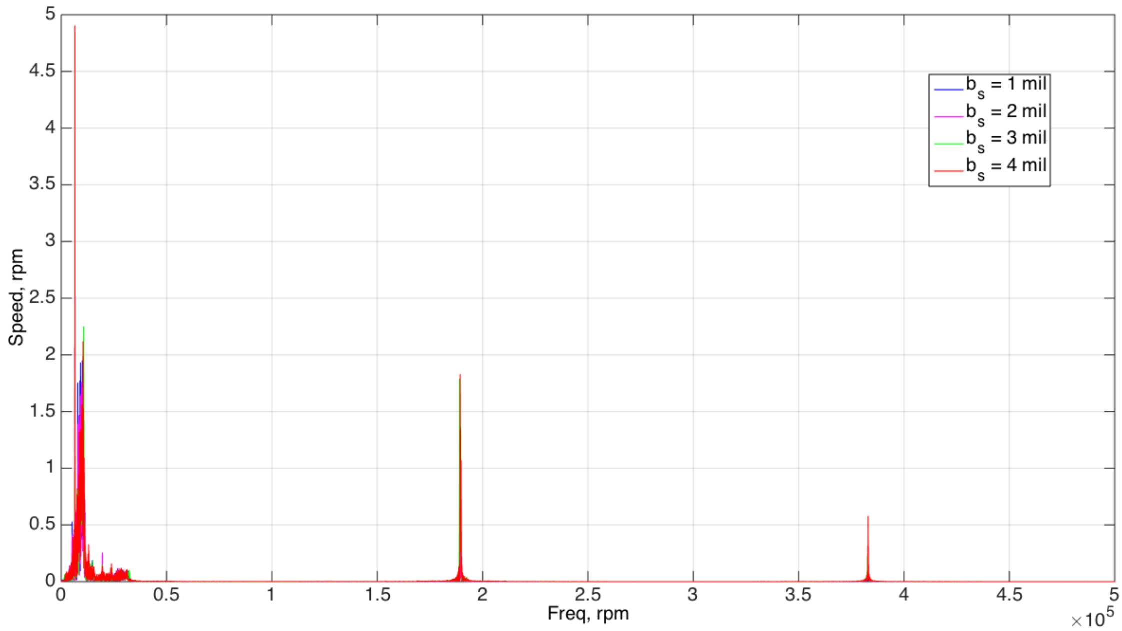

Figure 5.37: Rotational speed FFT with only backlash clearance variation over most of the frequency range.

Effects of varying the backlash clearance size on the responses at these peak frequencies is shown in Figure 5.38. Aside from the peak at 6,500 CPM, a range of frequencies between 7,000 and 11,000 CPM have comparable amplitudes. The location of the peak frequencies in that range vary with the size of the backlash clearance, where lower clearance produces larger amplitudes at lower frequencies. The peak at 6,500 CPM is insensitive to backlash clearance variation. For the 189,000 CPM frequency range, multiple peak frequencies are produced for each backlash clearance size. The results show that larger backlash clearance sizes produce larger rotational speed variations and this may be explained by the fact that a larger non-contact zone for the tangential displacements (and therefore velocity differences) to develop over before the tangential stiffness produces a restoring force. A similar trend with regards to backlash clearance can be observed for the frequencies around 383,000 CPM.

Results showing the FFT of the gear mesh stiffness over a range of backlash clearances appear in Figure 5.39 with a frequency range up to 14,000 CPM. Three dominant peaks are discernible: static (0 CPM), 6,500, and 13,000 CPM. In comparison to previous subsections, the peak frequencies of the gear mesh stiffness are substantially smaller in amplitude because the stiffness is proportional to net tangential displacements between the gear and pinion rather than being specified as a variation about a mean. The 13,000 and 6,500 CPM peaks show some sensitivity to the size of backlash clearance. Although it is difficult to discern the pattern of the variations in the 13,000 CPM peak, amplitudes at 6,500 CPM increase with larger clearance

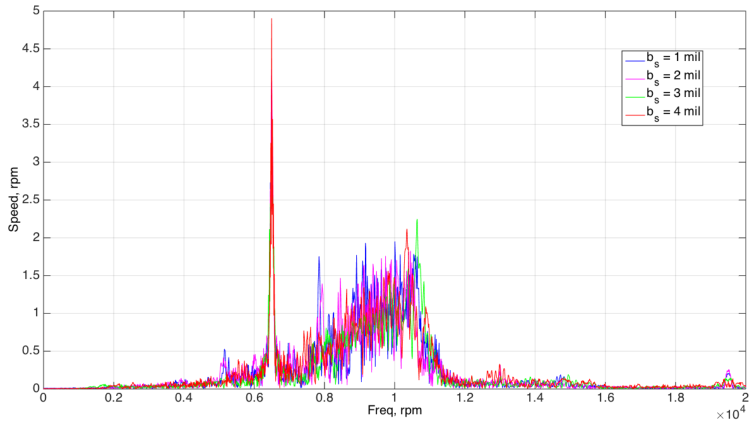

(a) Rotational speed FFT with only backlash clearance variation from 0 to 20,000 CPM.

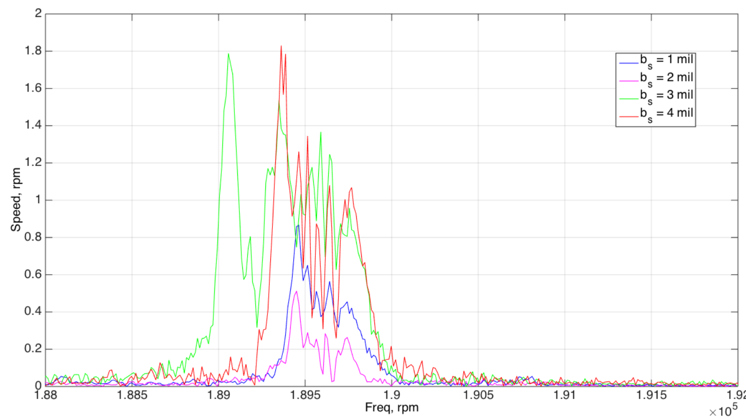

(b) Rotational speed FFT with only backlash clearance variation around $\omega_d = 189,000$ CPM.

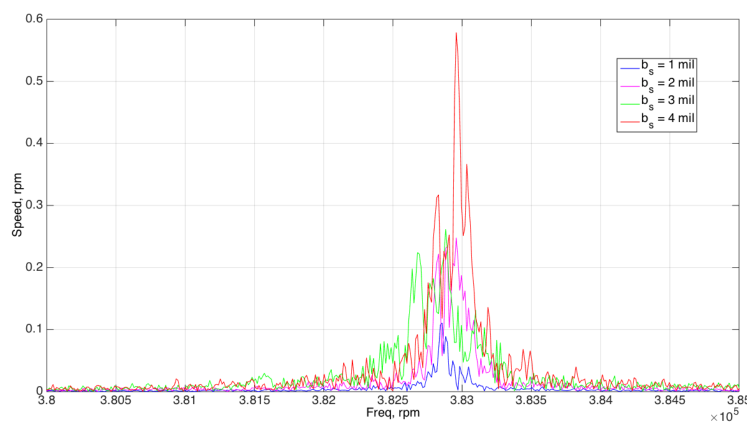

(c) Rotational speed FFT with only backlash clearance variation around $\omega_d = 383,000$ CPM.

Figure 5.38: Rotational speed FFT with only backlash clearance variation at peak frequencies.

sizes because the larger non-contact zone permits more tangential displacement between the gear and pinion before contact resumes.

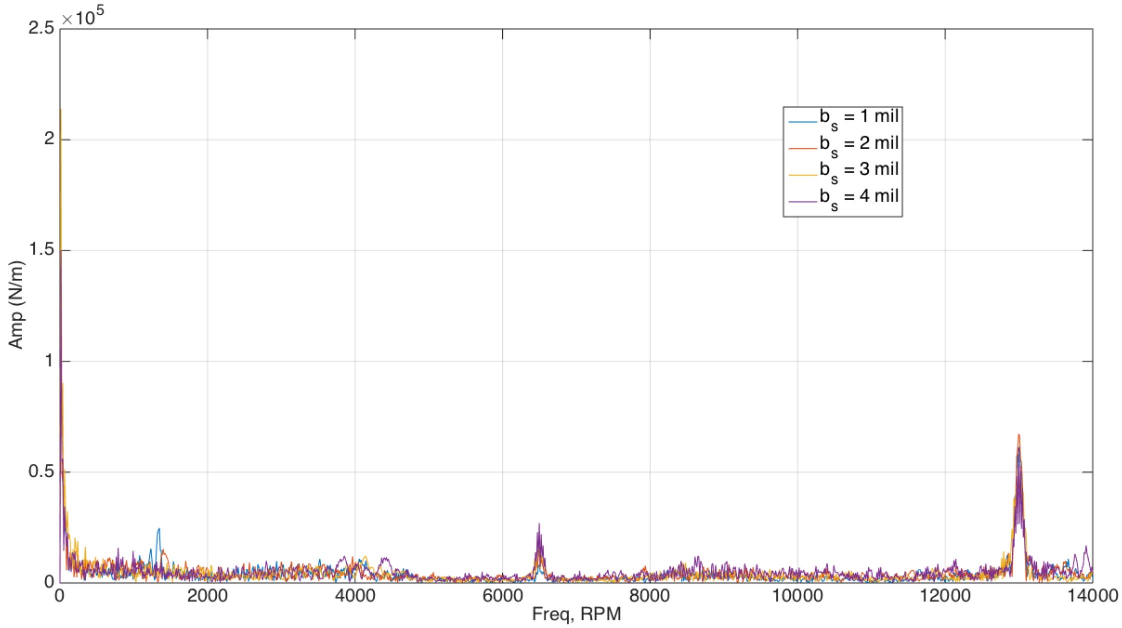

Figure 5.39: Gear stiffness FFT with only backlash clearance variation over 1-2x frequency range.

In summary, the following conclusions may be made regarding backlash clearance non-linearities. Smaller clearances produce larger mesh stiffness because the range of contact extends over a larger set of tangential displacements than if the clearance is bigger. In comparison to the average gear mesh stiffness, the stiffness due to backlash non-linearities is substantially less, even during tooth contact, because the stiffness varies linearly with net tangential displacement between the gear and pinion. This lower gear mesh stiffness reduces the damped natural frequencies of modes that are relevant to gear mesh excitation and produces noticeable peak frequencies in the vicinity of the dominant modes. Furthermore, rotational speed variation increases with increased backlash clearance because the net tangential displacements (and thus velocities) may increase more before the elastic restoring force of the gear mesh becomes active.

5.4.5 $\frac{K_a}{K_g}$ variation with backlash clearance, $b_s = 0.0254$ mm (1 mil)

Results are obtained with an unbalance of 720 g-mm and a fixed backlash clearance of 0.0254 mm or 1 mil while varying K_a. This corresponds to the 5^{th} set of rows in Table 5.5. X and Y displacement FFTs were generated and the trend for increasing $\frac{K_a}{K_g}$ from 0 to 0.5 is presented in Figure 5.40. Similar to what was observed when no backlash clearance was present, increasing K_a reduces the synchronous X and Y displacements. Effects of the backlash clearance non-linearity from the previous subsection may be observed as 15 μm peaks develop between 5,000 and 5,500 CPM.

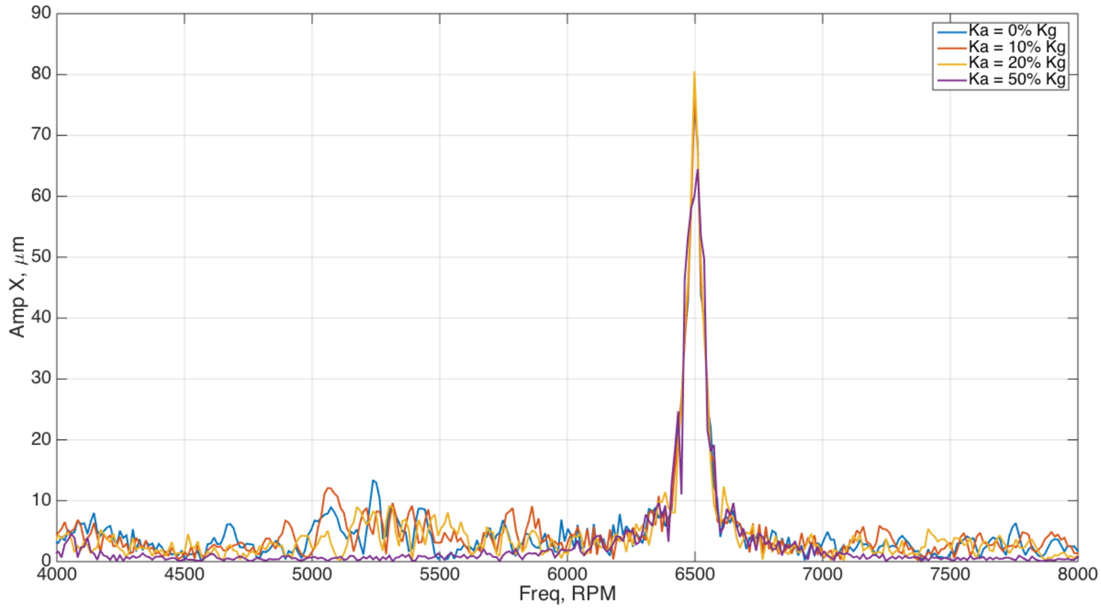

(a) Gear X displacement FFT with $\frac{K_a}{K_g}$ variation with 1 mil of backlash clearance at 1x.

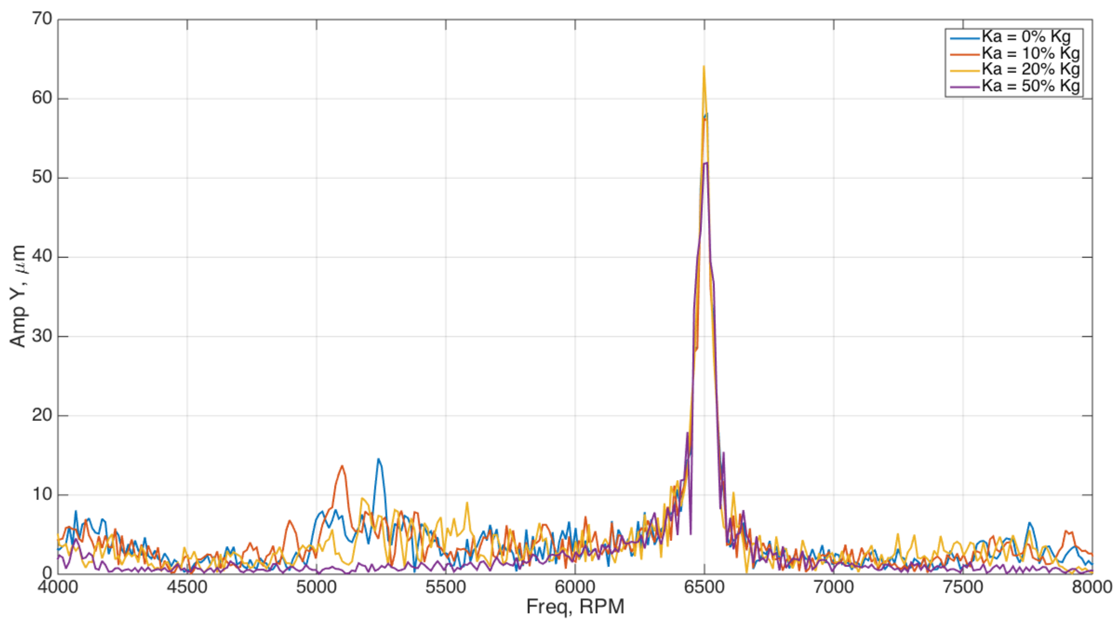

(b) Gear Y displacement FFT with $\frac{K_a}{K_g}$ variation with 1 mil of backlash clearance at 1x.

Figure 5.40: Gear X and Y displacement FFTs with $\frac{K_a}{K_g}$ variation with 1 mil of backlash clearance at 1x.

An FFT of the shaft rotational speed is shown in Figure 5.41. Three major peaks appear at the following frequencies 6,500, 189,000, and 383,000 CPM. Even with gear mesh stiffness variation K_a, the peak frequencies align with those from the case with only backlash clearance. This suggests that the backlash clearance plays a more dominant role in the system dynamics and this may be attributed to the reduction in effective mesh stiffness.

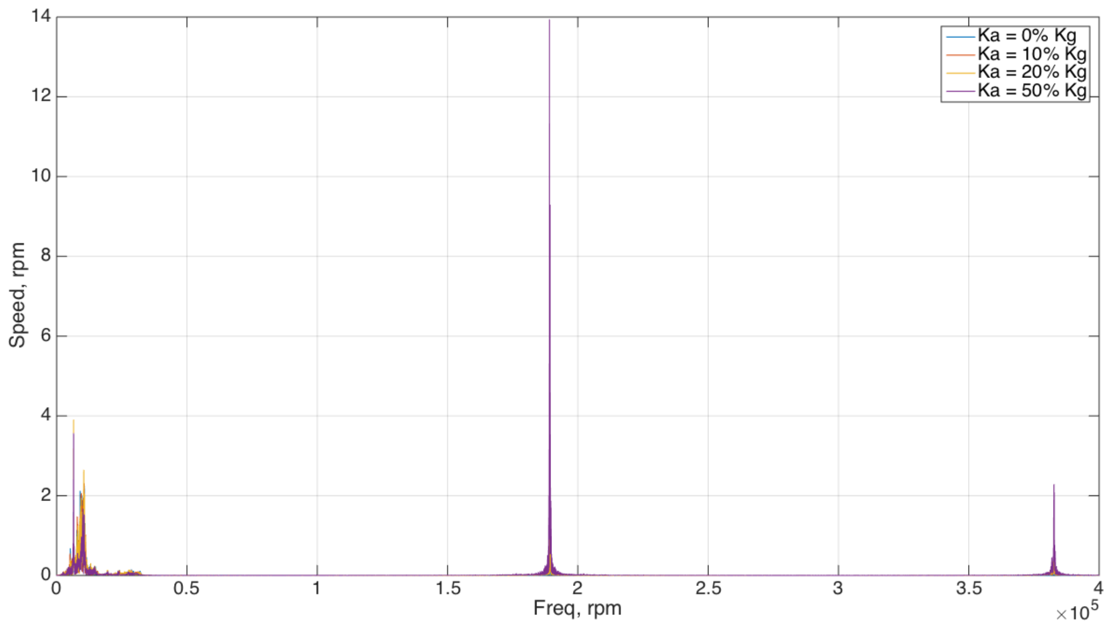

Figure 5.41: Rotational speed FFT with $\frac{K_a}{K_g}$ variation with 1 mil of backlash clearance over frequency range.

Figure 5.42 illustrates rotational speed variation sensitivity to changes in K_a at each of the three major frequency peaks. These results are similar to those with only backlash clearance variation. Peak amplitude at 6,500 CPM appears to vary somewhat in magnitude with different values of K_a, and the results suggest that lower values of gear mesh variation tend to increase additional peaks at 5,000 CPM and between 8,0000 and 11,000 CPM. It is at the higher end of the FFT frequency spectrum that the effects of K_a become more noticeable. Around 189,000 CPM, increasing K_a is shown to produce greater magnitude rotational speed variations. In addition, the frequency sensitivity of this amplification increases with increasing K_a and the presence of synchronous harmonics begin to appear. Similar observations may be made for frequencies centered around 383,000 CPM.

Gear mesh stiffness FFT results confirm that the frequency content with backlash clearance effects is substantially less than without it as shown in Figure 5.43. A possible reason is that the model for backlash clearance produces a smooth transition in stiffness between contact and no-contact and vice versa. Gear mesh frequency and other harmonics that had been observed with variations of $\frac{K_a}{K_g}$ without backlash clearance are insignificant in this FFT. Although peak frequencies are evident at 0 and 13,000 CPM (2x), their magnitudes appear insensitive to changes in K_a.

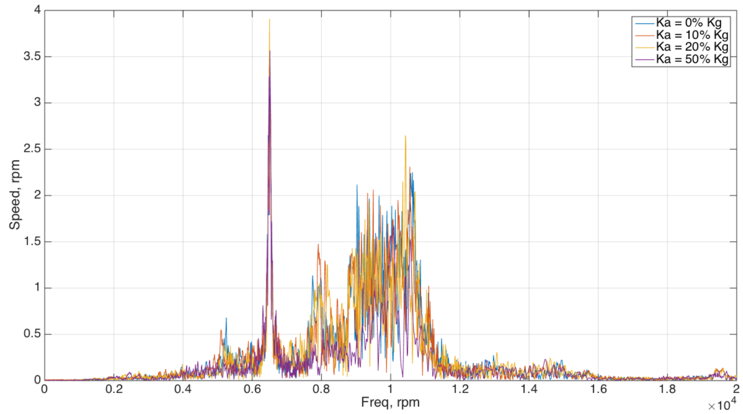

(a) Rotational speed FFT with $\frac{K_a}{K_g}$ variation with 1 mil of backlash clearance between 0 and 20,000 CPM.

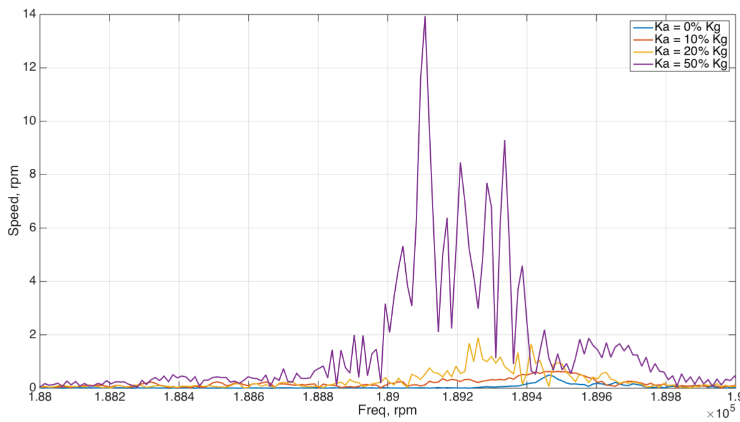

(b) Rotational speed FFT with $\frac{K_a}{K_g}$ variation with 1 mil of backlash clearance around $\omega_d = 189,000$ CPM.

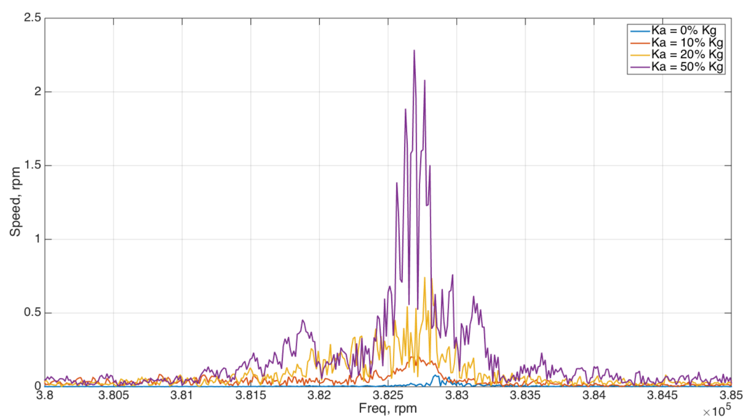

(c) Rotational speed FFT with $\frac{K_a}{K_g}$ variation with 1 mil of backlash clearance around $\omega_d = 383,000$ CPM.

Figure 5.42: Rotational speed FFT with $\frac{K_a}{K_g}$ variation with 1 mil of backlash clearance at peak frequencies.

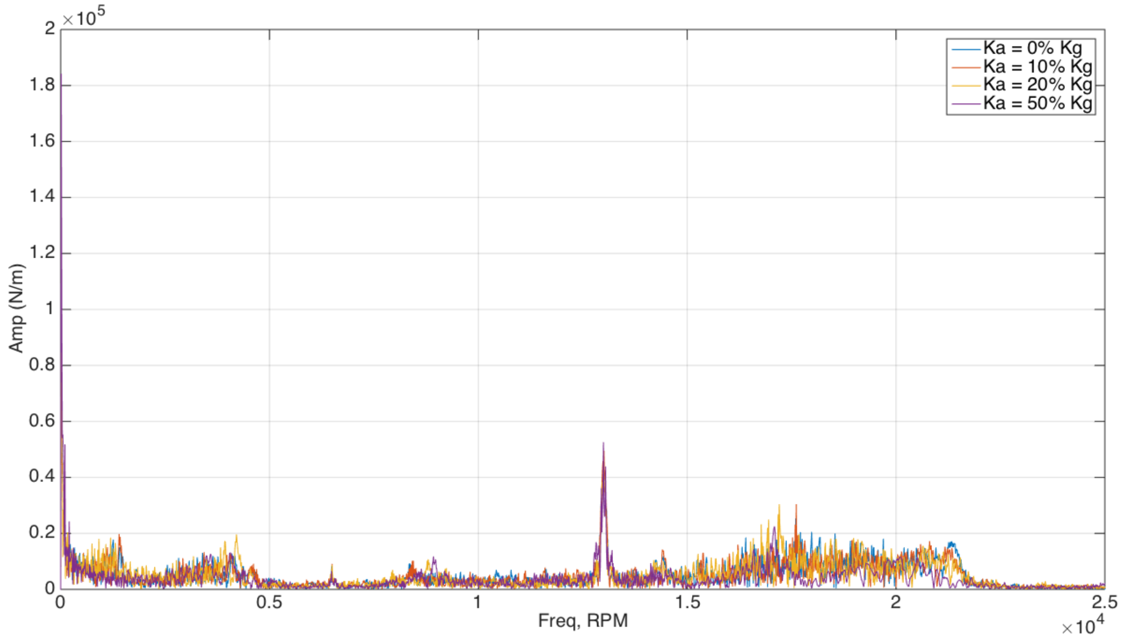

Figure 5.43: Gear stiffness FFT with $\frac{K_a}{K_g}$ variation with 1 mil of backlash clearance from 0 to 25,000 CPM.

These results confirm that backlash clearance modeling reduces the effective gear mesh stiffness substantially and therefore changes the dynamics such that variations in K_a are inconsequential except with high frequency rotational speed disturbances. Gear mesh frequencies and other harmonics do not appear in any of the FFTs regardless of the magnitude of $\frac{K_a}{K_g}$. X and Y displacement FFTs further demonstrated that lower gear mesh stiffness resulting from backlash clearance modeling excites some subsynchronous components between 5,000 and 5,500 CPM and that increasing K_a reduces their magnitudes.

5.4.6 Unbalance variation with $\frac{K_a}{K_g} = 0.2$ and $b_s = 0.0254$ mm (1 mil)

Results pertaining to the sensitivity of unbalance magnitude with fixed $\frac{K_a}{K_g}$ and backlash clearance, b_s are shown and analyzed in this subsection. X and Y displacement FFTs are generated in Figure 5.44. Results indicate that the displacement response at synchronous frequency is fairly insensitive to unbalance magnitude. Although the Y response increased from 60 to 80 μm from unbalance over the range of 720 to 1440 g-mm, the X magnitude at synchronous frequency decreased. Furthermore, additional frequency response appears in the displacements over the range from 5,000 to 6,000 CPM and increases with increasing unbalance magnitude.

Results from the shaft rotational speed FFT are presented in Figure 5.45 and reveal the same three major peak frequencies at 6,500, 189,000, and 383,000 CPM. Backlash clearance, as shown earlier in this section, has effectively reduced the gear mesh stiffness which has dropped the frequency of these peaks. The overall trend suggests that increased unbalance magnitude results in decreasing shaft rotational speed fluctuations.

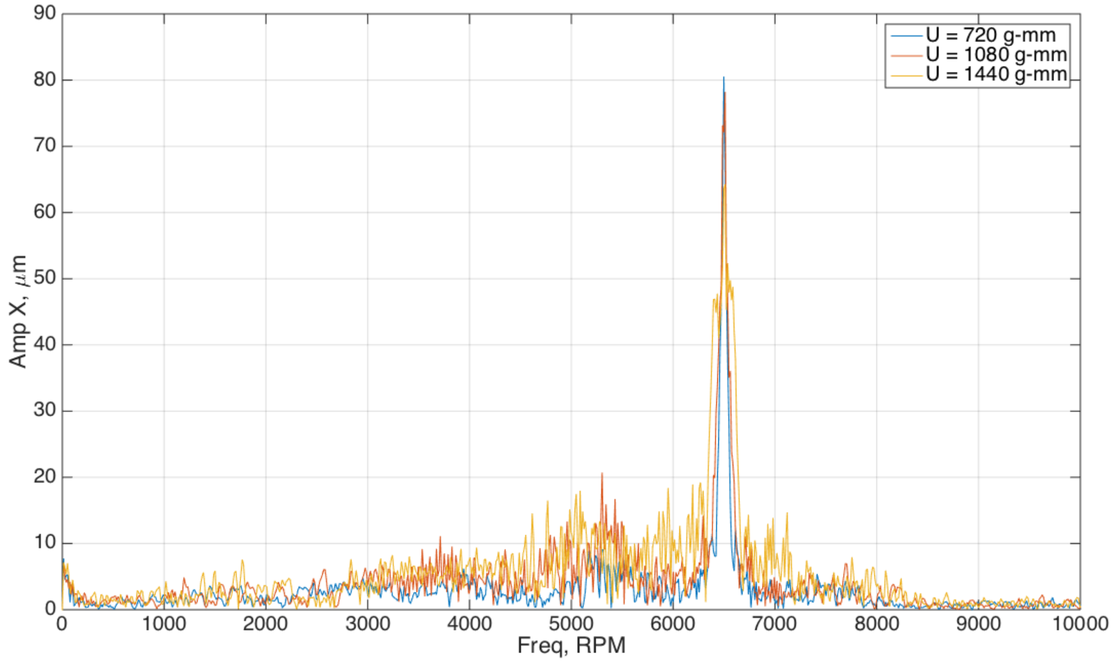

(a) Gear X displacement FFT with unbalance variation with $\frac{K_a}{K_g} = 0.2$ and 1 mil of backlash clearance at 1x.

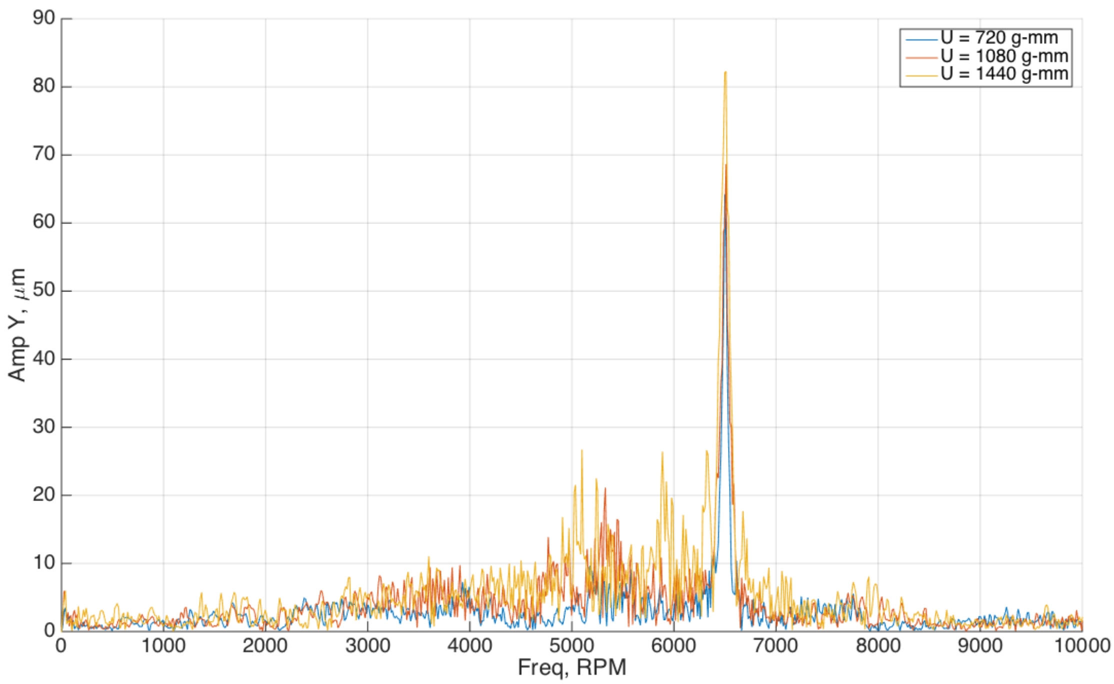

(b) Gear Y displacement FFT with unbalance variation with $\frac{K_a}{K_g} = 0.2$ and 1 mil of backlash clearance at 1x.

Figure 5.44: Gear X and Y displacement FFTs with unbalance variation with $\frac{K_a}{K_g} = 0.2$ and 1 mil of backlash clearance at 1x.

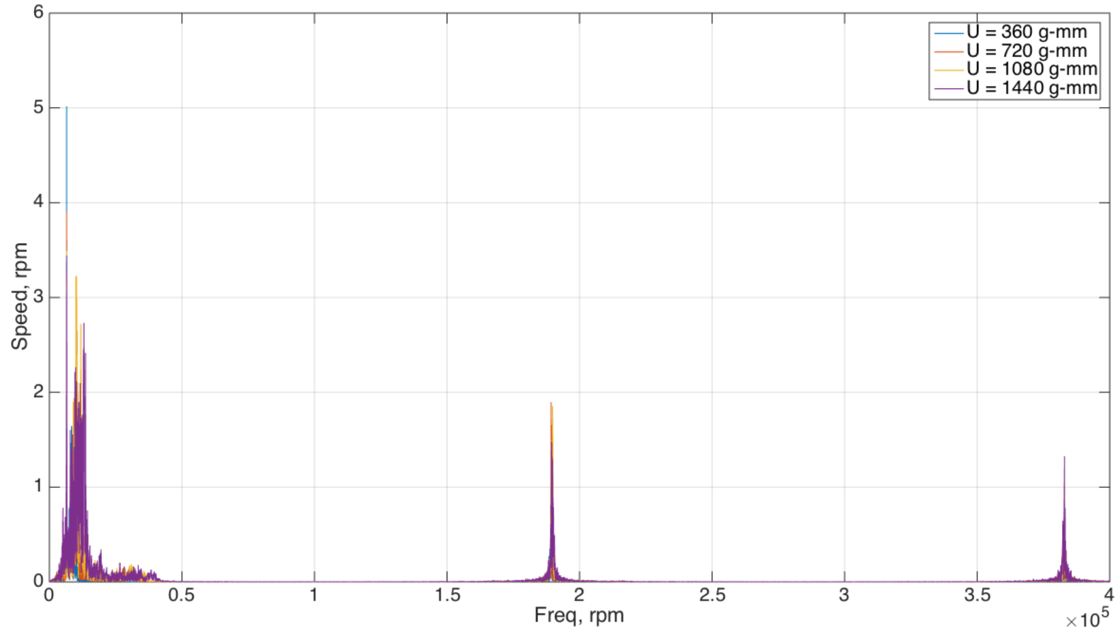

Figure 5.45: Rotational speed FFT with unbalance variation with $\frac{K_a}{K_g} = 0.2$ and 1 mil of backlash clearance over frequency range.

Figure 5.46 zooms in to the three major peak frequency regimes to better interpret the effects of increasing the unbalance magnitude on shaft rotational speed variations. Results for the 6,500 CPM component suggest that its magnitude decreases with increasing unbalance magnitude but supersynchronous frequencies are energized. In particular, the results suggest that the supersynchronous frequency of the peak increases with increasing unbalance magnitude. The shaft rotational speed variation in this frequency regime does not increase. At 217,000 CPM, the results illustrate that an increase in rotational speed variation occurs in comparison with results from the lowest unbalance magnitude (360 g-mm). However, as the unbalance magnitude is increased, the peak responses remain at similar amplitudes, although the largest unbalance produces additional sideband harmonics. For the 383,000 CPM regime, it is apparent that increasing unbalance magnitude does increase the peak response in addition to the sideband harmonics.

The presence of backlash clearance, as mentioned previously, has limited the frequency content of the gear mesh stiffness as shown in Figure 5.47. The range of frequencies of the gear mesh stiffness appears to grow with increasing unbalance magnitude, and so do the amplitudes of the different peaks. The trend of the 2x component (13,000 CPM)however, suggests that increasing unbalance magnitude decreases the gear mesh stiffness.

The effects of varying unbalance magnitude with $\frac{K_a}{K_g}$ and b_s held constant have been analyzed and suggest the following trends. It was expected that increasing unbalance magnitude would either uniformly increase the

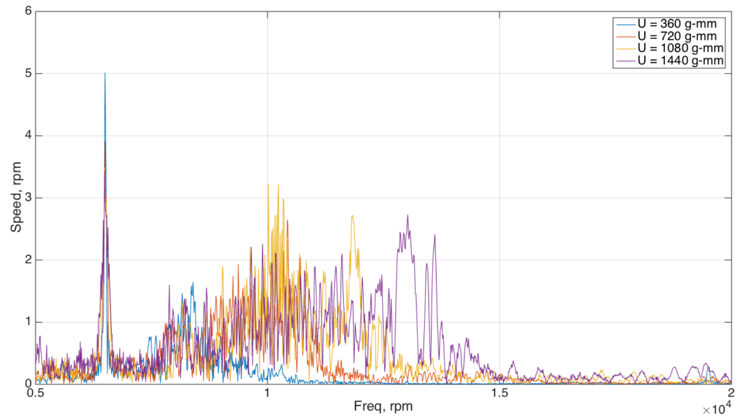

(a) Rotational speed FFT with unbalance variation with $\frac{K_a}{K_g} = 0.2$ and 1 mil of backlash clearance from 0 to 20,000 CPM.

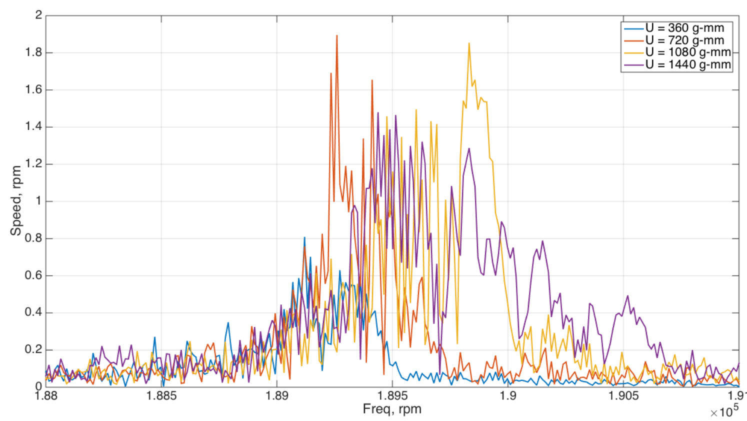

(b) Rotational speed FFT with unbalance variation with $\frac{K_a}{K_g} = 0.2$ and 1 mil of backlash clearance around $\omega_d = 189,000$ CPM.

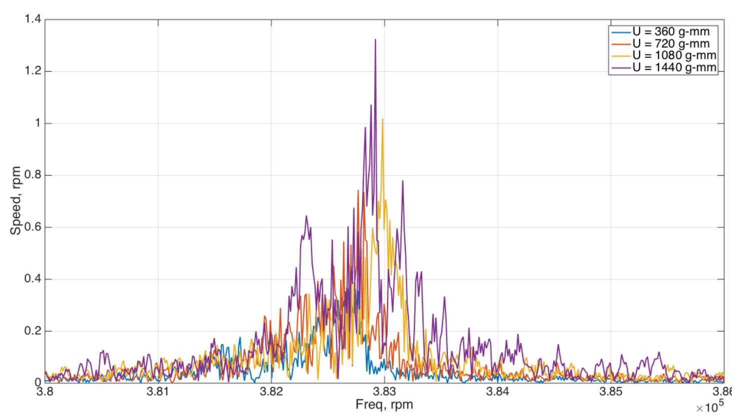

(c) Rotational speed FFT with unbalance variation with $\frac{K_a}{K_g} = 0.2$ and 1 mil of backlash clearance around $\omega_d = 383,000$ CPM.

Figure 5.46: Rotational speed FFT with unbalance variation with $\frac{K_a}{K_g} = 0.2$ and 1 mil of backlash clearance at peak frequencies.

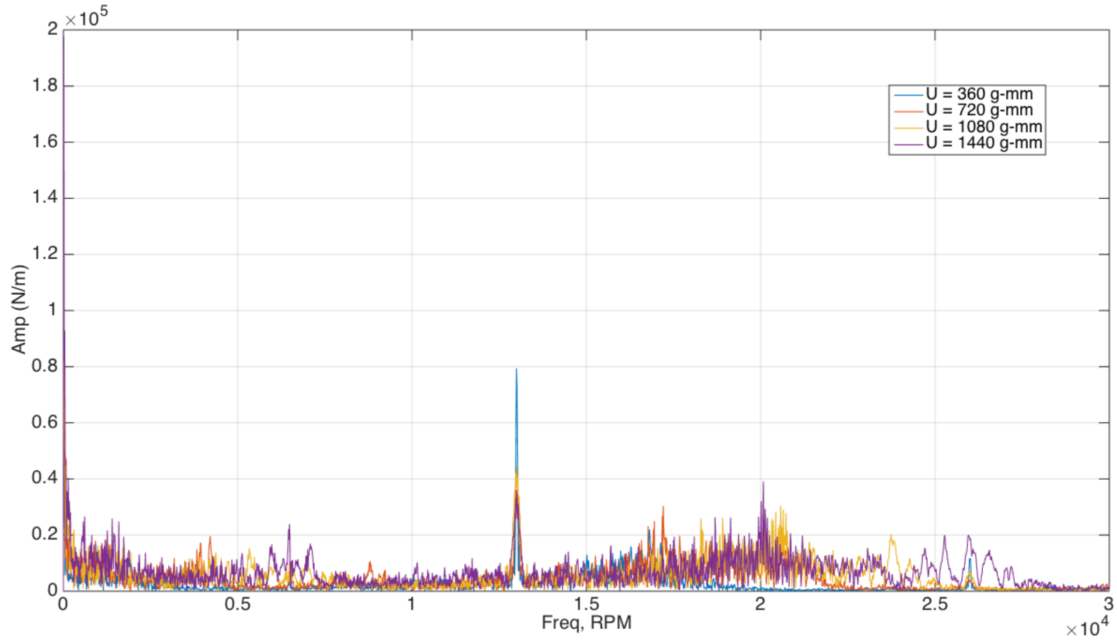

Figure 5.47: Gear stiffness FFT with unbalance variation with $\frac{K_a}{K_g} = 0.2$ and 1 mil of backlash clearance between 0 and 30,000 CPM.

magnitude of the frequency responses or that its effects would be most prevalent at synchronous speed (6,500 RPM). For the X and Y displacement FFTs, unbalance increase led to synchronous reductions in magnitude but increases in subsynchronous influence between 4,000 and 6,000 CPM. Backlash clearance reduced the effective gear mesh stiffness which lowered the three main frequencies of rotational speed fluctuation. The most prevalent observation regarding the effects of unbalance magnitude on shaft rotational speed fluctuation was that increased unbalance magnitude produced increases in the response of sideband harmonics but did not necessarily increase the responses at the major peaks. For gear mesh stiffness, the 2x component magnitude decreased with increasing unbalance magnitude but sub and supersynchronous peaks increased in magnitude. These results suggest that increases in unbalance magnitude generally result in a wider dispersion of energy across a broader frequency range and not an increase in the response at the peak frequency.

5.4.7 Contact ratio, c

Results presented in this subsection were generated with contact ratio, c, ranging from 1.25 to 1.75, where 1.592 had been the nominal value used in all previous analyses. There is no backlash clearance present and $\frac{K_a}{K_g} = 0.2$ with Fourier coefficients extending to 5 terms. X and Y displacement FFTs are generated in Figure 5.48 and display the response up to 13,000 CPM, which is 2x shaft speed. No noticeable increase or decrease in the synchronous response is observed with increasing the contact ratio.

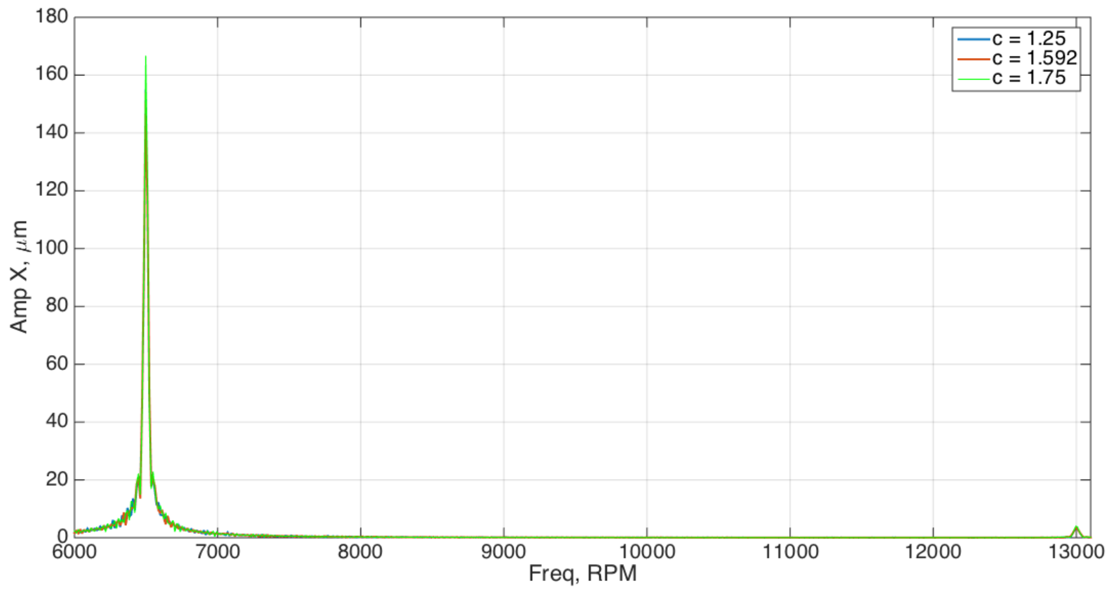

(a) Gear X displacement FFT with contact ratio variation with $\frac{K_a}{K_g} = 0.2$ and no backlash between 1 and 2x.

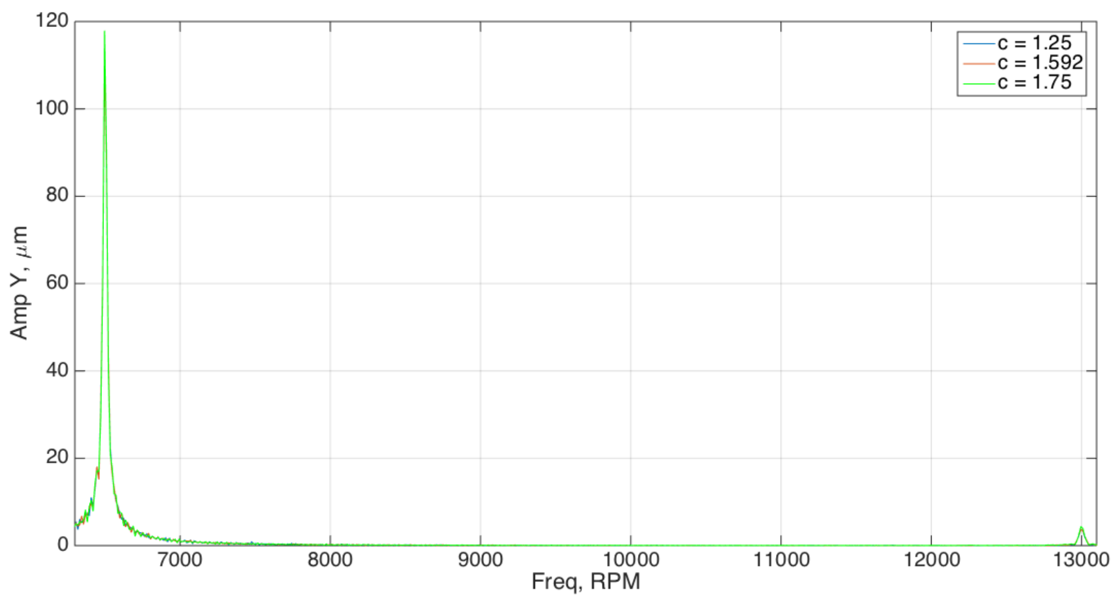

(b) Gear Y displacement FFT with contact ratio variation with $\frac{K_a}{K_g} = 0.2$ and no backlash between 1 and 2x.

Figure 5.48: Gear X and Y displacement FFTs with contact ratio variation with $\frac{K_a}{K_g} = 0.2$ and no backlash between 1 and 2x.

Analysis of the shaft rotational speed FFT, in Figure 5.49, reveals the presence of three peaks at 6,500, 217,000, and 399,000 CPM, which is consistent with results obtained without backlash clearance. No additional peak frequencies emerge upon varying the contact ratio.

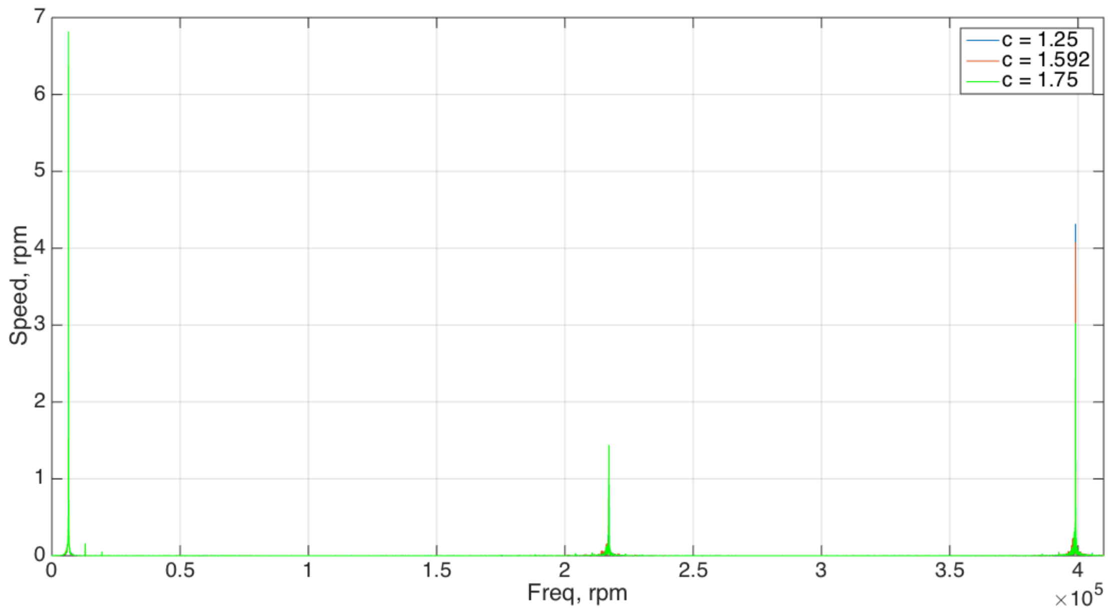

Figure 5.49: Rotational speed FFT with contact ratio variation with $\frac{K_a}{K_g} = 0.2$ and no backlash over frequency range.

FFTs of the individual frequency component ranges are shown in Figure 5.50. Zooming in towards the synchronous component of the shaft speed variation FFT reveals that it is insensitive to contact ratio variation. For 217,000 CPM, increasing the contact ratio produced the largest magnitude in shaft speed variation. However, contact ratios of 1.25 and 1.592 generated equal magnitude responses. This trend suggests that the 217,000 CPM frequency, which is consistent with the marginally stable lateral-torsional mode discussed earlier, is sensitive to larger increases in gear mesh stiffness over shorter time intervals. For the 399,000 CPM peak frequency, the results suggest that increasing the contact ratio decreases its amplitude. Contact ratios closer to 1.0 imply the gear mesh stiffness decreases farther but for shorter time intervals than compared with 1.50. A high frequency mode at 399,000 CPM became more energized with the smaller contact ratio rather than the larger one. Please refer to Figure 3.5 for details on the implications of varying the contact ratio between values of 1.25 and 2.0.

An FFT of the gear mesh stiffness is shown in Figure 5.51 and covers a range from 0 to 500,000 CPM. Although contact ratios of 1.25 and 1.75 are closer approximations to extremes because they imply that the rectangular waveform for the stiffness approaches sharp peaks, the largest peak responses are generated with $c = 1.592$ at the gear mesh frequency of 195,000 CPM and produce sidebands. Another frequency at

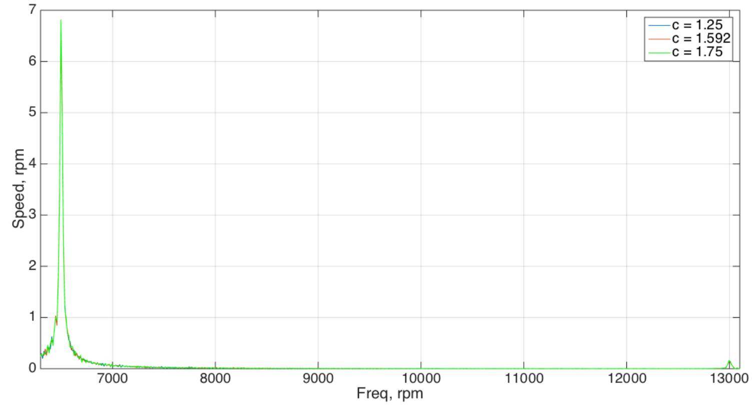

(a) Rotational speed FFT with contact ratio variation with $\frac{K_a}{K_g} = 0.2$ and no backlash from 1-2x.

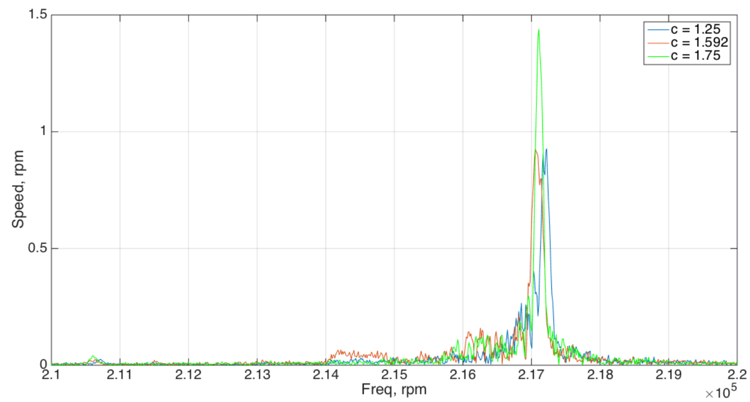

(b) Rotational speed FFT with contact ratio variation with $\frac{K_a}{K_g} = 0.2$ and no backlash around $\omega_d = 217,000$ CPM.

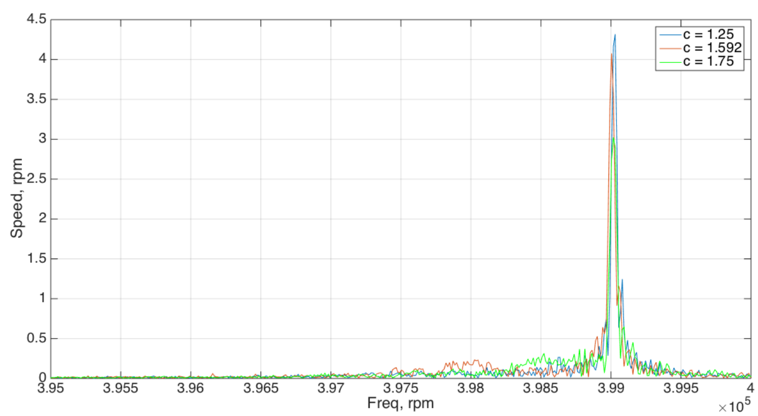

(c) Rotational speed FFT with contact ratio variation with $\frac{K_a}{K_g} = 0.2$ and no backlash around $\omega_d = 400,000$ CPM.

Figure 5.50: Rotational speed FFT with unbalance variation with contact ratio variation with $\frac{K_a}{K_g} = 0.2$ and no backlash at peak frequencies.

400,000 CPM is also excited. Contact ratios of 1.25 and 1.75 appear to excite gear mesh stiffness variations at approximately 290,000 CPM. The sharp and abrupt nature of their stiffness variation is likely to excite other modes as it more closely approximates an impulse excitation.

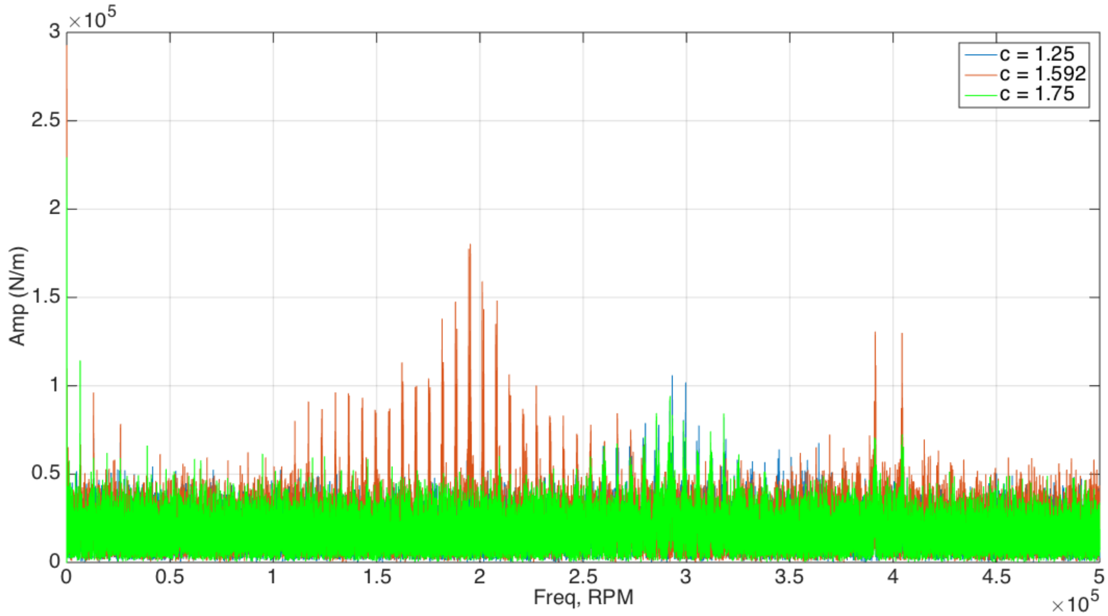

Figure 5.51: Gear stiffness FFT with unbalance variation with contact ratio variation with $\frac{K_a}{K_g} = 0.2$ and no backlash over frequency range.

Results from having varied the gear mesh contact ratio show several trends. The X and Y displacement magnitude responses appear to be insensitive and only the synchronous response is generated. With regards to the shaft rotational speed variation FFT, the three peak frequencies each showed different trends. The synchronous component of rotational speed variation is insensitive to changes in contact ratio, but the 217,000 and 399,000 CPM components demonstrate sensitivities to these changes. At 217,000 CPM, contact ratios of 1.25 and 1.592 produce similar peaks, but a contact ratio of 1.75 energized it further. In contrast, the 399,000 CPM peak increased for lower contact ratio, which suggests that altering the contact ratios may produce greater excitation for one mode and less for another. The gear mesh stiffness FFT illustrated this same trend of certain contact ratios energizing some frequencies greater than others. The contact ratio of 1.592 amplified the gear mesh frequency (195,000 CPM) and 400,000 CPM more than the others. Contact ratios of 1.25 and 1.75, however, energized a frequency around 300,000 CPM for the gear mesh stiffness.

5.5 Discussion

The analyses conducted on the single stage flexible shaft gearbox with 1:1 ratio produced several important trends from a rotor dynamics perspective. The effects of state-varying stiffness on the transient unbalance response of a simple 1:1 spur geared system were also explored in a systematic order. Using the same parameters for the nominal transient unbalance response in Section 5.3, a test matrix of runs was constructed in Table 5.5 to systematically study the effects of the following parameters on the X and Y displacements, shaft rotational speed oscillations, and the gear mesh stiffness: unbalance magnitude, ratio of variational mesh stiffness K_a to average mesh stiffness K_g, contact ratio, backlash clearance, and the number of Fourier terms.

Results confirm that some of these parameters had greater effects on the rotor dynamic performance than others. In particular, the transient analysis confirmed that non-linearities exist in the rotor dynamic equations of motion simply because the gear mesh reaction torque produces oscillations in shaft rotational speed that drive non-synchronous unbalance forces. In addition to the constant gear mesh stiffness case, the state-varying mesh stiffness energized additional lightly damped high frequency modes at 189,000 and 395,000 CPM. These results confirm that the direct Runge-Kutta numerical method is susceptible to the excitation of these unrealistic high frequency modes. The 189,000 CPM mode, however, is near the gear mesh frequency of 195,000 CPM and thus is more likely to be excited. Techniques such as adding artificial torsional damping at the gear mesh have been shown to successfully eliminate the excitation of the unrealistic modes.

Increasing the ratio of $\frac{K_a}{K_g}$ had the effect of decreasing the peak amplitude but increasing the amplitudes of sideband frequencies. Varying the number of Fourier coefficient terms, in general, did not affect the X and Y displacements but yielded a reduction in amplitude of shaft rotational speed variation for one mode but while increasing it for others. These effects are more prominent for higher frequency modes. In general, increasing the number of Fourier coefficients beyond 5 produced minimal changes and would be more likely to excite more higher order modes than what may be physically realistic. Results concerning backlash clearance variation showed that the model produces an effective mesh stiffness that is greatly reduced resulting in the reduction of the frequencies of several gear dominated modes. Increasing the backlash clearance results in larger variations of shaft rotational speed which feeds into general system non-linearity in addition to potential abrupt contact loss. When comparing the relative effects of $\frac{K_a}{K_g}$ with backlash clearance, backlash clearance dominated the system dynamics because of the reduced gear mesh stiffness and even produced excitations for subsynchronous frequencies. Increasing the unbalance magnitude with both $\frac{K_a}{K_g}$ and backlash clearance results in greater amplification of certain modes or the excitation of sideband frequencies. Finally, the gear mesh contact ratio was varied between 1.25 and 1.75, resulting in minimal effects on the displacements.

Contact ratios approaching 1.0 imply that the gear mesh stiffness undergoes a large decrease over shorter time intervals compared with a value of 1.50. In contrast, contact ratios closer to 2.0 produce larger increases in gear mesh stiffness over shorter time intervals. As these contact ratios approach 1.0 or 2.0, the gear mesh stiffness appears closer to an abrupt impulse, and it may energize specific modes that can affect the shaft rotational speed via lateral-torsional coupling.

Although detailed FEA models of gear teeth may generate more detailed results concerning these parameters, they are far more computationally expensive to run and may not be necessary. An application of these methods to an industrial power turbine compressor drive train is discussed in the next chapter.

Chapter 6

Application 3: Supersynchronous submesh frequency vibration related to a power turbine compressor

6.1 Introduction

This chapter discusses the investigation of a supersynchronous vibration problem experienced by a gearbox within a 36 MW power turbine compressor train and is a continuation of the work done by Cloud et al [69]. This double helical (or herringbone) gearbox functions as a speed increaser between the high-speed gas turbine and compressor and has the following parameters:

- Power rating: 36,770 KW
- Gear ratio: 1.6905
- Helix angle: 26.4924°
- Normal pressure angle: 20°
- Pinion operating speed: 5,700 RPM

6.2 Problem statement

The gearbox pinion experienced high amplitude vibrations under full-load and full-speed conditions. However, no problematic vibrations were observed during the no-load, uncoupled test conditions. Measurements from proximity probes on the pinion blind-end (BE) and an accelerometer on the housing casing indicated supersynchronous vibrations at a frequency around 57,000 RPM (10x pinion). This supersynchronous component reached an amplitude of 20-30 μm peak to peak at the pinion blind-end probes. Increasing the power turbine load, even with constant speed, resulted in increased vibration amplitude.

Supersynchronous vibration problems in gearboxes are typically associated with gear mesh frequency (GMF), which is the product of the number of gear teeth and its rotational speed. However, the problematic vibration frequency of 57,000 RPM is well below the GMF (239,400 RPM). Similar supersynchronous, sub-GMF vibration problems have scarcely been reported in industry. Memmott [67] reported similar vibration problems on three different single stage, double helical gearboxes, all of which shared the following characteristics:

- High vibration present only during loaded testing of the gearbox and compressors
- Vibration frequency of concern was 8x the pinion's speed
- Fundamental cause was attributed to a resonance of the pinion's fourth lateral mode
- Resolution of the problem involved removing or adding weight from the pinion shaft to increase the fourth mode's separation margin

Marin observed a fourth occurence in which the vibration frequency of concern was at the pinion's 7x instead of the 8x frequency [68]. All other characteristics were identical with those reported in Memmott [67]. Similar to these previously published cases, the gearbox and compressor manufacturers in the case considered here attributed the subject machine's high vibrations to a natural frequency corresponding to the fourth bending mode of the high-speed pinion. In an attempt to increase the damping of this mode, the manufacturers modified the clearance of the pinion journal bearings and moved the axial location of the blind-end journal bearing. Subsequent testing revealed that these modifications had little impact on attenuating the high-speed pinion radial vibration.

While shaft modifications were eventually implemented to reduce the amplification of the high speed pinion vibration, there continues to be much uncertainty about the nature of the problem. Industry has been unable to identify any unusual, or common, design or operational features that would distinguish the problematic machines from almost identical machines that do not experience such vibrations. Furthermore, nothing has been found to explain why the phenomenon has only occurred during full-load testing, and not during unloaded mechanical run testing of the gearboxes.

Given these uncertainties, this case study aims to determine the following:

- Lateral (or torsional and axial) modes that could be related to the supersynchronous vibration
- Force distribution needed to excite these modes
- Gear mesh factors that may have the greatest influence on this phenomenon

6.3 Modeling considerations

The gearbox and compressor manufacturers' rotor dynamic analyses investigated the gearbox pinion's lateral dynamics as an individual rotor, which is the typical practice within industry. Given that the high amplitude vibration was experienced during full-load conditions, a coupled, full drive-train analysis of the geared system would seem to have the best chance of identifying the problem's root cause or causes. Such a coupled analysis predicts the interaction between lateral, torsional and axial vibrations of the entire train with component substructures. Coupled lateral, torsional, and axial vibrations are a well-known phenomenon with drive trains involving gearboxes [61, 63].

Cloud et al [69] produced detailed 3-D finite element models of the shafts that were generated and tested in conjunction with other FEA analysis tools such as ANSYS to validate the detail and accuracy of the 2-D Timoshenko beam elements used in these analyses. An exploration of the free-free bending modes of the shafts were necessary for this model validation and all modes captured were within 3% of those from the 3-D FE models. Cloud et al [69] also produced detailed models for the two adjacent flexible couplings. These models were developed with many beam elements to help accurately determine their torsional and lateral dynamics at the high frequencies associated with the vibration problem. Representing each coupling by a single lateral or torsional spring element, similar to what is typically done for industrial torsional analyses, cannot capture higher frequency dynamics within the flexible coupling.

A 2-D beam finite element model of the shafts and spacers, using a similar element distribution to Cloud et al [69], is used in the subsequent analyses. Fewer elements were desired to reduce the computational effort needed to run several time-transient rotor dynamic analyses. Damped eigenvalue analyses were conducted with different element distributions to compare the modes and natural frequencies in the vicinity of the 10x vibration problem with what Cloud et al predicted. This would insure that model fidelity is not compromised.

Tilting pad journal bearings support the bull gear and pinion shafts and their frequency dependent dynamic characteristics must be determined. A finite element solution of the Reynold's equation was developed by

Cloud et al [69], and it models the effects of variable oil film viscosity, pad and pivot deformations, and directed flow characteristics of spray bar blockers. The bearings' dynamic stiffness and damping coefficients are calculated over eleven different torque levels, and three different bearing radial clearances.

All transient and steady-state analyses in this investigation are done using the bearings' synchronously-reduced dynamic coefficients due to current limitations within the solver. It is recommended that, in future work, these time-transient analyses be conducted using the full coefficients since use of full coefficients allows the bearings' stiffness and damping properties to vary as a function of the whirl frequency, an important characteristic given the nonsynchronous nature of the vibration problem. Pivot flexibility is also found to be an important characteristic because of its increasing effects at higher frequencies, as demonstrated in the steady-state damped eigenvalue analyses reported by Cloud et al [69]. If the pivots are assumed to be rigid, the frequency dependence of the reduced coefficients is almost negligible, which is a known characteristic for this machine's bearings which have high offset pivots [70]. However, when pivot flexibility is included, the bearings' dynamics become highly frequency dependent. Relative to their synchronous magnitudes, stiffness increases and damping decreases at the supersynchronous frequencies involved with the vibration problem.

Figure 6.1 shows the system configuration for the full-load full-speed test that produced the high supersynchronous vibration. It is assumed that the dynamics of the power turbine and compressor would have a negligible effect on the lateral vibration of the gearbox, but their torsional dynamics are important. The power turbine and compressor shafts are treated as rigid beam elements with their respective polar moments of inertia for the torsional dynamics. Furthermore, they are supported with very stiff bearings to further reduce their impact on the lateral modes of interest.

The double helical (or herringbone) gearbox was dynamically modeled as a pair of single helical gears using techniques developed by Kahraman [60, 62] and Kaplan [34]. The properties of the double helical gear mesh are provided in Table 6.1 are were supplied by Cloud et al [69]. This finite element based approach allows engagement of multiple rotors at any relative position. Vibrations in lateral, torsional, and axial directions are coupled together through the flexible gear mesh. The gear mesh was assumed to contribute no damping to the system in accordance with the worst-case scenario. The only damping source in the system was assumed to originate from the gearbox journal bearings.

Table 6.1: Double helical gear mesh characteristics.

Parameters	Value	Units
Average mesh stiffness (K_g)	8.298x10^9	$\frac{N}{m}$
Pinion radius (r_p)	0.217	m
Bull gear radius (r_b)	0.367	m
Pressure angle (α_n)	20	degrees
Helix angle (β)	29.492	degrees
Number of pinion teeth (N_p)	42	teeth
Number of bull gear teeth (N_b)	71	teeth
Contact ratio (c)	1.437	dim
Backlash (δ_s)	0.866	mm

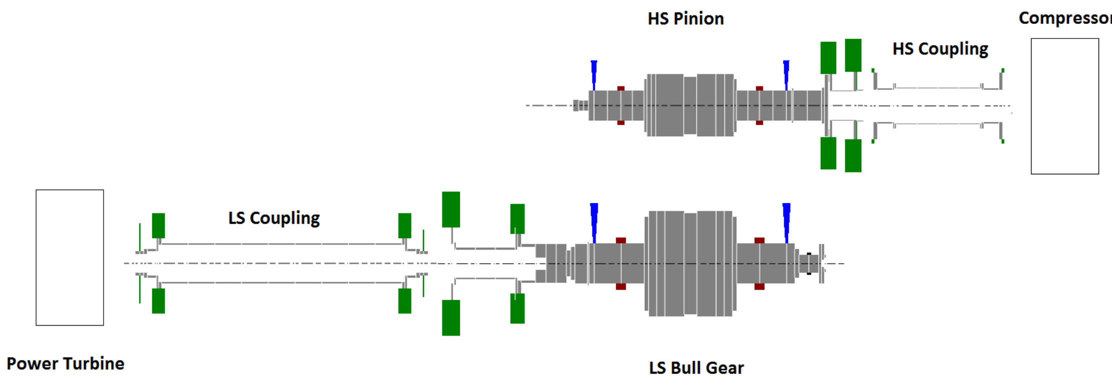

Figure 6.1: Finite element model of power turbine compressor gearbox and train.

6.4 Analysis and results

6.4.1 Damped eigenvalue analysis

The initial focus of the investigation was to understand the damped eigenvalues and eigenvectors. It is important to understand where modes are located, their damping, and their sensitivity to operating and bearing conditions. Unlike typical rotor dynamic investigations, the frequency search range for this damped eigenvalue analysis is around 10x operating speed of the pinion shaft, which is neither the synchronous nor the mesh frequency. A table of damped eigenvalues, damped natural frequencies and logarithmic decrements is shown in Table 6.2. Modes that have low logarithmic decrements (< 0.1) and have large components in the lateral direction are likely to be problematic and these include modes 50, 55, 56, 58, and 59. A detailed investigation of the mode shapes, which illustrates the areas of the shafts that have large modal participation, provide additional insight to help determine the problematic mode(s) involved. A sensitivity analysis of the damped natural frequencies using fewer nodes in the finite element model had been conducted and confirmed that several of the modes in the 10x frequency range remained unaffected.

Figures 6.2, 6.3, 6.4, 6.5, and 6.6 depict the modes with low logarithmic decrement and lateral components

Table 6.2: 15 damped eigenvalues of interest.

Mode Number	$\omega_{\mathbf{d}}$ (RPM)	**Log Dec**	**Direction**
45	38630	0.311	L
46	46379	0.381	L
47	49515	0.231	L
48	49811	0.000	A
49	50029	7.730	L
50	**51889**	**0.019**	**L-T**
51	52805	16.295	L
52	53657	0.201	L
53	53711	5.451	L
54	54655	0.196	L
55	**55692**	**0.088**	**L**
56	**59738**	**0.012**	**L**
57	60137	0.804	L
58	**60440**	**0.030**	**L**
59	**60690**	**0.019**	**L**
60	64494	0.777	L

within a frequency range near 57,000 RPM. The eigenvectors (or mode shapes) are scaled to values between -1 and 1 through division of the highest displacement node within each eigenvector .High amplitude vibration of the drive train had been observed along the blind-end pinion side and substantially lower amplitude vibration on the bull gear shaft. Knowledge of where to expect heavy modal participation is important to discern which of these modes is likely to be the one that is energized.

High modal participation in lateral bending is evident at the blind-end side of the pinion shaft for the laterally-torsionally coupled mode 50 as shown in Figure 6.2. This is largely consistent with the reported location of the vibration problem. In addition, there is sufficient modal participation at the gear mesh on the high speed pinion to suggest that the gear mesh stiffness may have a strong influence. Furthermore, mode 50 reveals a strong twisting motion along the drive-end of the bull gear shaft. Despite the fact that the required frequency needed to excite this mode is around 52,000 CPM instead of 57,000 CPM, mode 50 appears to be a likely candidate.

Mode 55, as shown in Figure 6.3, contains only a lateral component and may be energized at a frequency of 55,700 RPM, which is much closer to the reported 57,000 RPM vibration. There is high modal participation at the blind-end side of the high-speed pinion, which is consistent with the reported problem. In addition, there is also large lateral participation at the coupling end of the low-speed bull gear shaft, which was not reported. Despite this discrepancy, mode 55 is likely to contribute to the vibration reported in the field since its frequency is closer than that of mode 50.

Unlike modes 50 and 55, mode 56 has most of its participation in bending along the low-speed flexible coupling as shown in Figure 6.4. There is no participation along the high-speed pinion shaft and very little

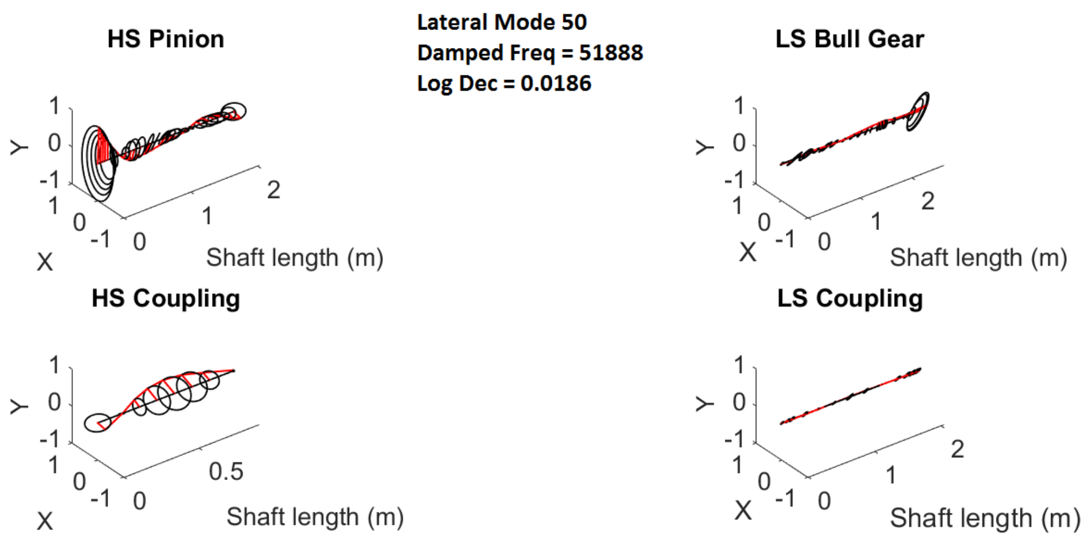

(a) Mode 50 lateral component.

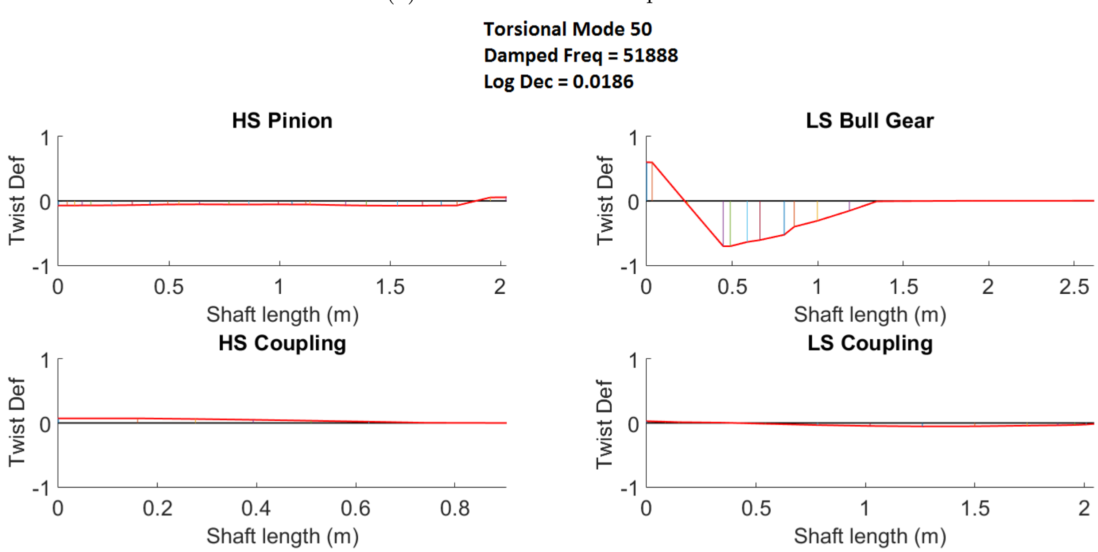

(b) Mode 50 torsional component.

Figure 6.2: Lateral and torsional components of mode 50.

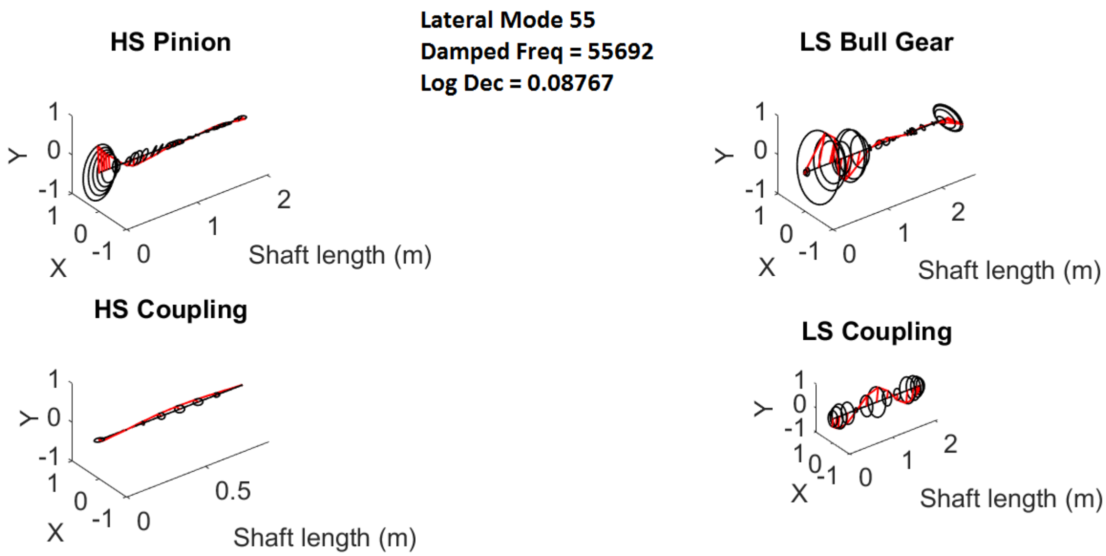

Figure 6.3: Lateral mode 55.

along the low-speed bull gear shaft. This is largely inconsistent with the reported vibration. In addition, its damped natural frequency is approximately 60,000 RPM, which is above the reported vibration of 57,000 RPM. Mode 56 is not likely to be energized unless the source originates in the low-speed coupling and is at 17x of bull gear running speed.

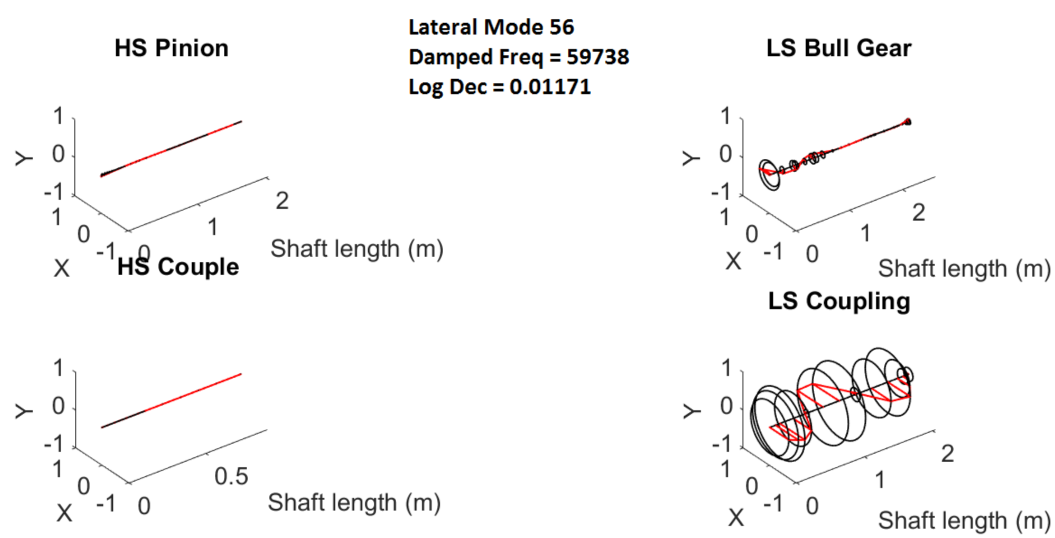

Figure 6.4: Lateral mode 56.

Mode 58 has similar characteristics to mode 56 except that there is some displacement at the blind end of the high-speed pinion shaft as shown in Figure 6.5. The damped frequency of this mode is approximately 60,400 RPM and most of the modal participation is along the low-speed coupling shaft. Therefore, mode 58 is not likely to be problematic unless the excitation source originates in the low-speed coupling.

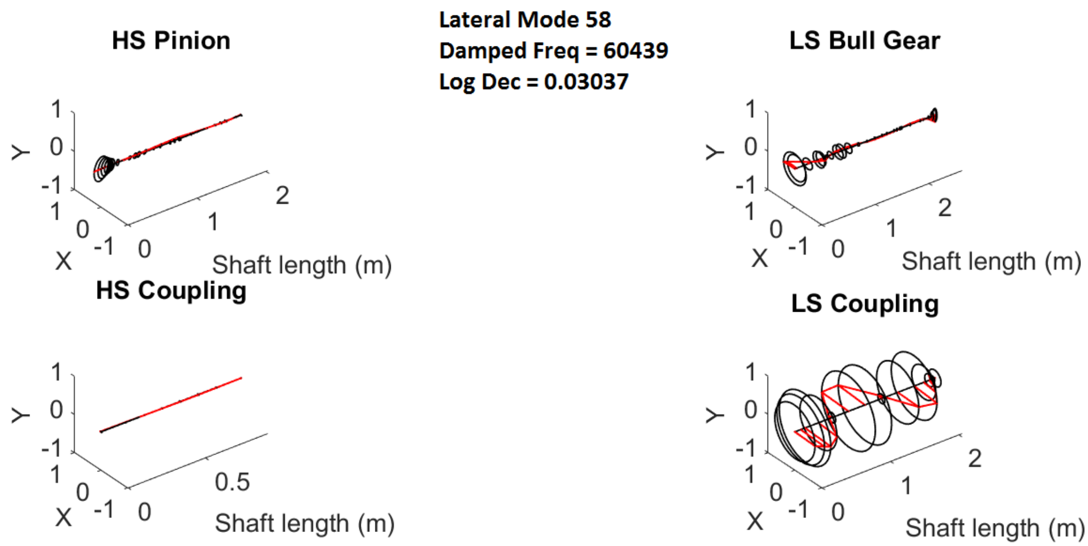

Figure 6.5: Lateral mode 58.

Figure 6.6 depicts mode 59, which is dominated by motion along the low-speed coupling similar to modes 56 and 58. There is some motion along the blind end of the high-speed pinion and the coupling end of the bull gear shaft. The damped natural frequency is approximately 60,700 RPM, and with most of the modal participation existing along the low-speed flexible coupling, it is unlikely that mode 59 is the mode of interest. A more thorough investigation of the rotational speeds, gear forces and torques may produce additional insights into how the model may be changed to reproduce the 57,000 RPM excitation.

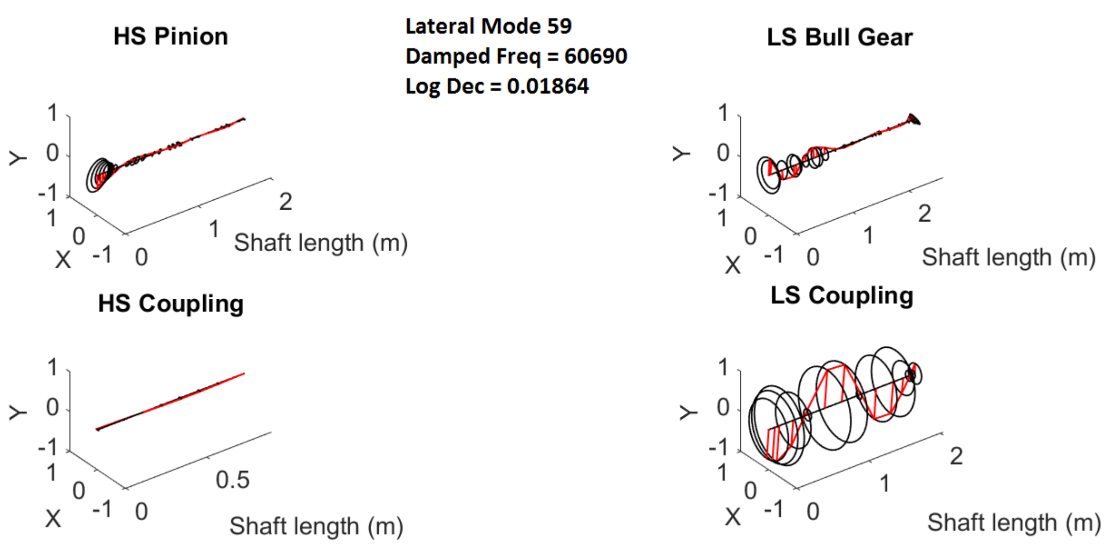

Figure 6.6: Lateral mode 59.

6.4.2 Transient response analysis

The problematic mode has been isolated to modes 50 or 55 based on the damped eigenvalue analysis in the previous subsection. A transient rotor dynamic analysis is performed on the power turbine compressor drive train using unbalance as the external forcing function. Unbalance operates at a frequency that matches the shaft rotational speeds (synchronous), but this may excite a wide range of frequencies because the shaft rotational speeds vary due to the gear mesh reaction torque, as discussed in Chapter 5. An unbalance of 10 oz-in (7,200 g-mm) is applied to the far blind-end side of the high-speed pinion to energize either mode 50 or 55. The magnitude of unbalance is chosen in accordance with API [37] as shown in Equation 4.1.

The transient analysis begins with assuming a constant gear mesh stiffness and therefore, the change in the gear node states determine the mesh forces and torques in time. Results appear from time $t = 0$ to $t = 0.5$ seconds using a simulation time step of 1×10^{-6} seconds. Additional transient responses were run with smaller simulation time steps to confirm that 1×10^{-6} seconds sufficiently captures the dynamics. X and Y displacement results are shown in Figures 6.7 and 6.8. They reveal that the vibration is primarily synchronous (5,700 RPM) and contains some subsynchronous contribution.

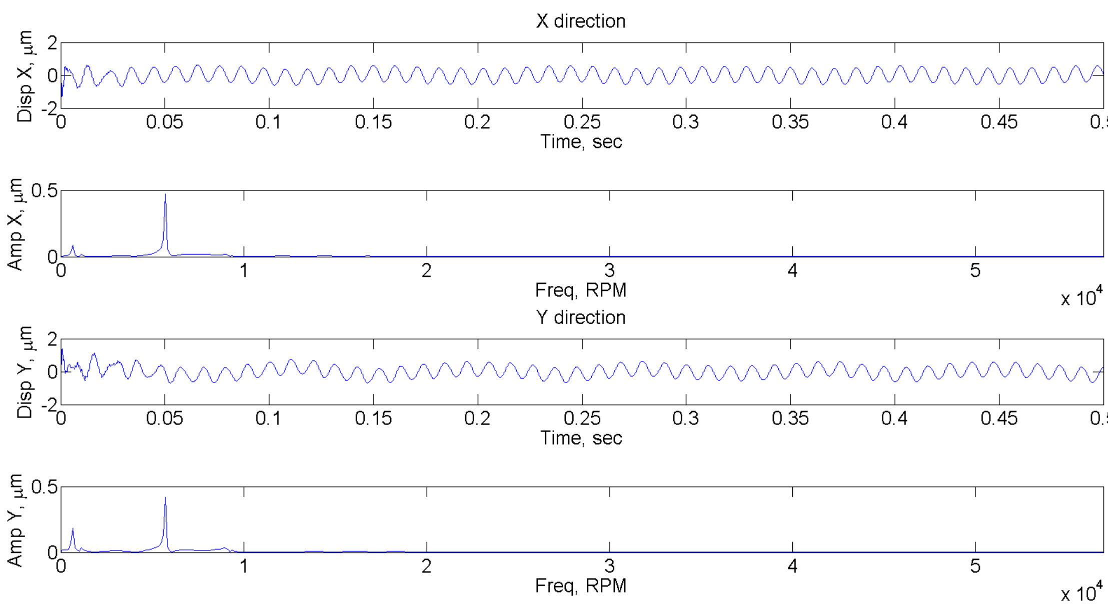

Figure 6.7: X and Y displacements of high-speed pinion gear node with $K_a = 0$.

A 3-D whirl plot of the entire high-speed pinion is shown in Figure 6.9 and indicates that the unbalance produced the desired bending in the shaft that is consistent with where the customer reported the high amplitude vibration. Vibration amplitudes for the low-speed bull gear shaft and both flexible couplings are more than 2 orders of magnitude smaller and may be ignored. A 2-D orbit plot depicting the orbit of the

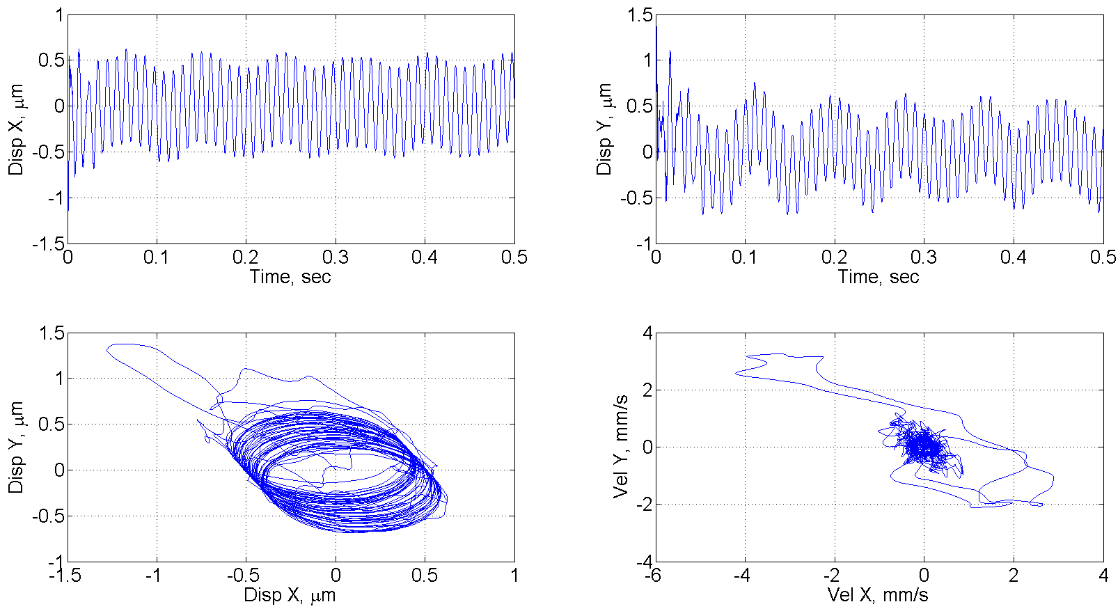

Figure 6.8: X and Y displacement orbits of high-speed pinion gear node with $K_a = 0$.

pinion node on that shaft is shown and indicates that the displacements are synchronous with the shaft rotational speed. No supersynchronous frequencies appear within the orbit trajectory.

As expected, the reaction gear mesh torque produces oscillations in the shaft rotational speed as shown in Figure 6.10. Typically, the rotational speed variation occurs at the same frequency as running speed, but two subsynchronous vibrations appear to be dominating. The rotational speed variation is quite small (0.2 RPM) and there appears to be some high frequency torsional vibration at the start that is quickly damped out. It is possible that additional gear mesh excitations are necessary to produce the problematic high frequency vibration. Rotational speed variations, as discussed in Chapter 5 have been shown to produce modulation in both amplitude and frequency of the unbalance force, which produces similar reactions at the gear mesh and the bearings.

Examining the X and Y velocities of the high-speed pinion node reveals both synchronous and supersynchronous influences as illustrated in Figure 6.11. The velocities are dominated by the synchronous component but other components appear at 9,000, and 57,000 RPM. Although these supersynchronous responses primarily exist at the beginning of the transient solution before attenuating, state-varying gear mesh excitations may augment their effects.

The high-speed pinion forces and torques are shown in time along with their FFTs in Figure 6.12. Subsynchronous, synchronous, and supersynchronous components are present. The major components are at 690 and 5,700 RPM and there are additional smaller components at 9,000, 52,000, 57,000, 74,000, and 81,000 RPM. The higher frequency components attenuate within 0.1 seconds, which suggests that additional

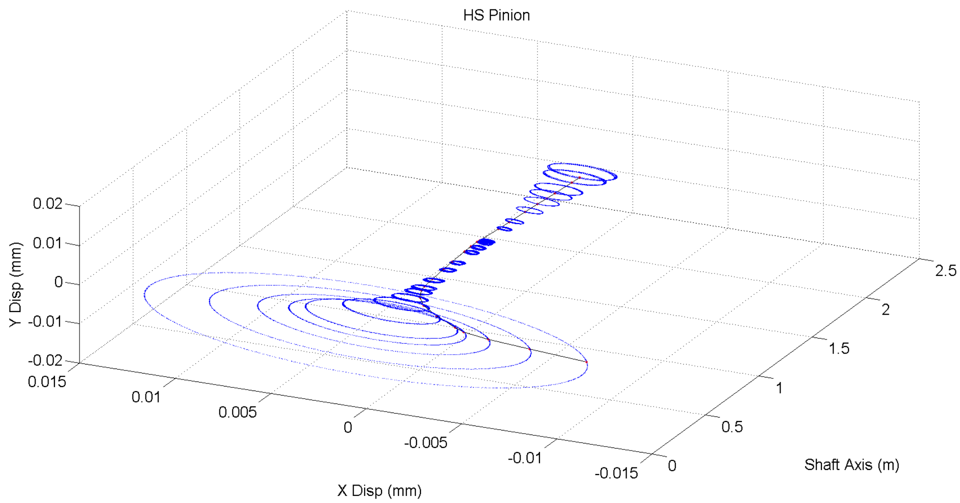

(a) 3-D whirl orbit of high-speed pinion shaft with $K_a = 0$.

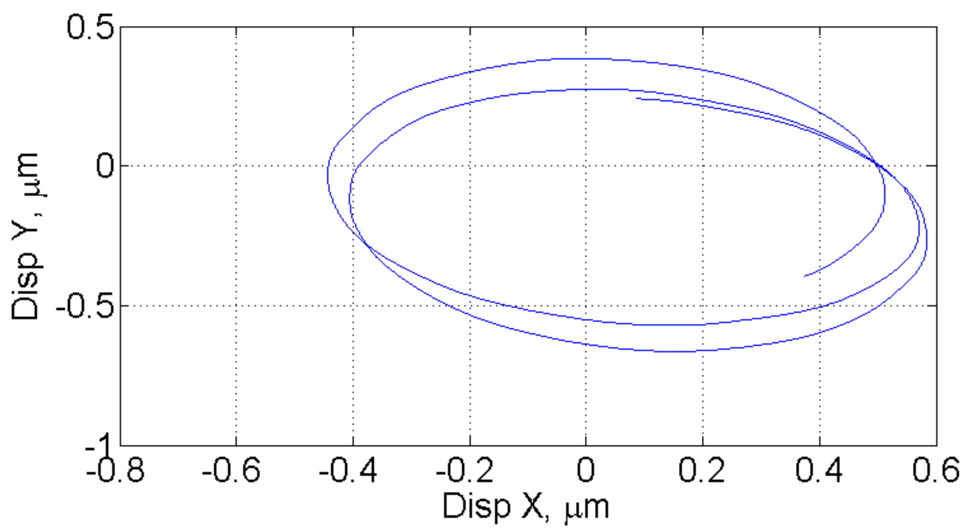

(b) X and Y displacements of pinion node with $K_a = 0$.

Figure 6.9: 3-D whirl orbit of high-speed pinion shaft and 2-D orbit of pinion node point with $K_a = 0$.

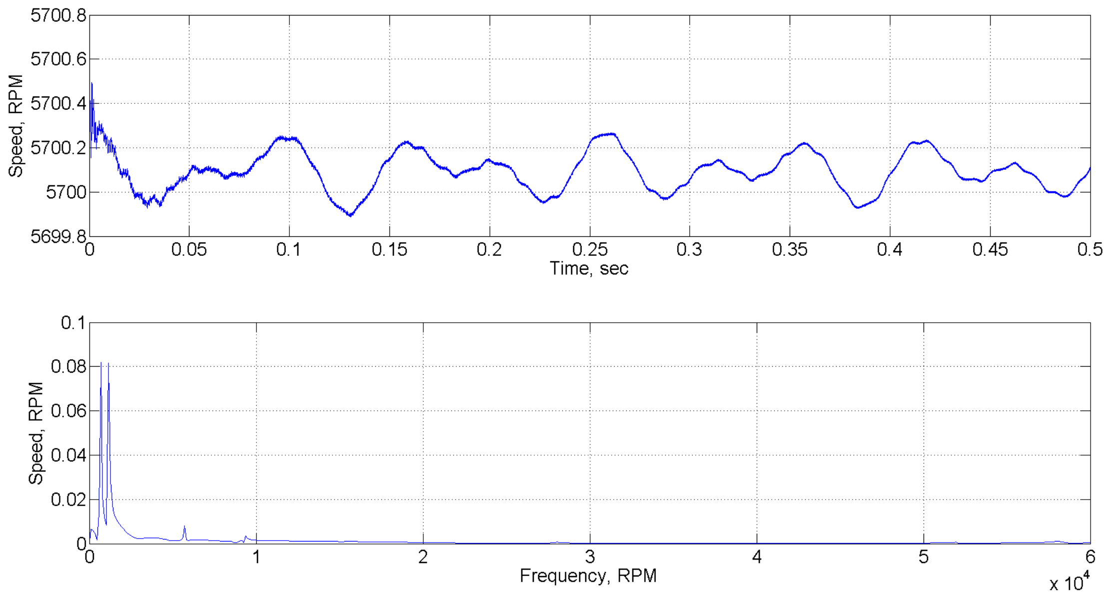

Figure 6.10: Rotational speed of HS pinion and its FFT with $K_a = 0$.

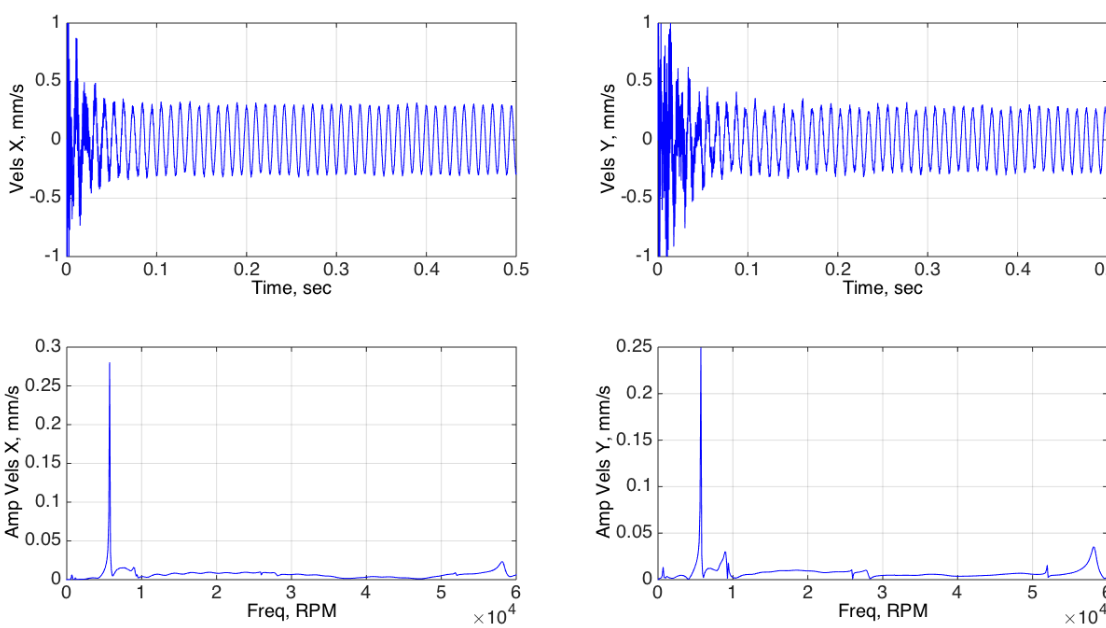

Figure 6.11: X and Y velocities of gear node with $K_a = 0$.

gear mesh excitations may be necessary to excite them. Such excitations may be expressed in the form of state-varying gear mesh stiffness, where the stiffness varies with a frequency that matches the number of gear teeth multiplied by the shaft rotational speed. Since the shaft rotational speeds vary with time, it is expected that the rectangular waveforms used to approximate the mesh stiffness variation may contain many harmonics of the shaft speed and not just the gear mesh frequency.

This subsection has explored the time transient unbalance response and gear mesh forces/moments of the power turbine compressor geared system using an assumed constant gear mesh stiffness. The results indicate that the dominant response is synchronous (1x) with operating speed although there exist initial transients that contain the 10x (57,000 RPM). Although these initial transient frequencies are consistent with the damped eigenvalue predictions presented in section 6.4.1, the fact that they attenuate quickly indicates that they are well-damped and that an additional excitation source is required. The inclusion of state-varying mesh stiffness effects is expected to provide that additional excitation source and is presented in the next subsection.

6.4.3 State-varying gear mesh effects

Previously, the gear mesh stiffness has been treated as constant and the relative displacements between the gear nodes on the low and high-speed shafts dictated the time-varying gear forces and torques. Although the synchronous component appeared to dominate the displacements, velocities, and forces, other frequency components appear and their sensitivity to additional gear mesh excitations remains to be addressed. This subsection addresses the effects of incorporating state-varying gear stiffness effects into the transient response. The excitation control may be expressed via the ratio $\frac{K_a}{K_g}$, which is the variational amplitude over the average gear mesh stiffness. Keeping the applied unbalance of 7,200 g-mm at the blind-end of the high-speed pinion fixed, the ratio $\frac{K_a}{K_g}$ was varied from 0 to 0.75 in increments of 0.25. Refer to Table 6.1 for parameters used to model the state-varying gear mesh stiffness. No backlash is included and the number of Fourier coefficients used to represent the rectangular waveforms is 5. Varying the gear mesh stiffness variational amplitude may provide insights into the sensitivity of the other frequencies that appear in the forces, displacements, and velocities.

X and Y displacement FFTs of the high-speed pinion node are generated in Figure 6.13 and illustrate the effects of raising K_a. Four noticeable frequencies are apparent: 900, 5,700, 9,000, and 57,000 CPM. While the first three frequency components appear unchanged with varying K_a, the supersynchronous 57,000 CPM noticeably increases in magnitude. This suggests that the gear mesh variation influences the sensitivity of this high frequency mode even though its frequency is neither synchronous nor gear mesh.

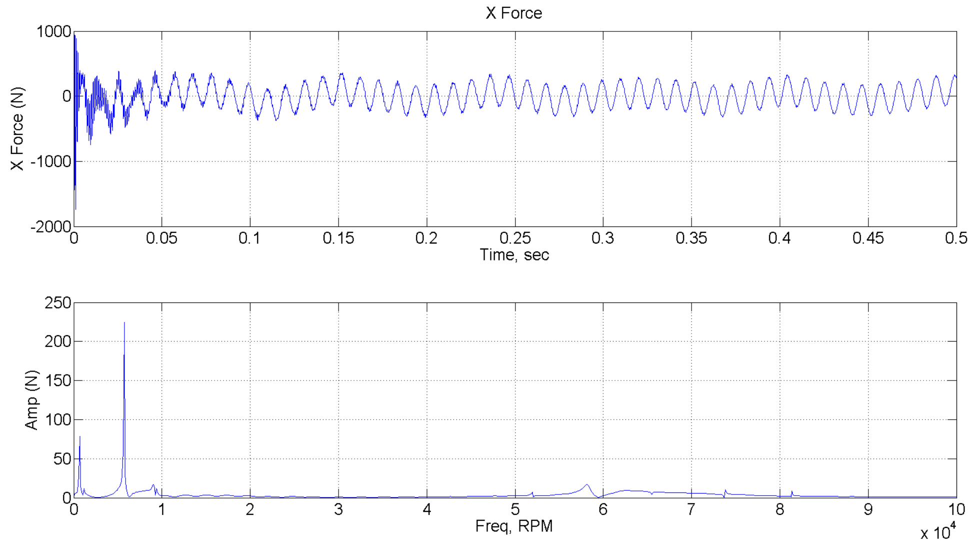

(a) HS pinion X Force with $K_a = 0$.

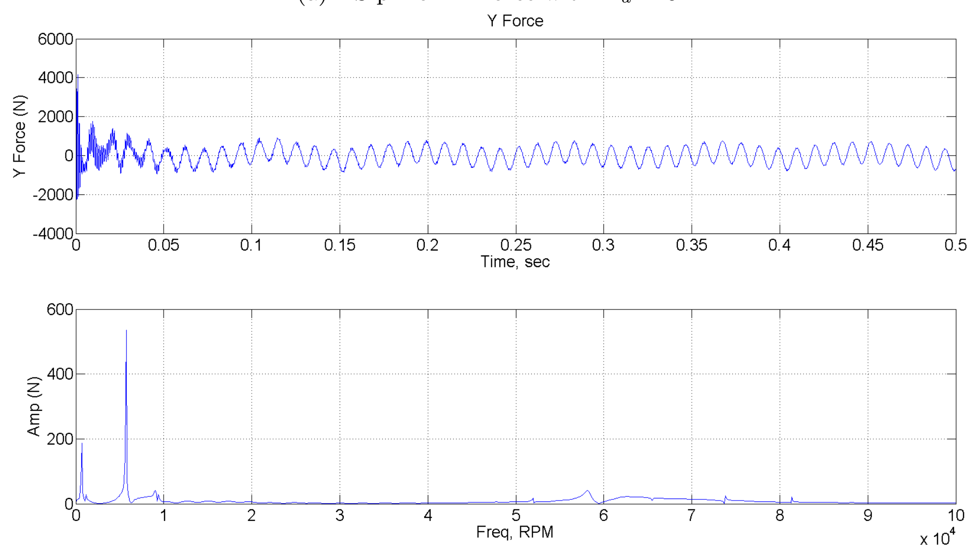

(b) HS pinion Y Force with $K_a = 0$.

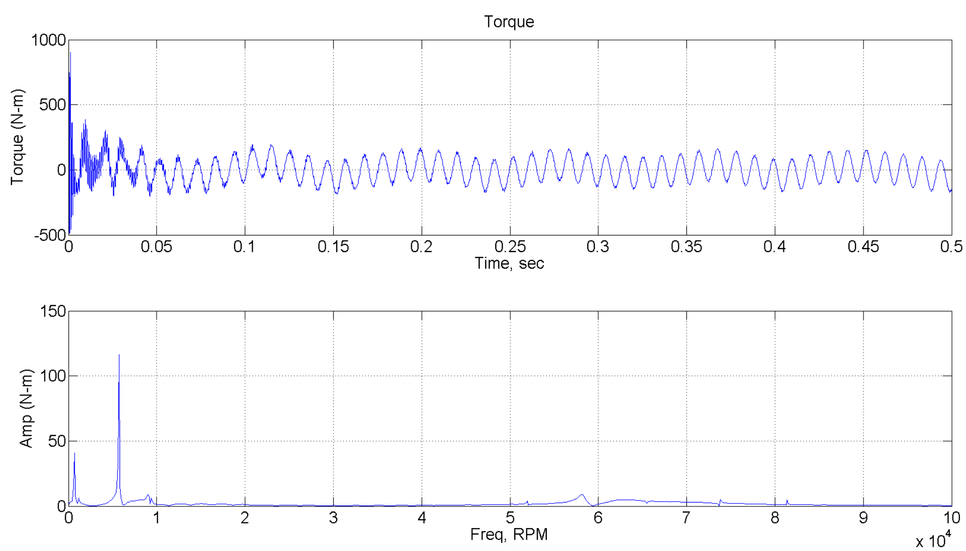

(c) HS pinion torque with $K_a = 0$.

Figure 6.12: HS pinion gear forces and torques with $K_a = 0$.

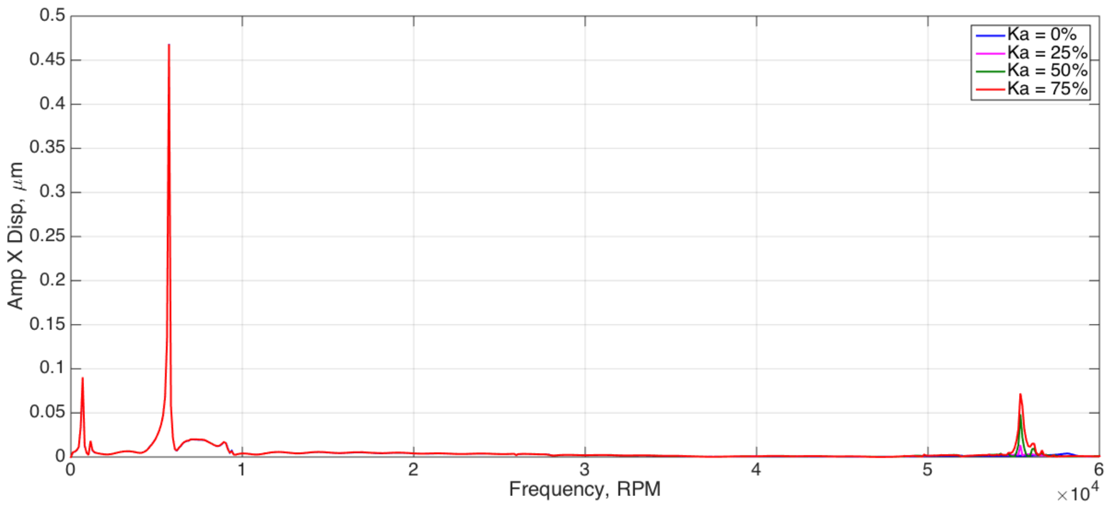

(a) X displacements with varying K_a.

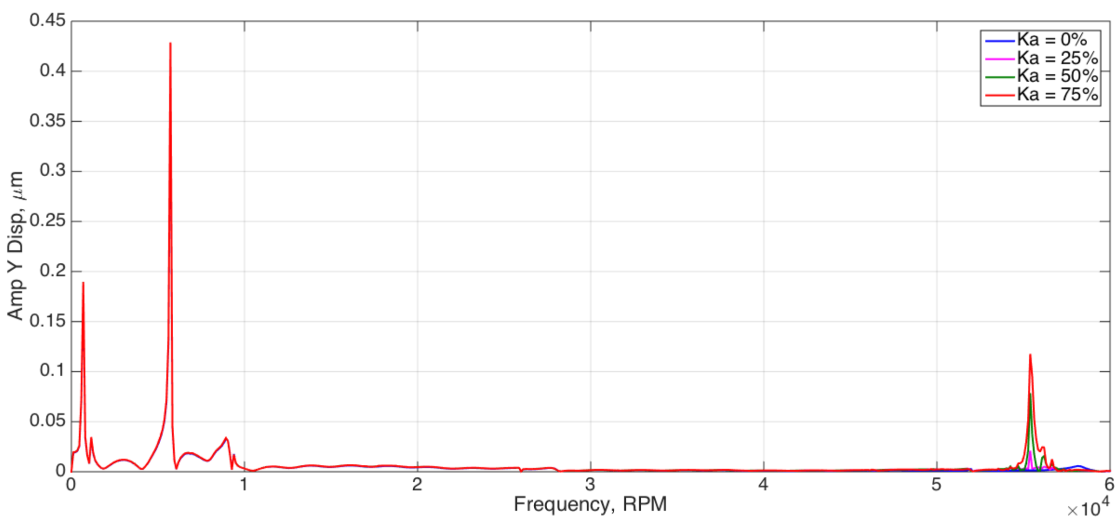

(b) Y displacements with varying K_a.

Figure 6.13: X and Y displacements with varying K_a.

A 3-D whirl representation of the X and Y displacements of the high-speed pinion shaft with $\frac{K_a}{K_g} = 0.5$ is shown in Figure 6.14. Although the general 3-D orbit of the high-speed pinion appears unchanged from the $K_a = 0$ case in Figure 6.9, a closer examination of the orbit at the pinion node displays the supersynchronous frequency as shown by the multiple orbits within one revolution. It is apparent that the size of the supersynchronous component is much smaller than that of the synchronous frequency, but the difference in relative amplitude of the modeled results in comparison with experimental data may be due to model simplification.

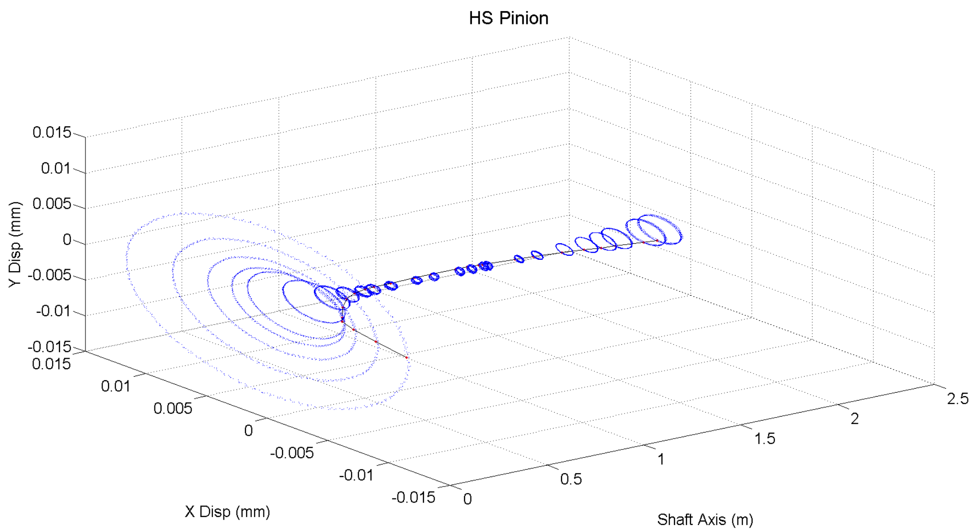

(a) 3-D whirl orbit of high-speed pinion shaft with $\frac{K_a}{K_g} = 0.5$.

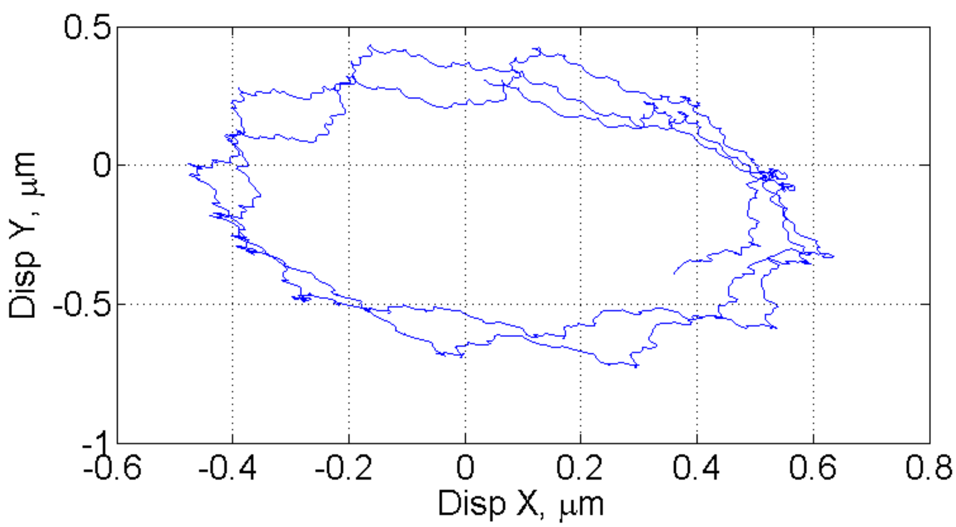

(b) X and Y displacements of pinion node with $\frac{K_a}{K_g} = 0.5$.

Figure 6.14: 3-D whirl orbit of high-speed pinion shaft and 2-D orbit of pinion node point with $\frac{K_a}{K_g} = 0.5$.

Exploring the FFTs of the high-speed pinion X and Y velocities may produce additional insights into other frequencies that may be sensitive to gear mesh stiffness variations. Figure 6.15 depicts this data and reveals several frequencies with substantial components as $\frac{K_a}{K_g}$ approaches 0.75. 57,000 CPM appears to have the largest component of vibration, but other frequencies such as 5,700, 239,000, 410,000, 680,000, and 900,000 RPM are clearly influenced as K_a is increased. These results suggest that lightly damped high frequency modes, calculated from a damped eigenvalue analysis, may be pertinent to both the initial transients and the steady-state responses because the varying gear mesh stiffness can produce the excitation frequency necessary to energize them.

Figure 6.16 shows the X and Y velocities zoomed between 0 and 60,000 RPM, in order to to explore the sensitivity of the 57,000 CPM response to varying K_a. Similarly to the X and Y displacement results at the high-speed pinion node, the X and Y synchronous response with the velocities was unaffected with changes in K_a. The increase in the magnitude of the velocities at 57,000 RPM is also nonlinear with respect to $\frac{K_a}{K_g}$. For example, doubling the ratio from 0.25 to 0.50 produced Y velocity changes from approxmately 0.12 to 0.45 $\frac{mm}{s}$.

Understanding the frequency characteristics of the gear mesh stiffness is crucial to understanding the gear mesh forces and torques. FFTs of the gear mesh stiffness are shown in Figure 6.17 and display the numerous excitation frequencies inherent in this model. The most prominent frequency is at 239,400 RPM, which is the gear mesh frequency (GMF) but there are several others that contain substantial contributions to the gear mesh stiffness. Zooming in towards the frequency range from 0 to 60,000 CPM reveals the direct dependency of the 57,000 CPM excitation on the ratio $\frac{K_a}{K_g}$. All other frequencies below 10x of the pinion have very low amplitudes, which indicates that gear mesh stiffness fluctuations have a large effect on the reported 10x vibration.

Figures 6.18 and 6.19 show the FFTs of the X and Y forces and torque of the high-speed pinion acting on the shaft while observing the effects of varying $\frac{K_a}{K_g}$. The first three plots show the wide range of excitation frequencies that contribute to the forces and the range extends as far as 2×10^6 CPM. It is apparent that as K_a increases, not only do the frequency components increase in amplitude but more frequencies enter the forces and torque spectrum as well. The most prominent frequency component for the X and Y forces and torque is at 57,000 CPM, which matches what was observed in the field. The second largest amplitude component of force and torque occurs at 663,000 CPM, which is more than 100x of pinion speed. The synchronous force and torque component appears to be the 3^{rd} largest and the magnitude noticeably decreases for $\frac{K_a}{K_g} > 0$.

Examining the FFT of the forces and torques between 0 and $60,000$ CPM reveals more details regarding the effects of increasing $\frac{K_a}{K_g}$. Excluding variational gear mesh stiffness produces a zero force component at

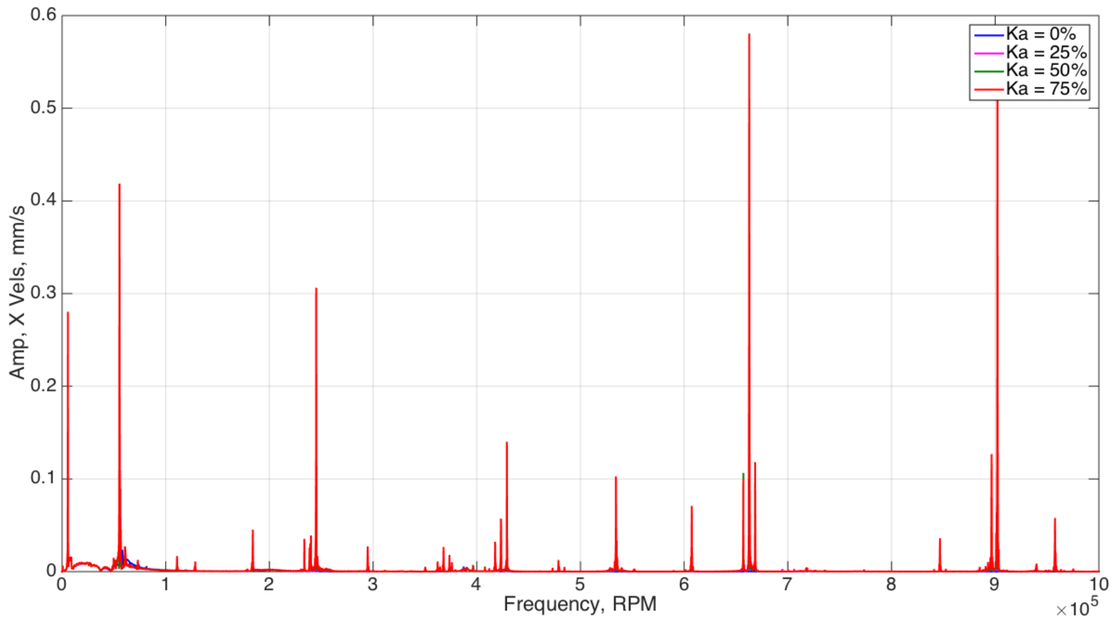

(a) X velocities with varying K_a.

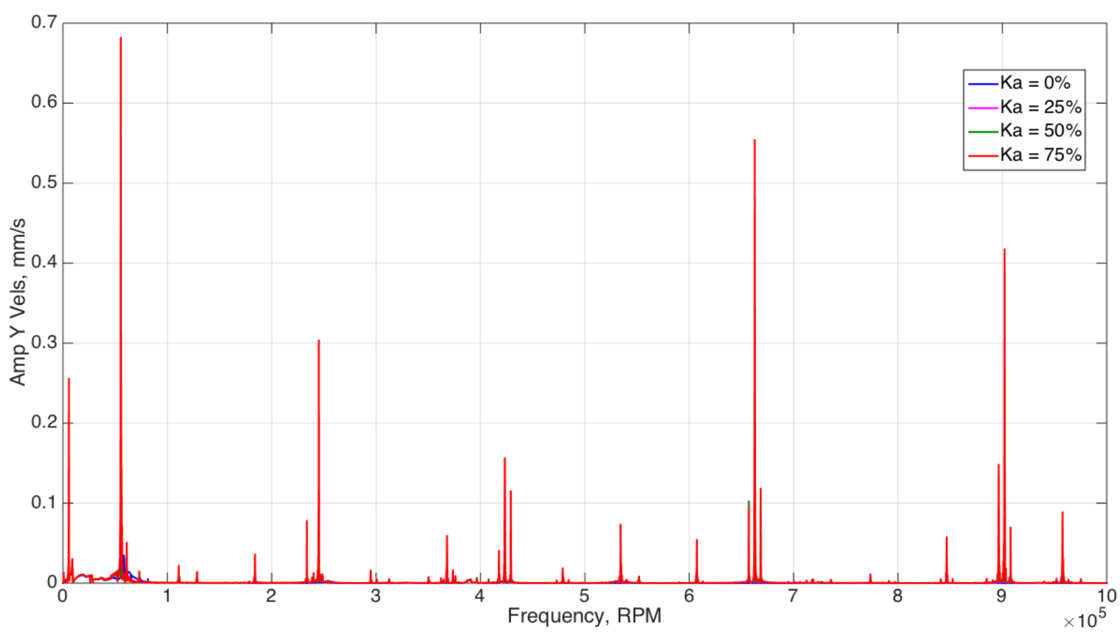

(b) Y velocities with varying K_a.

Figure 6.15: X and Y velocities with varying K_a.

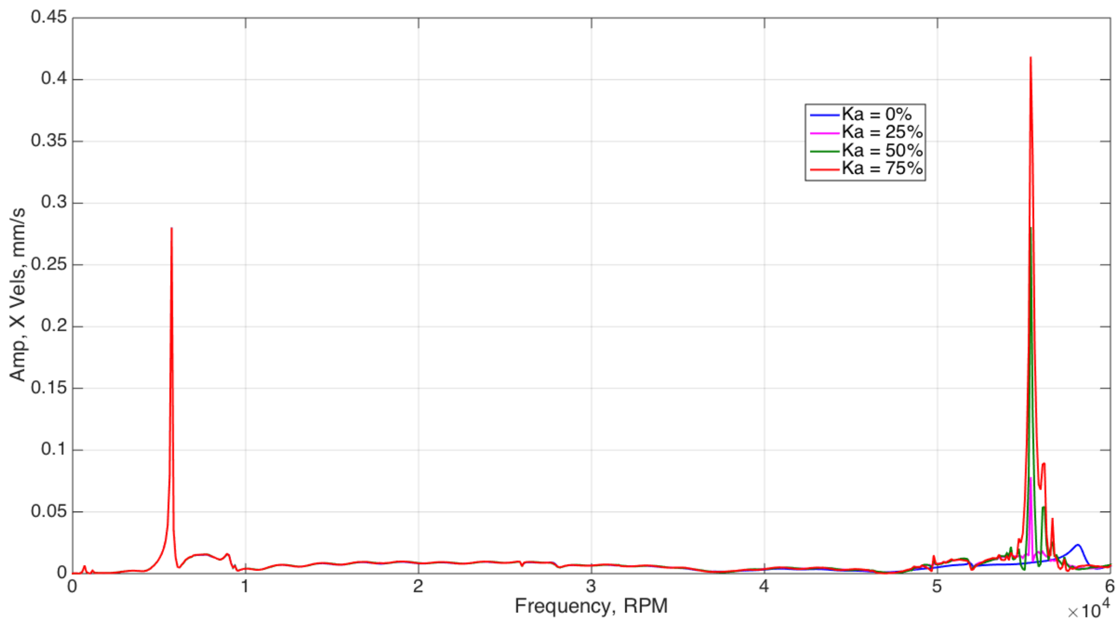

(a) X velocities with varying K_a.

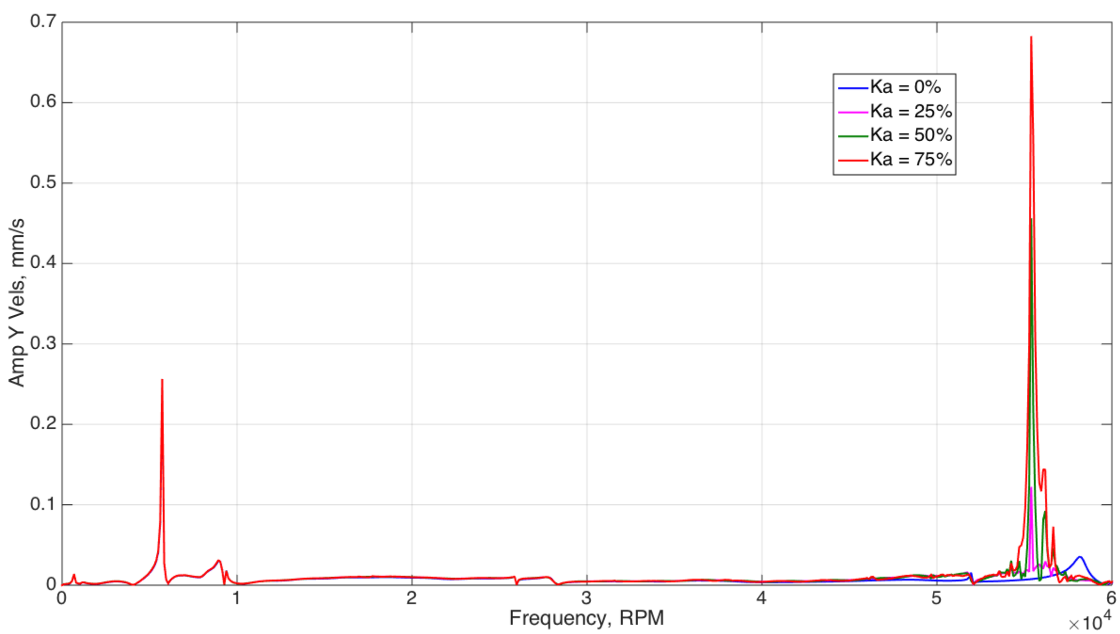

(b) Y velocities with varying K_a.

Figure 6.16: X and Y velocities with varying K_a.

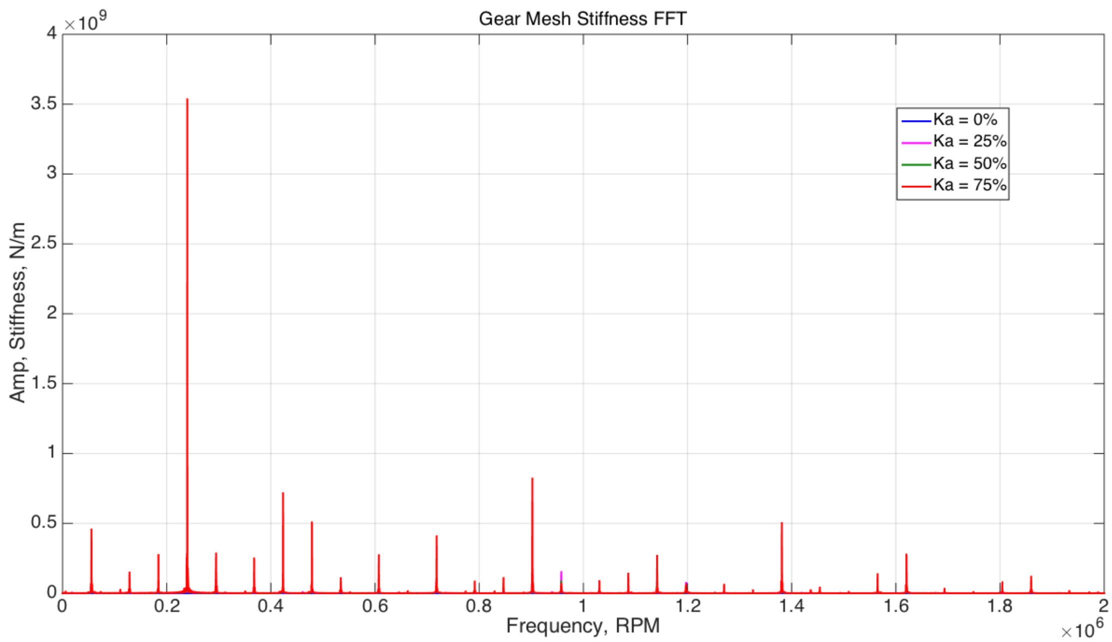

(a) Zoomed out view of gear mesh stiffness FFT with varying K_a.

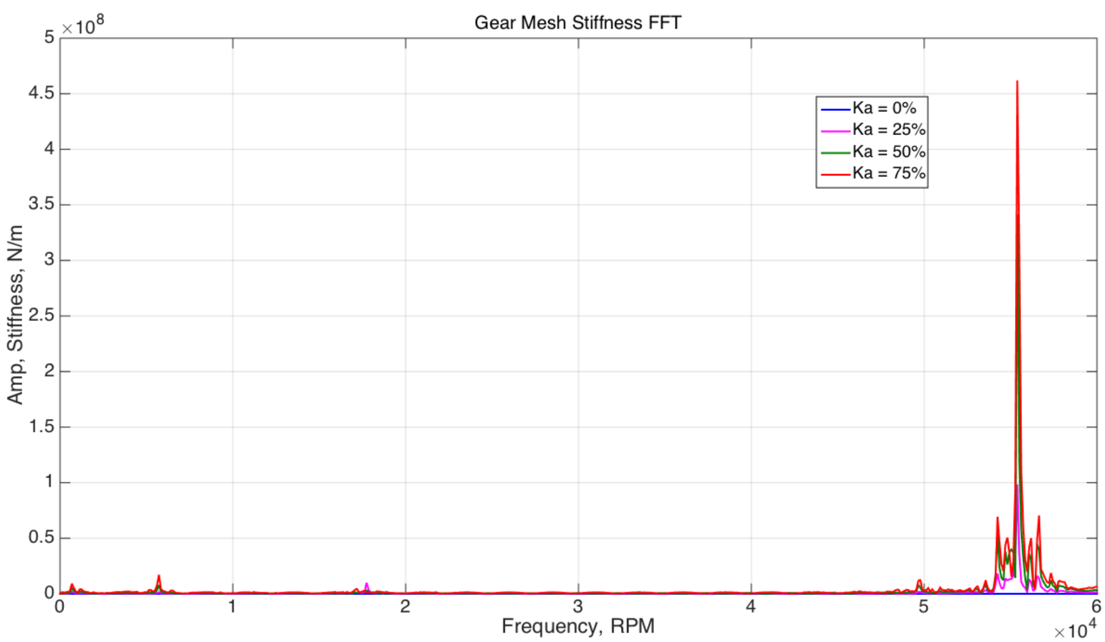

(b) Zoomed in view of gear mesh stiffness FFT with varying K_a.

Figure 6.17: Gear mesh stiffness FFT with varying K_a.

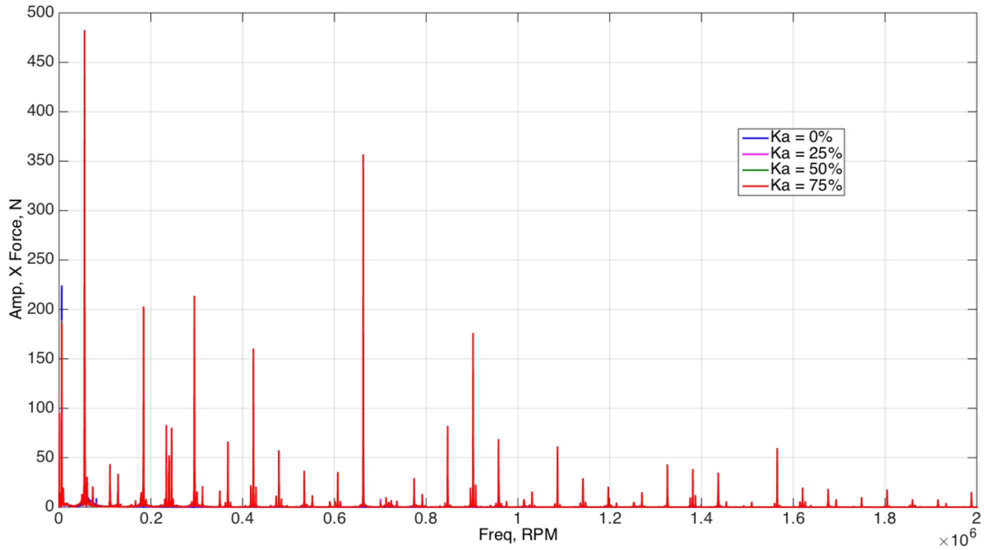

(a) Zoomed out view of HS pinion X force FFT with varying K_a.

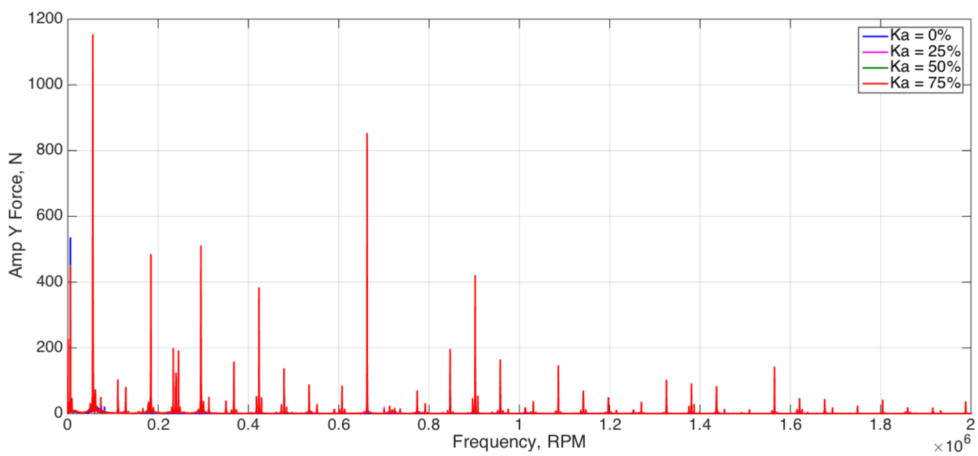

(b) Zoomed out view of HS pinion Y force FFT with varying K_a.

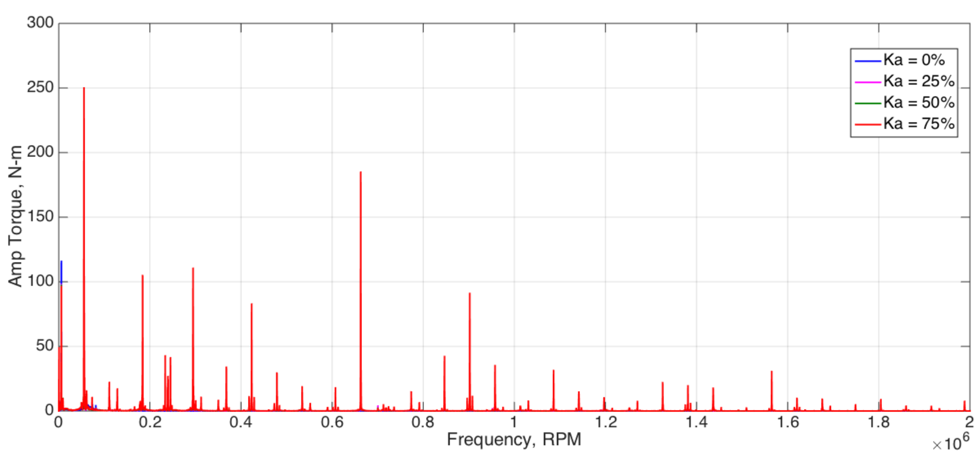

(c) Zoomed out view of HS pinion Torque FFT with varying K_a.

Figure 6.18: HS pinion forces and torque FFT with varying K_a.

the problematic 57,000 CPM frequency. As $\frac{K_a}{K_g}$ increases, the magnitude of the 10x component of force and torque increases nonlinearly. At $K_a = 25\%$, the Y magnitude of force is 200 N, but at $K_a = 50\%$, it increases to almost 800 N. These results illustrate that the 57,000 CPM force and torque component is very sensitive to gear mesh stiffness variation and that the gear mesh variation is a potential excitation source to produce the results that have been observed in the field. Although the damped eigenvalue analysis confirmed the existence of plausible modes that could match what was observed in the field, a transient analysis with geared rotor dynamics that includes mesh variational stiffness is able to determine potential excitation sources which could energize the mode of interest. An in-depth analysis of the gear force-velocity relationships that contribute to whirl promotion help explain the reason that the 57,000 CPM excitation contributes more to the vibration than the other high-frequency components.

6.5 Whirl energy considerations

The equivalent whirl promoting power for the bearings, high-speed pinion, flexible coupling, and modulated unbalance force may be computed for all t via Equation 6.1. It sums the product of the instantaneous forces and velocities to calculate each component's effective contribution to whirl promotion. For values of t when $P > 0$, the component is exerting forces on the shaft that promote whirl energy. If $P < 0$, then the component is dissipating whirl energy from the shaft. Because the bearing stiffness and damping coefficients are generalized to include cross-coupled terms, the equation of their X and Y forces are governed by Equation 6.2. Their contribution to whirl promotion is expected to be small since their dynamic coefficients were computed for tilting pad journal bearings. The sum of all of the contributions of whirl promoting power are used to evaluate the net gain in whirl energy over the elapsed time and depend on the force velocity relationships for the bearings, high-speed pinion, flexible coupling, and the modulated unbalance force.

$$P = F_x\dot{x} + F_y\dot{y} \tag{6.1}$$

$$\begin{aligned} F_{xbrg} &= -K_{xx}\Delta x - K_{xy}\Delta y - C_{xx}\Delta\dot{x} - C_{xy}\Delta\dot{y} \\ F_{ybrg} &= -K_{yy}\Delta y - K_{yx}\Delta x - C_{yy}\Delta\dot{y} - C_{yx}\Delta\dot{x} \end{aligned} \tag{6.2}$$

Although it is evident that the excitation of lateral mode 55, as shown in Figure 6.3, is sensitive to the variation gear mesh stiffness K_a, it is important to understand why this variable provides more energy towards that mode. Exploring how each of the components on the the high-speed pinion contribute to whirl promoting energy may address this consideration. The components of interest are the unbalance force, bearings, gear

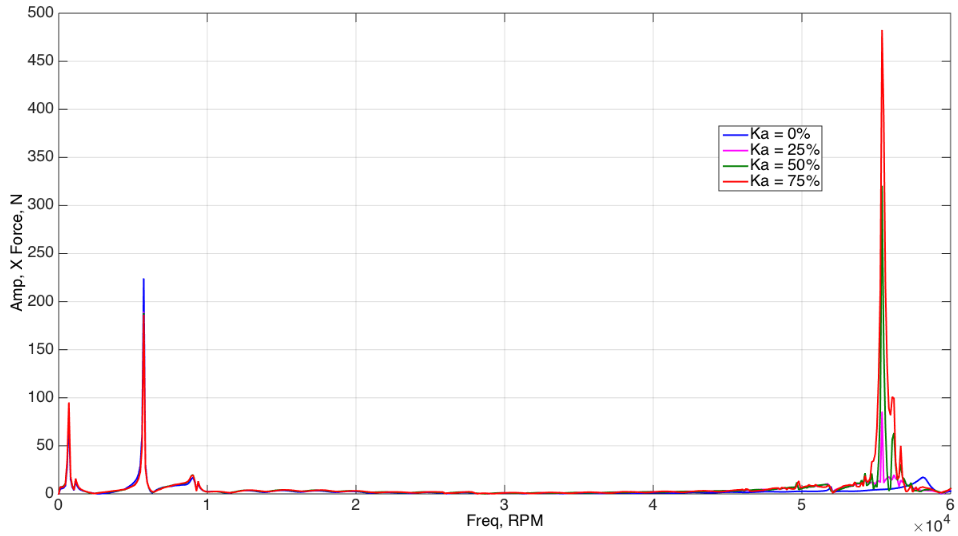

(a) Zoomed in view of HS pinion X force FFT with varying K_a.

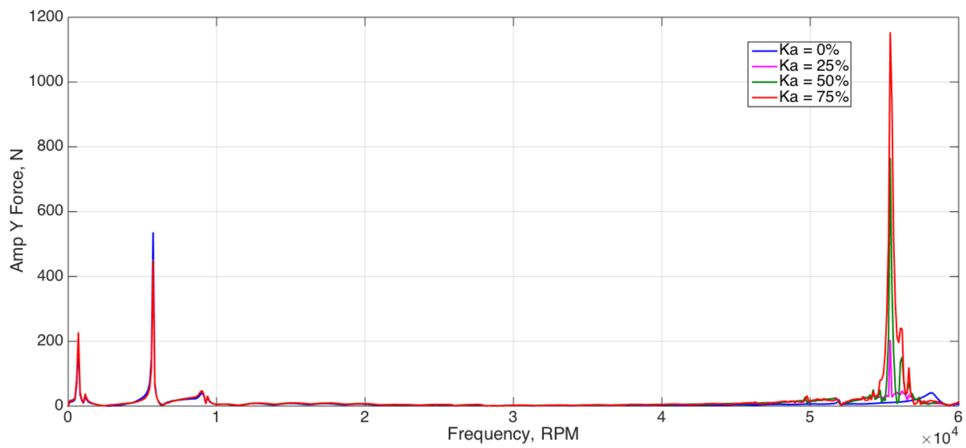

(b) Zoomed in view of HS pinion Y force FFT with varying K_a.

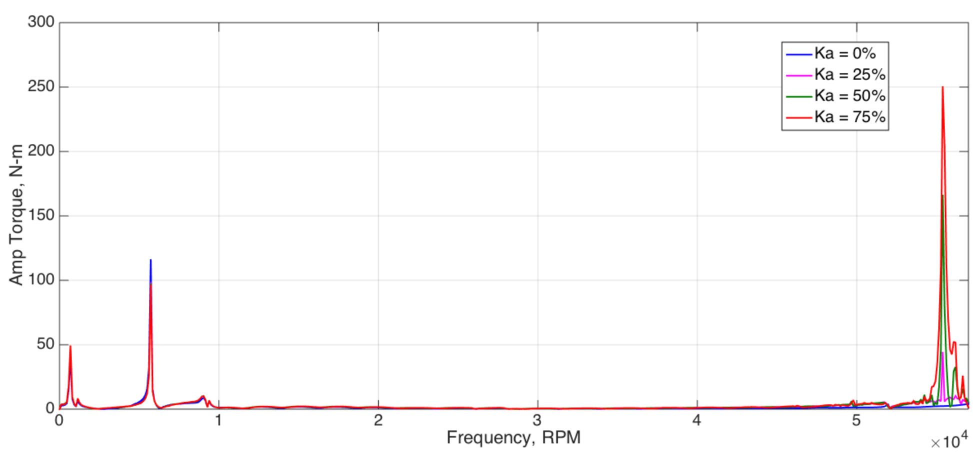

(c) Zoomed in view of HS pinion Torque FFT with varying K_a.

Figure 6.19: HS pinion forces and torque FFT with varying K_a.

mesh, and the flexible coupling and their whirl promoting contributions are determined for $\frac{K_a}{K_g} = 0$ and 0.5. The differences between the whirl promoting power of these components is illustrated in Figure 6.20.

When K_a is zero, the contributions of the bearings, high-speed pinion, and the flexible coupling become very small in comparison to the influence of the unbalance force. The bearings provide very little dissipation and yet the high-speed pinion shaft remains in a stable orbit because of the oscillating contribution of the unbalance force to the promotion of whirl. Cross-coupled stiffness effects in the bearing oil film contribute to whirl promotion and certainly counteract the damping forces. Furthermore, the unbalance whirl power maintains a very consistent frequency that matches the rotational speed of the high-speed pinion. Although the influence of the other components is small, it is important to assess the relationship between the X and Y force and velocity relationships to better understand the physics for the $K_a = 0$ case.

The whirl promoting power contributions of the components for the $\frac{K_a}{K_g} = 0.5$ case are very different. Although the amplitude of whirl power for the unbalance force is unchanged, the influences of the flexible coupling and the high-speed pinion are much larger than the $K_a = 0$ case. In fact, the flexible coupling power amplitude is nearly equal to and in phase with that of the unbalance force. The high-speed pinion also has a more noticeable effect on the dynamics since not only does it have a larger amplitude contribution to whirl power but that it contributes to the high frequency oscillations. Among these high frequency oscillations is the $57,000$ CPM that was observed in the field. In addition, although the high frequency oscillations primarily begin before 0.1 seconds, their effects remain in the steady-state response. The bearings provide very little power dissipation. As with the $K_a = 0$ case, investigating the X and Y force and velocity relationships will provide greater insights towards how these individual components affect whirl power growth or dissipation.

X directional force and velocity at the high-speed pinion for $\frac{K_a}{K_g} = 0$ and 0.5 are shown in Figure 6.21. The differences in the magnitudes for force and velocity for both K_a cases are immediately apparent as the steady-state X force amplitude for $\frac{K_a}{K_g} = 0$ is approximately 300 N, while the $\frac{K_a}{K_g} = 0.5$ one is closer to 1,500 N. The increase of the pinion X velocity for the larger K_a case is even greater than that of the force. Although there are multiple frequencies in the X force and velocities of both K_a cases, the phase difference between the high frequency peaks in the $\frac{K_a}{K_g} = 0$ case is approximately $180°$, which implies that only the synchronous frequency could experience whirl amplification as evidenced in the displacements and not the 10x that was reported in the field.

The high frequency dynamics of the $\frac{K_a}{K_g} = 0.5$ case are quite different as shown in Figure 6.22. It is important to note that the high-speed pinion X direction force and velocity are in phase, which suggests that the gear mesh contributes to the high frequency whirl in addition to the synchronous component. Exploration of the Y direction force and velocity of the gear may provide additional insights.

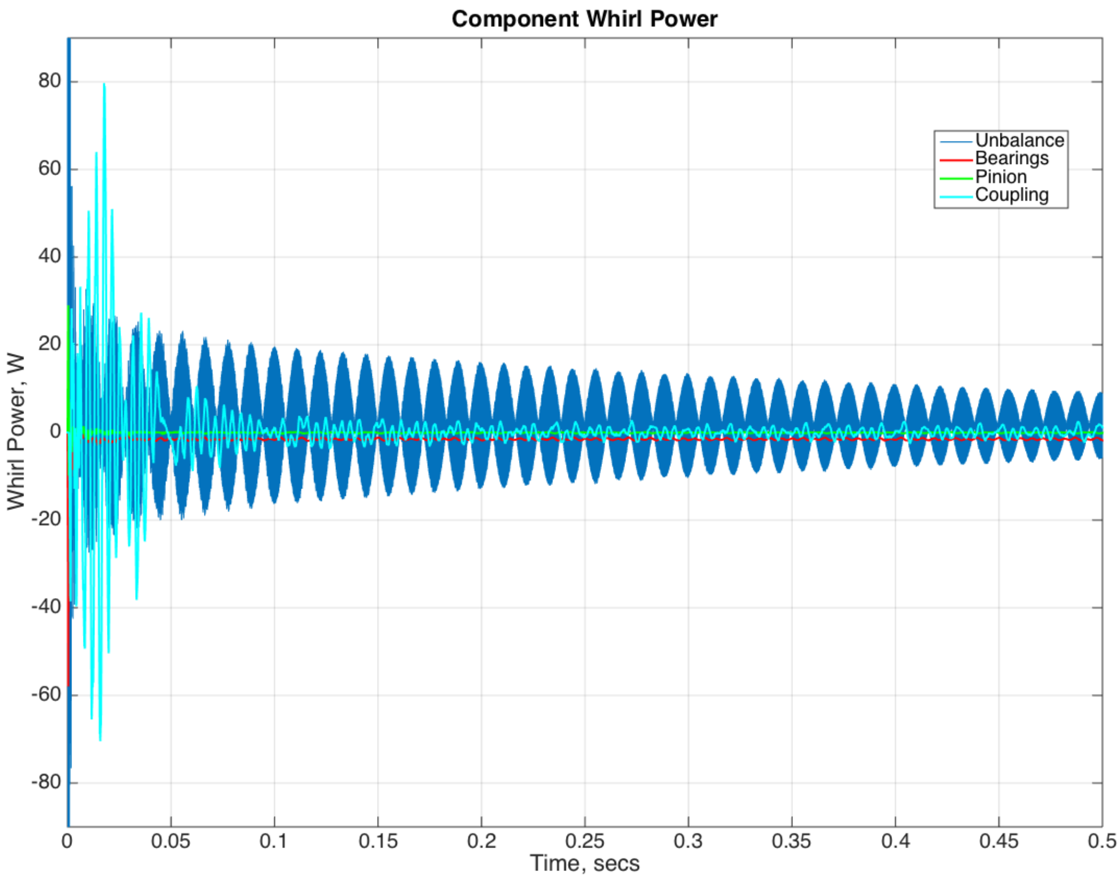

(a) Whirl power with $\frac{K_a}{K_g} = 0$.

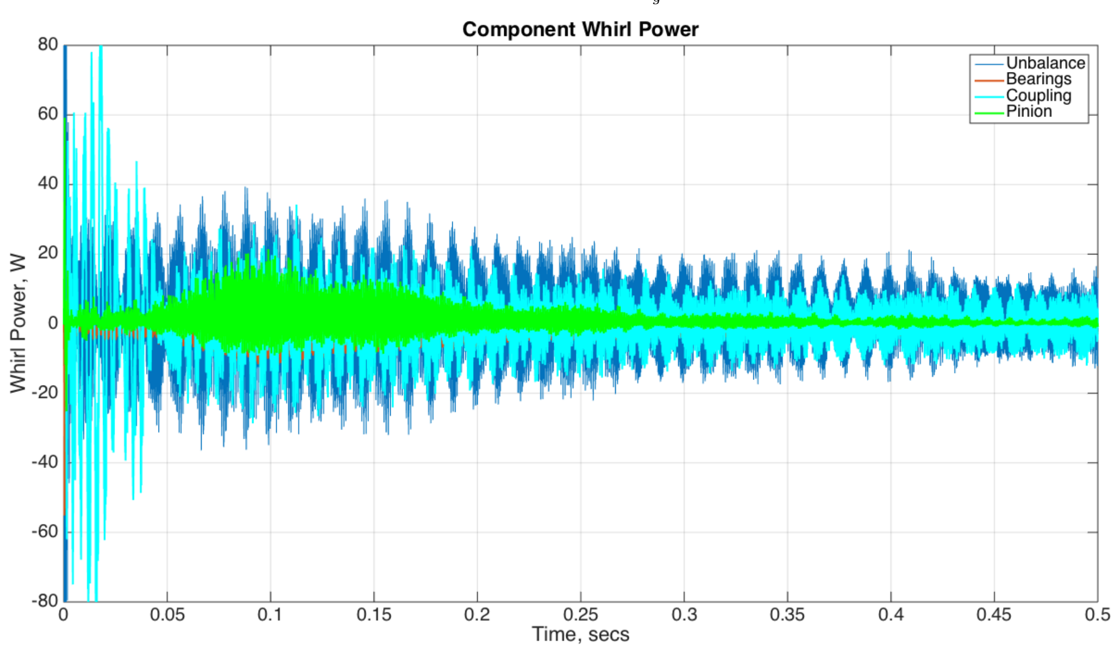

(b) Whirl power with $\frac{K_a}{K_g} = 0.5$.

Figure 6.20: Whirl power contributions with $\frac{K_a}{K_g} = 0$ and 0.5.

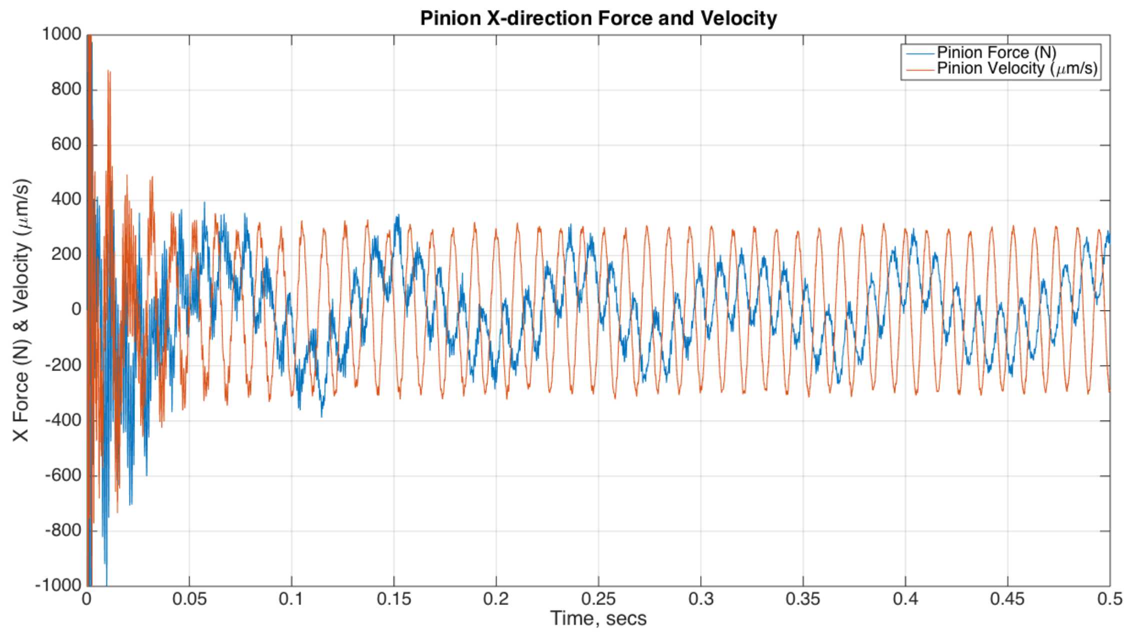

(a) Pinion X force and velocity with $\frac{K_a}{K_g} = 0$.

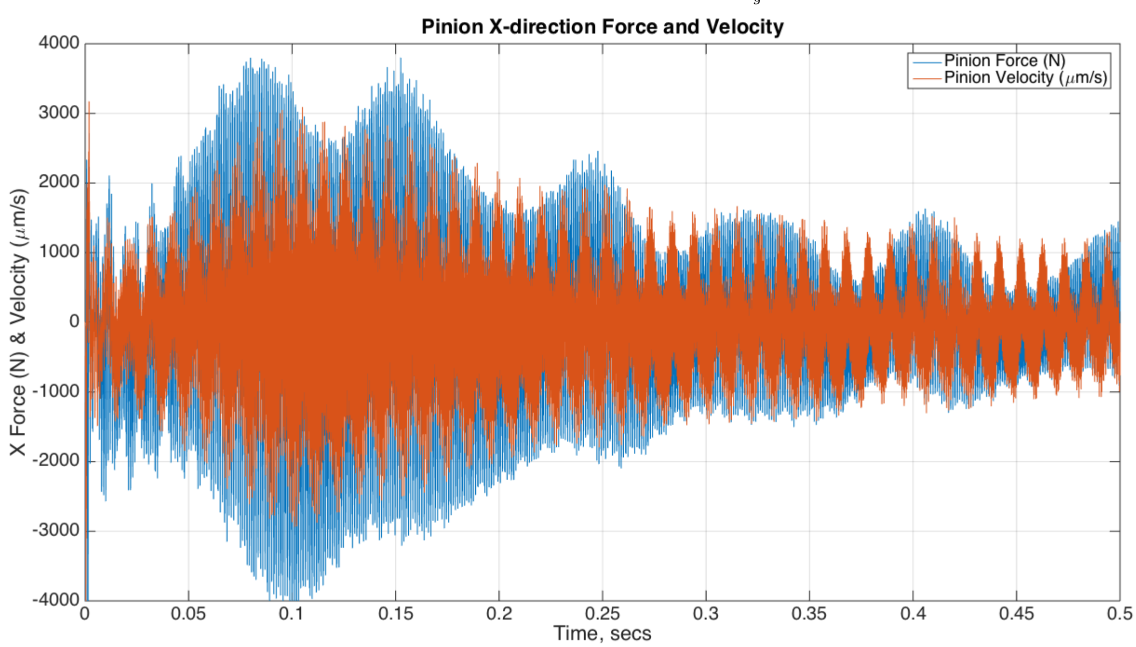

(b) Pinion X force and velocity with $\frac{K_a}{K_g} = 0.5$.

Figure 6.21: X-direction force and velocity of high-speed pinion with $\frac{K_a}{K_g} = 0$ and 0.5.

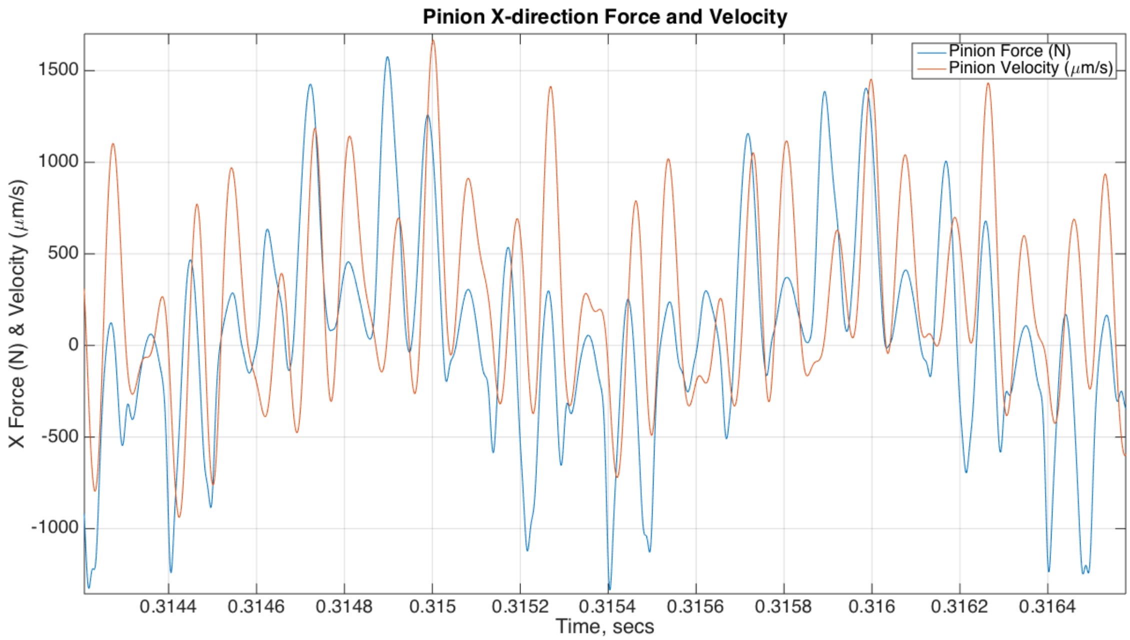

Figure 6.22: Zoomed in view of X force and velocity of pinion for $\frac{K_a}{K_g} = 0.5$.

Y force and velocity dynamics of the high-speed pinion are shown in Figure 6.23 for $\frac{K_a}{K_g} = 0$ and 0.5 respectively. Immediately apparent are the larger magnitudes of the forces and velocities in the Y direction in contrast to those in the X direction. Similar to the X direction, the velocity and force are nearly 180° out of phase with respect to the high frequency behavior for $\frac{K_a}{K_g} = 0$. This implies that the high frequency content of the Y force does not amplify the high frequency whirl amplitude. Only the synchronous content of the force contributes to whirl amplification. The Y direction force velocity relationship with $\frac{K_a}{K_g} = 0.5$ indicates that both the force and velocity oscillate at multiple frequencies and have much larger amplitudes than those with $\frac{K_a}{K_g} = 0$.

Zooming in on the high-speed pinion Y direction force and velocity dynamics provides more details on how the $57,000$ RPM vibration becomes more prominent with $\frac{K_a}{K_g} = 0.5$ as shown in Figure 6.24. Not only do the force and velocity share the same frequency in oscillations but they are also nearly in phase with one another. This suggests that the high-speed pinion force velocity dynamics encourage the growth of the $57,000$ RPM (10x) vibration.

6.6 Conclusions

This chapter investigated and explored a high amplitude vibration problem on a geared power turbine compressor train. A supersynchronous vibration problem was detected by proximity probes along the

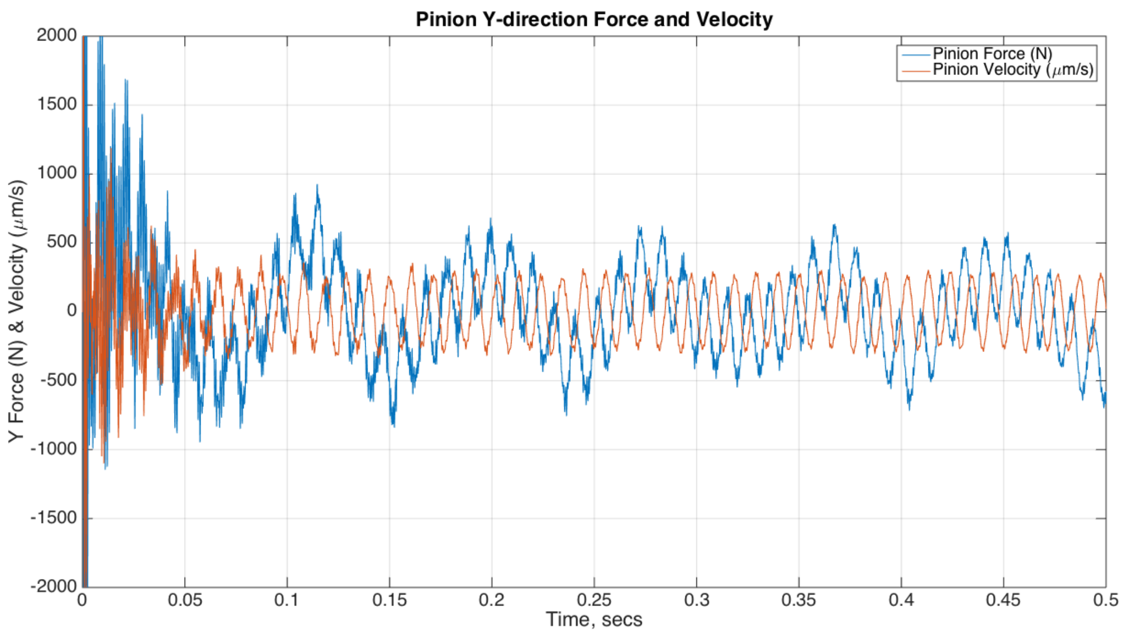

(a) Pinion Y force and velocity with $\frac{K_a}{K_g} = 0$.

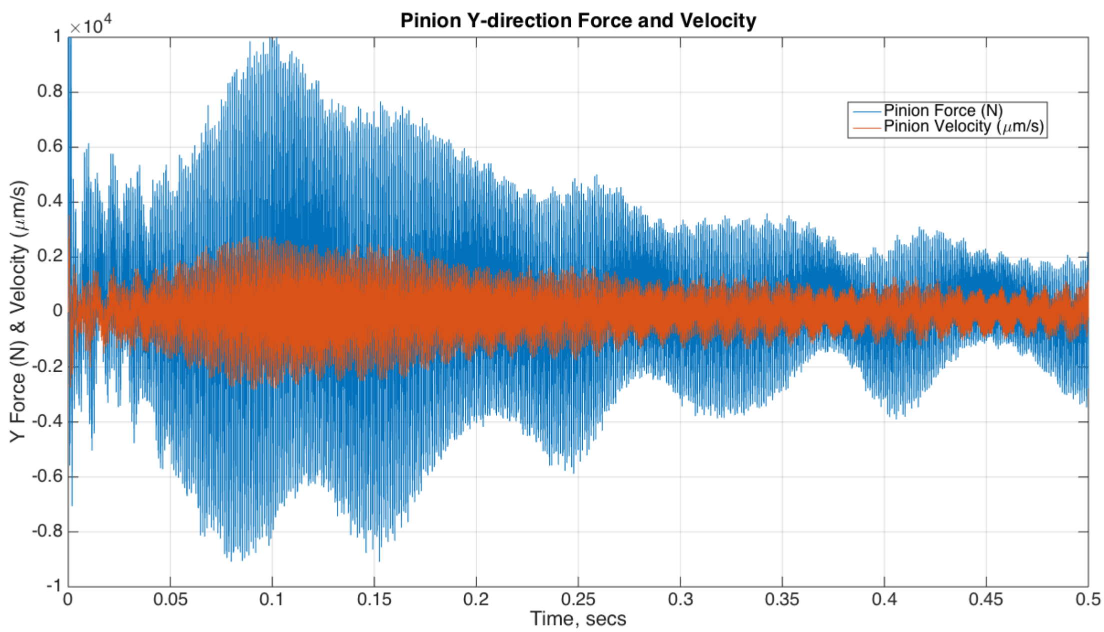

(b) Pinion Y force and velocity with $\frac{K_a}{K_g} = 0.5$.

Figure 6.23: Y-direction force and velocity of high-speed pinion with $\frac{K_a}{K_g} = 0$ and 0.5.

Figure 6.24: Zoomed in view of Y force and velocity of pinion for $\frac{K_a}{K_g} = 0.5$.

blind-end of the high-speed pinion and this analysis is a continuation of the work done by Cloud et al [69]. Unlike typical supersynchronous gearbox vibration problems that occur at gear mesh frequency (GMF), the problematic vibration existed at only 10x, where x is the operating speed of the high-speed pinion. In contrast, the GMF would have been at 42x. Cloud et al suspect that the problem originates from the excitation of two different modes that occur near 10x of the pinion speed. After conducting a damped eigenvalue analysis, they discovered several modes that exist near the 10x frequency and concluded that the problematic mode could involve the 5^{th} pinion mode or a lateral-torsional coupled mode involving similar lateral motions as the 5^{th} pinion mode. Their damped eigenvalue analysis with the Campbell diagram reasonably predicted the problematic mode, and they used those results to deduce that gear mesh stiffness excitation could be the root cause of the problem. A transient analysis with the capability of modeling state-varying gear mesh stiffness, as shown in this chapter, became necessary to explore the problem further.

As confirmation that the model used in this analysis could be comparable to Cloud et al's investigation, a damped eigenvalue analysis was conducted in this case study that revealed the presence of several modes around the 10x pinion speed. A sensitivity analysis of the damped natural frequencies using fewer nodes in the finite element model confirmed that several of the modes in the 10x frequency range remained unaffected. This would allow the transient model to be run with less computing time and with reassurance that model fidelity had not been compromised.

An unbalance magnitude of 7,200 g-mm was applied to the blind-end side of the high-speed pinion shaft in accordance with the expected force distribution needed to energize the problematic mode of interest. The unbalance magnitude was chosen in accordance with API 617 standards, which uses Equation 4.1. Allowing the simulation to run to $t = 0.5$ seconds with a simulation time step increment of 1×10^{-6} seconds proved to be sufficiently small to capture the dynamics. Results were obtained for four different values of $\frac{K_a}{K_g}$ to test whether variational gear mesh stiffness could be a potential source of excitation to excite the 10x mode. $\frac{K_a}{K_g}$ was studied for a range from 0 to 0.75 in increments of 0.25. The X and Y displacements, velocities, forces, torque, and gear mesh stiffness were computed for each of the four $\frac{K_a}{K_g}$ cases and presented in both time and frequency domains.

Prior to including state-varying mesh stiffness (i.e. $K_a = 0$), the results showed no supersynchronous amplification mechanism. The relative velocities contain the supersynchronous content only during the initial transients and not during steady-state. This suggests that additional excitation mechanisms, such as state-varying gear mesh stiffness, are needed to excite the problematic modes.

Including variational gear mesh stiffness produced the necessary excitation that is consistent with what was reported in the field. X and Y displacement FFTs with varying K_a illustrate that the synchronous and subsynchronous vibrations are insensitive to K_a, but the 10x frequency becomes more prominent with increasing K_a in the steady-state results. Observing the velocities and gear forces and torque reveal the presence of other superharmonics beyond the 10x that are energized by increasing K_a. In particular are prominent excitations and responses at 239,400, 670,000, and 900,000 RPM among others, but only the 10x (57,000 RPM) is energized in the displacement FFTs. It is because the 10x modes are initially energized by the gear mesh variational stiffness such that the gear forces and torque retain that frequency component. This leads to that component's continued excitement in the displacements for future time steps. The $K_a = 0$ case reveals that the 10x component is only present at the very start and quickly dampens out because there is no gear mesh variation to sustain it.

Analyzing the forces and velocities for each component acting on the high-speed pinion shaft from an energy perspective helps characterize how power is being distributed and how it adds to or detracts from shaft whirl. This may be achieved by multiplying the instantaneous X and Y forces and velocities for each component at each time step. Instantaneous whirl promoting power is recorded and plotted with time for unbalance force, bearings, flexible coupling, and the pinion at both $\frac{K_a}{K_g} = 0$ and 0.5. Results indicate that increasing the gear mesh variation to $\frac{K_a}{K_g} = 0.5$ produced substantially larger contributions to shaft whirl from the flexible coupling and the high-speed pinion. Although the magnitude of the whirl contribution of the unbalance force remained unchanged, a noticeable increase in its frequency is present and only appears during and after the pinion and coupling become more active.

Time series plots of the X and Y forces and velocities for the high-speed pinion are presented for both

$\frac{K_a}{K_g} = 0$ and 0.5. For $\frac{K_a}{K_g} = 0$, the peaks between pinion forces and velocities in both X and Y directions appear to be nearly 180° out of phase, which suggests that the high-speed pinion dynamics do not promote shaft whirl. In contrast, the $\frac{K_a}{K_g} = 0.5$ case shows that the high-frequency peaks of the forces and velocities for the X and Y components are mostly in phase, which suggest that the high-speed pinion promotes whirl at 57,000 RPM.

This case study presents an opportunity to validate the numerical methods outlined in Chapter 3 of this dissertation. Although there have been several instances in which this particular high amplitude vibration problem in gearboxes has appeared, the motivation to better understand the physics has typically ended with the identification of a lightly damped mode that matches the observed frequency. While this information is important because it provides the rotor dynamicist with potential redesign ideas, it is unable to identify the root cause of the excitation. Benefits from either successfully redesigning the shaft or bearings typically result in either shifting the frequency of the problematic mode away from the excitation source or producing better modal damping or both. In the case of excitations such as that presented here, producing greater modal damping is a better solution because the initial excitation source gradually locks on to the damped natural frequency as is evident in the results from this study.

Furthermore, no other simulation tool is known to exist by the author which combines the shaft dynamics with those at the gear mesh without going into complicated and computationally-intensive 3-D finite element modeling. Results from this chapter confirm that the gear mesh stiffness variation is a crucial component to the excitement of the 57,000 RPM high-speed pinion modes that was observed in the field. The primary difference between simulation and field results involves the amplitude of the vibration. While the simulation predicted vibration amplitudes less than 1 μm, actual field results reached vibration amplitudes between 20 and 30 μm. Such a discrepancy is likely the result of several simplifications made to the shaft finite element model of the high and low speed pinion and bull gear shafts that may have made the model less sensitive to the gear mesh stiffness variation. Potential future work would involve tweaking the detail of the finite element model to see if the sensitivity of the gearbox model to the gear mesh stiffness variation could increase. It is also recommended that, in future work, these time-transient analyses be conducted using the full coefficients for the tilting pad bearings, since use of full coefficients allows the bearings' stiffness and damping properties to vary as a function of the whirl frequency. Pivot flexibility is also found to be an important characteristic because of its increasing effects at higher frequencies, as demonstrated in the steady-state damped eigenvalue analyses reported by Cloud et al [69]. Relative to their synchronous magnitudes, stiffness increases and damping decreases at the supersynchronous frequencies involved with the vibration problem. The sensitivity to supersynchronous whirl frequencies inherent in the modeling of tilt pad rotation and pivot flexure could result in greater participation of the modes near 57,000 RPM, which would be consistent with what was reported in the field.

Chapter 7

Conclusions

Validation for the methods proposed in Chapter 3 are shown via results in Chapters 4 and 6 and are fundamental to the conclusions drawn in this chapter. Conclusions pertaining to the phenomena studied in Chapter 5 may also be explained with physical intuition.

7.1 Validation of damped eigenvalue solver with constant gear mesh stiffness K_g

7.1.1 Discussion of methods

Section 3.1 provides the basis for gear mesh modeling by introducing the finite element method as a tool to solving the rotor dynamic equations of motion for both steady-state and time-transient orbits. The shafts are modeled as 1-D Timoshenko beam elements with 6 degrees of freedom per node and the concept of gear mesh stiffness is introduced as a means of connecting the geared shafts via element stiffness matrices. A discussion of several gear geometric parameters is used to explain the average gear mesh stiffness and the subsequent transformation matrices that relate the generalized forces and displacements along the line of action to their components in the shaft reference frame. This represents the baseline linear time-invariant (LTI) modeling for geared rotor dynamics. Steady-state methods to solve the damped eigenvalue (or free vibration) problem for geared rotors with constant mesh stiffness are also applicable to this section and are instrumental in determining potentially excited modes shapes, natural frequencies, and assessing their stability.

7.1.2 Results

The gearbox of the steam-turbine-generator set in Chapter 4 exhibited high lateral vibration in the high-speed pinion that is consistent with a sub-synchronous instability at $0.86 - 0.89$X, where X is the running speed of the high-speed pinion. The instability was shown by analysis to be a rigid-body conical whirl mode that was driven by free oil entrainment in the high-speed flexible coupling. The instability occurred when the gearbox bearings were lightly loaded as the generator was decoupled for spin testing of the turbine. It was discovered that an oil leakage occurred from the turbine inboard bearing housing, and the oil became entrained in the high-speed coupling. Assuming that the entrained oil would produce destabilizing forces, the effects were modeled as a cross-coupled stiffness and were applied to the coupling. The instability was successfully reproduced in the model when the original bearings were lightly loaded and produced a log decrement of -2.41 and a whirl frequency ratio of 0.88X.

The analysis was able to reproduce the observed sub-synchronous frequency with low levels of cross-coupled stiffness applied to the flexible coupling. A 3-lobe bearing with two pressure dams on two of the pads was predicted to stabilize the gearbox high-speed pinion over the full range of generator load cases. Since replacing the existing bearings with the 3-lobe ones, the instability has vanished in the field. These results validate the methods used to predict the free oil instability in the flexible coupling of the steam-turbine generator gearbox using a damped eigenvalue solver. Reliable damped eigenvalue predictions for geared systems is crucial to the identification of lightly damped modes with frequencies that are within and well outside of shaft operating speeds.

7.2 Unbalance response considerations with constant gear mesh stiffness K_g

7.2.1 State-coupled unbalance forces with constant gear mesh stiffness K_g

Comparisons between the steady-state and the transient unbalance response analyses on the flexible shaft gearbox in Chapter 5 produced additional insights into the assumption that geared shaft rotational speeds remain constant during operation. Transient results indicate that the reaction forces and torques at the gear mesh produce oscillations in the shaft rotational speeds and that the amplitude of those oscillations is dependent on the magnitude of the gear torques and the shaft I_p . The rotor dynamic equations of motion, despite using linear representations of the shafts, bearings, and a constant gear mesh stiffness, are inherently non-linear when the shaft rotational speeds are non-constant as shown in Equation 7.1. The frequency of shaft rotational speed oscillations typically has a synchronous component but may contain other non-synchronous frequencies which can in turn energize other modes. In particular, a lightly damped high frequency lateral/torsional coupled mode at 217,000 CPM was energized and changed the steady-state behavior of the geared system. It was determined that this mode contributed to numerical instabilities in the solution, and therefore artificial torsional damping at the gear mesh interface was included to mitigate it. The only mode eliminated was the high frequency lateral-torsional one, and the new solution revealed an elliptical steady-state orbit that was smaller than what the linear steady-state geared system analysis predicted.

The consequences of non-constant shaft rotational speeds are also elaborated on in terms of its effect on the external unbalance force and the frequency dependent bearing stiffness and damping coefficients and gyroscopic moments in the equation of motion.

- Unbalance force magnitude and frequency are modulated in time as shown in Equation B.2.
- Damping terms have non-constant coefficients – $[C_{brg}(\Omega) + \Omega\,(t)\,G]\,\dot{u}$
- Stiffness terms have non-constant coefficients – $\left[K_{brg}(\Omega) + \dot{\Omega}\,(t)\,G\right] u$

$$M\ddot{u} + C_s\dot{u} + K_s u = F_{Mesh}\,(u, \dot{u}, t) + F_{Unb}\left(\Omega, \dot{\Omega}, t\right) - \left(C_{brg}(\Omega) + \Omega G\right)\dot{u} - \left(K_{brg}(\Omega) + \dot{\Omega} G\right) u \tag{7.1}$$

Results show that the phenomenon dominating the response is in the modulated unbalance force since its forcing magnitude is proportional to the rotational speed squared. If the rotational speeds are kept fixed, then the steady-state orbit sizes would have remained substantially larger. This implies that the gear mesh forces contained components that oppose the direction of the rotating unbalance. Damping and stiffness terms for the bearings, despite their frequency dependence, produce little to no effect on the non-linearities since the oscillations in these examples have been three orders of magnitude below the operating speed. Gyroscopic influences with regards to rotational speed and accelerations was also shown to have a minimal role in the non-linear responses studied in Chapter 4 for the same reason.

7.2.2 Bifurcation and whirl energy considerations

A steady-state unbalance response of the flexible gearbox shafts in Chapter 5 was compared with a transient simulation and the results were vastly different. Initial magnitudes of the X and Y response plots are in agreement with steady-state predictions but quickly deviate as a marginally stable high-frequency lateral-torsional mode became energized and unrealistically changed the dynamics after $t = 2.5$ seconds. FFTs of the transient response show the presence of synchronous and supersynchronous excitations although the initial unbalance forces are purely synchronous with operating speed. Although the gear mesh stiffness is acting as a constant, the variation of the shaft speeds with time dictates variations in the gear mesh forces. A damped eigenvalue analysis of the geared system showed the presence of that lightly damped lateral torsional mode with a natural frequency that matched with what was observed in the transient response. These results suggest that the methods used are susceptible to numerical instabilities that are generated from lightly damped high frequency modes. Caution should be taken in identifying what modes are physical and avoiding the excitations of artificial ones.

After confirming the presence of artificial lightly damped high frequency modes, additional investigations were conducted to examine how the force-velocity relationships influence the shaft whirl orbits. Such a technique is useful for concluding how the gear forces contribute to the promotion of shaft whirl. Despite the amplification of the gear forces and torques after $t = 2.5$ seconds, the whirl amplitude of the shafts decreased substantially. Investigating the gear, bearings, and unbalance X and Y forces in conjunction with their instantaneous X and Y velocity components produced further insights into how each of these forces acting on the shaft contribute to or attenuate whirl. Although the net whirl power of all components did not increase at the onset of this high frequency interference, the power contributions of the gears increased while those of unbalance decreased. These results suggest that the rotor-gear-bearing system dynamics changed after the excitation of the high frequency mode. The dynamics could be originally characterized as unbalance-dominated shaft whirl, but the onset of the high frequency mode changed them to gear tooth chatter. The gear mesh forces substantially increased despite their displacements and velocities having decreased. It is shown that frequency components of forces and velocities that remain in phase amplify the shaft whirl at that frequency, while substantial phase differences indicate no contribution of shaft whirl to that frequency.

Torsional damping at the gear mesh was later included to eliminate the high frequency mode from the results. Results confirmed that even 4% torsional damping is sufficient to eliminate the numerical instability source from the response. Although the mode was eliminated, the transient X and Y displacements continued to decrease relative to the predicted steady-state response. These results highlight the critical assumption of constant shaft rotational speed since that is the reason for the discrepancy even with the lateral-torsional mode having been eliminated. Despite the gear forces and torques retaining high frequency components, their interactions with the shaft displacements and velocities yield no contribution to high frequency whirl. Consideration of the X and Y gear forces with their respective nodal velocities confirm that there are sufficient phase differences between the higher frequencies, and that only the synchronous components contribute to the perpetuation of shaft whirl.

7.3 Unbalance response with state-varying mesh stiffness $\frac{K_a}{K_g}$ and backlash δ_s

7.3.1 Discussion of methods

Section 3.2 augments the definition of the gear mesh stiffness to include a state-varying contribution because multiple pairs of teeth are going into and out of engagement in time. The frequency of these engagement/disengagement transitions is referred to as the gear mesh frequency, and a Fourier series approximation of rectangular waves is introduced. Furthermore, the methods allow the shaft rotational speed to vary in time, which implies that additional gear mesh harmonics may appear in the rectangular wave form that approximates the change of tooth pairs. Uncertainty in the number of Fourier terms needed to accurately characterize the state-varying mesh stiffness is discussed with the conclusion that 5-10 terms is sufficient for rotor dynamics models. Additional Fourier terms produce sharper edges in the rectangular waveform which not only poorly represents tooth contact pair transitions but can also excite higher frequency modes that might not accurately represent the dynamics of the system. Other parameters such as the ratio of the state-varying amplitude to the average mesh stiffness and the contact ratio are suggested topics worth investigating.

Section 3.3 incorporates the backlash clearance into the dynamic force calculations and is dependent on the dynamic transmission error, which characterizes the difference in expected tangential displacements of the gear teeth. Backlash is a major source of non-linearity in gear dynamics because of the potential for sudden tooth contact loss. The complete dynamic mesh forces are summarized for a gear pair, and the non-linear state-varying rotor dynamic equations of motion are introduced. The inclusion of these non-linear gear forces, and acceleration-dependent unbalance forces and gyroscopic moments into the rotor dynamic models of shaft bearing systems provide a more realistic toolset for members of industry for either design or diagnostic purposes.

7.3.2 Results from flexible gearbox application from Chapter 5

The effects of state-varying stiffness on the transient unbalance response of a simple 1:1 spur geared system were also explored in a systematic order. Using the same parameters for the nominal transient unbalance response in Section 5.3, a test matrix of runs was constructed in Table 5.5 to systematically study the effects of the following parameters on the X and Y displacements, shaft rotational speed oscillations, and the gear mesh stiffness: unbalance magnitude, ratio of variational mesh stiffness K_a to average mesh stiffness K_g, contact ratio, backlash clearance, and the number of Fourier terms.

Results confirm that some of these parameters had greater effects on the rotor dynamic performance than others. In particular, the transient analysis confirmed that coupled effects exist in the rotor dynamic equations of motion simply because the gear mesh reaction torque produces oscillations in shaft rotational speed that drive non-synchronous unbalance forces. In addition to the constant gear mesh stiffness case, the state-varying mesh stiffness energized additional lightly damped high frequency modes at 189,000 and 395,000 CPM. These results confirm that the direct Runge-Kutta numerical method is susceptible to the excitation of these unrealistic high frequency modes. The 189,000 CPM mode, however, is near the gear mesh frequency of 195,000 CPM and thus is more likely to be excited. Techniques such as adding artificial torsional damping at the gear mesh have been shown to successfully eliminate the excitation of the unrealistic modes.

Increasing the ratio of $\frac{K_a}{K_g}$ had the effect of decreasing the peak amplitude but increasing the amplitudes of sideband frequencies. Varying the number of Fourier coefficient terms, in general, did not affect the X and Y displacements but yielded a reduction in amplitude of shaft rotational speed variation for one mode but while increasing it for others. These effects are more prominent for higher frequency modes. In general, increasing the number of Fourier coefficients beyond 5 produced minimal changes and would be more likely to excite more higher order modes than what may be physically realistic. Results concerning backlash clearance variation showed that the model produces an effective mesh stiffness that is greatly reduced resulting in the reduction of the frequencies of several gear dominated modes. Increasing the backlash clearance results in larger variations of shaft rotational speed which feeds into state-induced unbalance forces in addition to potential abrupt contact loss. When comparing the relative effects of $\frac{K_a}{K_g}$ with backlash clearance, backlash clearance dominated the system dynamics because of the reduced gear mesh stiffness and even produced excitations for subsynchronous frequencies. Increasing the unbalance magnitude with both $\frac{K_a}{K_g}$ and backlash clearance results in greater amplification of certain modes or the excitation of sideband frequencies. Finally, the gear mesh contact ratio was varied between 1.25 and 1.75, resulting in minimal effects on the displacements. Contact ratios approaching 1.0 imply that the gear mesh stiffness undergoes a large decrease over shorter time intervals compared with a value of 1.50. In contrast, contact ratios closer to 2.0 produce larger increases in gear mesh stiffness over shorter time intervals. As these contact ratios approach 1.0 or 2.0, the gear mesh stiffness appears closer to an abrupt impulse, and it may energize specific modes that can affect the shaft rotational speed via lateral-torsional coupling.

7.3.3 Results from the power-turbine compressor application from Chapter 6

High amplitude vibration on a geared power turbine compressor train was discovered during heavy loaded string testing. A supersynchronous vibration problem was detected along the blind-end of the high-speed pinion and this analysis is a continuation of the work done by Cloud et al [69]. Unlike typical supersynchronous gearbox vibration problems that occur at the gear mesh frequency (GMF), the problematic vibration existed at only 10x, where x is the operating speed of the high-speed pinion. In contrast, the GMF would have been at 42x. Cloud et al suspected that the problem originates from the excitation of a lightly damped mode around the 10x pinion speed. After conducting a damped eigenvalue analysis, they discovered several modes that exist near the 10x frequency and concluded that the problematic mode could be either the 5^{th} pinion mode or a lateral-torsional coupled mode involving similar lateral motions as the 5^{th} pinion mode. Although their damped eigenvalue analysis with the Campbell diagram could reasonably predict the problematic mode, the source of the excitation remained unknown and there was only speculation that the gear mesh could be the root cause of the problem. A transient analysis with the capability of modeling state-varying gear mesh stiffness enabled the exploration of the source of this problem further.

Transient results were obtained for four different values of $\frac{K_a}{K_g}$ to test whether variational gear mesh stiffness could be a potential source of excitation needed to excite the 10x mode. Values of $\frac{K_a}{K_g}$ ranging from 0 to 0.75 in increments of 0.25 were studied. X and Y displacements, velocities, forces, torque, and gear mesh stiffness were computed for each of the four $\frac{K_a}{K_g}$ cases and presented in both time and frequency domains. Prior to including state-varying mesh stiffness ($K_a = 0$), the results showed no amplification mechanism since although the gear mesh forces and torques contained the 10x excitation, the displacements retained only the synchronous component. These details suggest that there is no positive feedback loop because the gear mesh forces are only related to the relative displacements and not the relative velocities. The relative velocities contain the supersynchronous content and can influence the gear mesh forces and torques only through state-varying mesh stiffness modeling in these studies.

Including variational gear mesh stiffness, however, produced the necessary amplification that is consistent with what was reported in the field. X and Y displacement FFTs with varying K_a illustrate that the synchronous and subsynchronous vibrations are insensitive to K_a, but the 10x frequency becomes more prominent with increasing K_a. Observing the velocities and gear forces and torque reveal the presence of other superharmonics beyond the 10x that are energized by increasing K_a. In particular are prominent excitations and responses at $239,400$, $670,000$, and $900,000$ RPM among others, but only the 10x (57,000 RPM) frequency is energized in the displacement FFTs. This is because the 10x frequency in the displacements is initially energized by the gear mesh variational stiffness such that the gear mesh forces and torque retain that frequency component. Since the gear mesh forces and torque contain the supersynchronous frequency component, this leads to further vibration amplification of the gear chatter mode for future time steps. The $K_a = 0$ case reveals that the 10x component is only present at the start of the simulation and quickly dampens out because there is no gear mesh variation to sustain it.

Analyzing the forces and velocities for each component acting on the high-speed pinion shaft from an energy perspective helped clarify how power is distributed and how it adds to or detracts from shaft whirl. This analysis is achieved by multiplying the instantaneous X and Y forces and velocities for each component at each time step. Instantaneous whirl promoting power was recorded and plotted with time for unbalance force, bearings, flexible coupling, and the pinion at both $\frac{K_a}{K_g} = 0$ and 0.5. Results indicate that increasing the gear mesh variation to $\frac{K_a}{K_g} = 0.5$ produced substantially larger contributions to shaft whirl power from the flexible coupling and the high-speed pinion. Although the magnitude of the whirl contribution of the unbalance force remained unchanged, a noticeable increase in its frequency is present and only appears during and after the pinion and coupling become more active.

Time series plots of the X and Y forces and velocities for the high-speed pinion were presented for both $\frac{K_a}{K_g} = 0$ and 0.5. For $\frac{K_a}{K_g} = 0$, the peaks between pinion forces and velocities in both X and Y directions are nearly 180° out of phase, which suggests that the high-speed pinion dynamics detract from promoting shaft whirl. In contrast, the $\frac{K_a}{K_g} = 0.5$ case shows that the high-frequency peaks of the gear forces and velocities for the X and Y components are in phase, suggesting that the high-speed pinion promotes whirl at 57,000 RPM.

7.4 Discussion of objectives

Analytical methods, as defined in Chapter 3, have been applied to case studies in Chapters 4, 5, and 6 with the intention of meeting the following research objectives as part of this dissertation. A discussion of each of these bullet points is discussed in the following subsections.

- Assess the influence of non-constant stiffness and damping coefficients due to shaft rotational speed fluctuations
- Investigate the lateral-torsional coupling of geared systems by observing the damping characteristics of torsional modes, which are typically treated as undamped
- Assess the influence of shaft dynamics on the overall gear-rotor-bearing system response using Timoshenko beam finite elements
- Investigate the sensitivity of vibration response due to the following factors:
    - Unbalance magnitude
    - Size of backlash clearance
    - Number of Fourier series rectangular wave coefficients to model state-varying mesh stiffness
    - Contact ratio

- Relative amplitude of state-varying mesh stiffness to average mesh stiffness

7.4.1 Non-constant stiffness and damping coefficients due to shaft rotational speed fluctuations

As shown in Equation 7.1, stiffness and damping terms from the bearings and shaft gyroscopic moments must be included as external forcing functions that appear on the right hand side due to their frequency dependence. It has been shown that there may be substantial rotational speed fluctuations in the transient unbalance response for geared systems, even with constant gear mesh stiffness and this induces modulations in both the unbalance force magnitude and frequency. Results under constant rotational speed conditions indicate that none of the bearing or gyroscopic non-linear terms substantially influenced the results.

Bearing damping and stiffness variations would vary linearly with changes in shaft rotational speed, and because the variations in $\Omega(t)$ were small, so were their coefficient variations. Gyroscopic terms are also directly proportional to $\Omega(t)$ and $\dot{\Omega}(t)$ and also result in small variations for small $\dot{\Omega}(t)$. The primary source of non-synchronous phenomena, however, appeared in the unbalance force since its magnitude is dependent on $\Omega^2(t)$ and its frequency is dictated by $\Omega(t)$. Therefore, small changes in $\Omega(t)$ may produce not only large variations in unbalance force magnitude but also fundamentally change the forcing function from synchronous excitation to non-synchronous. Because the gear mesh forces and torques are driven by the gear node displacements and shaft rotational speed (Ω), and these states are determined at the next time step from integrating the shaft accelerations, potential feedback loops are possible and have appeared in the results in the form of energized high frequency modes.

7.4.2 Damping and excitation of lateral-torsional coupled modes

Excitation of a lightly damped lateral-torsional mode was confirmed in the flexible shaft gearbox model in Chapter 5 using a damped eigenvalue solver and matching its frequency with what was observed in the transient response. The damped eigenvalue solver predicts coupled lateral-torsional mode shapes because of the gear mesh finite element stiffness matrix properties. Lateral-torsional and axial coupling is incorporated in the form of transformation matrices relating the generalized displacements and forces at the pitch point along the line of action (LOA) with those at the geometric center of the shafts. The same element stiffness matrix is also included in the transient solver.

Observation of the torsional component of the mode shape revealed that the primary location of modal participation was at the gear nodes. Torsional excitation of this mode may be attributed to unbalance forces because of the lateral-torsional coupling of the gear mesh element even though unbalance acts laterally on the shafts. Introducing artificial torsional damping at the gear mesh produced substantial effects on the attenuation of the high-frequency lateral-torsional mode. Calculated torsional modal damping up to 4% was sufficient to completely eliminate the high frequency lateral-torsional mode and the variation of transient responses with less modal damping is also shown. Implications from these analyses confirm the necessity to accurately model this lateral-torsional coupling effect in the gear mesh not only to assess damping of torsional modes but to also gauge the effects of potential excitation sources from lateral phenomena such as unbalance, blade out, etc in a wide variety of geared systems.

7.4.3 Sensitivity of response to unbalance magnitude, backlash, Fourier series terms, contact ratio, and $\frac{K_a}{K_g}$

The analyses conducted on the single stage flexible shaft gearbox with 1:1 ratio in Chapter 5 produced several important trends from a rotor dynamics perspective. The effects of state-varying stiffness on the transient unbalance response were explored in a systematic order. Using the same parameters for the nominal transient unbalance response in Section 5.3, a test matrix of runs was constructed (Table 5.5) to study the effects of the following parameters – unbalance magnitude, ratio of variational mesh stiffness K_a to average mesh stiffness K_g, contact ratio, backlash clearance, and the number of Fourier terms – on the gear displacements, shaft rotational speed oscillations, and the gear mesh stiffness.

Results confirm that some of these parameters had greater effects on rotor dynamic performance than others. In particular, the transient analysis confirms that non-synchronous forces exist in the rotor dynamic equations of motion simply because the gear mesh reaction torque produces oscillations in the shaft rotational speeds. The gear mesh forces themselves become non-linear as the spring stiffness representing tooth contact is allowed to increase and decrease in accordance with not only tangential displacements but with rotational speed. Increasing the ratio of $\frac{K_a}{K_g}$ had the effect of decreasing the peak amplitude but increasing the amplitudes of sideband frequencies in increments of synchronous frequency. Varying the number of Fourier coefficient terms, in general, did not affect the X and Y displacements but yielded a reduction in the amplitude of shaft rotational speed variation for one mode while increasing it for another. These effects are more prominent for higher frequency modes. In general, increasing the number of Fourier coefficients beyond 5 produced minimal changes and would be more likely to excite more higher order modes than what may be physically realistic. Results concerning backlash clearance variation showed that the model produces an effective mesh stiffness that is greatly reduced from the original constant mesh stiffness, which drops the frequencies of several gear dominated modes. Increasing the backlash clearance results in larger variations of shaft rotational speed which feeds into non-synchronous forces in addition to potential abrupt tooth contact loss. When comparing the relative effects of $\frac{K_a}{K_g}$ with backlash clearance, backlash clearance dominated the system dynamics because of the reduced gear mesh stiffness and even produced excitations at subsynchronous frequencies. Increasing the unbalance magnitude with both $\frac{K_a}{K_g}$ and backlash clearance results in greater amplification of certain modes or the excitation of sideband frequencies. Lastly, gear mesh contact ratio was varied between 1.25 and 1.75 and showed minimal effects on the displacements. Contact ratios closer to 1.0 imply the gear mesh stiffness, in a single tooth pass, undergoes a large decrease but for shorter time intervals compared with a value of 1.50, while ratios closer to 2.0 produce larger increases in gear mesh stiffness but over shorter time intervals. As these contact ratios approach 1.0 or 2.0, the gear mesh stiffness appears closer to an abrupt impulse and whether it is increasing or decreasing may energize or take energy away from certain modes that affect the shaft rotational speed.

7.4.4 Coupling shaft and gear dynamics

Three separate applications involving detailed finite element models of geared systems are introduced and examined in this dissertation. Although no contradictory models depicting rigid lumped geared systems were analyzed in comparison with the finite element models, results from each of the application chapters provide compelling evidence to suggest that shaft dynamics are essential to the successful modeling of real industrial vibration problems. Each of the high vibration phenomena encountered in these applications were amplifications of lightly damped high frequency modes that may involve both lateral and torsional participation. Representations of the shafts as spring elements are a gross approximation to the complexities inherent in geared machines because these mode shapes would never be discovered without the use of finite elements.

The opposite extreme has been to rely on complex 3-D solid elements for the gears to predict the forced response of geared systems. Accuracy of such detailed gear FEA models is not guaranteed if details governing the rotor dynamic equations of motion are neglected. This includes the use of skew-symmetric matrices to model gyroscopic moments, cross-coupled stiffness, and other effects that may have substantial influence on shaft whirl depending on the mode being excited. Furthermore, the use of 3-D solid elements in a transient analysis considerably increases computational time and demand for larger memory storage due to the increased size of the global matrices. Results from this dissertation indicate that using 1-D Timoshenko beam elements to represent the stiffness and inertial properties of the shafts and a 12x12 stiffness element for their geared connection, produced sufficient accuracy to successfully model excitations that are present in actual industrial applications.

Appendices

Appendix A

Finite elements for shafts, disks, bearings, and flexible couplings

This appendix section describes the Timoshenko beam finite elements used for shaft modeling and are ubiquitous in rotor dynamics. Their cubic polynomial shape functions promote sufficient accuracy of deflection, stress, and strain within each element while keeping matrix sizes fairly small. The primary difference between Timoshenko and Bernoulli-Euler beam theory is the inclusion of shear deformation in addition to classical bending, which is represented as Φ. Shaft rotary inertia is also affected. In addition to bending and shearing, the shaft elements also have torsional and axial degrees of freedom on each node. Each beam element may be represented by Figure A.1 where the six degrees of freedom for each node are shown.

The displacement vector $\{u\}$ is defined as:

$$\{u\} = \{z \;\; x \;\; y \;\; \theta_z \;\; \theta_x \;\; \theta_y\}^T \tag{A.1}$$

In order to incorporate shear effects, Φ is defined as:

$$\Phi = \frac{12EI}{GAkL^2} \tag{A.2}$$

Mass, stiffness, damping, and gyroscopic matrices are defined for the shaft finite elements and the convention for the degrees of freedom is defined in Equation A.1.

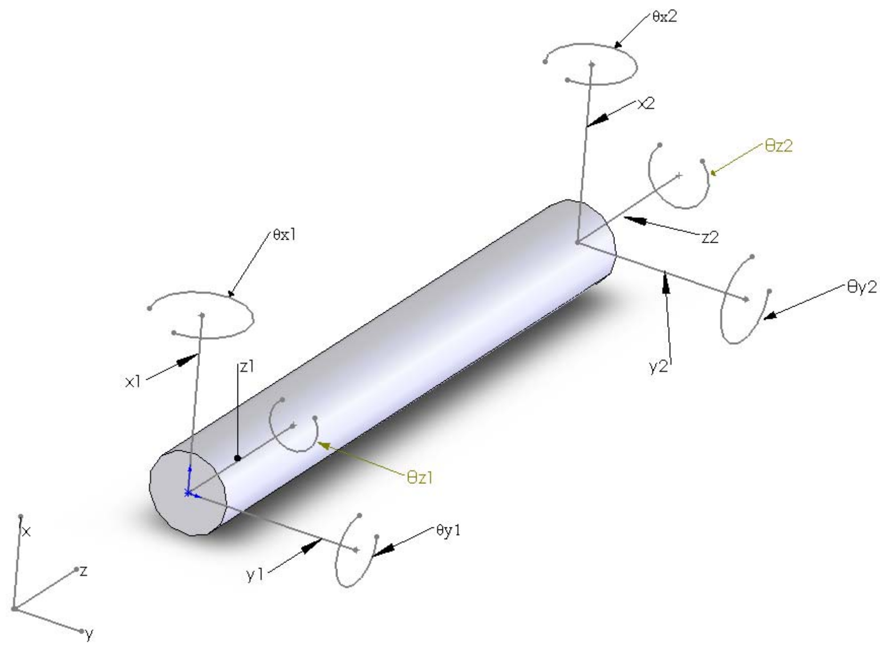

Figure A.1: Coordinate System and degrees of freedom of Timoshenko beam element for shaft modeling.

The elemental mass matrix is defined as:

$$[M]^{(e)} = \rho AL \begin{bmatrix} \frac{1}{3} & 0 & 0 & 0 & 0 & 0 & \frac{1}{6} & 0 & 0 & 0 & 0 & 0 \\ 0 & frA & 0 & 0 & 0 & frC & 0 & frB & 0 & 0 & 0 & -frD \\ 0 & 0 & frA & 0 & -frC & 0 & 0 & 0 & frB & 0 & frD & 0 \\ 0 & 0 & 0 & \frac{2I}{3A} & 0 & 0 & 0 & 0 & 0 & \frac{2I}{6A} & 0 & 0 \\ 0 & 0 & -frC & 0 & frE & 0 & 0 & 0 & -frD & 0 & frF & 0 \\ 0 & frC & 0 & 0 & 0 & frE & 0 & frD & 0 & 0 & 0 & frF \\ \frac{1}{6} & 0 & 0 & 0 & 0 & 0 & \frac{1}{3} & 0 & 0 & 0 & 0 & 0 \\ 0 & frB & 0 & 0 & 0 & frD & 0 & frA & 0 & 0 & 0 & -frC \\ 0 & 0 & frB & 0 & -frD & 0 & 0 & 0 & frA & 0 & frC & 0 \\ 0 & 0 & 0 & \frac{2I}{6A} & 0 & 0 & 0 & 0 & 0 & \frac{2I}{3A} & 0 & 0 \\ 0 & 0 & frD & 0 & frF & 0 & 0 & 0 & frC & 0 & frE & 0 \\ 0 & -frD & 0 & 0 & 0 & frF & 0 & -frC & 0 & 0 & 0 & frE \end{bmatrix} \tag{A.3}$$

where

$$frA = \frac{\frac{13}{35} + \frac{7}{10}\Phi + \frac{1}{3}\Phi^2 + \frac{6I}{5AL^2}}{(1+\Phi)^2} \tag{A.4}$$

$$frB = \frac{\frac{9}{70} + \frac{3}{10}\Phi + \frac{1}{6}\Phi^2 - \frac{6I}{5AL^2}}{(1+\Phi)^2} \tag{A.5}$$

$$frC = \frac{(\frac{11}{210} + \frac{11}{120}\Phi + \frac{1}{24}\Phi^2 + (\frac{1}{10} - \frac{\Phi}{2})\frac{I}{AL^2})L}{(1+\Phi)^2} \tag{A.6}$$

$$frD = \frac{(\frac{13}{420} + \frac{3}{40}\Phi + \frac{1}{24}\Phi^2 - (\frac{1}{10} - \frac{\Phi}{2})\frac{I}{AL^2})L}{(1+\Phi)^2} \tag{A.7}$$

$$frE = \frac{(\frac{1}{105} + \frac{1}{60}\Phi + \frac{1}{120}\Phi^2 + (\frac{2}{15} + \frac{\Phi}{6} + \frac{\Phi^2}{3})\frac{I}{AL^2})L^2}{(1+\Phi)^2} \tag{A.8}$$

$$frF = \frac{(-\frac{1}{140} - \frac{1}{60}\Phi - \frac{1}{120}\Phi^2 + (-\frac{1}{30} - \frac{\Phi}{6} + \frac{\Phi^2}{6})\frac{I}{AL^2})L^2}{(1+\Phi)^2}. \tag{A.9}$$

The elemental stiffness matrix is defined as:

$$[K]^{(e)} = \frac{EI}{(1+\Phi)L^3}\begin{bmatrix} \frac{AE}{L*Const} & 0 & 0 & 0 & 0 & 0 & -\frac{AE}{L*Const} & 0 & 0 & 0 & 0 & 0 \\ 0 & 12 & 0 & 0 & 0 & 6L & 0 & -12 & 0 & 0 & 0 & 6L \\ 0 & 0 & 12 & 0 & -6L & 0 & 0 & 0 & -12 & 0 & -6L & 0 \\ 0 & 0 & 0 & \frac{2GI}{L*Const} & 0 & 0 & 0 & 0 & 0 & -\frac{2GI}{L*Const} & 0 & 0 \\ 0 & 0 & -6L & 0 & (4+\Phi)L^2 & 0 & 0 & 0 & 6L & 0 & (2-\Phi)L^2 & 0 \\ 0 & 6L & 0 & 0 & 0 & (4+\Phi)L^2 & 0 & -6L & 0 & 0 & 0 & (2-\Phi)L^2 \\ -\frac{AE}{L*Const} & 0 & 0 & 0 & 0 & 0 & \frac{AE}{L*Const} & 0 & 0 & 0 & 0 & 0 \\ 0 & -12 & 0 & 0 & 0 & -6L & 0 & 12 & 0 & 0 & 0 & -6L \\ 0 & 0 & -12 & 0 & 6L & 0 & 0 & 0 & 12 & 0 & 6L & 0 \\ 0 & 0 & 0 & -\frac{2GI}{L*Const} & 0 & 0 & 0 & 0 & 0 & \frac{2GI}{L*Const} & 0 & 0 \\ 0 & 0 & -6L & 0 & (2-\Phi)L^2 & 0 & 0 & 0 & 6L & 0 & (4+\Phi)L^2 & 0 \\ 0 & 6L & 0 & 0 & 0 & (2-\Phi)L^2 & 0 & -6L & 0 & 0 & 0 & (4+\Phi)L^2 \end{bmatrix} \tag{A.10}$$

where

$$Const = \frac{EI}{(1+\Phi)L^3}. \tag{A.11}$$

The shaft elemental gyroscopic matrix is defined as:

$$[G]^{(e)} = 2\rho AL \begin{bmatrix} 0 & 0 & 0 & 0 & 0 & 0 & 0 & 0 & 0 & 0 & 0 & 0 \\ 0 & 0 & f\bar{r}A & 0 & f\bar{r}B & 0 & 0 & 0 & -f\bar{r}A & 0 & f\bar{r}B & 0 \\ 0 & -f\bar{r}A & 0 & 0 & 0 & f\bar{r}B & 0 & f\bar{r}A & 0 & 0 & 0 & f\bar{r}B \\ 0 & 0 & 0 & 0 & 0 & 0 & 0 & 0 & 0 & 0 & 0 & 0 \\ 0 & -f\bar{r}B & 0 & 0 & 0 & f\bar{r}C & 0 & f\bar{r}B & 0 & 0 & 0 & f\bar{r}D \\ 0 & 0 & -f\bar{r}B & 0 & -f\bar{r}C & 0 & 0 & 0 & f\bar{r}B & 0 & f\bar{r}D & 0 \\ 0 & 0 & 0 & 0 & 0 & 0 & 0 & 0 & 0 & 0 & 0 & 0 \\ 0 & 0 & -f\bar{r}A & 0 & -f\bar{r}B & 0 & 0 & 0 & f\bar{r}A & 0 & -f\bar{r}B & 0 \\ 0 & f\bar{r}A & 0 & 0 & 0 & -f\bar{r}B & 0 & -f\bar{r}A & 0 & 0 & 0 & -f\bar{r}B \\ 0 & 0 & 0 & 0 & 0 & 0 & 0 & 0 & 0 & 0 & 0 & 0 \\ 0 & -f\bar{r}B & 0 & 0 & 0 & -f\bar{r}D & 0 & f\bar{r}B & 0 & 0 & 0 & f\bar{r}C \\ 0 & 0 & -f\bar{r}B & 0 & -f\bar{r}D & 0 & 0 & 0 & f\bar{r}B & 0 & -f\bar{r}C & 0 \end{bmatrix} \tag{A.12}$$

where

$$f\bar{r}A = \frac{6I}{5A(1+\Phi)^2L^2} \tag{A.13}$$

$$f\bar{r}B = (\frac{1}{10} - \frac{1}{2}\Phi)\frac{I}{A(1+\Phi)^2L} \tag{A.14}$$

$$f\bar{r}C = (\frac{2}{15} + \frac{1}{6}\Phi + \frac{1}{3}\Phi^2)\frac{I}{A(1+\Phi)^2} \tag{A.15}$$

$$f\bar{r}D = -(\frac{1}{30} + \frac{1}{6}\Phi - \frac{1}{6}\Phi^2)\frac{I}{A(1+\Phi)^2L}. \tag{A.16}$$

These elemental matrices are combined for each element to make the global mass, gyroscopic and stiffness matrices of the rotor. Shaft internal damping is neglected and therefore does not appear in the rotor element matrices. Additional components are added to the global matrices and these may be in the form of disks (infinitely rigid mass), flexible couplings, and bearings. Formulation of the gear stiffness element connecting the shaft nodes is defined via Chapter 3.

Disks on the shaft are modeled as infinitely rigid mass elements and therefore contain mass and gyroscopic properties that are lumped onto a single node. Their inertia properties are defined in Equation A.17 and include not only translatory terms (mass) but also rotational inertia about all three axes.

$$[M]^{(disk)} = \begin{bmatrix} m & 0 & 0 & 0 & 0 & 0 \\ 0 & m & 0 & 0 & 0 & 0 \\ 0 & 0 & m & 0 & 0 & 0 \\ 0 & 0 & 0 & I_p & 0 & 0 \\ 0 & 0 & 0 & 0 & I_t & 0 \\ 0 & 0 & 0 & 0 & 0 & I_t \end{bmatrix} \tag{A.17}$$

Gyroscopic matrices for disks are defined in Equation A.18 and have substantial effects in rotor dynamics analyses for $\frac{I_p}{I_t} > 2.0$, which represents large diameter disks with short axial lengths. Gyroscopic effects are important in rotor dynamics because they couple the lateral tilt degrees of freedom (θ_x and θ_y) of the shafts, which contribute to or detract from forward or backward whirl.

$$[G]^{(disk)} = \begin{bmatrix} 0 & 0 & 0 & 0 & 0 & 0 \\ 0 & 0 & 0 & 0 & 0 & 0 \\ 0 & 0 & 0 & 0 & 0 & 0 \\ 0 & 0 & 0 & 0 & 0 & 0 \\ 0 & 0 & 0 & 0 & 0 & I_p \\ 0 & 0 & 0 & 0 & -I_p & 0 \end{bmatrix} \tag{A.18}$$

Next the bearing matrices need to be added to the global stiffness and damping matrices. Radial bearings can be expressed in the following form as stiffness and damping matrices that are superposed on the shaft global matrices. The same principle may be applied to seals. These 6×6 matrices define the flexible connections between a node in the rotating reference frame and the stationary one (ground). Furthermore, these 8-coefficient dynamic stiffness and damping models are whirl frequency dependent and may be retrieved as outputs from a bearing code that incorporates elasto-hydrodynamic effects associated with different whirl frequencies, speeds, and load cases. Typically, the whirl frequency is modeled as matching the shaft rotational speed but the presence of rotor dynamic instabilities that trigger additional whirl frequencies render that assumption invalid.

$$[K]^{radialbearing} = \begin{bmatrix} 0 & 0 & 0 & 0 & 0 & 0 \\ 0 & K_{xx} & K_{xy} & 0 & 0 & 0 \\ 0 & K_{yx} & K_{yy} & 0 & 0 & 0 \\ 0 & 0 & 0 & 0 & 0 & 0 \\ 0 & 0 & 0 & 0 & 0 & 0 \\ 0 & 0 & 0 & 0 & 0 & 0 \end{bmatrix} \tag{A.19}$$

$$[C]^{radialbearing} = \begin{bmatrix} 0 & 0 & 0 & 0 & 0 & 0 \\ 0 & C_{xx} & C_{xy} & 0 & 0 & 0 \\ 0 & C_{yx} & C_{yy} & 0 & 0 & 0 \\ 0 & 0 & 0 & 0 & 0 & 0 \\ 0 & 0 & 0 & 0 & 0 & 0 \\ 0 & 0 & 0 & 0 & 0 & 0 \end{bmatrix} \tag{A.20}$$

Thrust bearings support axial loads and therefore may be modeled in the following form where only axial stiffness and damping are relevant. Their dynamic properties are also speed and load dependent and should be input from a thrust bearing code that predicts speed, load, and whirl frequency dependent elasto-hydrodynamic effects between the thrust runner and bearing. Similarly to the radial bearings, these 6×6 matrices are superposed on the shaft global matrices at the appropriate nodal locations.

$$[K]^{thrustbearing} = \begin{bmatrix} K_{zz} & 0 & 0 & 0 & 0 & 0 \\ 0 & 0 & 0 & 0 & 0 & 0 \\ 0 & 0 & 0 & 0 & 0 & 0 \\ 0 & 0 & 0 & 0 & 0 & 0 \\ 0 & 0 & 0 & 0 & 0 & 0 \\ 0 & 0 & 0 & 0 & 0 & 0 \end{bmatrix} \tag{A.21}$$

$$[C]^{thrustbearing} = \begin{bmatrix} C_{zz} & 0 & 0 & 0 & 0 & 0 \\ 0 & 0 & 0 & 0 & 0 & 0 \\ 0 & 0 & 0 & 0 & 0 & 0 \\ 0 & 0 & 0 & 0 & 0 & 0 \\ 0 & 0 & 0 & 0 & 0 & 0 \\ 0 & 0 & 0 & 0 & 0 & 0 \end{bmatrix} \tag{A.22}$$

Unlike bearings that attach the rotating model to the stationary reference frame (ground), flexible couplings connect a node on one shaft with a node on a different shaft. The difference between couplings and gears, however, is that couplings require that the connected shafts rotate at the same speed and in the same direction and gears do not. The flexible coupling stiffness and damping properties are defined in Equations A.23 and A.24. They are of similar format to the gear mesh stiffness matrix defined in Equation 3.5 because of the connection between 2 nodes in the finite element model. In addition, the couplings are modeled as connecting the axial, lateral, and torsional degrees of freedom, but the directions remain uncoupled.

$$[K]^{coupling} = \begin{bmatrix} \begin{bmatrix} K_{zz} & 0 & 0 & 0 & 0 & 0 \\ & K_{xx} & 0 & 0 & 0 & 0 \\ & & K_{yy} & 0 & 0 & 0 \\ & & & K_{\theta_z\theta_z} & 0 & 0 \\ & & & & K_{\theta_x\theta_x} & 0 \\ & & & & & K_{\theta_y\theta_y} \end{bmatrix} & \begin{bmatrix} -K_{zz} & 0 & 0 & 0 & 0 & 0 \\ 0 & -K_{xx} & 0 & 0 & 0 & 0 \\ 0 & 0 & -K_{yy} & 0 & 0 & 0 \\ 0 & 0 & 0 & -K_{\theta_z\theta_z} & 0 & 0 \\ 0 & 0 & 0 & 0 & -K_{\theta_x\theta_x} & 0 \\ 0 & 0 & 0 & 0 & 0 & -K_{\theta_y\theta_y} \end{bmatrix} \\ Symm & \begin{bmatrix} K_{zz} & 0 & 0 & 0 & 0 & 0 \\ & K_{xx} & 0 & 0 & 0 & 0 \\ & & K_{yy} & 0 & 0 & 0 \\ & & & K_{\theta_z\theta_z} & 0 & 0 \\ & & & & K_{\theta_x\theta_x} & 0 \\ & & & & & K_{\theta_y\theta_y} \end{bmatrix} \end{bmatrix} \tag{A.23}$$

$$[C]^{coupling} = \begin{bmatrix} \begin{bmatrix} C_{zz} & 0 & 0 & 0 & 0 & 0 \\ & C_{xx} & 0 & 0 & 0 & 0 \\ & & C_{yy} & 0 & 0 & 0 \\ & & & C_{\theta_z\theta_z} & 0 & 0 \\ & & & & C_{\theta_x\theta_x} & 0 \\ & & & & & C_{\theta_y\theta_y} \end{bmatrix} & \begin{bmatrix} -C_{zz} & 0 & 0 & 0 & 0 & 0 \\ 0 & -C_{xx} & 0 & 0 & 0 & 0 \\ 0 & 0 & -C_{yy} & 0 & 0 & 0 \\ 0 & 0 & 0 & -C_{\theta_z\theta_z} & 0 & 0 \\ 0 & 0 & 0 & 0 & -C_{\theta_x\theta_x} & 0 \\ 0 & 0 & 0 & 0 & 0 & -C_{\theta_y\theta_y} \end{bmatrix} \\ Symm & \begin{bmatrix} C_{zz} & 0 & 0 & 0 & 0 & 0 \\ & C_{xx} & 0 & 0 & 0 & 0 \\ & & C_{yy} & 0 & 0 & 0 \\ & & & C_{\theta_z\theta_z} & 0 & 0 \\ & & & & C_{\theta_x\theta_x} & 0 \\ & & & & & C_{\theta_y\theta_y} \end{bmatrix} \end{bmatrix} \tag{A.24}$$

This completes the details regarding the finite element modeling of shafts, disks, radial and thrust bearings, and flexible couplings. Assumptions regarding the element effects on the inertia, stiffness, and damping of the complete rotor dynamic system have been represented.

Appendix B

Direct Runge-Kutta method

This section includes details regarding the use of the Runge-Kutta method and how it is applied to the rotor dynamic equations of motion of geared-rotor-bearing systems. The non-linear state-varying equations of motion for rotor dynamics may be expressed in Equation B.1.

$$M\ddot{u}(t) + [C + \Omega(t)G]\,\dot{u}(t) + \left[K + \dot{\Omega}(t)G\right]u(t) = F_{Mesh}\,(u, \dot{u}, t) + F_{Unb}\left(\Omega, \dot{\Omega}, t\right) \tag{B.1}$$

It is evident from this equation that the shaft rotational velocities and accelerations are state-varying and therefore significantly change the effects of the gyroscopic terms in comparison with the steady-state equations of motion shown in Equation 3.10. Furthermore, the unbalance force magnitudes and frequencies are further influenced by shaft rotational accelerations as shown in Equation B.2. The non-linear dynamic gear forces defined in Equation 3.28 appear on the right-hand-side of the equations of motion within F_{Mesh} and are no longer represented as elements within the global stiffness matrix $\mathbf{K}$.

$$\begin{aligned} F_{XUnb} &= me_u\Omega^2\cos(\Omega t + \phi) + me_u\dot{\Omega}\sin(\Omega t + \phi) \\ F_{YUnb} &= me_u\Omega^2\sin(\Omega t + \phi) - me_u\dot{\Omega}\sin(\Omega t + \phi) \end{aligned} \tag{B.2}$$

To solve the equations of motion with non-constant rotating speed, the left side must contain terms that are independent of running speed and the right contains the terms that depend on rotating speed as shown in Equation B.3.

$$M\ddot{u} + C_s\dot{u} + K_s u = F_{Mesh}\,(u, \dot{u}, t) + F_{Unb}\left(\Omega, \dot{\Omega}, t\right) - (C_{brg}(\Omega) + \Omega G)\,\dot{u} - \left(K_{brg}(\Omega) + \dot{\Omega}G\right)u \tag{B.3}$$

The resulting problem is implicit numerically because the rotating speed, Ω, is the axial angular rotating speed, $\dot{\theta}_z$, and the rotational acceleration, $\dot{\Omega}$, is the axial angular acceleration, $\ddot{\theta}_z$. The equations of motion may be solved via the direct Runge-Kutta method and are converted into state-space form in Equation B.4. At each time step, the axial rotational acceleration, $\ddot{\theta}_z$ or $\dot{\Omega}$, must be solved using a shooting method according to the current displacements and velocities.

$$\begin{aligned}
&\begin{bmatrix} M & 0 \\ 0 & M \end{bmatrix}\begin{bmatrix} \dot{u} \\ \ddot{u} \end{bmatrix} + \begin{bmatrix} 0 & -M \\ K & C \end{bmatrix}\begin{bmatrix} u \\ \dot{u} \end{bmatrix} \\
= &\begin{bmatrix} 0 \\ F_{Mesh}\left(u, \dot{u}, t\right) + F_{Unb}\left(\Omega, \dot{\Omega}, t\right) \end{bmatrix} + \begin{bmatrix} 0 \\ -\left(C_{brg}(\Omega) + \Omega G\right)\dot{u} - \left(K_{brg}(\Omega) + \dot{\Omega} G\right) u \end{bmatrix}
\end{aligned} \tag{B.4}$$

To simplify the equations of motion, let the following variables be defined.

$$\begin{aligned}
&V = \begin{bmatrix} u \\ \dot{u} \end{bmatrix}, A = \begin{bmatrix} M & 0 \\ 0 & M \end{bmatrix}, B = \begin{bmatrix} 0 & -M \\ K & C \end{bmatrix} \\
&F = \begin{bmatrix} 0 \\ F_{Mesh}\left(u, \dot{u}, t\right) + F_{Unb}\left(\Omega, \dot{\Omega}, t\right) \end{bmatrix} + \begin{bmatrix} 0 \\ -\Omega G \dot{u} - \dot{\Omega} G u \end{bmatrix} + \begin{bmatrix} 0 \\ -C_{brg}(\Omega)\dot{u} - K_{brg}(\Omega) u \end{bmatrix}
\end{aligned} \tag{B.5}$$

Equation B.4 may now be expressed as the following in state-space form.

$$A\dot{V} + BV = F \tag{B.6}$$

The state-space form converts the 2nd order ODE into 1st order form to be solved using the 4th order Runge-Kutta method. The matrix size increases from $N \times N$ to $2N \times 2N$, where N is the total number of degrees of freedom.

The Runge-Kutta method may be applied to the initial value problem shown in Equation B.7, where V_0 is a vector of length $2N$. The first N values correspond to the initial displacements and the second N values correspond to initial velocities. The default assumes that the displacements are zeroes, while the rotational velocities are user-specified.

$$\begin{aligned} A\dot{V} + BV &= F \\ V(t_0) &= V_0 \end{aligned} \tag{B.7}$$

From the initial conditions, the displacements and velocities are calculated at each time-step using the classical 4$^{\text{th}}$ order Runge-Kutta method shown in Equation B.8.

$$\begin{aligned} V_{i+1} &= V_i + \tfrac{\Delta t}{6}\left(s_1^i + 2s_2^i + 2s_3^i + s_4^i\right) \\ t_{i+1} &= t_i + \Delta t \end{aligned} \tag{B.8}$$

The 4 Runge-Kutta terms are evaluated at each time step, i, as dictated by Equation B.9. Each of these terms is used to weigh the relative change in V_i with respect to time at the previous time step, the midpoint, and the current time-step. This Runge-Kutta method uses fixed time-steps, but an adaptive integration scheme is recommended for computational efficiency in future models. The recommended fixed time-step should be less than 0.4× the period corresponding to the highest natural frequency calculated.

$$\begin{aligned} s_1^i &= \left(-A^{-1}B\right)V_i + A^{-1}F\left(\dot{V}_i, V_i, t_i\right), \\ s_2^i &= \left(-A^{-1}B\right)(V_i + \tfrac{\Delta t}{2}s_1^i) + A^{-1}F\left(\dot{V}_i, (V_i + \tfrac{\Delta t}{2}s_1^i), (t_i + \tfrac{\Delta t}{2})\right), \\ s_3^i &= \left(-A^{-1}B\right)(V_i + \tfrac{\Delta t}{2}s_2^i) + A^{-1}F\left(\dot{V}_i, (V_i + \tfrac{\Delta t}{2}s_2^i), (t_i + \tfrac{\Delta t}{2})\right), \\ s_4^i &= \left(-A^{-1}B\right)(V_i + \Delta t s_3^i) + A^{-1}F\left(\dot{V}_i, (V_i + \Delta t s_3^i), (t_i + \Delta t)\right), \end{aligned} \tag{B.9}$$

Accelerations at each time-step may be evaluated using the shooting method, shown in Equation B.10, which is an iterative technique ranging from $k = 0, 1, 2, ...$ until convergence. This method not only helps with convergence but it also effectively smooths the response under large transients.

$$\begin{aligned} \dot{V}_i^0 &= \dot{V}_{i-1}, \\ \dot{V}_i^1 &= \left(-A^{-1}B\right)V_i + A^{-1}F\left(\dot{V}_i^0, V_i, t_i\right), \\ \dot{V}_i^2 &= \left(-A^{-1}B\right)V_i + A^{-1}F\left(\dot{V}_i^1, V_i, t_i\right), \\ \dot{V}_i^3 &= \left(-A^{-1}B\right)V_i + A^{-1}F\left(\dot{V}_i^2, V_i, t_i\right), \\ &.... \\ until|\dot{V}_i^k &- \dot{V}_i^{k-1}| < error \\ \dot{V}_i &= \dot{V}_i^k \end{aligned} \tag{B.10}$$

This appendix illustrates the methods used to solve the rotor dynamic equations of motion for geared-rotor-bearing systems discussed in this dissertation. The original system of second order differential equations is broken into twice the number of first order ones using the state-space method. From there, the rotor dynamic equations of motion for geared-rotor-bearing systems are solved using an implicit Runge-Kutta method with fixed time-steps. The results include displacements, and velocities of all degrees of freedom in the finite element model at each time-step.

Bibliography

[1] Nevzat Ozguven, H., and Houser, D. R., 1988,“Mathematical models used in gear dynamics: a review,” Journal of Sound and Vibration, 121(3) pp. 383-411.

[2] Bollinger, J., and Harker, R., 1967,“Instability potential of high speed gearing,” Journal of the Industrial Mathematics, 17 pp. 39-55.

[3] Benton, M., and Seireg, A., 1981,“Factors influencing instability and resonances in geared systems,” Journal of Mechanical Design, 103(2) pp. 372-378.

[4] Nataraj, C., and Whitman, A., 1997, “Parameter excitation effects in gear dynamics,” ASME Design Engineering Technical Conferences.

[5] Fukuma, H., Furukawa, T., and Aida, T., 1973, “Fundamental research on gear noise and vibration:(6th Report, Generation Mechanism of Radial and Axial Vibration of Spur Gears),” Bulletin of JSME, 16(97) pp. 1094-1107.

[6] Tuplin, W.A., 1958, “Dynamic load on gear teeth,” Proceedings of the international conference on gearing, Institution of Mechanical Engineers, pp. 24-30.

[7] Rettig, H., 1976,“Vibrations in gear drives; test results and calculation method for dynamic tooth forces.”

[8] Salzer, M. W., 1975, “The dynamics of a layshaft gearbox,” Ph.D. Thesis, Cambridge University.

[9] Tordion, G. V., 1962, “The mechanical impedance approach to the dynamics (torsional vibrations) of geared systems,” American Gear Manufacturers Association Paper No. 209.04.

[10] Wang, S., and Morse, I. E., 1972, “Torsional response of a gear train system,” Journal of Manufacturing Science and Engineering, 94(2) pp. 583-592.

[11] Wang, S., 1974, “Analysis of nonlinear transient motion of a geared torsional,” Journal of Manufacturing Science and Engineering, 96(1) pp. 51-59.

[12] Kisher, B., 1979,“Effect of gear errors on non-linear vibrations of a gear train system,” Proceedings of the International Federation of the Theory of Machines and Mechanisms Fifth World Congress, Montreal, Canada, pp. 1122-1125.

[13] Kasuba, R., 1971, “Dynamic loads on spur gear teeth by analog computation,” American Society of Mechanical Engineers, Paper No. 71-DE-26.

[14] Lees, A. W., 1984, “Dynamic loads in gear teeth,” Proceedings of the Third International Conference on Vibrations in Rotating Machinery, Institution of Mechanical Engineers, pp. 73-79.

[15] Theodossiades, S., and Natsiavas, S., 2000, “Non-linear dynamics of gear-pair systems with periodic stiffness and backlash,” Journal of Sound and Vibration, 229(2) pp. 287-310.

[16] Moradi, H., and Salarieh, H., 2012,“Analysis of nonlinear oscillations in spur gear pairs with approximated modeling of backlash nonlinearity,” Mechanism and Machine Theory, 51pp. 14-31.

[17] Amezketa, M., Iriarte, X., Ros, J., and Pinto, J., 2009, “Dynamic model of a helical gear pair with backlash and angle-varying mesh stiffness,” Multibody Dynamics, ECCOMAS Thematic Conference, K. Arczewski, J. Fraczek and M. and Wojtyra, eds.

[18] Siyu, C., Jinyuan, T., Caiwang, L., 2011, “Nonlinear dynamic characteristics of geared rotor bearing systems with dynamic backlash and friction,” Mechanism and Machine Theory, 46pp. 466-478.

[19] Nataraj, C., and Arakere, N. K., September 12-15, 1999, “Dynamic response and stability of a spur gear pair,” 1999 ASME Design Engineering Technical Conferences, Las Vegas, Nevada, USA, DETC99/VIB-8110, pp. 1-8.

[20] Amabili, M., and Rivola, A., 1997, “Dynamic analysis of spur gear pairs: steady-state response and stability of the sdof model with state-varying meshing damping,” Mechanical Systems and Signal Processing, 11(3) pp. 375-390.

[21] Theodossiades, S., and Natsiavas, S., 2001, “Periodic and chaotic dynamics of motor-driven gear-pair systems with backlash,” Chaos, Solitons and Fractals, 12(13) pp.2427-2440.

[22] Cai-Wan, C., 2013, “Bifurcation and chaos of gear pair.

[23] Kahraman, A., and Singh, R., 1991, “Interactions between state-varying mesh stiffness and clearance non-linearities in a geared system,” Journal of Sound and Vibration, 146(1) pp. 135-156.

[24] Walha, L., Fakhfakh, T., and Haddar, M., 2009, “Nonlinear dynamics of a two-stage gear system with mesh stiffness fluctuation, bearing flexibility and backlash,” Mechanism and Machine Theory, 44(5) pp. 1058-1069.

[25] Lin, J., and Parker, R. G., 2002, “Mesh stiffness variation instabilities in two-stage gear systems,” Journal of Vibration and Acoustics, 124(1) pp. 68-76.

[26] Al-Shyyab, A. S., 2003, “Non-linear dynamic analysis of a multi-mesh gear train using multi-term harmonic balance method.”

[27] Tordion, G., and Gauvin, R., 1977, “Dynamic stability of a two-stage gear train under the influence of variable meshing stiffnesses,” Journal of Manufacturing Science and Engineering, 99(3) pp. 785-791.

[28] Parker, R., Vijayakar, S., and Imajo, T., 2000, “Non-linear dynamic response of a spur gear pair: modeling and experimental comparisons,” Journal of Sound and Vibration, 237(3) pp. 435-455.

[29] Sato, K., and Yamamoto, S., 1991, “Bifurcation sets and chaotic states of a gear system subjected to harmonic excitation,” Computational Mechanics, 7(3) pp. 173-182.

[30] Blankenship, G. W., and Singh, R., 1995, “Analytical solution for modulation sidebands associated with a class of mechanical oscillators,” Journal of Sound and Vibration, 179(1) pp. 13-36.

[31] Kahraman, A., and Blankenship, G., 1996, “Interactions between commensurate parametric and forcing excitations in a system with clearance,” Journal of Sound and Vibration, 194(3) pp. 317-336.

[32] Blankenship, G., and Kahraman, A., 1995, “Steady state forced response of a mechanical oscillator with combined parametric excitation and clearance type non-linearity,” Journal of Sound and Vibration, 185(5) pp. 743-765.

[33] Kaplan, J., 2012, “Gearbox dynamics in the modeling of rotating machinery,” MS thesis. University of Virginia.

[34] Kaplan, J., Dousti, S., Allaire, P., Nichols, B., Dimond, T., and Untaroiu, A., 2013, “Rotor dynamic modeling of gears and geared systems,” ASME Proceedings, GT2013-94654.

[35] Chaudhry, J. A., 2008, “Rotor dynamic analysis in MATLAB framework,” MS thesis. University of Virginia.

[36] D.B. Stringer, P.N. Sheth. 2009. “Geared rotor dynamic methodologies for advancing prognostic modeling capabilities in rotary-wing transmission systems.” PhD Dissertation. University of Virginia.

[37] American Petroleum Institute. 2014. “Axial and centrifugal compressors and expander-compressors for petroleum, chemical, and gas industry services.” API Standard 617, 8th Edition.

[38] Ehrich, F.F.,1999, Handbook of rotordynamics, Krieger Publishing Co, Inc.

[39] Ehrich, F.F.,1967, “The influence of trapped fluids on high speed rotor vibration”, Journal of Eng. Ind., 89, (B), pp. 806–812.

[40] Wolf, J.A.,1968, “Whirl dynamics of a rotor partially filled with liquid”, Journal of Applied Mechanics, 35, (4), pp. 676–682.

[41] Kirk, R.G., and Donald, G.N., 1983, “Design criteria for improved stability of centrifugal compressors.” Rotor Dynamical Instability, G00227, ASME, New York, June. pp. 59–71.

[42] Nicholas, J.C., 1986-1990. “Stabilizing turbomachinery with pressure dam bearings”, Encyclopedia of Fluid Mechanics, 2, pp. 1–18.

[43] S.L. Harris. 1958. “Dynamic loads on the teeth of spur gears.” Proceedings of the Institution of Mechanical Engineers 172: 87-112.

[44] H. Lin, R.L. Huston, and J.J. Coy. 1984. “Dynamic analysis of straight and involute tooth forms.” American Society of Mechanical Engineers Paper 84-DET-226.

[45] D.B. Wallace and A. Seireg. 1973. “Computer simulation of dynamic stress, deformation and fracture of gear teeth.” Journal of Engineering for Industry, Transactions of the American Society of Mechanical Engineers 95: 1108-1115.

[46] K.L. Wang and H.S. Cheng. 1981. “A numerical-solution to the dynamic load, film thickness, and surface temperatures of spur gears: Part 1 Analysis.” Journal of Mechanical Design, Transactions of the American Society of Mechanical Engineers 103: 177-187.

[47] J.Ishikawa. 1951. “Deflection of gear (in Japanese).” Trans Japan Soc. Mech. Engres 17: 103-106.

[48] K. Umezawa, S. Sato, and K. Kohno. 1984. “Influence of gear errors on rotational vibration of power transmission spur gears, 1. Pressure angle error and normal pitch error.” Bulletin of the Japanese Society of Mechanical Engineers 27: 569-575.

[49] D.C. Johnson. 1962. “Modes and frequencies of shafts coupled by straight spur gears.” Journal of Mechanical Engineering Science 4, 241-250.

[50] S. Kiyono, T. Aida, and Y. Fujii. 1978. "Vibration of helical gears 1: theoretical analysis." Bulletin of the Japanese Society of Mechanical Engineers 21: 915-922.

[51] C. Troeder, H. Peeken, A. Laschet, and K. Tooten. 1983. "Causes and effect of torque in hammering of toothed gears." Proceedings of the International Federation of the Theory of Machines and Mechanisms 6th World Congress, New Delhi, 2: 936-943.

[52] F. Kucukay. 1984. "Dynamic behavior of high speed gears." Proceedings of the Third International Conference on Vibrations in Rotating Machinery, Institution of Mechanical Engineers, 81-90.

[53] H. N. Ozguven. 1991. "A non-linear mathematical model for dynamic analysis of spur gears including shaft and bearing dynamics." Journal of Sound and Vibration 145(2): 239-260.

[54] L.D. Mitchell and J.W. Daws. 1983. "A basic approach to gearbox noise prediction." Society of Automotive Engineers Transactions 9: 3366-3379.

[55] T. Iwatsubo, S. Arii, and R. Kawai. 1984. "Coupled lateral-torsional vibration of rotor system trained by gears (I. Analysis by transfer-matrix method)." Bulletin of the Japanese Society of Mechanical Engineers 27: 271-277.

[56] Y. Cai. 1995. "Simulation on the rotational vibration of helical gears in consideration of the tooth separation phenomenon (a new stiffness function of helical involute tooth pair)." Journal of Mechanical Design, ASME 117 (3): 460-469.

[57] J. Brauer. 2004. "A general element model of involute gears." Finite elements in analysis and design 40(13-14): 1857-1872.

[58] Chien-Hsing Li, Hong-Shun Chiou and Chinghua Hung, et al. 2002. "Integration of finite element analysis and optimum design of gear systems." Finite elements in analysis and design 38 (3): 179-192.

[59] S. Chowdhury. 2010. "Effect of shaft vibration on the dynamics of gear and belt drives." PhD Dissertation from Ohio State University. UMI Dissertation Publishing.

[60] A. Kahraman, H.N. Ozguven, D.R. Houser, and J.J. Zakrajsek. 1992. "Dynamic analysis of geared rotors by finite elements." ASME Journal of Mechanical Design 114: 507-514.

[61] Choi, S. H., Glienicke, J., Han, D.C., and Urlichs, K., 1999, "Dynamic gear loads due to coupled lateral, torsional and axial vibrations in a helical geared system", Journal of Vibration and Acoustics, 124, 2, pp. 141–148.

[62] Kahraman, A. “Dynamic analysis of a multi-mesh helical gear train.” ASME Journal of Mechanical Design 116 (September 1994) 706-712.

[63] Schwibinger, P., Nordmann, R. “The influence of torsional-lateral coupling on the stability behavior of geared rotor systems.” ASME Journal of Engineering for Gas Turbines and Power110 (October 1988) 563-571.

[64] Luo, Z., and Sun, X., 1996, “Coupled torsional-lateral-axial vibration of a geared shaft system using substructure synthesis”, Mechanism and Machine Theory, 31, 3, pp. 345–352.

[65] Neriya, S.V., Bhat, R.B., and Sankar, T.S., 1985, “Coupled torsional-flexural vibration of a geared shaft system using finite element analysis”, Shock and Vibration Bulletin, 55, pp. 13–25.

[66] W. Sun, T. Chen, and X. Zhang. 2011. “A new method to calculate bending deformation of involute helical gear.” U.P.B. Science Bulletin, Series D 73 (3): 17-30.

[67] Memmott, E.A. “Case histories of high pinion vibration when eight times running speed coincides with the pinion’s fourth natural frequency.” Insights: A Publication of Dresser-Rand 10(2) (2007) 16-23.

[68] Marin, M. “Practical uses of advanced rotor dynamics tools to ensure trouble-free operation of a gearbox.” Case Study Presentation at Texas A&M 38th Turbomachinery Symposium (2009).

[69] Cloud, C. H, Byrne, J.M, He, M., Vasquez, J.A, Hattenbach, T.J. 2014. “Analysis of Super-synchronous, Sub-mesh Frequency Vibrations in a Speed Increaser Gearbox.”

[70] White, M.F., Chan, S.H. “The subsynchronous dynamic behavior of tilting-pad journal bearings.” ASME Journal of Tribology 114 (1992) 167-173.

[71] Buckingham, E. Spur gears. McGraw Hill. 1928